Mathematical Modelling and Numerical Simulation with Applications

Editor-in-Chief
Mehmet Yavuz, PhD

MATHEMATICAL MODELLING AND NUMERICAL SIMULATION WITH APPLICATIONS

- **Kumar, Sunil** - National Institute of Technology, India

- **Lupulescu, Vasile** - Constantin Brâncuşi University of Târgu-Jiu, Romania

- **Merdan, Hüseyin** - TOBB University of Economy and Technology, Department of Mathematics, Türkiye

- **Mohammed S. Abdo** - Hodeidah University, Al-Hodeidah, Department of Mathematics, Yemen

- **Muñoz-Pacheco, Jesus Manuel** - Faculty of Electronics Sciences at the Autonomous University of Puebla (BUAP), Mexico

- **Noeiaghdam, Samad** - Irkutsk National Research Technical University, Russian Federation

- **Owolabi, Kolade** - Federal University of Technology, Nigeria

- **Otero-Espinar, Maria Victoria** - University of Santiago de Compostela, Spain

- **Panigoro, Hasan S.** - Universitas Negeri Gorontalo, Indonesia

- **Povstenko, Yuriy** - Jan Dlugosz University in Czestochowa, Poland

- **Qureshi, Sania** - Mehran University of Engineering and Technology, Pakistan

- **Sabatier, Jocelyn** - Bordeaux University, France

- **Safaei, Mohammad Reza** - Florida International University, USA

- **Salahshour, Soheil** - Bahçeşehir University, Türkiye

- **Sarı, Murat** - Yıldız Technical University, Türkiye

- **Singh, Jagdev** - JECRC University, India

- **Valdés, Juan Eduardo Nápoles** - Universidad Nacional del Nordeste, Argentina

- **Veeresha, Pundikala** - Christ University, India

- **Weber, Gerhard-Wilhelm** - Poznan University of Technology, Poland

- **Xu, Changjin** - Guizhou University of Finance and Economics, China

- **Yang, Xiao-Jun** - China University of Mining and Technology, China

- **Yuan, Sanling** - University of Shanghai for Science and Technology, China

Contents

Research Articles

RESEARCH PAPER

Mathematical approaches to controlling COVID-19: optimal control and financial benefits

Saida Id Ouaziz [ID] [1,*,‡] and **Mohammed El Khomssi** [ID] [1,‡]

[1]Department of Mathematics, Laboratory of Modeling and Mathematical Structures, Sidi Mohamed Ben Abdellah University, Route d'Ilmouzzer, 30000 Fez, Morocco

*Corresponding Author
‡ saidaidouaziz7@gmail.com (Saida Id Ouaziz); khomsixmath@yahoo.fr (Mohammed El Khomssi)

Abstract

The global population has suffered extensively as an effect of the coronavirus infection, with the loss of many lives, adverse financial consequences, and increased impoverishment. In this paper, we propose an example of the non-linear mathematical modeling of the COVID-19 phenomenon. Using the fixed point theorem, we established the solution's existence and unicity. We demonstrate how, under the framework, the basic reproduction number can be redefined. The different equilibria of the model are identified, and their stability analyses are carefully examined. According to our argument, it is illustrated that there is a single optimal control that can be used to reduce the expense of the illness load and applied processes. The determination of optimal strategies is examined with the aid of Pontryagin's maximum principle. To support the analytical results, we perform comprehensive digital simulations using the Runge-Kutta 4th-order. The data simulated suggest that the effects of the recommended controls significantly impact the incidence of the disease, in contrast to the absence of control cases. Further, we calculate the incremental cost-effectiveness ratio to assess the cost and benefits of each potential combination of the two control measures. The findings indicate that public attention, personal hygiene practices, and isolating oneself will all contribute to slowing the spread of COVID-19. Furthermore, those who are infected can readily decrease their virus to become virtually non-detectable with treatment consent.

Keywords: Cost-effectiveness; optimal control; system dynamics
AMS 2020 Classification: 34D20; 92D30; 49J15; 34C60

1 Introduction

The world is facing an unprecedented threat. The pandemic of COVID-19 has spread rapidly throughout the worldwide community. As a result of this epidemic, suffering has spread, the lives of billions of people have turned upside down, and the global economy is under threat. Even

wealthy countries with robust healthcare systems are under pressure as the wave of this pandemic begins to reach countries already suffering humanitarian crises from conflicts, natural disasters, and climate change.

The first instance of a virus whose etiology is completely unexplained was identified in the Chinese, on December 31, 2019 [1]. Moreover, this pandemic demands immediate and sustained international action. While reducing the scale of the terrible human and economic toll across the globe is our primary concern, we are also very concerned about the underlying problems that this emergency reveals, particularly for those most at risk of disastrous consequences. This group of viruses called coronaviruses is responsible for gastrointestinal and respiratory illnesses in many different world locations. Both the common cold and more severe illnesses can be respiratory disorders. Since they resemble coronas under the microscope, coronaviruses received their name. An infused envelope surrounds the genetic material center of the virus. It resembles a crown as a result of this. In Latin, the corona is a word that signifies "crown". Most people infected with the virus have minor or moderate lung disease and recover without seeking treatment. Some, however, get severe illnesses and need to see a doctor. Seniors and patients with prior illnesses such as cancer, glucose intolerance, permanent lung illness, or heart disease are more prone to have a severe variation. The most effective strategy to avoid and limit transmission of COVID-19 is to be knowledgeable about the illness and how it is spread. Anyone, at any age, can contract the illness and become extremely ill or die from it.

The World Health Organization (WHO) has designated the 2019 coronavirus disease (COVID-19) as a global epidemic. To stop the virus from spreading further, a concerted international effort is required. "Occurring over a huge geographic area and impacting an extraordinarily high proportion of the population" is how a pandemic is described. The H1N1 flu pandemic in 2009 was the most recent pandemic to be reported globally. Mathematical models hold significance as they elucidate the fundamental mathematical structure of a specific phenomenon without delving into extraneous details. The purpose is to concentrate on certain facets of the issue, abstracting away other dimensions. Consequently, mathematical models remain pertinent by showcasing the essential mathematical core within a given context devoid of excess information [2] (see also [3], [4], [5] and reference therein).

To reduce the COVID-19 disease's transmission dynamics, the authors of [6] studied and discussed an optimal control model. The limitations of the illness and the associated expenses are also minimized by suggesting the most appropriate control measures. They established its existence and specificity. Further data simulations are performed to observe the importance of control efforts to stop the propagation of the illness in society according to a study that was done on the spread of disease between countries based on an estimated COVID-19 mathematical model. The study in [7] explores a mathematical model that involves the effects of resource constraints on COVID-19 transmission patterns in the population through the use of the Caputo derivative. The basic reproduction rate R_0 was determined, and the suggested model's asymptotic stability was investigated. According to their findings, the number of people with the virus increases, while cure rates by hospitalization increase. The authors of [8] analyze the dynamics of a fractional-order COVID-19 model and suggest an efficient computational technique based on the domain discretization and memory concept to numerically solve this fractional-order corona model The coronavirus is an enclosed virus with a single-stranded, positive-sense RNA that is a component of the Nidovirales demand and the relative Coronaviridae. It is widely transmitted among mammals and humans [9]. To understand COVID-19's effects on the environment, the authors suggest mathematical modeling and data analysis in [10]. Such a pandemic is mathematically modeled as a deterministic infectious illness. They use the fixed-point theorem to confirm the originality of the solution, and it is inferred that the sample displays both endemic and disease-free equilibrium points. Further,

they propose an optimal control to find the best strategy to eliminate the virus.

With the Atangana-Baleanu derivative, [11] provides a rigorous mathematical analysis of the intricacies of smoking behavior and its public health implications. The authors in [12] propose and analyze a compartmental deterministic framework to explain the behavior of the student population's illicit drug usage. The bifurcation phenomenon is identified using the Center Manifold Theorem. Efficiency analysis is applied to understand how the dynamics of illicit drug use by the student group are influenced by the settings of the system. Assessing the epidemiology of the patients, the clinical course of the condition, and the available treatment options, Tang et al. created a model [13]. A sensitivity analysis suggests that actions regarding isolation and quarantine can lower it. Numerous mathematical model types use statistical techniques to research the COVID-19 virus (see, for example, [14]).

The authors of [15] Create a compartmental model to evaluate the effects of mask use on the population as a whole among the general, asymptomatic public, some of whom may be asymptomatically infected. They imply that the public's adoption of face masks has a strong potential for reducing the spread of the pandemic and its burden. The study in [16] examines the affordability and effectiveness of three malaria-prevention measures. They found that one of the conclusions was that treating infected people and spraying insecticides was the most cost-effective way of eliminating malaria. The authors of [17] treat three disease compartments: infectious, quarantined, and exposed-asymptomatic, and they indicate that the rate of treatment is a saturated type to account for the impact of scarce medical facilities. By taking into account the implications on infection transmission rates caused by the adoption of lockdown policies by numerous countries, they also developed an optimal control issue. In [18], a decision analytical model of different cases of ratios of people without symptoms of COVID-19 and dangerous intervals predicts propagation from untreated persons for more than half of all transmissions. Thus, the virus mitigation measures that can halt the disease's circulation must receive resources and health information.

The literature contains several mathematical models that explain how COVID-19 propagates and recommend measures to optimize virus transmission. The authors in [19] observed that, in the absence of immunization, using either physical distancing or social separation procedures is the most economical and successful management approach in Saudi Arabia. In [20], a study introduces a mathematical framework for monitoring and predicting the spread of COVID-19 in India, using data up to April 30, 2020. The authors calculate the ratio R_0 and perform local and global stability analyses. The template expects a significant spread with a peak after almost 60 days, implying the persistence of the illness even after reaching a certain level. The study in [21] presents a new mathematical model to analyze the omicron variant of COVID-19, exploring stability conditions and extensions. Using realistic data from South Africa, numerical simulations highlight the effectiveness of WHO recommendations in reducing infection. Investigations on the transmission of COVID-19 and epidemic patterns concentrate on sample selection and adequate control measures. The essay [22] reviews mathematical models, highlighting the importance of reasonable parameter control and combined multi-model modeling for future interventions. The previously mentioned literature serves as an inspiration for our work's motivation and originality. In our case, we have adopted this model as the most realistic example as it deals with the predominant classes in society for this virus by presenting declared and undeclared infections, as well as contributing to a more thorough comprehension of the course of the disease and enabling Morocco to modify its disorder treatment tactics.

The structure of this essay is as detailed below: In Section 2, we present some theorems used in this essay. The mathematical model is developed in Section 3. In Section 4, the well-established nature of the system is examined. The ratio $\mathcal{R}_0$ is given, as are the local and global stability of the equilibrium points. Section 5 illustrates the importance of every model factor concerning

$\mathcal{R}_0$. In Section 6, an analysis of an optimal control model is provided. Data of simulation and verification are given in Section 7, while, Section 8 is dedicated to the model's cost-effectiveness analysis. Eventually, Section 9 summarizes the current work.

2 Fundamental prerequisites

The upcoming sections of the paper will utilize the following theorems:

The following theorems (see [23, 24]), whose proofs will be given in the later sections, will be used to discuss the constancy of the template's steadiness point:

Theorem 3
If $\mathcal{R}_0 < 1$, the point of disease-free equilibrium DFE is locally asymptotically stable; nevertheless, if $\mathcal{R}_0 > 1$, it is unstable.

Theorem 4
If $\mathcal{R}_0 < 1$, the DFE, $\mathcal{E}_0$ of model (2), is globally equilibrium-stable.

Theorem 6
Where $\mathcal{R}_0 > 1$, the persistent steadiness point $\tilde{\mathcal{E}}$ is locally asymptotically stable.

Theorem 7
The only persistent steadiness state of (2) is globally asymptotically stable when $\mathcal{R}_0 > 1$.

3 Description of the model

To establish a new deterministic model, we begin by analyzing crucial characteristics of the COVID-19 pandemic, such as the presence of individuals who evaluated positively for the virus but did not exhibit any indications of illness and the splitting of pathogenic categories into two crucial categories: Contaminated people and ill individuals who have not yet received an official diagnosis. The general community $N(t)$ is partitioned into six sub-populations: sensitive $\mathfrak{S}_I(t)$, unprotected $E_I(t)$, contaminated or exhibiting indications $I(t)$, those who are ill but are not yet officially diagnosed $\mathcal{I}_{nd}$ recuperated individuals $R(t)$ and healthy $H(t)$, Π is the recruitment number, μ is the natural mortality rate, μ_1 is the patient mortality due to human coronavirus infection. ν represents the rate of infection diffusion from E_I to $\mathfrak{S}_I$, and σ is the saturation constant, β stands for incidence rate, α indicates the percentage of people from the exposed compartment who join the diseased subpopulation, δ is the rate at which those who are exposed to an infection contract it, γ is the interaction between $I_n d$ and R, while θ is the rate at which susceptible people become uninfected, η is the rate of recovered individuals from COVID-19, when the entire population grows to a level equivalent to $N = \mathfrak{S}_I + E_I + I + \mathcal{I}_{nd} + R + H$. Without estimating the number of pathogens present within each individual, models built on this type of construction merely represent the infected individuals' community attitude. Our model, based on an illustration depicting the biological mechanism of coronavirus in humans, is depicted in Figure 1.

To consistently explore a mathematical framework of a real-world phenomenon, it is vital to specify these criteria by indicating a set of conditions. We enumerate these conditions in the above section, as outlined in [25]:

(a) Depending on the prototype, an estimated intake of susceptible individuals costs Π per unit of time.

(b) It simply considers how the pandemic progresses among individuals.

(c) The framework provides for the natural death of each sub-population in proportion to its size. Although most studies indicate that all people are contaminated with the virus, it is not possible to exclude the minority who are not (the individuals H), which is due to immunity and lifestyle. The dynamics of infection in the human populace are represented by the following set of six distinct equations and can be formulated in the following manner:

$$
\begin{cases}
\dfrac{d\mathfrak{S}_I}{dt} & = \Pi - \nu\mathfrak{S}_I I - (\mu + \theta)\mathfrak{S}_I, \\[2mm]
\dfrac{dE_I}{dt} & = \nu\mathfrak{S}_I I - \delta E_I - \mu E_I, \\[2mm]
\dfrac{dI}{dt} & = \alpha\delta E_I - \eta I - (\mu + \mu_1)I, \\[2mm]
\dfrac{d\mathcal{I}_{nd}}{dt} & = (1-\alpha)\delta E_I - \gamma\mathcal{I}_{nd} - (\mu + \mu_1)\mathcal{I}_{nd}, \\[2mm]
\dfrac{dR}{dt} & = \eta I + \gamma\mathcal{I}_{nd} - \mu R, \\[2mm]
\dfrac{dH}{dt} & = \theta\mathfrak{S}_I - \mu H,
\end{cases}
\tag{1}
$$

with the initial condition: $\mathfrak{S}_I(0 \geq 0, E_I(0) \geq 0, I(0) \geq 0, \mathcal{I}_{nd}(0) \geq 0, R(0) \geq 0, H(0) \geq 0$.

- **Characteristics of susceptible individuals:**

The population recruits susceptible members $\mathfrak{S}_I$ at a constant rate, Π, and the natural mortality rate μ reduces their numbers, the population $\mathfrak{S}_I$ will join the subpopulation I passing through E_I at the rate ν, although some of these individuals will have contact with H at a steady rate θ.

- **Characteristics of exposed people:**

The rate at which the exposed person E_I declines is δ for asymptomatic people and μ for natural death. Individuals E_I and sensitive individuals $\mathfrak{S}_I$ shall immediately interact at a steady rate of ν, E_I gets sicker by a fixed percentage α at a rate δ, where part of this population is not declared as diseased $((1-\alpha)\delta)$.

- **Characteristics of undeclared people:**

Without a diagnosis, the classes $\mathcal{I}_{nd}$ are transferred to the recovery classes at the rate γ.

- **Characteristics of healthy individual:**

Sensitive individuals $\mathfrak{S}_I$ interact with individuals in the population that is immune and has never contracted the disease (H) at a θ rate.

- **Characteristics of individuals with disease signs:**

The unaffected people give birth to the affected people when the coronavirus clinical symptoms progress. A constant share α of the exposed people transitions to the affected classes at a rate of δ. the class I transferred at a rate of η to the recover classes.

- **Characteristics of recuperated individuals:**

It can be presumed that the population that has recovered has long-lasting protection against coronavirus. Individual $\mathcal{I}_{nd}$ and population I recover from the coronavirus at γ and η rates, respectively. The rate of recovery deaths is μ.

- Characteristics of healthy individuals:

According to a study by Imperial College London, people with a high quantity of T cells (white blood corpuscle that contributes to the organism's defense against infection) from the coronaviruses responsible for the common cold are less likely to contract SARS-CoV-2, the virus responsible for COVID-19. So we named these individuals 'healthy' H. Thus, the sensible population $\mathfrak{S}_I$ moved to the category H at a rate of θ. Table 1 lists the parameters and variables in detail.

Table 1. Model parameters and their meanings

Parameters	Description
$\mathfrak{S}_I(t)$	The portion of sensitive individuals who are in direct interaction with an infected individual.
$E_I(t)$	The portion of those revealed to I that does not maintain them out.
$I(t)$	The portion of those who are impacted.
$\mathcal{I}_{nd}(t)$	The portion of non-reported infected person.
$R(t)$	The portion of rescued people.
$H(t)$	The portion of strictly asymptomatic individuals who have never caught the infection.
Π	Recruitment number
μ	The rate of natural mortality
μ_1	Natural death rate of human coronavirus illness patients
ν	Rate of diffusion of infection from E_I to $\mathfrak{S}_I$
σ	The constant of saturation
β	Incidence rate
α	Percentage of people from the exposed compartment who eventually migrate to the sick subpopulation
δ	The rate of illness in exposed individuals
η	Rate of COVID-19 patients that have recovered
γ	The rate at which $\mathcal{I}_{nd}$ interacts with R
θ	The rate at which sensitive persons become uninfected

4 Qualitative analysis of the model

This section will investigate a few key aspects of the suggested model, including its boundary, the presence of a steady state, and the fundamental reproduction number.

The presence and singular nature of the solutions to the framework

With applying the fixed point theorem and the premises that $\mathcal{H} = (\mathfrak{C}(\mathfrak{J}))^6$, and $\mathfrak{C}(\mathfrak{J})$ remains a Banach domain for continuous functions along the interval $\mathfrak{J}$ during the norm

$$\|\mathfrak{g}_i(t)\|_{i=1,\dots,6} = \sum_{i=1}^{6} \|\mathfrak{g}_i\|_\infty,$$

where, $(\mathfrak{g}_1, \mathfrak{g}_2, \mathfrak{g}_3, \mathfrak{g}_4, \mathfrak{g}_5, \mathfrak{g}_6) = (\mathfrak{S}_I, E_I, I, \mathcal{I}_{nd}, R, H)$.
It can be demonstrated that the configuration outlined (1) has a valid outcome. Here, $\|.\|_\infty$ represents the maximum norm in $\mathfrak{C}(\mathfrak{J})$.

For the sake of simplicity, let us examine:

$$\Theta_1(t, \mathfrak{S}_I) = \Pi - \nu \mathfrak{S}_I I - (\mu + \theta)\mathfrak{S}_I,$$
$$\Theta_2(t, E_I) = \nu \mathfrak{S}_I I - \delta E_I - \mu E_I,$$
$$\Theta_3(t, I) = \alpha \delta E_I - \eta I - (\mu + \mu_1)I,$$
$$\Theta_4(t, \mathcal{I}_{nd}) = (1 - \alpha)\delta E_I - \gamma \mathcal{I}_{nd} - (\mu + \mu_1)\mathcal{I}_{nd},$$
$$\Theta_5(t, R) = \eta I + \gamma \mathcal{I}_{nd} - \mu R,$$
$$\Theta_6(t, H) = \theta \mathfrak{S}_I - \mu H.$$

To prove this theorem, we suppose that
$\|\mathfrak{S}_I\| \le \mathfrak{w}_1, \|E_I\| \le \mathfrak{w}_2, \|I\| \le \mathfrak{w}_3, \|\mathcal{I}_{nd}\| \le \mathfrak{w}_4, \|R\| \le \mathfrak{w}_5, \|H\| \le \mathfrak{w}_6$ where $\mathfrak{w}_i, i = 1, ..., 6$ are constant positives. Hence, we denote

$$\mathfrak{k}_1 = \nu \mathfrak{w}_3 + \theta + \mu,$$
$$\mathfrak{k}_2 = \alpha \delta + \delta + \mu,$$
$$\mathfrak{k}_3 = \eta + \mu + \mu_1,$$
$$\mathfrak{k}_4 = \gamma + \mu + \mu_1,$$
$$\mathfrak{k}_5 = \mathfrak{k}_6 = \mu.$$

Theorem 1 *If the proposed inequality is true, the $\Theta_{i=1,...6}$ are adapted to the Lipschitz state and compaction.*

$$0 \le \mathfrak{k}_{i=1,...,6} < 1.$$

Proof Consider the functions $\mathfrak{S}_{I_1}$ and $\mathfrak{S}_{I_2}$, so

$$\|\Theta_1(t, \mathfrak{S}_{I_1}) - \Theta_1(t, \mathfrak{S}_{I_2})\| = \| - (\nu I + \mu + \theta)(\mathfrak{S}_{I_1} - \mathfrak{S}_{I_2})\| \le (\nu \mathfrak{w}_3 + \theta + \mu)\|\mathfrak{S}_{N_1}(t) - \mathfrak{S}_{N_2}(t)\|.$$

Thus

$$\|\Theta_1(t, \mathfrak{S}_{I_1}) - \Theta_1(t, \mathfrak{S}_{I_2})\| \le \mathfrak{k}_1 \|\mathfrak{S}_{I_1}(t) - \mathfrak{S}_{I_2}(t)\|.$$

The Lipschitz criterion is achieved for Θ_1. Similarly, the Lipschitz condition for Θ_2, Θ_3, Θ_4, Θ_5, and Θ_6 may be easily proven and is the same as stated previously:

$$\|\Theta_2(t, E_{I_1}) - \Theta_2(t, E_{I_2})\| \le \mathfrak{k}_2 \|E_{I_1}(t) - E_{I_2}(t)\|,$$

$$\|\Theta_3(t, I_1) - \Theta_3(t, I_2)\| \le \mathfrak{k}_3 \|I_1(t) - I_2(t)\|,$$

$$\|\Theta_4(t, U_{d_1}) - \Theta_4(t, U_{d_2})\| \le \mathfrak{k}_4 \|U_{d_1}(t) - U_{d_2}(t)\|,$$

$$\|\Theta_5(t, R_1) - \Theta_5(t, R_2)\| \le \mathfrak{k}_5 \|R_1(t) - R_2(t)\|,$$

$$\|\Theta_6(t, H_1) - \Theta_6(t, H_2)\| \leq \mathfrak{k}_6 \|H_1(t) - H_2(t)\|.$$

The solution's positivity

State variables of model (1) and relative factors must be positive for the foreseeable future, as this model predicts the population of individuals, which will be established by the following theorem:

Theorem 2 *For model (1), the feasible area is specified by:*

$$\mathcal{C} = \left\{ (\mathfrak{S}_I, E_I, I, \mathcal{I}_{nd}, R, H) \in R_+^6; \middle| \; \mathfrak{S}_I, E_I, I, \mathcal{I}_{nd}, R, H \geq 0, N \leq \frac{\Pi}{\mu} \right\}.$$

Proof Count on the value of factors to be continuous. Predicting the following from system (1) is straightforward (see [26]):

$$\frac{d\mathfrak{S}_I}{dt} \geq -(\nu I + \theta + \mu)\mathfrak{S}_I.$$

After that, applying the constant variation formula:

$$\frac{d\mathfrak{S}_I}{dt} \geq \mathfrak{S}_I(0) \exp(-(\nu I + \theta + \mu)t) \geq 0.$$

In the same way, we prove that: $\frac{dE_I}{dt} \geq 0, \frac{dI}{dt} \geq 0, \frac{d\mathcal{I}_{nd}}{dt} \geq 0, \frac{dR}{dt} \geq 0, \frac{dH}{dt} \geq 0$. As a result, when $t \geq 0$, all solutions are positive.
Or,

$$N = \mathfrak{S}_I + E_I + I + \mathcal{I}_{nd} + R + H.$$

Then we have

$$\frac{dN}{dt} = \Pi - \mu N(t) - \mu_1(I + \mathcal{I}_{nd}).$$

When the illness is absent

$$\frac{dN}{dt} = \Pi - \mu N(t),$$

then

$$\int \frac{dN}{dt} = \int (\Pi - \mu N(t)) dt.$$

So

$$N(t) = N(0) \exp(-\int_0^t \mu ds) + \int_0^t \Pi \exp(-\int_s^t \mu d\vartheta),$$

if

$$N(0) \leq \frac{\Pi}{\mu},$$

thus,

$$N(t) \leq \frac{\Pi}{\mu} \exp\left(-\int_0^t \mu ds\right) + \int_0^t \Pi \exp(-\mu(t-s)ds) \leq \frac{\Pi}{\mu} \exp\left(-\int_0^t \mu ds\right) + \frac{\Pi}{\mu},$$

when

$$t \to +\infty, \qquad N(t) \leq \frac{\Pi}{\mu}.$$

It indicates that the region $\mathcal{C}$ is a positively invariant set for system (1).

Local stability of DFE

Because $H(t)$ has not been presented in the first five equations, system (1) can be expressed below

$$\begin{cases} \dfrac{d\mathfrak{S}_I}{dt} = \Pi - \nu\mathfrak{S}_I I - (\mu + \theta)\mathfrak{S}_I, \\ \dfrac{dE_I}{dt} = \nu\mathfrak{S}_I I - \delta E_I - \mu E_I, \\ \dfrac{dI}{dt} = \alpha\delta E_I - \eta I - (\mu + \mu_1)I, \\ \dfrac{d\mathcal{I}_{nd}}{dt} = (1-\alpha)\delta E_I - \gamma\mathcal{I}_{nd} - (\mu + \mu_1)\mathcal{I}_{nd}, \\ \dfrac{dR}{dt} = \eta I + \gamma\mathcal{I}_{nd} - \mu R. \end{cases} \tag{2}$$

The model's disease-free equilibrium point is reached by setting all of the model (2)'s formulas to zero and disabling them:

$$\mathcal{E}_0 = (\mathfrak{S}_I^0, E_I^0, I^0, \mathcal{I}_{nd}^0, R_0),$$

where $E_I = I = \mathcal{I}_{nd} = R = 0$, and $\mathfrak{S}_I^0 = \frac{\Pi}{\theta + \mu}$.

The effective reproduction number $\mathcal{R}_0$

The threshold provided by the dimensionless basic reproduction number is vital in determining whether the disease survives or disappears in the individual. $\mathcal{R}_0$ can be defined more broadly as the number of new infections produced by a typical infective population at an infection spot zero-point equilibrium analysis of the stability of the equilibrium points depends on the model's effective reproduction number. Moreover, the projected number of indirect connections caused by the implementation of a newly discovered member among a sensitive group is estimated using $\mathcal{R}_0$. Using the notion of a next-generation matrix (see [27]), it is possible to calculate the basic reproduction number $\mathcal{R}_0$. Starting with the categories that were most recently infected, we recast

the model's equations:

$$
\begin{cases}
\dfrac{dE_I}{dt} = \nu \mathcal{S}_I I - (\delta + \mu)E_I, \\[2mm]
\dfrac{dI}{dt} = \alpha \delta E_I - (\eta + \mu)I, \\[2mm]
\dfrac{d\mathcal{I}_{nd}}{dt} = (1 - \alpha)\delta E_I - (\gamma + \mu)\mathcal{I}_{nd}, \\[2mm]
\dfrac{dR}{dt} = \eta I + \gamma \mathcal{I}_{nd} - \mu R.
\end{cases}
\tag{3}
$$

Deriving the fundamental reproduction number $\mathcal{R}_0$ involves utilizing the spectrum's diameter ρ in the generation matrix FV^{-1}. In this process, we consider the non-negative matrix F and the non-singular matrix V, representing the creation of new infections and the transition component in the system (2), respectively.

$$
\mathbb{F} = \begin{pmatrix} \nu I \mathcal{S}_I \\ 0 \\ 0 \\ 0 \end{pmatrix}, \quad \text{and} \quad
\mathbb{V} = \begin{pmatrix} (\delta + \mu)E_I \\ -\alpha \delta E_I + (\eta + \mu + \mu_1)I \\ -(1 - \alpha)\delta E_I + (\gamma + \mu + \mu_1)\mathcal{I}_{nd} \\ -\eta I - \gamma \mathcal{I}_{nd} + \mu R \end{pmatrix},
$$

as $F = [\frac{\partial \mathbb{F}}{\partial X_j}]$, and $V = [\frac{\partial \mathbb{V}}{\partial X_j}]$, we have $(X_j = (E_I, I, \mathcal{I}_{nd}, R))$

$$
F = \frac{\partial \mathbb{F}}{\partial X_j}(\mathcal{E}_0) = \begin{pmatrix} 0 & \nu \mathcal{S}_I^0 & 0 & 0 \\ 0 & 0 & 0 & 0 \\ 0 & 0 & 0 & 0 \\ 0 & 0 & 0 & 0 \end{pmatrix},
$$

and

$$
V = \frac{\partial \mathbb{V}}{\partial X_j}(\mathcal{E}_0) = \begin{pmatrix} (\delta + \mu) & 0 & 0 & 0 \\ -\alpha \delta & (\eta + \mu + \mu_1) & 0 & 0 \\ -(1 - \alpha)\delta & 0 & (\gamma + \mu + \mu_1) & 0 \\ 0 & -\eta & -\gamma & \mu \end{pmatrix}.
$$

We have

$$
|V| = \mu(\gamma + \eta)(\eta + \mu)(\delta + \mu).
$$

Then

$$
com(V) = \begin{pmatrix} \mathfrak{w}_{11} & \mathfrak{w}_{12} & \mathfrak{w}_{13} & \mathfrak{w}_{14} \\ \mathfrak{w}_{21} & \mathfrak{w}_{22} & \mathfrak{w}_{23} & \mathfrak{w}_{24} \\ \mathfrak{w}_{31} & \mathfrak{w}_{32} & \mathfrak{w}_{33} & \mathfrak{w}_{34} \\ \mathfrak{w}_{41} & \mathfrak{w}_{42} & \mathfrak{w}_{43} & \mathfrak{w}_{44} \end{pmatrix},
$$

with

$$\mathfrak{w}_{11} = \mu(\eta + \mu + \mu_1)(\gamma + \mu + \mu_1),$$
$$\mathfrak{w}_{12} = \mu(\gamma + \mu + \mu_1)\alpha\delta,$$
$$\mathfrak{w}_{13} = \mu(1 - \alpha)\delta(\eta + \mu + \mu_1),$$
$$\mathfrak{w}_{14} = \eta(\gamma + \eta)\alpha\delta + \gamma(1 - \alpha)\delta(\eta + \mu),$$
$$\mathfrak{w}_{22} = \mu(\delta + \mu)(\gamma + \mu + \mu_1),$$
$$\mathfrak{w}_{23} = -\mu,$$
$$\mathfrak{w}_{24} = \eta(\gamma + \mu + \mu_1)(\delta + \mu),$$
$$\mathfrak{w}_{32} = -\mu,$$
$$\mathfrak{w}_{33} = \mu(\delta + \mu)(\eta + \mu + \mu_1),$$
$$\mathfrak{w}_{34} = \gamma(\delta + \mu)(\eta + \mu + \mu_1),$$
$$\mathfrak{w}_{44} = (\gamma + \mu + \mu_1)(\delta + \mu)(\eta + \mu + \mu_1),$$
$$\mathfrak{w}_{21} = \mathfrak{w}_{31} = \mathfrak{w}_{41} = \mathfrak{w}_{42} = \mathfrak{w}_{43} = 0,$$

then

$$V^{-1} = \frac{1}{|V|} \begin{pmatrix} \mathfrak{w}_{11} & \mathfrak{w}_{21} & \mathfrak{w}_{31} & \mathfrak{w}_{41} \\ \mathfrak{w}_{12} & \mathfrak{w}_{22} & \mathfrak{w}_{32} & \mathfrak{w}_{42} \\ \mathfrak{w}_{13} & \mathfrak{w}_{23} & \mathfrak{w}_{33} & \mathfrak{w}_{43} \\ \mathfrak{w}_{14} & \mathfrak{w}_{24} & \mathfrak{w}_{34} & \mathfrak{w}_{44} \end{pmatrix}$$

$$= \frac{1}{|V|} \begin{pmatrix} \mu(\eta + \mu + \mu_1)(\gamma + \mu + \mu_1) & 0 & 0 & 0 \\ \mu(\gamma + \mu + \mu_1)\alpha\delta & \mu(\delta + \mu)(\gamma + \mu + \mu_1) & -\mu & 0 \\ \mu(1 - \alpha)\delta(\eta + \mu + \mu_1) & -\mu & \mathfrak{w}_{33} & 0 \\ \varsigma_1 & \varsigma_2 & \varsigma_3 & \varsigma_4 \end{pmatrix},$$

$$\varsigma_1 = \eta(\gamma + \mu)\alpha\delta + \gamma(1 - \alpha)\delta(\eta + \mu + \mu_1),$$
$$\varsigma_2 = \eta(\gamma + \mu + \mu_1)(\delta + \mu),$$
$$\varsigma_3 = \gamma(\delta + \mu)(\eta + \mu + \mu_1),$$
$$\varsigma_4 = (\gamma + \mu + \mu_1)(\delta + \mu)(\eta + \mu + \mu_1),$$

thus

$$FV^{-1} = \frac{1}{|V|} \begin{pmatrix} \nu\mathbb{S}_I^0\mathfrak{w}_{12} & \nu\mathbb{S}_I^0\mathfrak{w}_{22} & \nu\mathbb{S}_I^0\mathfrak{w}_{32} & \nu\mathbb{S}_I^0\mathfrak{w}_{42} \\ 0 & 0 & 0 & 0 \\ 0 & 0 & 0 & 0 \\ 0 & 0 & 0 & 0 \end{pmatrix}.$$

Therefore, the reproduction number ($\mathcal{R}_0$) is given below:

$$\mathcal{R}_0 = \rho(FV^{-1}) = \frac{\nu\mathbb{S}_I^0\mathfrak{w}_{12}}{|V|} = \frac{\nu\Pi\alpha\delta}{(\theta + \mu)(\eta + \mu + \mu_1)(\delta + \mu)}.$$

Theorem 3 *If $\mathcal{R}_0 < 1$, the DFE point is locally asymptotically stable; if $\mathcal{R}_0 > 1$, it is unstable.*

Proof To prove this theorem, we start the Jacobian matrix for the given set of equations in the model (2):

$$J = \begin{pmatrix} -(\nu I + \theta + \mu) & 0 & -\nu \mathfrak{S}_I & 0 & 0 \\ \nu I & -(\delta + \mu) & \nu \mathfrak{S}_I & 0 & 0 \\ 0 & \alpha \delta & -(\eta + \mu + \mu_1) & 0 & 0 \\ 0 & (1-\alpha)\delta & 0 & -(\gamma + \mu + \mu_1) & 0 \\ 0 & 0 & \eta & \gamma & -\mu \end{pmatrix}. \tag{4}$$

Calculating the Jacobean matrix (4) at the point $\mathcal{E}_0$ yields the next results:

$$J(\mathcal{E}_0) = \begin{pmatrix} -(\theta + \mu) & 0 & -\frac{\nu \Pi}{\theta + \mu} & 0 & 0 \\ 0 & -(\delta + \mu) & \frac{\nu \Pi}{\theta + \mu} & 0 & 0 \\ 0 & \alpha \delta & -(\eta + \mu + \mu_1) & 0 & 0 \\ 0 & (1-\alpha)\delta & 0 & -(\gamma + \mu + \mu_1) & 0 \\ 0 & 0 & \eta & \gamma & -\mu \end{pmatrix}.$$

The next form of an eigenvalue polynomial has been computed by using the Jacobian matrix:

$$\mathfrak{P}(\lambda) = -(\mu + \lambda)(\theta + \mu)(\gamma + \mu + \mu_1 + \lambda)\bar{\mathfrak{P}}(\lambda), \tag{5}$$

where

$$\bar{\mathfrak{P}}(\lambda) = (\delta + \mu + \lambda)(\eta + \mu + \mu_1 + \lambda) - \frac{\alpha \delta \nu \Pi}{\theta + \mu},$$

$$= \lambda^2 + \lambda(\eta + \mu + \mu_1 + \delta + \mu) + (\delta + \mu)(\eta + \mu + \mu_1) - \frac{\alpha \delta \nu \Pi}{\mu}.$$

From equation (5), we have

$$\lambda_1 = -\mu < 0,$$
$$\lambda_2 = -(\gamma + \mu + \mu_1) < 0,$$
$$\lambda_3 = -(\theta + \mu) < 0.$$

From the expression of $\bar{\mathcal{P}}(\lambda)$, we have

$$\Delta = (\eta + \mu + \mu_1 + \delta + \mu)^2 + 4\left(\frac{\alpha \delta \nu \Pi}{\theta + \mu} - (\delta + \mu)(\eta + \mu + \mu_1)\right) > 0.$$

As

$$\frac{\alpha \delta \nu \Pi}{\theta + \mu} \geq (\delta + \mu)(\eta + \mu + \mu_1), \text{ then } \Delta > 0.$$

Furthermore

$$\lambda_3 = -\frac{(\eta + \mu + \mu_1 + \delta + \mu) + \sqrt{\Delta}}{2} < 0, \quad \lambda_4 = \frac{-(\eta + \mu + \mu_1 + \delta + \mu) + \sqrt{\Delta}}{2},$$

$$\lambda_4 < 0 \text{ for } \Delta < (\eta + \mu + \mu_1 + \delta + \mu)^2,$$

means

$$\frac{\nu\Pi\alpha\delta}{\mathcal{R}_0(\theta + \mu)} > \frac{\alpha\delta\nu\Pi}{(\theta + \mu)} - \frac{(\delta + \mu + \eta + \mu + \mu_1)^2}{4},$$

then,

$$\frac{1}{\mathcal{R}_0} > 1 - \frac{(\delta + \mu + \eta + \mu + \mu_1)^2(\theta + \mu)}{4\nu\Pi\alpha\delta},$$

this implies, $\mathcal{R}_0 < 1$. Therefore, after using the Jacobian stability approach, $\mathcal{E}_0$ is locally asymptotically steadfast. If the initial population size of the affected individuals falls inside the lower set of the point $\mathcal{E}_0$, then the virus can be partially eradicated.

Global stability of DFEs

Theorem 4 *If $\mathcal{R}_0 < 1$, the DFE, $\mathcal{E}_0$ of model (2), is globally equilibrium-stable.*

Proof In this case, we shall use the system (1) since we need the vector X to be 2-dimensional at least. We have written equation system (1) based on [28, 29] in the following structure.

$$\begin{cases} \dfrac{dX}{dt} = \mathcal{M}(X - X_{\mathcal{E}_0,n}) + \mathcal{M}_1, \\ \dfrac{dY}{dt} = \mathcal{M}_2 Y, \end{cases} \tag{6}$$

where $Y = (E_I, I, \mathcal{I}_{nd}, R)$ is the proportion of people who are ill, $X_{\mathcal{E}_0,n}$ is a vector at the unaffected stability spot with the equal vector magnitude as X, and $X = (\mathfrak{S}_I, H)$ reflects the number of healthy people. By the above [28], For the free-of-illness equilibrium point $\mathcal{E}_0 = (\frac{\Pi}{\mu}, 0, 0, 0, 0, \frac{\Pi\theta}{\mu(\mu+\theta)})$ of system (1) to be globally asymptotically steady, several requirements must be satisfied:

1) The matrix $\mathcal{M}$ must have real negative eigenvalues.

2) $\mathcal{M}_2$ ought to be a Metzler matrix.

We have $X_{\mathcal{E}_0,n} = (\frac{\Pi}{\mu}, \frac{\Pi\theta}{\mu(\mu+\theta)})^T$.
The combination of Eq. (6) and Eq. (1) makes up the following system of equations:

$$\begin{pmatrix} \Pi - \nu\mathfrak{S}_I I - (\mu + \theta)\mathfrak{S}_I \\ \theta\mathfrak{S}_I - \mu H \end{pmatrix} = \mathcal{M} \begin{pmatrix} \mathfrak{S}_I - \frac{\Pi}{\theta+\mu} \\ H - \frac{\Pi\theta}{\mu(\theta+\mu)} \end{pmatrix} + \mathcal{M}_1 \begin{pmatrix} E_I \\ I \\ \mathcal{I}_{nd} \\ R \end{pmatrix},$$

and

$$\begin{pmatrix} \nu\mathfrak{S}_I I - (\delta + \mu)E_I \\ \alpha\delta E_I - (\eta + \mu + \mu_1)I \\ (1 - \alpha)\delta E_I - (\gamma + \mu + \mu_1)\mathcal{I}_{nd} \\ \eta I + \gamma\mathcal{I}_{nd} - \mu R \end{pmatrix} = \mathcal{M}_2 \begin{pmatrix} E_I \\ I \\ \mathcal{I}_{nd} \\ R \end{pmatrix}.$$

The Jacobian matrix of the ensemble of Eq. (1) is the one below:

$$
J(\mathcal{E}_0) = \begin{pmatrix}
-(\mu + \theta) & 0 & -\frac{\nu \Pi}{\theta + \mu} & 0 & 0 & 0 \\
0 & -(\delta + \mu) & \frac{\nu \Pi}{\theta + \mu} & 0 & 0 & 0 \\
0 & \alpha \delta & -(\eta + \mu + \mu_1) & 0 & 0 & 0 \\
0 & (1 - \alpha)\delta & 0 & -(\gamma + \mu + \mu_1) & 0 & 0 \\
0 & 0 & \eta & \gamma & -\mu & 0 \\
\theta & 0 & 0 & 0 & 0 & -\mu
\end{pmatrix}.
$$

The matrix $\mathcal{M}$, $\mathcal{M}_1$ and $\mathcal{M}_2$ are:

$$
\mathcal{M} = \begin{pmatrix} -(\mu + \theta) & 0 \\ \theta & -\mu \end{pmatrix}, \quad
\mathcal{M}_1 = \begin{pmatrix} 0 & -\frac{\nu \Pi}{\theta + \mu} & 0 & 0 \\ 0 & 0 & 0 & 0 \end{pmatrix},
$$

and

$$
\mathcal{M}_2 = \begin{pmatrix}
-(\delta + \mu) & \frac{\nu \Pi}{\theta + \mu} & 0 & 0 \\
\alpha \delta & -(\eta + \mu + \mu_1) & 0 & 0 \\
(1 - \alpha)\delta & 0 & -(\gamma + \mu + \mu_1) & 0 \\
0 & \eta & \gamma & -\mu
\end{pmatrix}.
$$

Thus, all the roots of $\mathcal{M}$ have strictly negative real roots, and the matrix $\mathcal{M}_2$ is a Metzler matrix. Therefore the point, $\mathcal{E}_0$ is globally stable if $\mathcal{R}_0 < 1$.
Instead, we can use the Lyapunov function $\mathfrak{K}$ to prove the equilibrium global of the point, $\mathcal{E}_0$, where

$$
\mathfrak{K} = \varkappa_1 E_I + \varkappa_2 I. \tag{7}
$$

We chose this function meticulously because of its efficacy in examining the equilibrium of evolving structures with more intricate behavior. In which there are a pair of positive coefficients, $\varkappa_1$ and $\varkappa_2$.
If we differentiate Eq. (7) with respect to t, we find

$$
\frac{d\mathfrak{K}}{dt} = \varkappa_1 \frac{dE_I}{dt} + \varkappa_2 \frac{dI}{dt}.
$$

By replacing $\frac{dE_I}{dt}$, and $\frac{dI}{dt}$ of template (2), we have:

$$
\frac{d\mathfrak{K}}{dt} = (\varkappa_1 \nu \mathfrak{S}_I - (\eta + \mu + \mu_1)\varkappa_2)I + (\alpha \delta \varkappa_2 - (\delta + \mu)\varkappa_1)E_I.
$$

In this case, we take $\varkappa_1 = \frac{\delta \alpha}{(\delta + \mu)}\varkappa_2$, then since $\mathfrak{S}_I < \mathfrak{S}_I^0$, we have:

$$
\frac{d\mathfrak{K}}{dt} = (\frac{\alpha \delta \nu}{\delta + \mu}\mathfrak{S}_I - (\eta + \mu + \mu_1))\varkappa_2 I
$$

$$
< (\frac{\alpha \delta \nu}{\delta + \mu}\mathfrak{S}_I^0 - (\eta + \mu + \mu_1))\varkappa_2 I.
$$

Taking $\varkappa_2 = 1$, and substituting $\mathcal{R}_0$, we get

$$\frac{d\mathfrak{K}}{dt} < (\mathcal{R}_0 - 1)I.$$

So then, if and only if $I = 0$, $I < I^0$, and $\frac{d\mathfrak{K}}{dt} \leq 0$, for $\mathcal{R}_0 < 1$, and $\frac{d\mathfrak{K}}{dt} = 0$. As a consequence, in field $\mathcal{C}$, $\mathcal{E}_0$ evolves globally asymptotically steady by the LaSalle principle of invariance.

The persistent steadiness $\tilde{\mathcal{E}}$

There is a unique persistent stable $\tilde{\mathcal{E}}$ form of model (2) $\tilde{\mathcal{E}} = (\tilde{\mathfrak{S}}_I, \tilde{E}_I, \tilde{I}, \tilde{I}_{nd}, \tilde{R})$, from where $\tilde{\mathcal{E}}$ is the solution to the persistent steadiness of the ongoing virus in the community. We can achieve this by zeroing each equation in (2):

$$\frac{d\mathfrak{S}_I}{dt} = \frac{dE_I}{dt} = \frac{dI}{dt} = \frac{d\mathcal{I}_{nd}}{dt} = \frac{dR}{dt} = 0.$$

Then, we obtain

$$\tilde{\mathfrak{S}}_I = \frac{\Pi}{\theta + \mu + \nu\tilde{I}}, \quad \tilde{E}_I = \frac{\nu\Pi\tilde{I}}{(\delta + \mu)(\nu\tilde{I} + \theta + \mu)},$$

$$\tilde{I} = \frac{\alpha\delta\Pi}{(\eta + \mu + \mu_1)(\delta + \mu)} - \frac{\theta + \mu}{\nu} = (\mathcal{R}_0 - 1)(\theta + \mu), \tag{8}$$

$$\tilde{I}_{nd} = \frac{(1 - \alpha)\delta\nu\Pi\tilde{I}}{(\gamma + \mu + \mu_1)(\delta + \mu)(\nu\tilde{I} + \theta + \mu)}, \quad \tilde{R} = \frac{\gamma(1 - \alpha)\delta\nu\Pi\tilde{I}}{\mu(\gamma + \mu)(\delta + \mu)(\nu\tilde{I} + \theta + \mu)} + \frac{\eta}{\mu}\tilde{I}_{nd}.$$

All the expressions are in terms of the $\tilde{I}$, due to the non-negative assumption for all model parameters. Consequently, we arrived at the following result:

Lemma 1 *When $\mathcal{R}_0 > 1$, system (2) has a unique persistent steadiness (positive) but not otherwise.*

Theorem 5 *A singular persistent steadiness for the model (2) whenever $\mathcal{R}_0 > 1$, as signified by $\tilde{\mathcal{E}} = (\tilde{\mathfrak{S}}_I, \tilde{E}_I, \tilde{I}, \tilde{I}_{nd}, \tilde{R})$, where the expressions of $\tilde{\mathfrak{S}}_I, \tilde{E}_I, \tilde{I}, \tilde{I}_{nd}$ and $\tilde{R}$ are given in (8).*

Local stability of $\tilde{\mathcal{E}}$

Theorem 6 *If $\mathcal{R}_0 > 1$, the endemic equilibrium point $\tilde{\mathcal{E}}$ is locally asymptotically stable.*

Proof To validate the above theorem, let us derive the Jacobian matrix for model (2):

$$J = \begin{pmatrix} -(\nu I + \theta + \mu) & 0 & -\nu\mathfrak{S}_I & 0 & 0 \\ \nu I & -(\delta + \mu) & \nu\mathfrak{S}_I & 0 & 0 \\ 0 & \alpha\delta & -(\eta + \mu) & 0 & 0 \\ 0 & (1 - \alpha)\delta & 0 & -(\gamma + \mu + \mu_1) & 0 \\ 0 & 0 & \eta & \gamma & -\mu \end{pmatrix}. \tag{9}$$

The characteristic polynomial for Eq. (9) at the specified point $\tilde{\mathcal{E}}$ is:

$$\mathfrak{A}(\lambda) = (\mu + \lambda)(\gamma + \mu + \mu_1 + \lambda)\bar{\mathcal{Q}}(\lambda), \tag{10}$$

$$
\begin{aligned}
\bar{\mathcal{Q}}(\lambda) &= -\lambda^3 - \lambda^2(\nu\tilde{I} + \theta + \delta + \eta + 3\mu) \\
&\quad -\lambda[(\nu\tilde{I} + \theta + \mu)(\delta + \mu) + (\nu\tilde{I} + \theta + \delta + 2\mu)(\eta + \mu + \mu_1) - \alpha\delta\nu\tilde{\mathfrak{S}}_I] \\
&\quad +\alpha\delta\nu\tilde{\mathfrak{S}}_I(\nu\tilde{I} + \theta + \mu) - [(\nu\tilde{I} + \theta + \mu)(\delta + \mu)(\eta + \mu + \mu_1) + \nu^2\alpha\delta\tilde{\mathfrak{S}}_I{}^2] \\
&= a_3\lambda^3 + a_2\lambda^2 + a_1\lambda + a_0,
\end{aligned}
$$

where

$$
\begin{aligned}
a_1 &= -[(\nu\tilde{I} + \theta + \mu)(\delta + \mu) + (\nu\tilde{I} + \theta + \delta + 2\mu)(\eta + \mu + \mu_1) - \alpha\delta\nu\tilde{\mathfrak{S}}_I], \\
a_2 &= -(\nu\tilde{I} + \theta + \delta + \eta + 3\mu + \mu_1), \\
a_0 &= \alpha\delta\nu\tilde{\mathfrak{S}}_I(\nu\tilde{I} + \theta + \mu) - [(\nu\tilde{I} + \theta + \mu)(\delta + \mu)(\eta + \mu + \mu_1) + \nu^2\alpha\delta\tilde{\mathfrak{S}}_I{}^2].
\end{aligned}
$$

From Eq. (10), we have

$$
\begin{aligned}
\lambda_1 &= -\mu < 0, \\
\lambda_2 &= -(\gamma + \mu + \mu_1) < 0.
\end{aligned}
$$

From the expression of $\bar{\mathcal{Q}}$, we have

$$a_0 + \lambda a_1 + \lambda^2 a_2 + a_3\lambda^3 = 0.$$

$$
\begin{array}{c|ccc}
\lambda^3 & a_3 & a_1 & 0 \\
\lambda^2 & a_2 & a_0 & 0 \\
\lambda & b_1 & 0 & 0
\end{array}
$$

$$b_1 = -\frac{1}{a_2}\begin{vmatrix} a_3 & a_1 \\ a_2 & a_0 \end{vmatrix} = \frac{a_1 a_2 + a_0}{a_2} = -\frac{\alpha\delta\nu(\nu\tilde{I}+\theta+\mu) - [\nu\tilde{I}+\theta+\mu)(\delta+\mu)(\eta+\mu+\mu_1) + \nu^2\alpha\delta\tilde{\mathfrak{S}}_I{}^2]}{(\nu\tilde{I}+\theta+\delta+\eta+3\mu+\mu_1)} - \zeta,$$

where

$$\zeta = [\nu\tilde{I} + \theta + \mu)(\delta + \mu) + (\nu\tilde{I} + \theta + \delta + 2\mu)(\eta + \mu + \mu_1) - \alpha\delta\tilde{\mathfrak{S}}_I].$$

Applying the Routh-Hurwitz criteria, it is determined that the real root of Eq. (5) is strictly non-negative iff $a_2 < 0$ and $b_1 < 0$. Clearly, we see that $a_2 < 0$ because it is the sum of positive parameters and we have $b_1 < 0$ if $\mathcal{R}_0 > \nu\Pi(\frac{\nu\tilde{I}}{\theta+\mu} + 1) > 1$.

Hence, the persistent steadiness $\tilde{\mathcal{E}}$ is locally indicating asymptotic steadiness.

Global stability of the point $\tilde{\mathcal{E}}$

Theorem 7 *The only endemic steady state of* (2) *exhibits global asymptotic steady when* $\mathcal{R}_0 > 1$.

Proof Consider the following Lyapunov function, which is commonly used and discussed in [30]:

$$\eth(\wp) = \wp - 1 - ln(\wp).$$

$\eth(\wp)$ is non-negative in $\in R_+^5$ except at $\wp = 1$, where it become zero. Then,

$$\mathfrak{T}(\mathfrak{S}_I, I) = \varkappa_1 \tilde{\mathfrak{S}}_I \eth(\frac{\mathfrak{S}_I}{\tilde{\mathfrak{S}}_I}) + \varkappa_2 \tilde{I} \eth(\frac{I}{\tilde{I}}). \tag{11}$$

Let $\varkappa_1 > 0$ and $\varkappa_2 > 0$ be positive constants to be determined subsequently. Clearly, $\mathfrak{T}$ is C^1, $\mathfrak{T}(\tilde{\mathcal{E}}) = 0$, and $\mathfrak{T}$ is positively nonzero at other locations.
Differentiating the equation with respect to t, we get

$$\frac{d\mathfrak{T}(\mathfrak{S}_I, I)}{dt} = \varkappa_1 (1 - \frac{\tilde{\mathfrak{S}}_I}{\mathfrak{S}_I}) \frac{d\mathfrak{S}_I}{dt} + \varkappa_2 (1 - \frac{\tilde{I}}{I}) \frac{dI}{dt}. \tag{12}$$

By substituting $\frac{d\mathfrak{S}_I}{dt}$ and $\frac{dI}{dt}$ in model (2), we obtain,

$$\frac{d\mathfrak{T}}{dt} = \frac{\varkappa_1}{\mathfrak{S}_I}(\mathfrak{S}_I - \tilde{\mathfrak{S}}_I)(\Pi - (\nu I + \mu)\mathfrak{S}_I) + \frac{\varkappa_2}{I}(I - \tilde{I})(\alpha \delta E_I - (\eta + \mu + \mu_1)I)$$

$$< \varkappa_1 \frac{(\mathfrak{S}_I - \tilde{\mathfrak{S}}_I)}{\mathfrak{S}_I}\Pi - \varkappa_1 (\nu I + \mu)(\mathfrak{S}_I - \tilde{\mathfrak{S}}_I) + \frac{\varkappa_2 (I - \tilde{I})\alpha \delta E_I)}{I}.$$

For $\varkappa_1 = \frac{\mathfrak{S}_I(I - \tilde{I})}{(\mathfrak{S}_I - \tilde{\mathfrak{S}}_I)}$ and $\varkappa_2 = 1$, we find,

$$\frac{d\mathfrak{T}}{dt} < (\Pi - \frac{\mathcal{R}_0(\eta + \mu + \mu_1)(\delta + \mu)(\theta + \mu)\mathfrak{S}_I}{\alpha \delta \Pi} - (\theta + \mu)\mathfrak{S}_I + \frac{\alpha \delta E_I}{I})(I - \tilde{I})$$

$$< (\Pi - \frac{\mathcal{R}_0(\eta + \mu + \mu_1)(\delta + \mu)(\theta + \mu)\mathfrak{S}_I}{\alpha \delta \Pi} + \frac{\alpha \delta E_I}{I})(I - \tilde{I}).$$

Thus, $\frac{d\mathfrak{T}}{dt} < 0$ only if, $\mathcal{R}_0 > \frac{\Pi^2 \alpha \delta}{(\eta + \mu + \mu_1)(\delta + \mu)(\theta + \mu)}$, and $\frac{d\mathfrak{T}}{dt} \le 0$ if $I = \tilde{I}$, then the point, $\tilde{\mathcal{E}}$ is globally asymptotically stable.

5 Exploring the responsiveness of the model variables to $\mathcal{R}_0$

The examination of structure sensitivity is applied to calculate the difference in implementation speed due to changes in strategy variables. Implementation effort is assumed to be a differentiable function of structure, at most undersized in the proximity of the current strategy point. Moreover, To suggest the most appropriate methods to decrease human permanence and illness, it is essential to understand the relative importance of the numerous factors that influence the new coronavirus's spread. Further, it permits us to determine how a condition variable varies correspondingly whenever a system factor adapts. Since the first spread of illness is restricted to the rate $\mathcal{R}_0$, we calculate the sensitivity indicators about these factors of system (2). Thus, we construct the next sensitivity factor [31, 32]:

$$\mathfrak{F}_x^{\mathcal{R}_0} = \frac{\partial \mathcal{R}_0}{\partial x} \frac{x}{\mathcal{R}_0}.$$

Table 2. Sensitivity indicators

Setting symbol	Index of sensitivity
μ	-0.8463
δ	+0.1176
Π	+1
ν	+1
η	-0.8366
α	+1
μ	-0.6423
θ	-0.8789

$$\mathfrak{F}_{\mu}^{\mathcal{R}_0} = -\frac{(3\mu^2 + 2\mu(\theta + \eta + \delta + \mu_1) + \theta\eta + (\theta + \eta)\delta)\mu}{(\theta + \mu)(\eta + \mu + \mu_1)(\delta + \mu)},$$

$$\mathfrak{F}_{\eta}^{\mathcal{R}_0} = -\frac{\eta}{\eta + \mu + \mu_1},$$

$$\mathfrak{F}_{\delta}^{\mathcal{R}_0} = \frac{\mu}{(\delta + \mu)},$$

$$\mathfrak{F}_{\theta}^{\mathcal{R}_0} = -\frac{\theta}{\theta + \mu},$$

$$\mathfrak{F}_{\mu_1}^{\mathcal{R}_0} = -\frac{\mu_1}{\eta + \mu + \mu_1},$$

$$\mathfrak{F}_{\nu}^{\mathcal{R}_0} = 1,$$

$$\mathfrak{F}_{\Pi}^{\mathcal{R}_0} = 1,$$

$$\mathfrak{F}_{\alpha}^{\mathcal{R}_0} = 1.$$

We have, $\mathfrak{F}_{\delta}^{\mathcal{R}_0}, \mathfrak{F}_{\Pi}^{\mathcal{R}_0}, \mathfrak{F}_{\nu}^{\mathcal{R}_0}, \mathfrak{F}_{\alpha}^{\mathcal{R}_0} > 0$ while, $\mathfrak{F}_{\mu}^{\mathcal{R}_0}, \mathfrak{F}_{\eta}^{\mathcal{R}_0}, \mathfrak{F}_{\mu_1}^{\mathcal{R}_0}, \mathfrak{F}_{\theta}^{\mathcal{R}_0} < 0$. It implies that $\mathcal{R}_0$ is reduced in μ and η but raised in δ, Π, ν and α, while $\mathfrak{F}_{\gamma}^{\mathcal{R}_0} = 0$ since $\mathcal{R}_0$ does not rely on γ.

6 Expansion to an optimal control problem

In this section, we provide an effective control technique that will aid governments in developing nations in regaining control of the circumstances at the lowest possible price. Researchers are constantly seeking effective ways to prevent the spread of new viruses, including vaccination, isolation, and quarantine. However, isolation and quarantine procedures can reduce and eradicate the impact of the virus in the absence of effective vaccination. Thus, from [33] the controlled model results in:

$$\begin{cases} \dfrac{d\mathfrak{S}_I}{dt} = \Pi - \nu(1 - \mathfrak{v}_1)\mathfrak{S}_I I - (\mu + \theta)\mathfrak{S}_I, \\[2mm] \dfrac{dE_I}{dt} = \nu(1 - \mathfrak{v}_1)\mathfrak{S}_I I - \delta(1 - \mathfrak{v}_2)E_I - \mu E_I, \\[2mm] \dfrac{dI}{dt} = \alpha\delta(1 - \mathfrak{v}_2)E_I - (\eta + \mu + \mu_1)I - \mathfrak{v}_2 I, \\[2mm] \dfrac{d\mathcal{I}_{nd}}{dt} = (1 - \alpha)\delta(1 - \mathfrak{v}_2)E_I - (\gamma + \mu + \mu_1)\mathcal{I}_{nd} - \mathfrak{v}_2\mathcal{I}_{nd}, \\[2mm] \dfrac{dR}{dt} = \eta I + \gamma\mathcal{I}_{nd} + \mathfrak{v}_2(I + \mathcal{I}_{nd}) - \mu R. \end{cases} \tag{13}$$

To sample the methods of control and affect its influence in Morocco, we raise in the model a two controls variable that represents a comprehensive approach to prevention, including personal hygiene, social isolation, and creating sensitivity across all midpoints, to keep the virus away from people vulnerable to infection, and treatment support for infectious diseases (as the best care for sick people in isolation institutions), denoted by $\mathfrak{v}_1$ and $\mathfrak{v}_2$, respectively. The value $\mathfrak{v}_1(t) = 0$ denotes that no isolation measure is performed, while the value 1 corresponds to full effort on preventing the infectious disease. The value $\mathfrak{v}_2(t) = 0$ signifies the absence of treatment support, and $\mathfrak{v}_2(t) = 1$ represents the effective application of the treatment to reduce the propagation of COVID-19.

In the model, we pursue the $\mathfrak{v}_1$ and $\mathfrak{v}_2$ values that downplay the functionally objective subject to the differential Eq. (14). The supplied objective functional is:

$$J(\mathfrak{v}_1, \mathfrak{v}_2) = \int_0^T (I(t) + \mathcal{I}_{nd}(t) + \frac{\wp_1}{2}\mathfrak{v}_1^2(t) + \frac{\wp_2}{2}\mathfrak{v}_2^2(t))dt. \tag{14}$$

Consider

$$\Lambda = (\mathfrak{S}_I, E_I, I, \mathcal{I}_{nd}, R), \quad \mathfrak{v} = (\mathfrak{v}_1, \mathfrak{v}_2), \quad \mathfrak{v} = (\mathfrak{v}_1, \mathfrak{v}_2),$$

and

$$\wp(t, \Lambda, \mathfrak{v}) = I(t) + \mathcal{I}_{nd}(t) + \frac{\wp_1}{2}\mathfrak{v}_1^2(t) + \frac{\wp_2}{2}\mathfrak{v}_2^2(t),$$

if the relative cost factors $\wp_1 > 0$ and $\wp_2 > 0$ are available. They are selected to contrast the respective strengths of $\mathfrak{v}_1(t)$ and $\mathfrak{v}_2(t)$ at instant t, where T is the final instance. Or, we want to find the optimal controls $\mathfrak{v}_1^*$ and $\mathfrak{v}_2^*$, where,

$$J(\mathfrak{v}_1^*, \mathfrak{v}_2^*) = \min_{\mathfrak{v}_1, \mathfrak{v}_2 \ inU} J(\mathfrak{v}_1, \mathfrak{v}_2). \tag{15}$$

With, F defined as the subset of eligible controls

$$F = \left\{ \mathfrak{v}_1, \mathfrak{v}_2 \in F \middle| \ 0 \leq \mathfrak{v}_1(t) \leq 1 \ and \ 0 \leq \mathfrak{v}_1(t) \leq 1, t \in [0, T] \ \right\}. \tag{16}$$

Existence of the optimal controls

Here, we demonstrate the existence of such ideal control functions that lower prices in a limited time. For this purpose, we stick to the results presented in [34].

Theorem 8 *In set F, there is an optimal control couple, $\mathfrak{v}_1^*$ and $\mathfrak{v}_2^*$ with $J(\mathfrak{v}_1^*, \mathfrak{v}_2^*) = \min_{\mathfrak{v}_1, \mathfrak{v}_2 \in F} J(\mathfrak{v}_1, \mathfrak{v}_2)$ relating to the control system (13-14).*

Proof The following conditions should be fulfilled as stated in (Theorem 4.1 pg. 68 in [35]):

a) In the case of the system (13) with control variables in F, the set of solutions is non-void.
b) The steadier approach can be defined as a linear function of the control coefficients with factors set on the term and value of the parameters since the set F is closed and convex.
c) The integral of the function $\wp$ is convex in the domain F, and the function $\wp(t, \Lambda, \mathfrak{v}) \geq \wp(\mathfrak{v})$,

where $\wp$ is a continuous function that realizes the following property:

$$|\mathfrak{v}|^{-1}\wp(\mathfrak{v}) \xrightarrow[\mathfrak{v}\to\infty]{} \infty,$$

where $|.|$ indicates the classical Euclid norm.

Since $\lim_{t\to\infty} N(t) \leq \dfrac{\Pi}{\mu}$, then, all solutions of system (13) are bounded in F. For each of the bounded control variables in F, the system (13)'s solutions are bound. The system's (13) right-hand side functions meet the Lipschitz criterion about state variables. As a result, condition (a) is satisfied according to the Picard-Lindelöf theorem (see [36]). F satisfies the requirement of being closed and convex by definition. With coefficients that rely on state variables, the system (13) is linear in the control variable $\mathfrak{v}$. So, we accomplish condition (b).

According to the biquadratic and quadratic nature of the control variable $\mathfrak{v}$, $\int_0^T \wp(t, \Lambda, \mathfrak{v})dt$ is convex and $\wp(t, \Lambda, \mathfrak{v}) = I(t) + \mathcal{I}_{nd}(t) + \frac{\varpi_1}{2}\mathfrak{v}_1^2(t) + \frac{\varpi_2}{2}\mathfrak{v}_2^2(t) \geq \frac{\varpi_1}{2}\mathfrak{v}_1^2(t) + \frac{\varpi_2}{2}\mathfrak{v}_2^2(t)$. After selecting $\wp(u) = \mathfrak{w}_1(\mathfrak{v}_1^2 + \mathfrak{v}_2^2)$, where $\mathfrak{w}_1 = \min(\varpi_1, \varpi_2) > 0$, we get then $\wp(t, X, \mathfrak{v}) \geq \wp(\mathfrak{v})$. It is evident that $\wp(\mathfrak{v})$ is a continuous function and satisfies the condition $|\mathfrak{v}|^{-1}\wp(\mathfrak{v}) \to \infty$ when $\mathfrak{v} \to \infty$, which gives us condition (c). As a result, utilizing the findings from [34], the existence of the optimal control is confirmed.

Characterization of the optimal control

We use Pontryagin's maximum principle and the Hamiltonian at the time t defined to derive the requirements for optimal control:

$$\tilde{H} = I(t) + \mathcal{I}_{nd}(t) + \frac{\varpi_1}{2}\mathfrak{v}_1^2(t) + \frac{\varpi_2}{2}\mathfrak{v}_2^2(t) + \sum_{i=1}^{5} \lambda_i(t)f_i(\Lambda).$$

$\Lambda = (\mathfrak{S}_I, E_I, I, \mathcal{I}_{nd}, R)$ and the function f_i is the start of the (13) differences equations for the *ith* variable value.

Theorem 9 *In light of the state system solutions that reduce the impact of J on F and the optimal controls $\mathfrak{v}_1^*$, $\mathfrak{v}_2^*$ and $\mathfrak{S}_I, E_I, I, \mathcal{I}_{nd}$ and R, respectively, adjacent variables, such as $\lambda_1, \ldots, \lambda_5$, are used.*

$$
\begin{aligned}
\frac{d\lambda_1}{dt} &= \lambda_1 \nu(1-\mathfrak{v}_1)I + \lambda_1(\mu+\theta) - \lambda_2 \nu(1-\mathfrak{v}_1)I, \\
\frac{d\lambda_2}{dt} &= \lambda_2 \delta(1-\mathfrak{v}_2) + \lambda_2 \mu - \lambda_3 \alpha\delta(1-\mathfrak{v}_2) - \lambda_4(1-\alpha)\delta(1-\mathfrak{v}_2), \\
\frac{d\lambda_3}{dt} &= -1 + \lambda_1 \nu(1-\mathfrak{v}_1)\mathfrak{S}_I - \lambda_2 \nu(1-\mathfrak{v}_1)\mathfrak{S}_I + \lambda_3(\eta+\mu+\mu_1+\mathfrak{v}_2) - \lambda_5(\eta+\mathfrak{v}_2), \quad (17) \\
\frac{d\lambda_4}{dt} &= -1 + \lambda_4(\gamma+\mu+\mu_1) + \lambda_4\mathfrak{v}_2 - \lambda_5(\gamma+\mathfrak{v}_2), \\
\frac{d\lambda_5}{dt} &= \lambda_5\mu,
\end{aligned}
$$

such as the requirements of transversality: $\lambda_{i=1,2,5}(t_f) = 0$ and $\lambda_{i=3,4}(t_f) = -1$.

Proof As well as

$$\tilde{H} = I(t) + \mathcal{I}_{nd}(t) + \frac{\omega_1}{2}\mathfrak{v}_1^2(t) + \frac{\omega_2}{2}\mathfrak{v}_2^2(t) + \sum_{i=1}^{5}\lambda_i(t)f_i(\Lambda),$$

where $f_1 = \Pi - \nu(1-\mathfrak{v}_1)\mathfrak{S}_I I - (\mu+\theta)\mathfrak{S}_I$, $f_2 = \nu(1-\mathfrak{v}_1)\mathfrak{S}_I I - \delta(1-\mathfrak{v}_2)E_I - \mu E_I$,
$f_3 = \alpha\delta(1-\mathfrak{v}_2)E_I - (\eta+\mu+\mu_1)I - \mathfrak{v}_2 I$, $f_4 = (1-\alpha)\delta(1-\mathfrak{v}_2)E_I - (\gamma+\mu+\mu_1)\mathcal{I}_{nd} - \mathfrak{v}_2\mathcal{I}_{nd}$
and $f_5 = \eta I + \gamma\mathcal{I}_{nd} + \mathfrak{v}_2(I + \mathcal{I}_{nd}) - \mu R$.
The maximum principle of Pontryagin [37] is then applied, and we obtain,

$$
\begin{aligned}
\frac{d\lambda_1}{dt} &= -\frac{\partial\tilde{H}}{\partial\mathfrak{S}_I} = \lambda_1\nu(1-\mathfrak{v}_1)I + \lambda_1(\mu+\theta) - \lambda_2\nu(1-\mathfrak{v}_1)I, \\
\frac{d\lambda_2}{dt} &= -\frac{\partial\tilde{H}}{\partial E_I} = \lambda_2\delta(1-\mathfrak{v}_2) + \lambda_2\mu - \lambda_3\alpha\delta(1-\mathfrak{v}_2) - \lambda_4(1-\alpha)\delta(1-\mathfrak{v}_2), \\
\frac{d\lambda_3}{dt} &= -\frac{\partial\tilde{H}}{\partial I} = -1 + \lambda_1\nu(1-\mathfrak{v}_1)\mathfrak{S}_I - \lambda_2\nu(1-\mathfrak{v}_1)\mathfrak{S}_I + \lambda_3(\eta+\mu+\mu_1+\mathfrak{v}_2) - \lambda_5(\eta+\mathfrak{v}_2), \\
\frac{d\lambda_4}{dt} &= -\frac{\partial\tilde{H}}{\partial\mathcal{I}_{nd}} = -1 + \lambda_4(\gamma+\mu+\mu_1) + \lambda_4\mathfrak{v}_2 - \lambda_5(\gamma+\mathfrak{v}_2), \\
\frac{d\lambda_5}{dt} &= -\frac{\partial\tilde{H}}{\partial R} = \lambda_5\mu.
\end{aligned}
\tag{18}
$$

The accompanying optimal controls $\mathfrak{v}_1^*$ and $\mathfrak{v}_2^*$ are thus established from $\frac{\partial\tilde{H}}{\partial\mathfrak{v}_1} = 0$, and $\frac{\partial\tilde{H}}{\partial\mathfrak{v}_2} = 0$. In light of this, we developed the characteristic equation involving the control boundary limits in the type of proposed control argument as follows:

$$
\begin{aligned}
\mathfrak{v}_1^* &= \min\left\{1, \max(0, \frac{\nu\mathfrak{S}_I^* I^*(\lambda_2-\lambda_1)}{\omega_1})\right\}, \\
\mathfrak{v}_2^* &= \min\left\{1, \max(0, \frac{\lambda_3\alpha\delta E_I^* + \lambda_3 I^* + \lambda_4(1-\alpha)\delta E_I^* - \lambda_2\delta E_I^*}{\omega_2})\right\}.
\end{aligned}
\tag{19}
$$

7 Discussions and numerical simulation

Without numerical validation of the statistics, the analytical study cannot be considered complete. To trace the behavior of the framework (2), we have shown some numerical simulations in this part for a variety of initial circumstances and parameters found in Table 3 and Table 4. Thus, we employed the fourth order RK technique in Matlab program to solve this issue. We considered the variables stated in Table 3 as well as the various beginning condition values provided in Table 4. Applying the fourth-order Runge-Kutta technique and the system's present solution round, the adjoint Eq. (17) is solved backward in time. These factors were used to estimate the reproduction number, and the results show that $\mathcal{R}_0 = 0.2132654$. Figure 2 makes it abundantly evident that the system's solution profiles converge to the disease-free state, with $\mathcal{E}_0 = (0.059 \times 10^7, 0, 0, 0, 0)$. The endemic equilibrium is asymptotically stable as determined by Theorem 7 when the value of α is changed to 0.0002, as seen in Figure 3. Or, the system's solution of (2) converges to $\tilde{\mathcal{E}} = (1.1234 \times 10^7, 0.7000 \times 10^7, 1.3476 \times 10^7, 1.5632 \times 10^7, 2.1000 \times 10^7, 3.1000 \times 10^7)$. Figure 4 demonstrates how the class H maintains stability and advances to the virus-free equilibrium point when $\mathcal{R}_0 < 1$ for each of the three various starting values of H. Figure 5 clearly shows that our solution for the classes I and E_I converges to $\mathcal{E}_0$ for $\mathcal{R}_0 < 1$ and is asymptotically stable. Figure 6 illustrates how the two classes I and E_I for the three distinct initial circumstances become stable at

the point, $\tilde{\mathcal{E}}$, when $\mathcal{R}_0 > 1$. Figure 7 shows how the population $\mathcal{I}_{nd}$ is asymptotically stable and converges to $\mathcal{E}_0$ when $\mathcal{R}_0 < 1$ (case 1), while the same class remains stable and converges to $\tilde{\mathcal{E}}$ in case $\mathcal{R}_0 > 1$ (case 2). Figure 8 shows the same category, but this time for the class R. We can see that system (2)'s solution is stable and converges to $\mathcal{E}_0$ in all three starting values of the recovered class when $\mathcal{R}_0 < 1$, but with the same beginning values of R and $\alpha = 0.210$, so that $\mathcal{R}_0 > 1$ the solution converges to $\tilde{\mathcal{E}}$. The theoretical findings of the local and global asymptotic stability of the endemic and disease-free equilibrium described in the preceding parts are, in sum, supported by all of the results of this section.

Furthermore, we use a fourth-order Runge-Kutta technique for the numeric estimation of the extremum provided by Theorem 8. With a forward fourth-order Runge-Kutta scheme and the transversality requirements $\lambda_{i=1,2,5}(t_f) = 0$ and $\lambda_{i=3,4}(t_f) = -1$, while, $\mathfrak{S}_I = \frac{\mathfrak{S}_I}{N}$, $E_I = \frac{E_I}{N}$, $I = \frac{I}{N}$, $\mathcal{I}_{nd} = \frac{\mathcal{I}_{nd}}{N}$ and $R = \frac{R}{N}$. This iterative approach solves the system in Eq. (13) with an estimate for the controls across the period interval $[0, T]$. A convex pair of the preceding controls and the results from (19), together with the current controls, for upgrading the controls. If the coefficients of the unresolved from the prior iteration are substantially similar to the ones from the present execution, the iteration is over. Concerning the digital simulations, we use $\mathfrak{v}_{\max} = 0.5$, with the end time value of $T = 1$ (months) plus the predetermined variables from Table 3, and with the following starting conditions:

$$\mathfrak{S}_I(0) = 0.4, \quad E_I(0) = 0.2, \quad I(0) = 0.17, \quad \mathcal{I}_{nd}(0) = 0.11 \quad \text{and} \quad R(0) = 0.5. \tag{20}$$

In Figure 9, when we use the technique $\mathfrak{v}_2$, we notice a reduction in the infected population. Only the control $\mathfrak{v}_1$, is employed (Strategy$_1$). The goal of this plan is to safeguard more people from COVID-19. Figure 10 shows a reduction in the number of people exposed, causing a decline in the count of individuals affected, which underlines the need to raise public awareness of the seriousness of the COVID-19 virus through preventive measures such as frequent manual hygiene, especially after snatching, and the use of safety covers to restrict the spread of the virus. The results in Figure 11 indicate that Strategy$_2$ reduces the number of people with the virus. The main objective of this procedure is to prevent the disease from spreading, which confirms that the essential purpose of therapy is to prevent the spread of the coronavirus. Furthermore, we observe a substantial reduction in the quantity of those infected with the two types of I and Ind when we incorporate the optimal control $\mathfrak{v}_1$ and $\mathfrak{v}_2$ (Strategy$_3$). Such is because stringent precautions, like isolation with therapy, occur, as depicted in Figure 12, and the approach also depends on sensitization efforts. It is clear that the controls implemented in this numerical simulation function well by reducing the population of diseased people and augmenting the number of cured people. Thus, we notice that the number of retrieved persons rises when we employ two distinct approaches. Additionally, we discovered, as shown in Figure 13, that there is an appealing correlation between $\mathcal{R}_0$ and the illness transmission coefficient in all afflicted groups, and this correlation is called α. This implies that α is the most important factor that needs to be decreased in order to regulate infections and lessen coronavirus. Our model relies on available epidemiological data, which may be subject to reporting bias or variations in screening capacity from one region to another. Moreover, the dynamic nature of the COVID-19 pandemic introduces uncertainties that may impact the accuracy of our forecasts. We have made assumptions about the homogeneity of the population and the uniformity of intervention measures, which may not fully reflect the complexity of real scenarios. In addition, the model considers simplified transmission dynamics without taking into account potential variations in viral strains or the influence of emerging variants. While we aim to provide valuable information, we recognize that

these simplifications and assumptions are necessary trade-offs and may influence the accuracy of our results. Future iterations of this model should incorporate more nuanced data and refine assumptions to improve accuracy and applicability.

Table 3. The baseline factor's value for the system (2)

factor	Value	Source
ν	0.9031	Presumption
α	0.4110	[25]
Π	20.000	Presumption
δ	$1/7 day^{-1}$	[38]
η	0.1130	Presumption
μ	$0.0062 day^{-1}$	[25]
θ	0.021	Presumption
$\wp_1$	30	Assumption
$\wp_2$	80	Assumption

Table 4. The beginning values for the system'(2)s factors

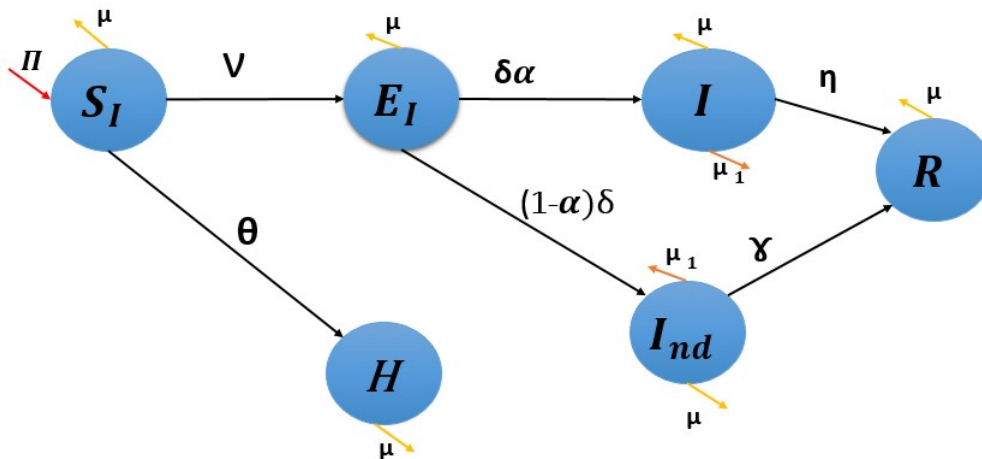| Starting values	State 1	State 2	State 3
N	397405	401405	360530
$\mathfrak{S}_I(0)$	163638	173638	118763
$E_I(0)$	93507	94507	95507
$I(0)$	70130	71130	72130
$\mathcal{I}_{nd}(0)$	46753	47753	48753
$R(0)$	23377	24377	25377

Figure 1. Prototype (1)'s diagram, or $\nu = \frac{\beta \mathfrak{S}_I I}{1 + \sigma I}$

8 Cost-effectiveness

A mathematical technique called cost-effectiveness is used to establish if an intervention's benefits outweigh its costs. So, cost-effectiveness is a methodology to evaluate which intervention provides the highest value for the associated price. The value of an intervention in a cost-effectiveness analysis is measured using quantity-adjusted life years, also known as Qualis. Simply put, this is a generic measure of the burden of disease that includes not only quantity but also quality of life
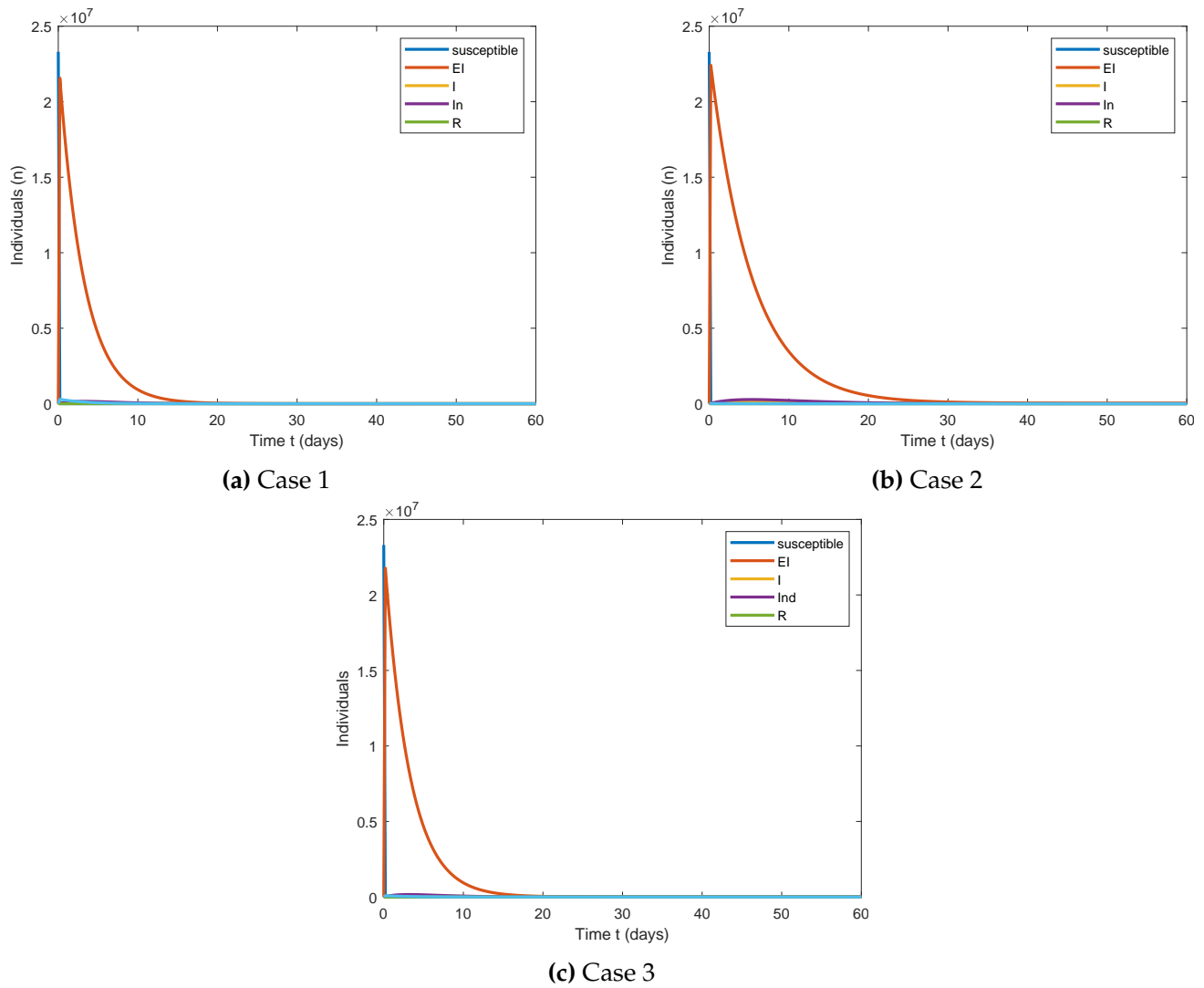
(a) Case 1

(b) Case 2

(c) Case 3

Figure 2. This figure shows that the unaffected steady-state framework (2) is $(2.180 \times 10^7, 0, 0, 0, 0)$.

after the intervention. This technique compares the cost and the effect of two interventions, and it is summarized using an incremental cost-effectiveness ratio, also known as an ISA. The total expense incurred during the whole duration is:

$$\varsigma(\mathfrak{v}) = \int_0^T (\varsigma(\mathfrak{v}_1, \mathfrak{v}_2)) dt = \int_0^T \frac{\wp_1}{2} \mathfrak{v}_1^2(t) + \frac{\wp_2}{2} \mathfrak{v}_2^2(t)) dt. \tag{21}$$

The incremental cost-effectiveness ratio (ICER) is expressed as follows (see [39]):

$$ICER = \frac{\text{Difference in costs of interventions } \mathfrak{v}_1 \text{ and } \mathfrak{v}_2}{\text{Difference in effect of interventions } \mathfrak{v}_1 \text{ and } \mathfrak{v}_2}.$$

This ratio shows the incremental costs over incremental quality-adjusted life years between the two comparators.

To be more precise, considering two concurrent strategies, $\mathcal{B}_1$ and $\mathcal{B}_2$, where Strategy $\mathcal{B}_2$ is more efficient than Strategy $\mathcal{B}_1$ ($TA(\mathcal{B}_1) < TA(\mathcal{B}_2)$), Implement ideas in [40–43]. ICER rates are

(a) Case 1

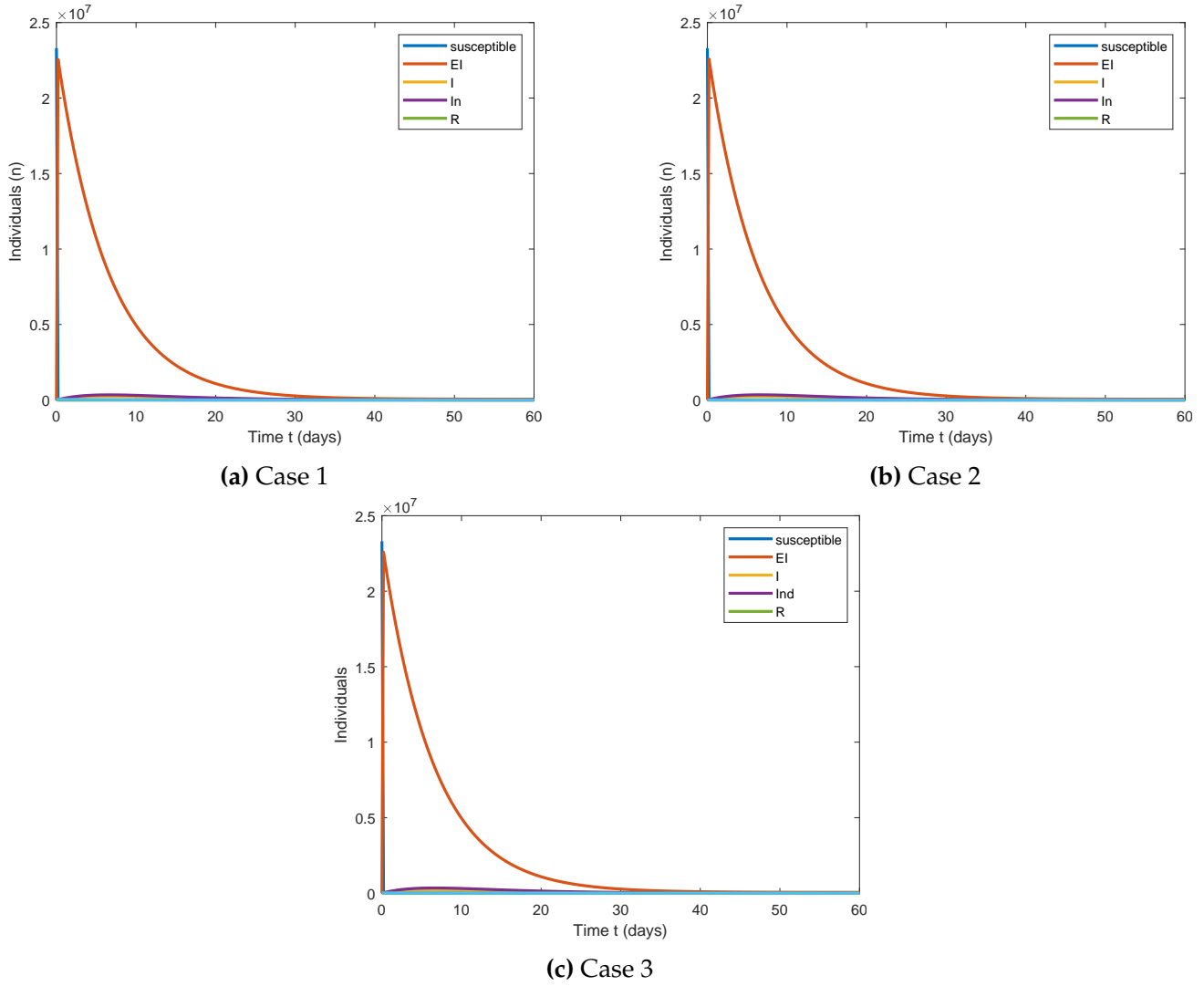**(b)** Case 2

(c) Case 3

Figure 3. This figure shows that the persistent steadiness of model (2) is
$(2.5468 \times 10^7, 0.9096 \times 10^7, 3.65859 \times 10^7, 1.7484 \times 10^7, 1.0857 \times 10^7, 3.6583 \times 10^7)$.

computed via the following equations:

$$ICER(\mathcal{B}_1) = \frac{TC(\mathcal{B}_1)}{TA(\mathcal{B}_1)}, \tag{22}$$

$$ICER(\mathcal{B}_2) = \frac{TC(\mathcal{B}_2) - TC(\mathcal{B}_1)}{TA(\mathcal{B}_2) - TA(\mathcal{B}_1)}. \tag{23}$$

In our analysis, the total expenditures (TC) and the total incidents prevented (TA) for the approach
selected i for $i = 1, 2$, and 3 are defined as follows during a specific duration:

$$TC(\mathcal{B}_1) = \sum_{t=0}^{T-1} \varpi_1 \mathfrak{v}_1^*(E_I + \mathfrak{S}) + \varpi_2 \mathfrak{v}_1^*(I + \mathcal{I}_{nd}), \tag{24}$$
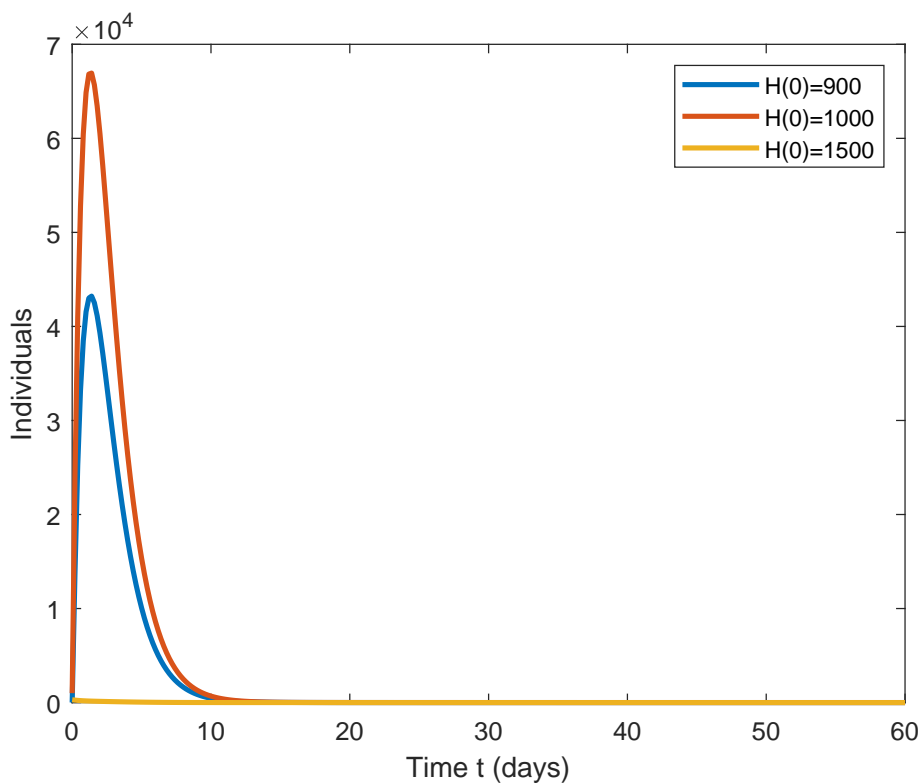
Figure 4. The model's digital solutions for the variables and various starting points of H, where $\mathcal{R}_0 = 0.0143613$. The equilibrium of the point $\mathcal{E}_0$ is stable.
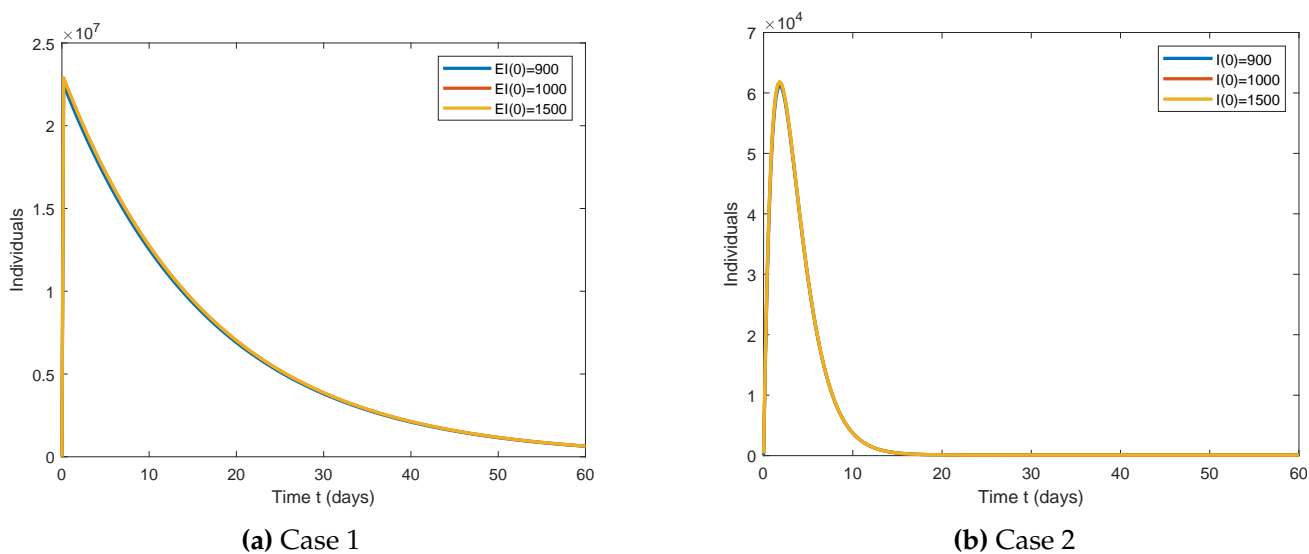

(a) Case 1

(b) Case 2

Figure 5. The model (2) numerical solutions for the factors and various starting conditions of E_I and I listed in Table 3 and Table 4, with the rate $\mathcal{R}_0 = 0.1352631$.

$$TA(\mathcal{B}_1) = \sum_{t=0}^{T} I + \mathcal{I}_{nd} - (I^* + \mathcal{I}_{nd}^*). \tag{25}$$

where I^* and $\mathcal{I}_{nd}^*$ represent the optimal solution linked to the optimal controls $\mathfrak{v}_1^*$ and $\mathfrak{v}_2^*$, while ϖ_1 and ϖ_2 represent the person-unit costs of the two potential interventions. We ordered our control measures in Table 2 according to the higher number of cases avoided under the template's computations.
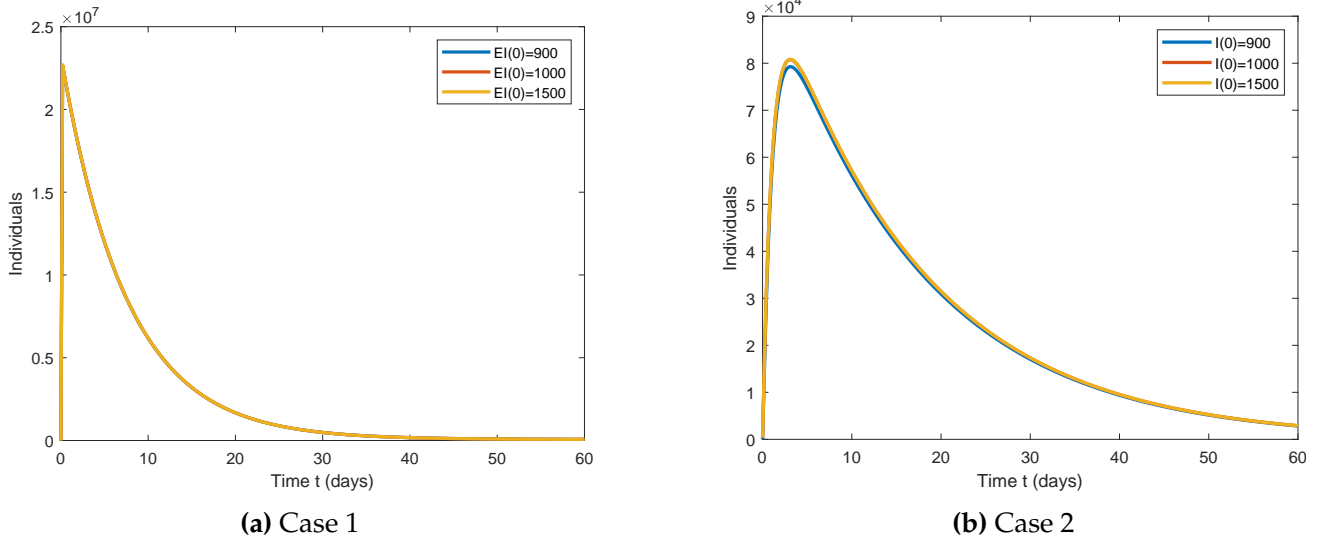
(a) Case 1

(b) Case 2

Figure 6. The system (2) numerical solutions for the parameters and various starting conditions of E_I and I listed in Table 3 and Table 4, here $\mathcal{R}_0 = 2.272166591341701$, the point $\tilde{\mathcal{E}}$ remains steady as well.
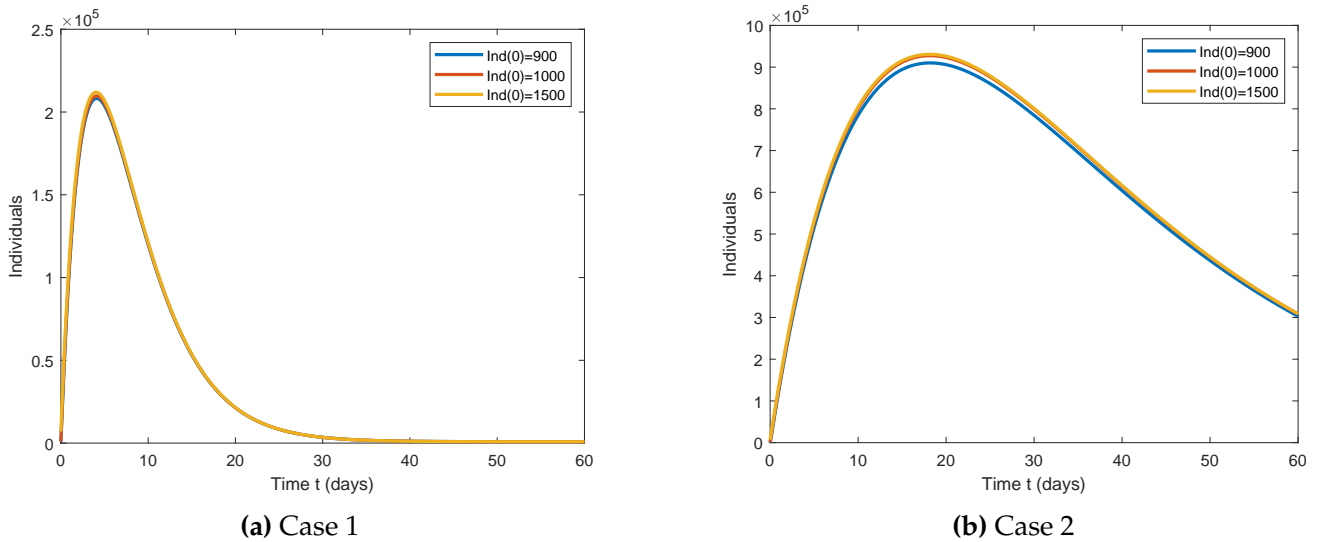

(a) Case 1

(b) Case 2

Figure 7. Digital solutions of the system (2) for factors and diverse starting state of $\mathcal{I}_{nd}$, here $\mathcal{R}_0 = 0.1352631$ in Case 1 and $\mathcal{R}_0 = 2.272166591341701$ in Case 2.

Strategy$_1$ (Processing $\mathfrak{v}_1$): Encourage the population to adopt a comprehensive approach to prevention, which includes self-care, social separation, and the sensitization of all levels, to keep the virus away from people vulnerable to infection.

Strategy$_2$ (Processing $\mathfrak{v}_2$): Control of infectious disorders therapy support (as the finest care for ill patients in isolation facilities).

Strategy$_3$ (Processing $\mathfrak{v}_1$ and $\mathfrak{v}_2$): Integrating Strategy$_1$ and Strategy$_2$ and employing controls $\mathfrak{v}_1$ and $\mathfrak{v}_2$. Based on the simulation results, we have ranked our control techniques in Table 3 according to the number of diseases avoided and given in Eq. (20). Table 2 compares Strategy $\mathcal{B}_1$ and Strategy $\mathcal{B}_2$ in terms of increased efficiency. In terms of improved efficiency, Strategy$_1$ and

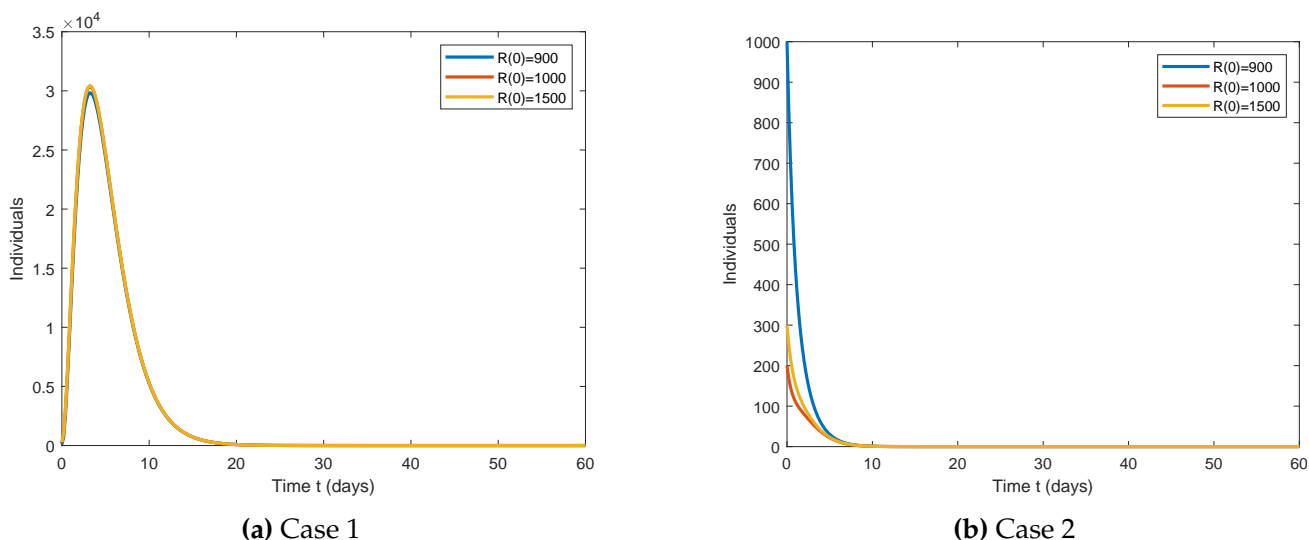**(a)** Case 1   **(b)** Case 2

Figure 8. For parameters and various beginning conditions of R, numerical solutions of the model (2) are presented in Table 3 and Table 4, where $\mathcal{R}_0 = 3.193363191340714$ in Case 2, and $\mathcal{R}_0 = 0.2132654$ in Case 1
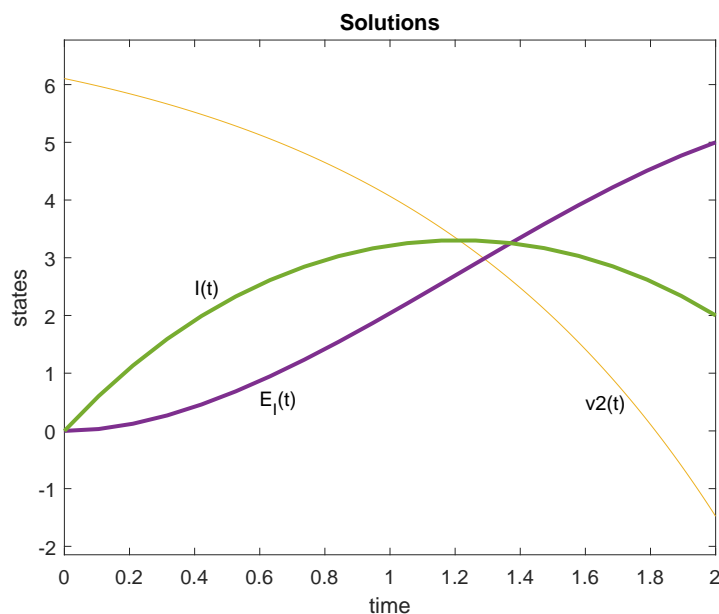
.

Figure 9. Application of the Strategy $\mathfrak{v}_2$

Strategy$_2$ are contrasted. The ICER values are calculated as follows:

$$ICER(1) = \frac{TC(1)}{TA(1)} = \frac{1.73 \times 10^2}{3 \times 10^2} = 0.57,$$

$$ICER(2) = \frac{TC(2) - TC(1)}{TA(2) - TA(1)} = \frac{1.9 \times 10^2 - 1.73 \times 10^2}{3.03 \times 10^2 - 3 \times 10^2} = 39.$$

(26)

$ICER(2)$ is superior to $ICER(1)$. This indicates that plan (1) is more dominant than plan (2). Consequently, Strategy$_2$ is not featured in the list of options.
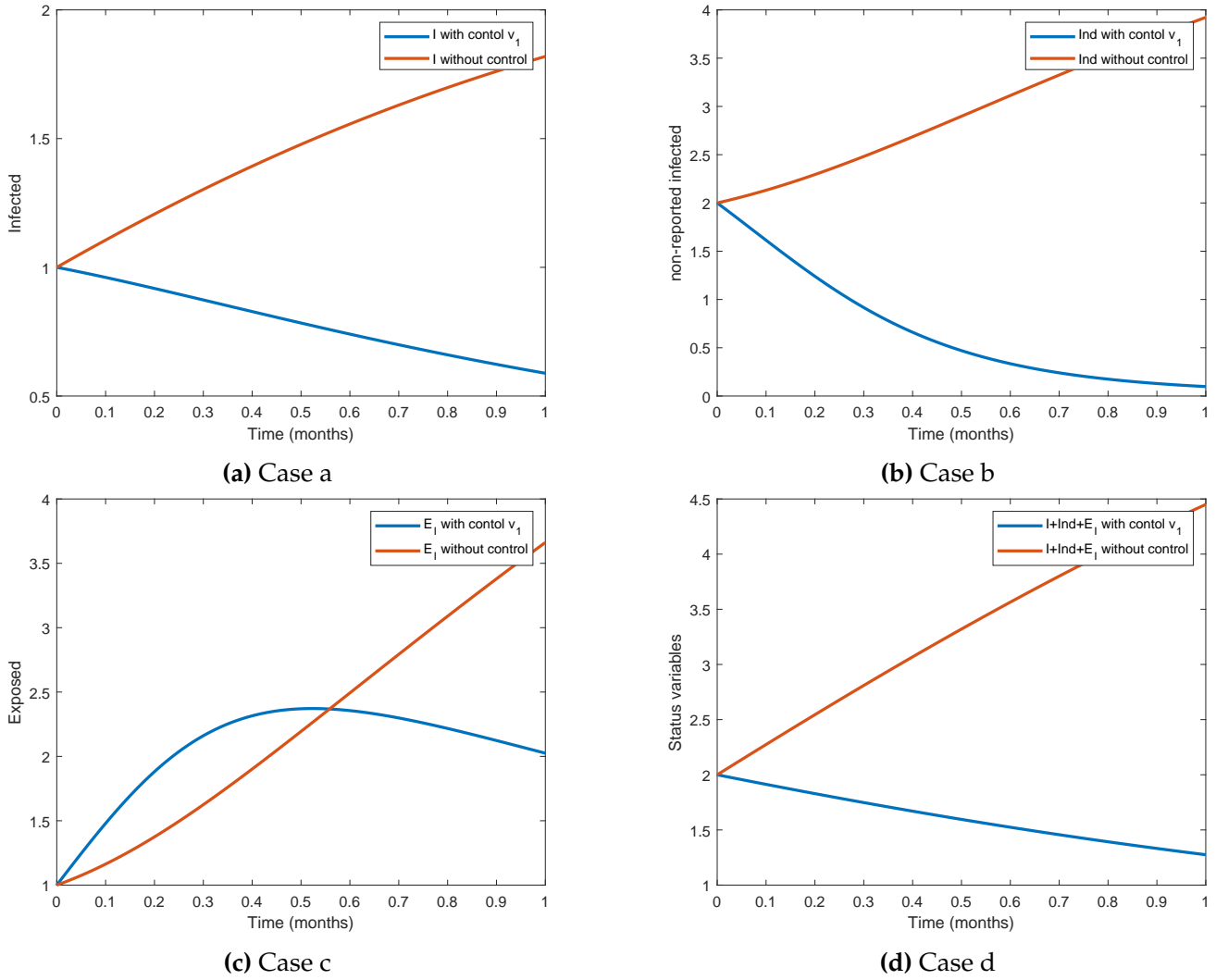
(a) Case a

(b) Case b

(c) Case c

(d) Case d

Figure 10. The progression of the number of individuals with control $\mathfrak{v}_1$

Next, we examined how cost-effective Strategy$_1$ and Strategy$_3$ were:

$$ICER(3) = \frac{TC(3)}{TA(3)} = \frac{1.52 \times 10^2}{2.5 \times 10^2} = 0.608,$$

$$ICER(1) = \frac{TC(1) - TC(3)}{TA(1) - TA(3)} = \frac{1.73 \times 10^2 - 1.52 \times 10^2}{3 \times 10^2 - 2.5 \times 10^2} = 0.42.$$

(27)

According to the analysis, Strategy$_1$ is more affordable than Strategy$_3$. Consequently, method 1 is the most advantageous of all the strategies evaluated, as it is simultaneously approachable and healthy.

Table 5. Total expenses and total illnesses prevented across all techniques

Strategy	TA	TC
1	3×10^2	1.73×10^2
2	3.03×10^2	1.9×10^2
3	2.5×10^2	1.52×10^2

(a) Case a

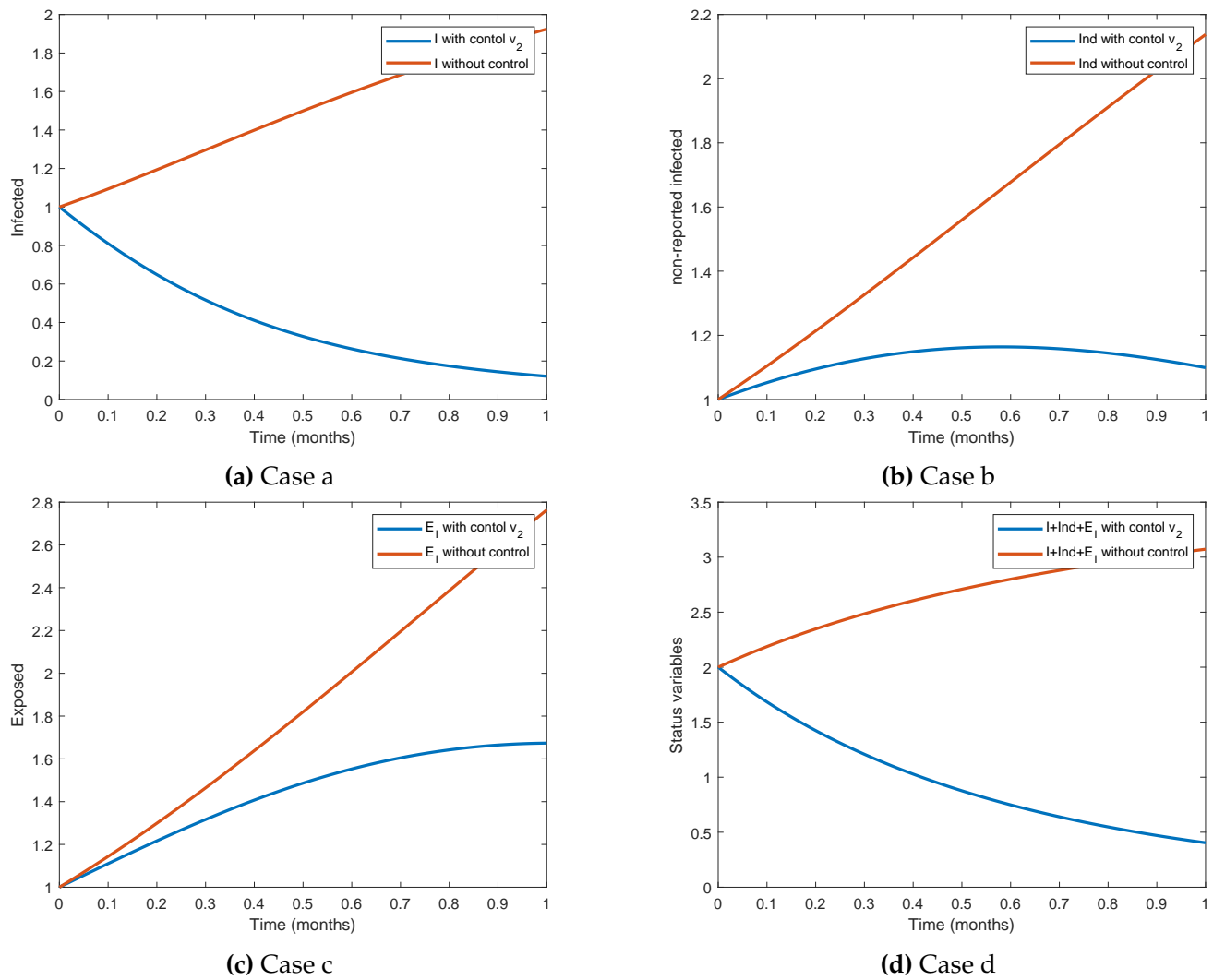**(b)** Case b

(c) Case c

(d) Case d

Figure 11. The progression of the number of individuals with control $\mathfrak{v}_2$

9 Conclusion

Multiple models have been proposed for the analysis of the COVID-19 pandemic. In this sample, we have highlighted the distinctive properties of COVID-19 and suggested an approach that explains how the virus transformed in Morocco while providing a reasonable representation of the actual pandemic in that country. The model's objective is to investigate the process of COVID-19 transmission while accounting for both reported and undeclared infections. These two categories were necessary, as many people have not reported their infection with the COVID-19 virus or even failed to take the necessary precautions to limit the spread of the virus and protect others, we also included a class of individuals who never got infected by COVID-19 (compartment H).

We suggest a compartmental epidemic model for newly emerging coronavirus infections, which considers COVID-19 infection to be a contagious disease. The dynamics of the interaction among the groups can be expressed mathematically by a framework of ODEs. We prove the solution's existence and uniqueness and compute the rate $\mathcal{R}_0$, which assisted in illustrating the equilibrium's stability. One can distinguish between what is globally stable and what is asymptotically stable. Similarly, the study uses the idea of normalized forward sensitivity to highlight the significance of every factor for the spread of COVID-19. We investigate the optimal control problem numerically in further detail, and our results show that the control strategies implemented reduce the prevalence of the virus in society during the period of the interaction. Moreover, we examined
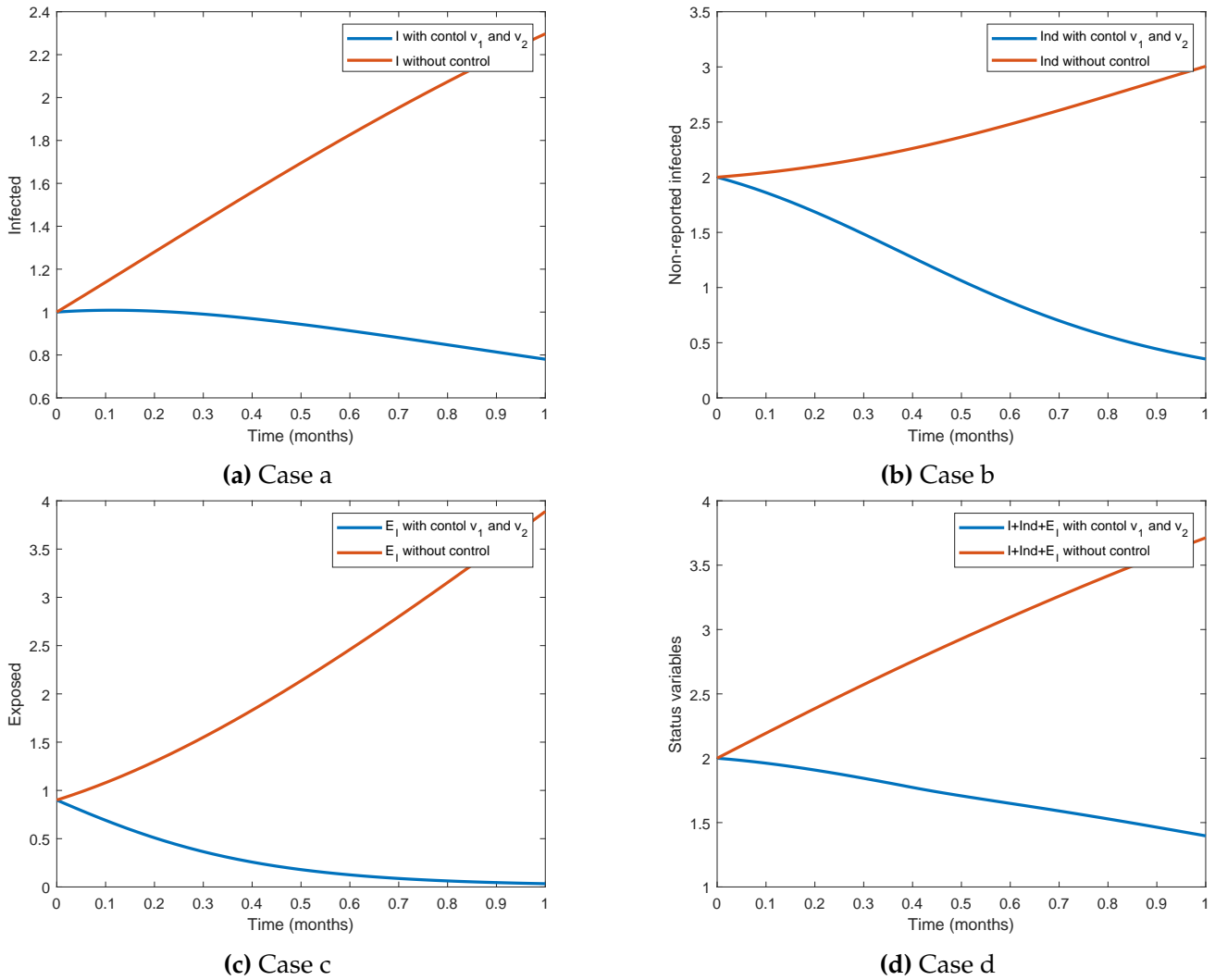
Figure 12. The admissible control set in Eq. (16), the starting factors in Eq. (20), and the optimal state values for the control problem in Eqs. (13)−(15), in contrast to control-free trajectories

the cost-effectiveness of control measures to determine the best way to manage COVID-19 while consuming as few resources as possible. We demonstrate, via the ICER cost-effectiveness approach, that while approach 3 (which promotes applying the two control $\mathfrak{v}_1$ and $\mathfrak{v}_2$) is the most effective, it does not minimize disease. In terms of cost, approach 2 (apply the control $\mathfrak{v}_2$) is the most expensive. Nevertheless, this tactic shows remarkable results in controlling disease transmission and reducing infection rates. Despite the high cost of this method, the Moroccan government is committed to adopting it. Likewise, it is essential to keep spreading the word about the value of immunization and prevention while stepping up efforts to target those who follow the guidelines and motivate them to share their understanding of and adherence to them. Ultimately, the 4th-order Runge-Kutta forward-backwards method in Matlab is used for numerical simulations to validate the analytical results. As a further work, we plan to use fractional calculus in our subsequent work and add more aspects to our analysis in future research, as it can provide a more precise description of natural occurrences than can be achieved using conventional differential. It can entail cooperation with experts in epidemiology, sociology, economics, and other relevant fields to create more comprehensive models.
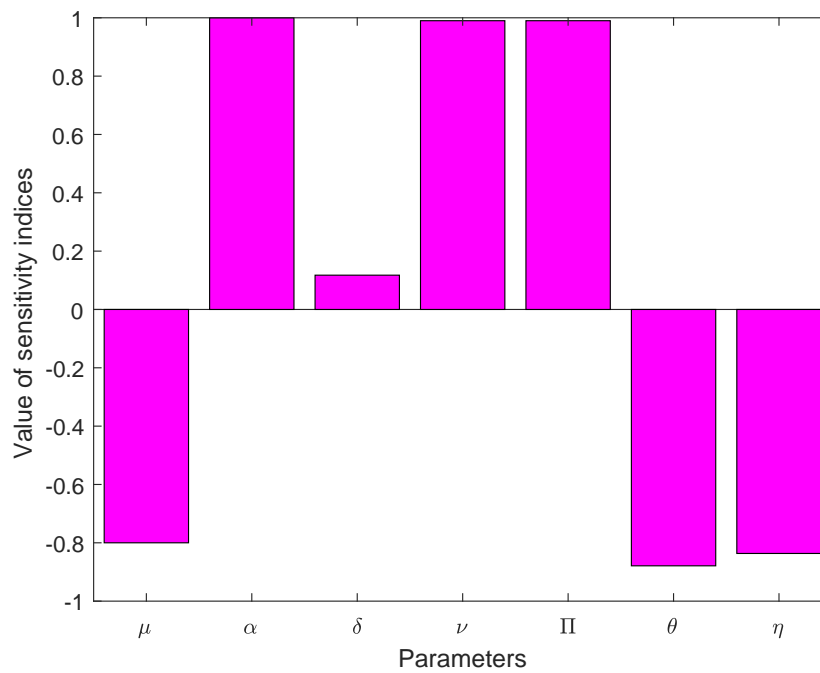
Figure 13. The outcome shows the normalized forward sensitivity indices for the fundamental ratio $\mathcal{R}_0$ with respect to each of the typical variables of the model

Declarations

Use of AI tools

The authors declare that they have not used Artificial Intelligence (AI) tools in the creation of this article.

Data availability statement

Data sharing is not applicable to this article as no datasets were generated or analyzed during the current study.

Ethical approval

The authors state that this research complies with ethical standards. This research does not involve either human participants or animals.

Consent for publication

Not applicable

Conflicts of interest

The authors declare that they have no known competing financial interests or personal relationships that could have appeared to influence the work reported in this paper.

Funding

No funding was obtained for this study.

Author's contributions

S.I.O.: Methodology, Conceptualization, Validation, Software, Data Curation, Writing - Original Draft. M.E.K.: Writing-Review & Editing, Supervision. All authors have read and agreed to the

published version of the manuscript.

References

[1] World Health Organization (WHO), Coronavirus (COVID-19), Events as They Happen, 31.07.2020. https://www.who.int/emergencies/diseases/novel-coronavirus-2019/events-as-they-happen.

[2] Cavallo, J.J., Donoho, D.A. and Forman, H.P. Hospital capacity and operations in the coronavirus disease 2019 (COVID-19) pandemic—planning for the Nth patient. *JAMA Health Forum*, 1(3), e200345, (2020). [CrossRef]

[3] Ahmed, H.M., Elbarkouky, R.A., Omar, O.A.M. and Ragusa, M.A. Models for COVID-19 daily confirmed cases in different countries. *Mathematics*, 9(6), 659, (2021). [CrossRef]

[4] Alansari, M. and Shagari, M.S. Analysis of fractional differential inclusion models for COVID-19 via fixed point results in metric space. *Journal of Function Spaces*, 2022, 8311587, (2022). [CrossRef]

[5] Mustafa, H.I., Al-shami, T.M. and Wassef, R. Rough set paradigms via containment neighborhoods and ideals. *Filomat*, 37(14), 4683-4702, (2023). [CrossRef]

[6] Kifle, Z.S. and Lemecha Obsu, L. Optimal control analysis of a COVID-19 model. *Applied Mathematics in Science and Engineering*, 31(1), 2173188, (2023). [CrossRef]

[7] Akanni, J.O., Fatmawati and Chukwu, C.W. On the fractional-order modeling of COVID-19 dynamics in a population with limited resources. *Communications in Mathematical Biology and Neuroscience*, 2023, 12, (2023). [CrossRef]

[8] Singh, H., Srivastava, H.M., Hammouch, Z. and Nisar, K.S. Numerical simulation and stability analysis for the fractional-order dynamics of COVID-19. *Results in Physics*, 20, 103722, (2021). [CrossRef]

[9] Chen, Y., Liu, Q. and Guo, D. Emerging coronaviruses: genome structure, replication, and pathogenesis. *Journal of Medical Virology*, 92(4), 418-423, (2020). [CrossRef]

[10] Ouaziz, S.I. and Khomssi, M.E. Dynamics and optimal control methods for the COVID-19 model. IN *Mathematical Modeling and Intelligent Control for Combating Pandemics* (pp. 21-38). Springer Optimization and Its Applications, 203, (2023). [CrossRef]

[11] Uçar, S., Uçar, E., Özdemir, N. and Hammouch, Z. Mathematical analysis and numerical simulation for a smoking model with Atangana–Baleanu derivative. *Chaos, Solitons & Fractals*, 118, 300-306, (2019). [CrossRef]

[12] Makinde, O.D., Akanni, J.O. and Abidemi, A. Modelling the impact of drug abuse on a nation's education sector. *Journal of Applied Nonlinear Dynamics*, 12(1), 53-73, (2023). [CrossRef]

[13] Tang, B., Wang, X., Li, Q., Bragazzi, N.L., Tang, S., Xiao, Y. and Wu, J. Estimation of the transmission risk of the 2019-nCoV and its implication for public health interventions. *Journal of Clinical Medicine*, 9(2), 462, (2020). [CrossRef]

[14] Srivastava, A. and Chowell, G. Understanding spatial heterogeneity of COVID-19 pandemic using shape analysis of growth rate curves. *MedRxiv*, (2020). [CrossRef]

[15] Eikenberry, S.E., Mancuso, M., Iboi, E., Phan, T., Eikenberry, K., Kuang, Y. et al. To mask or not to mask: Modeling the potential for face mask use by the general public to curtail the COVID-19 pandemic. *Infectious Disease Modelling*, 5, 293-308, (2020). [CrossRef]

[16] Okosun, K.O., Rachid, O. and Marcus, N. Optimal control strategies and cost-effectiveness analysis of a malaria model. *BioSystems*, 111(2), 83-101, (2013). [CrossRef]

[17] Ghosh, J.K., Biswas, S.K., Sarkar, S. and Ghosh, U. Mathematical modelling of COVID-19: a case study of Italy. *Mathematics and Computers in Simulation*, 194, 1-18, (2022). [CrossRef]

[18] Johansson, M.A., Quandelacy, T.M., Kada, S., Prasad, P.V., Steele, M., Brooks, J.T. et al. SARS-CoV-2 transmission from people without COVID-19 symptoms. *JAMA Network Open*, 4(1), e2035057, (2021). [CrossRef]

[19] Asamoah, J.K.K., Okyere, E., Abidemi, A., Moore, S.E., Sun, G.Q., Jin, Z. et al. Optimal control and comprehensive cost-effectiveness analysis for COVID-19. *Results in Physics*, 33, 105177 (2022). [CrossRef]

[20] Samui, P., Mondal, J. and Khajanchi, S. A mathematical model for COVID-19 transmission dynamics with a case study of India. *Chaos, Solitons & Fractals*, 140, 110173, (2020). [CrossRef]

[21] Khan, M.A. and Atangana, A. Mathematical modeling and analysis of COVID-19: a study of new variant Omicron. *Physica A: Statistical Mechanics and its Applications*, 599, 127452, (2022). [CrossRef]

[22] Yang, H., Lin, X., Li, J., Zhai, Y. and Wu, J. A review of mathematical models of COVID-19 transmission. *Contemporary Mathematics*, 4(1), 75-98, (2023). [CrossRef]

[23] Capasso, V. and Serio, G. A generalization of the Kermack-McKendrick deterministic epidemic model. *Mathematical Biosciences*, 42(1-2), 43–61, (1978). [CrossRef]

[24] Buonomo, B., d'Onofrio, A. and Lacitignola, D. Global stability of an SIR epidemic model with information dependent vaccination. *Mathematical Biosciences*, 216(1), 9-16, (2008). [CrossRef]

[25] Khajanchi, S., Sarkar, K. and Mondal, J. Dynamics of the COVID-19 pandemic in India. *ArXiv Preprint, ArXiv:2005.06286*, (2020). [CrossRef]

[26] Akanni, J.O., Akinpelu, F.O., Olaniyi, S., Oladipo, A.T. and Ogunsola, A.W. Modelling financial crime population dynamics: optimal control and cost-effectiveness analysis. *International Journal of Dynamics and Control*, 8, 531–544, (2020). [CrossRef]

[27] Diekmann, O., Heesterbeek, J.A.P. and Roberts, M.G. The construction of next-generation matrices for compartmental epidemic models. *Journal of the Royal Society Interface*, 7(47), 873–885, (2010). [CrossRef]

[28] Iggidr, A., Mbang, J., Sallet, G. and Tewa, J.J. Multi-compartment models. *Discrete and Continuous Dynamical Systems Supplement*, 2007, 506-519, (2007). [CrossRef]

[29] Cvetković, A. Stabilizing the Metzler matrices with applications to dynamical systems. *Calcolo*, 57, 1, (2020). [CrossRef]

[30] Korobeinikov, A. and Maini, P.K. A Lyapunov function and global properties for SIR and SEIR epidemiological models with nonlinear incidence. *Mathematical Biosciences & Engineering*, 1(1), 57–60, (2004). [CrossRef]

[31] Chitnis, N., Hyman, J.M. and Cushing, J.M. Determining important parameters in the spread of malaria through the sensitivity analysis of a mathematical model. *Bulletin of Mathematical Biology*, 70, 1272–1296, (2008). [CrossRef]

[32] Berhe, H.W. and Makinde, O.D. Computational modelling and optimal control of measles epidemic in human population. *Biosystems*, 190, 104102, (2020). [CrossRef]

[33] Abidemi, A., Akanni, J.O. and Makinde, O.D. A non-linear mathematical model for analysing the impact of COVID-19 disease on higher education in developing countries. *Healthcare Analytics*, 3, 100193, (2023). [CrossRef]

[34] Gaff, H.D., Schaefer, E. and Lenhart, S. Use of optimal control models to predict treatment time for managing tick-borne disease. *Journal of Biological Dynamics*, 5(5), 517–530, (2011). [CrossRef]

[35] Fleming, W.H. and Rishel, R.W. *Deterministic and Stochastic Optimal Control* (Vol. 1). New York: Springer-Verlag, (1975). [CrossRef]

[36] Coddington, E.A., Levinson, N. and Teichmann, T. Theory of ordinary differential equations. *Physics Today*, 9(2), 18, (1956).

[37] Aseev, S.M. and Kryazhimskii, A.V. The Pontryagin maximum principle and optimal economic growth problems. *Proceedings of the Steklov Institute of Mathematics*, 257, 1–255, (2007). [CrossRef]

[38] World Health Organization (WHO), Coronavirus disease (COVID-19). https://www.who.int/emergencies/diseases/novel-coronavirus-2019.

[39] Kouidere, A., Kada, D., Balatif, O., Rachik, M. and Naim, M. Optimal control approach of a mathematical modeling with multiple delays of the negative impact of delays in applying preventive precautions against the spread of the COVID-19 pandemic with a case study of Brazil and cost-effectiveness. *Chaos, Solitons & Fractals*, 142, 110438, (2021). [CrossRef]

[40] Abidemi, A. and Akanni, J.O. Dynamics of illicit drug use and banditry population with optimal control strategies and cost-effectiveness analysis. *Computational and Applied Mathematics*, 41, 53, (2022). [CrossRef]

[41] Alhassan, A., Momoh, A.A., Abdullahi, A.S. and Kadzai, M.T.Y. Optimal control strategies and cost effectiveness analysis of a malaria transmission model. *Mathematical Theory and Modeling*, 7(6), 123-138, (2017).

[42] Kada, D., Labzai, A., Balatif, O., Rachik, M. and Labriji, E. H. Spread of COVID-19 in Morocco discrete mathematical modeling: optimal control strategies and cost-effectiveness analysis. *Journal of Mathematical and Computational Science*, 10(5), 2070-2093, (2020). [CrossRef]

[43] Marsudi, Hidayat, N. and Wibowo, R.B.E. Optimal control and cost-effectiveness analysis of HIV model with educational campaigns and therapy. *Matematika*, 123-138, (2019).

[44] Dietz, K. The estimation of the basic reproduction number for infectious diseases. *Statistical Methods in Medical Research*, 2(1), 23-41, (1993). [CrossRef]

Mathematical Modelling and Numerical Simulation with Applications (MMNSA)
(https://dergipark.org.tr/en/pub/mmnsa)

RESEARCH PAPER

A novel Touchard polynomial-based spectral matrix collocation method for solving the Lotka-Volterra competition system with diffusion

Mohammad Izadi 🄳 1,‡, Ahmed El-Mesady 🄳 2,*,‡ and Waleed Adel 🄳 3,4,‡

[1]Department of Applied Mathematics, Faculty of Mathematics and Computer, Shahid Bahonar University of Kerman, Kerman, Iran, [2]Department of Physics and Engineering Mathematics, Faculty of Electronic Engineering, Menoufia University, Menouf, 32952, Egypt, [3]Laboratoire Interdisciplinaire de l'Universite´ Francaise d'Egypte (UFEID Lab), Universite´ Francaise d'Egypte, Cairo, 11837, Egypt, [4]Department of Mathematics and Engineering Physics, Faculty of Engineering, Mansoura University, 35511, Egypt

*Corresponding Author
‡ izadi@uk.ac.ir (Mohammad Izadi); ahmed.ibrahiem81@el-eng.menofia.edu.eg (Ahmed El-Mesady); waleed.ouf@ufe.edu.eg (Waleed Adel)

Abstract

This paper presents the computational solutions of a time-dependent nonlinear system of partial differential equations (PDEs) known as the Lotka-Volterra competition system with diffusion. We propose a combined semi-discretized spectral matrix collocation algorithm to solve this system of PDEs. The first part of the algorithm deals with the time-marching procedure, which is performed using the well-known Taylor series formula. The resulting linear systems of ordinary differential equations (ODEs) are then solved using the spectral matrix collocation technique based on the novel Touchard family of polynomials. We discuss and establish the error analysis and convergence of the proposed method. Additionally, we examine the stability analysis and the equilibrium points of the model to determine the stability condition for the system. We perform numerical simulations using diverse model parameters and with different Dirichlet and Neumann boundary conditions to demonstrate the utility and applicability of our combined Taylor-Touchard spectral collocation algorithm.

Keywords: Collocation points; convergent analysis; stability; Touchard polynomials; Taylor series
AMS 2020 Classification: 65L60; 41A10; 34A12; 35N70; 65L20

1 Introduction

During the past few years, the Lotka-Volterra population model has garnered significant attention from scientists due to its efficacy in describing the interaction between two species in a closed

ecosystem. Originating in 1925 from the work of renowned scientist Alfred Lotka and independently developed by Vito Volterra in 1926, this model has become a cornerstone in ecological, biological, epidemiological, and economic studies [1–4]. One notable application of this model in economics is in modeling the interaction between firms within a market [5], while in epidemiology, it finds use in understanding the spread of infectious diseases [6]. The fundamental assumptions of the model posit that the population sizes of the predator and prey species are determined solely by their interactions with each other and their environment.

Specifically, the model assumes (1) exponential growth of the prey population in the absence of predators, (2) exponential decline of the predator population in the absence of prey, (3) proportional growth of the predator population relative to the prey population, and (4) proportional decline of the prey population relative to the predator population. The simplest form of the Lotka-Volterra population model can be expressed as a system of two coupled first-order ordinary differential equations, one for the prey population and one for the predator population. This formulation serves as a foundational framework for further analysis and applications

$$\begin{cases} \dfrac{dv}{dt} = a\,v - b\,vw, \\ \dfrac{dw}{dt} = -c\,w + d\,vw, \end{cases} \tag{1}$$

where v and w represent the population sizes of the prey and predator, respectively, and $a, b, c,$ and d are parameters governing the growth rates and interactions between the two populations. The Lotka-Volterra model exhibits several intriguing and significant features. Among these is the presence of periodic solutions, which depict the cyclic behavior of predator and prey populations within a closed ecosystem. These cycles, often referred to as predator-prey cycles or limit cycles, are a characteristic aspect of the model.

Moreover, the model has been extended in various ways to encompass more complex ecological interactions. One notable extension is the diffusive Lotka-Volterra competition model, which describes the interactions among two or more competing species within a spatially heterogeneous environment. Unlike the classical Lotka-Volterra competition model, which assumes that the population sizes of competing species are solely determined by their interactions and environment, the diffusive Lotka-Volterra competition system accounts for the effects of spatial heterogeneity on species competition. Given these important variations of the Lotka-Volterra model, numerous efforts have been made to find accurate solutions to such models. For instance, Ni et al. [7] investigated the model's global stability and pattern formation, considering dynamical resources. Lin et al. [8] discussed traveling wave solutions for the delayed Lotka-Volterra model using Schauder's fixed point theorem. Wijeratne et al. [9] conducted a detailed bifurcation analysis for the diffusive model, with potential applications in market share at duopoly, including a case study in Sri Lanka. Cherniha et al. [10] provided a review of up-to-date solutions for the diffusive model, presenting a wide range of exact solutions for its applications.

Numerous other works on the simulation and discussion of dynamics in the diffusive model can be found in [11–14] and references therein. In this research paper, our primary focus is on the approximate solutions of a system of partial differential equations (PDEs) comprising two nonlinear equations with quadratic terms (see [15]):

$$\begin{cases} \frac{\partial v}{\partial \tau} - D_1 \frac{\partial^2 v}{\partial x^2} = v(A_1 - B_1 \, v - C_1 \, w), \\[2mm] \frac{\partial w}{\partial \tau} - D_2 \frac{\partial^2 w}{\partial x^2} = w(A_2 - B_2 \, w - C_2 \, v), \end{cases} \quad (x, \tau) \in \Omega_L \times \Omega_T, \tag{2}$$

where $\Omega_L := [0, L]$ and $\Omega_T := [0, T]$ with the initial conditions

$$v(x, \tau = 0) = f(x), \quad w(x, \tau = 0) = g(x), \quad x \in \Omega_L. \tag{3}$$

Here, by $v = v(x, \tau)$ and $w = w(x, \tau)$ we denote the population densities of two given competing species at time τ and f, g are two (smooth) given functions. Also, D_1 and D_2 are diffusion coefficients and are assumed to be positive constants. The non-negative constants A_1, A_2 show the growth rate of the respective species, $B_1, B_2 \geq 0$ represent the related dead rates, and $C_1, C_2 \geq 0$ are the interaction rates between two competing species. The boundary conditions are supplemented either in the form of Dirichlet

$$\begin{cases} v(x = 0, \tau) = v_0(\tau), & v(x = L, \tau) = v_L(\tau), \\ w(x = 0, \tau) = w_0(\tau), & w(x = L, \tau) = w_L(\tau), \end{cases} \quad \tau \in \Omega_T, \tag{4}$$

or as the Neumann boundary conditions are given by

$$\begin{cases} \frac{\partial v}{\partial x}(x = 0, \tau) = v_0(\tau), & \frac{\partial v}{\partial x}(x = L, \tau) = v_L(\tau), \\[2mm] \frac{\partial w}{\partial x}(x = 0, \tau) = w_0(\tau), & \frac{\partial w}{\partial x}(x = L, \tau) = w_L(\tau), \end{cases} \quad \tau \in \Omega_T, \tag{5}$$

where the functions $v_0(\tau), w_0(\tau), v_L(\tau)$, and $w_L(\tau)$ are some familiar functions. A few analytical and computational strategies have been developed to deal with the model problem (2) with initial condition (3) accompanied with boundary condition (4) or (5). Let us mention the G'/G-expansion approach [16], the finite difference scheme [17], and the compact implicit-explicit RK type techniques [18]. To acquire the approximate solution of model (2) along with its conditions, we shall adopt a spectral matrix collocation algorithm based on a novel Touchard family of polynomials accompanied by the Taylor expansion technique [19–22]. The applications of the spectral collocation approach with exponential-order accuracy have been examined for various model problems in physical sciences. For example, we may draw your attention to the recently published works [23–30]. The Touchard polynomials, also known as Touchard-Riordan polynomials or exponential polynomials, constitute a family of functions prominent in combinatorics and partition theory [31]. Named after the French mathematician Jacques Touchard, who introduced them in 1934, these polynomials are defined through exponential generating functions and exhibit close ties to Bell polynomials and Stirling numbers of the second kind [32].

Offering several intriguing properties, they find applications across various mathematical domains, including combinatorics, number theory, and algebraic geometry. Their utility extends to the realm of modeling, where they have been increasingly employed in recent years. Touchard polynomials have found utility in analyzing stochastic models such as branching processes, random walks, and queueing systems. In these contexts, they have been instrumental in deriving exact and asymptotic expressions for key parameters, including the probability of extinction, expected particle counts,

and waiting time distributions. Despite their versatility, their application in solving mathematical models has been relatively limited. For instance, Sabermahani [33] adapted Touchard polynomials to solve fractional-order Fokker-Planck equations, representing one of the few reported instances of their use in mathematical modeling. Motivated by this gap in the literature, the current study explores the application of Touchard polynomials in simulating the model described in (2). As far as the authors are aware, this represents the first instance of Touchard polynomials being utilized to solve diffusive Lotka-Volterra competition systems.

The manuscript is structured as follows: Section 2 introduces the time-advancement approach used for discretizing the time variable in the main model. In Section 3, we conduct a stability analysis of the model, identifying equilibrium points and discussing the conditions for stable solutions. Section 4 provides a comprehensive review of Touchard polynomials, highlighting their relevant properties for subsequent sections. The hybrid Taylor-Touchard algorithm is then elaborated upon in Section 5, followed by a validation of the theoretical framework through several examples in Section 6. Finally, Section 7 presents the conclusions drawn from the study.

2 Time-advancement approach

Here and in this part, we first apply the Taylor formula to discretize the given system of PDEs (2) in time direction. For this purpose, we consider a uniform partitioning of $[0, T]$ into K subdivisions with nodes

$$\tau_0 = 0 < \tau_1 = \Delta\tau < \ldots < \tau_K = K\Delta\tau = T.$$

Here $\Delta\tau = \tau_{k+1} - \tau_k$ indicates the time step of the mesh for $k \in \mathbb{K} := \{0, 1, \ldots, K-1\}$. By v^k, w^k, we denote the approximations to the true exact solutions $v(x, \tau), w(x, \tau)$ at time level τ_k, respectively. Namely, we set

$$v^k \equiv v^k(x) := v(x, \tau_k), \quad w^k \equiv w^k(x) := w(x, \tau_k), \quad x \in \Omega_L.$$

The given equations at time step τ_k are

$$\begin{cases} v_\tau^k = D_1 \, v_{xx}^k + A_1 \, v^k - B_1 \, (v^k)^2 - C_1 \, v^k \, w^k, \\ w_\tau^k = D_2 \, w_{xx}^k + A_2 \, w^k - B_2 \, (w^k)^2 - C_2 \, v^k \, w^k. \end{cases} \tag{6}$$

Using the Taylor series formula, we find that

$$\begin{cases} v_\tau^k = (v^{k+1} - v^k)/\Delta\tau + \Delta\tau \, v_{\tau\tau}^k/2 + \mathcal{O}(\Delta\tau^2), \\ w_\tau^k = (w^{k+1} - w^k)/\Delta\tau + \Delta\tau \, w_{\tau\tau}^k/2 + \mathcal{O}(\Delta\tau^2), \end{cases} \tag{7}$$

if we differentiate system (6) with regard to τ, we shall have

$$\begin{cases} \Delta\tau \, v_{\tau\tau}^k &= D_1(v_{xx}^{k+1} - v_{xx}^k) + A_1(v^{k+1} - v^k) - 2B_1 \, v^k(v^{k+1} - v^k) - C_1 \, (v^{k+1} - v^k) \, w^k \\ &\quad -C_1 \, v^k(w^{k+1} - w^k), \\ \Delta\tau \, w_{\tau\tau}^k &= D_2(w_{xx}^{k+1} - w_{xx}^k) + A_2(w^{k+1} - w^k) - 2B_2 \, w^k(w^{k+1} - w^k) - C_2 \, v^k \, (w^{k+1} - w^k) \\ &\quad -C_2(v^{k+1} - v^k)w^k, \end{cases} \tag{8}$$

in which we have replaced all terms in the forms v_τ^k, w_τ^k by their difference first-order quotients $(v^{k+1} - v^k)/\Delta\tau$, $(w^{k+1} - w^k)/\Delta\tau$ respectively on the right-hand side.

Now, it is sufficient to insert the two above relations (8) into (7). Then, the left-hand sides of relations (7) will be equated to those related relations given in (6). After some manipulations and collecting the same terms together, we reach the discretized linearized set of equations for (2). In the matrix form, we get

$$\boldsymbol{M}_1^k(x)\frac{d^2}{dx^2}\boldsymbol{U}^{k+1}(x) + \boldsymbol{M}_2^k(x)\,\boldsymbol{U}^{k+1}(x) = \boldsymbol{H}^k(x), \quad k \in \mathbb{K}, \tag{9}$$

where

$$\boldsymbol{U}^{k+1}(x) := \begin{bmatrix} v^{k+1} \\ w^{k+1} \end{bmatrix}, \boldsymbol{M}_1^k(x) := \begin{bmatrix} -D_1\,\Delta\tau & 0 \\ 0 & -D_2\,\Delta\tau \end{bmatrix}, \boldsymbol{H}^k(x) := \begin{bmatrix} D_1\,\Delta\tau\,v_{xx}^k + (2 + A_1\,\Delta\tau)v^k \\ D_2\,\Delta\tau\,w_{xx}^k + (2 + A_2\,\Delta\tau)w^k \end{bmatrix},$$

and

$$\boldsymbol{M}_2^k(x) := \begin{bmatrix} 2 + \Delta\tau\left(-A_1 + 2B_1\,v^k + C_1\,w^k\right) & C_1\,\Delta\tau\,v^k \\ C_2\,\Delta\tau\,w^k & 2 + \Delta\tau\left(-A_2 + 2B_2\,w^k + C_2\,v^k\right) \end{bmatrix}.$$

To compute the approximate solution of Eq. (9), one first requires the expression $\boldsymbol{U}^0(x)$, which is obtained from the initial conditions $v^0(x) = f(x)$ and $w^0(x) = g(x)$. Besides the functions $v^0(x) = f(x)$ and $w^0(x) = g(x)$, the second-order derivative of them also appears in the vector function $\boldsymbol{H}^0(x)$. The boundary conditions (4) or (5) will be converted accordingly. Under the prescription of Dirichlet boundary conditions we have the following at $x = 0, L$

$$\boldsymbol{U}^{k+1}(0) = \boldsymbol{B}_0^{k+1} := \begin{bmatrix} v_0^{k+1} \\ w_0^{k+1} \end{bmatrix} = \begin{bmatrix} v_0(\tau_{k+1}) \\ w_0(\tau_{k+1}) \end{bmatrix}, \quad \boldsymbol{U}^{k+1}(L) = \boldsymbol{B}_L^{k+1} := \begin{bmatrix} v_L^{k+1} \\ w_L^{k+1} \end{bmatrix} = \begin{bmatrix} v_L(\tau_{k+1}) \\ w_L(\tau_{k+1}) \end{bmatrix}. \tag{10}$$

In an analog manner, we can handle the Neumann boundary conditions (5) as

$$\frac{d}{dx}\boldsymbol{U}^{k+1}(0) = \boldsymbol{B}_0^{k+1}, \qquad \frac{d}{dx}\boldsymbol{U}^{k+1}(L) = \boldsymbol{B}_L^{k+1}, \tag{11}$$

where two vectors $\boldsymbol{B}_0^{k+1}$ and $\boldsymbol{B}_L^{k+1}$ are defined in system (10).

3 Qualitative analysis of the model

This section is devoted to the qualitative study of the Lotka-Voltral PDE model (2). First, we derive the equilibria of system (2). Then, we discuss the stability of each point.

The equilibrium points of the system

Let us consider both non-diffusive model

$$\begin{cases} \dfrac{dv}{dt} = v(A_1 - B_1\,v - C_1\,w), \\[2mm] \dfrac{dw}{dt} = w(A_2 - B_2\,w - C_2\,v), \end{cases} \tag{12}$$

and diffusive model

$$
\begin{cases}
\dfrac{\partial v}{\partial \tau} - D_1 \dfrac{\partial^2 v}{\partial x^2} = v(A_1 - B_1\, v - C_1\, w), \\[2mm]
\dfrac{\partial w}{\partial \tau} - D_2 \dfrac{\partial^2 w}{\partial x^2} = w(A_2 - B_2\, w - C_2\, v),
\end{cases}
\qquad (x,\tau) \in \Omega_L \times \Omega_T.
\tag{13}
$$

The equilibrium points of these systems are obtained by equating the right-hand side of system (13) to zero as follows [34, 35]:

$$
\begin{cases}
v(A_1 - B_1\, v - C_1\, w) = 0, \\[2mm]
w(A_2 - B_2\, w - C_2\, v) = 0.
\end{cases}
\tag{14}
$$

Hence, by solving the system (14), the equilibrium points of this system are as follows:

$$
\begin{cases}
(v^1, w^1) = (0,0), \\[2mm]
(v^2, w^2) = (0, \dfrac{A_2}{B_2}), \\[2mm]
(v^3, w^3) = (\dfrac{A_1}{B_1}, 0), \\[2mm]
(v^4, w^4) = (\dfrac{A_1 B_2 - A_2 C_1}{B_1 B_2 - C_1 C_2}, \dfrac{A_2 B_1 - A_1 C_2}{B_1 B_2 - C_1 C_2}).
\end{cases}
\tag{15}
$$

The stability of the equilibrium points

The non-diffusive model can be described by the following system:

$$
\begin{cases}
\dfrac{dv}{dt} = v(A_1 - B_1\, v - C_1\, w) = \varphi(v,w), \\[2mm]
\dfrac{dw}{dt} = w(A_2 - B_2\, w - C_2\, v) = \psi(v,w).
\end{cases}
\tag{16}
$$

The Jacobian matrix corresponding to system (16) is as follows:

$$
J = \begin{bmatrix}
\dfrac{\partial \varphi}{\partial v} & \dfrac{\partial \varphi}{\partial w} \\[2mm]
\dfrac{\partial \psi}{\partial v} & \dfrac{\partial \psi}{\partial w}
\end{bmatrix}.
$$

The characteristic equation can be represented by

$$
\lambda^2 - \left(\frac{\partial \varphi}{\partial v} + \frac{\partial \psi}{\partial w} \right) \lambda + \left(\frac{\partial \varphi}{\partial v}\frac{\partial \psi}{\partial w} - \frac{\partial \varphi}{\partial w}\frac{\partial \psi}{\partial v} \right) = 0.
\tag{17}
$$

Suppose that we are at the steady state $v = v^{ss}, w = w^{ss}$. Therefore, we can conclude that the equilibrium point (v^{ss}, w^{ss}) is locally asymptotically stable according to Routh–Hurwitz criteria if

the next conditions are fulfilled at the equilibrium point

$$
\begin{cases}
\dfrac{\partial \varphi}{\partial v} + \dfrac{\partial \psi}{\partial w} < 0, \\[2mm]
\dfrac{\partial \varphi}{\partial v} \dfrac{\partial \psi}{\partial w} - \dfrac{\partial \varphi}{\partial w} \dfrac{\partial \psi}{\partial v} > 0.
\end{cases}
\tag{18}
$$

From system (16), we have

$$
\begin{cases}
\dfrac{\partial \varphi}{\partial v} = A_1 - 2B_1\, v - C_1\, w, \\[2mm]
\dfrac{\partial \varphi}{\partial w} = -C_1\, v, \\[2mm]
\dfrac{\partial \psi}{\partial v} = -C_2\, v, \\[2mm]
\dfrac{\partial \psi}{\partial w} = A_2 - 2B_2\, w - C_2\, v.
\end{cases}
\tag{19}
$$

Since we have four equilibrium points, there are four cases:

Case 1: For $(v^{ss}, w^{ss}) = (v^1, w^1) = (0,0)$, the partial derivatives in (19) can be written as follows:

$$
\begin{cases}
\dfrac{\partial \varphi}{\partial v} = A_1, \\[2mm]
\dfrac{\partial \varphi}{\partial w} = 0, \\[2mm]
\dfrac{\partial \psi}{\partial v} = 0, \\[2mm]
\dfrac{\partial \psi}{\partial w} = A_2.
\end{cases}
\tag{20}
$$

Therefore, we can write

$$
\begin{cases}
\dfrac{\partial \varphi}{\partial v} + \dfrac{\partial \psi}{\partial w} = A_1 + A_2 \geq 0, \\[2mm]
\dfrac{\partial \varphi}{\partial v} \dfrac{\partial \psi}{\partial w} - \dfrac{\partial \varphi}{\partial w} \dfrac{\partial \psi}{\partial v} = A_1 A_2 \geq 0.
\end{cases}
\tag{21}
$$

Hence the equilibrium point $(v^1, w^1) = (0,0)$ is unstable.

Case 2: For $(v^{ss}, w^{ss}) = (v^2, w^2) = (0, \frac{A_2}{B_2})$, the partial derivatives in (19) can be written as follows:

$$
\begin{cases}
\dfrac{\partial \varphi}{\partial v} = A_1 - C_1 \dfrac{A_2}{B_2}, \\[2mm]
\dfrac{\partial \varphi}{\partial w} = 0, \\[2mm]
\dfrac{\partial \psi}{\partial v} = 0, \\[2mm]
\dfrac{\partial \psi}{\partial w} = -A_2.
\end{cases}
\tag{22}
$$

Consequently, we can write

$$
\begin{cases}
\dfrac{\partial \varphi}{\partial v} + \dfrac{\partial \psi}{\partial w} = A_1 - C_1 \dfrac{A_2}{B_2} - A_2, \\[2mm]
\dfrac{\partial \varphi}{\partial v}\dfrac{\partial \psi}{\partial w} - \dfrac{\partial \varphi}{\partial w}\dfrac{\partial \psi}{\partial v} = (C_1 \dfrac{A_2}{B_2} - A_1)A_2.
\end{cases}
\tag{23}
$$

Hence the equilibrium point $(v^2, w^2) = (0, \frac{A_2}{B_2})$ will be asymptotically stable if $A_1 - C_1\frac{A_2}{B_2} - A_2 < 0$ and $(C_1\frac{A_2}{B_2} - A_1)A_2 > 0$.

Case 3: For $(v^{ss}, w^{ss}) = (v^3, w^3) = (\frac{A_1}{B_1}, 0)$, the partial derivatives in (19) can be written as follows:

$$
\begin{cases}
\dfrac{\partial \varphi}{\partial v} = -A_1, \\[2mm]
\dfrac{\partial \varphi}{\partial w} = -C_1 \dfrac{A_1}{B_1}, \\[2mm]
\dfrac{\partial \psi}{\partial v} = -C_2 \dfrac{A_1}{B_1}, \\[2mm]
\dfrac{\partial \psi}{\partial w} = A_2 - C_2 \dfrac{A_1}{B_1}.
\end{cases}
\tag{24}
$$

Thus, we can write

$$
\begin{cases}
\dfrac{\partial \varphi}{\partial v} + \dfrac{\partial \psi}{\partial w} = A_2 - A_1 - C_2 \dfrac{A_1}{B_1}, \\[2mm]
\dfrac{\partial \varphi}{\partial v}\dfrac{\partial \psi}{\partial w} - \dfrac{\partial \varphi}{\partial w}\dfrac{\partial \psi}{\partial v} = (C_2 \dfrac{A_1}{B_1} - A_2)A_1 - C_1 C_2 (\dfrac{A_1}{B_1})^2.
\end{cases}
\tag{25}
$$

Hence, the equilibrium point $(v^3, w^3) = (\frac{A_1}{B_1}, 0)$ will be asymptotically stable if $A_2 - A_1 - C_2\frac{A_1}{B_1} < 0$ and $(C_2\frac{A_1}{B_1} - A_2)A_1 - C_1 C_2(\frac{A_1}{B_1})^2 > 0$.

Case 4: For $(v^{ss}, w^{ss}) = (v^4, w^4) = (\frac{A_1 B_2 - A_2 C_1}{B_1 B_2 - C_1 C_2}, \frac{A_2 B_1 - A_1 C_2}{B_1 B_2 - C_1 C_2})$, the partial derivatives in (19) can be written as follows:

$$
\begin{cases}
\dfrac{\partial \varphi}{\partial v} = A_1 - 2B_1(\dfrac{A_1 B_2 - A_2 C_1}{B_1 B_2 - C_1 C_2}) - C_1(\dfrac{A_2 B_1 - A_1 C_2}{B_1 B_2 - C_1 C_2}), \\[2mm]
\dfrac{\partial \varphi}{\partial w} = -C_1(\dfrac{A_1 B_2 - A_2 C_1}{B_1 B_2 - C_1 C_2}), \\[2mm]
\dfrac{\partial \psi}{\partial v} = -C_2(\dfrac{A_1 B_2 - A_2 C_1}{B_1 B_2 - C_1 C_2}), \\[2mm]
\dfrac{\partial \psi}{\partial w} = A_2 - 2B_2(\dfrac{A_2 B_1 - A_1 C_2}{B_1 B_2 - C_1 C_2}) - C_2(\dfrac{A_1 B_2 - A_2 C_1}{B_1 B_2 - C_1 C_2}).
\end{cases}
\tag{26}
$$

Hence the equilibrium point $(v^4, w^4) = (\frac{A_1 B_2 - A_2 C_1}{B_1 B_2 - C_1 C_2}, \frac{A_2 B_1 - A_1 C_2}{B_1 B_2 - C_1 C_2})$ is asymptotically stable if

$$
\begin{aligned}
\frac{\partial \varphi}{\partial v} + \frac{\partial \psi}{\partial w} &= A_1 - 2B_1 (\frac{A_1 B_2 - A_2 C_1}{B_1 B_2 - C_1 C_2}) - C_1 (\frac{A_2 B_1 - A_1 C_2}{B_1 B_2 - C_1 C_2}) \\
&\quad + A_2 - 2B_2 (\frac{A_2 B_1 - A_1 C_2}{B_1 B_2 - C_1 C_2}) - C_2 (\frac{A_1 B_2 - A_2 C_1}{B_1 B_2 - C_1 C_2}) < 0, \\
\frac{\partial \varphi}{\partial v} \frac{\partial \psi}{\partial w} - \frac{\partial \varphi}{\partial w} \frac{\partial \psi}{\partial v} &= (A_1 - 2B_1 (\frac{A_1 B_2 - A_2 C_1}{B_1 B_2 - C_1 C_2}) - C_1 (\frac{A_2 B_1 - A_1 C_2}{B_1 B_2 - C_1 C_2})) \\
&\quad \times (A_2 - 2B_2 (\frac{A_2 B_1 - A_1 C_2}{B_1 B_2 - C_1 C_2}) - C_2 (\frac{A_1 B_2 - A_2 C_1}{B_1 B_2 - C_1 C_2})) \\
&\quad - C_1 C_2 (\frac{A_1 B_2 - A_2 C_1}{B_1 B_2 - C_1 C_2})^2 > 0.
\end{aligned}
\tag{27}
$$

The diffusive model can be written as follows:

$$
\begin{cases}
\dfrac{\partial v}{\partial \tau} = D_1 \dfrac{\partial^2 v}{\partial x^2} + \varphi(u, v), \\[2mm]
\dfrac{\partial w}{\partial \tau} = D_2 \dfrac{\partial^2 w}{\partial x^2} + \psi(u, v).
\end{cases}
\tag{28}
$$

Now, we linearize the diffusive model by taking $\tilde{v} = v - v_{ss}$ and $\tilde{w} = w - w_{ss}$. Hence, system (28) is transformed to

$$
\begin{cases}
\dfrac{\partial \tilde{v}}{\partial \tau} = D_1 \dfrac{\partial^2 \tilde{v}}{\partial x^2} + \dfrac{\partial \varphi}{\partial v} \tilde{v} + \dfrac{\partial \varphi}{\partial w} \tilde{w}, \\[2mm]
\dfrac{\partial \tilde{w}}{\partial \tau} = D_2 \dfrac{\partial^2 \tilde{w}}{\partial x^2} + \dfrac{\partial \psi}{\partial v} \tilde{v} + \dfrac{\partial \psi}{\partial w} \tilde{w}.
\end{cases}
\tag{29}
$$

By taking $\tilde{v}(x, t) = v^* e^{\sigma t} \sin \alpha x$ and $\tilde{w}(x, t) = w^* e^{\sigma t} \sin \alpha x$, then (29) is transformed to

$$
\begin{cases}
\sigma v^* = -\alpha^2 D_1 v^* + \dfrac{\partial \varphi}{\partial v} v^* + \dfrac{\partial \varphi}{\partial w} w^*, \\[2mm]
\sigma w^* = -\alpha^2 D_2 w^* + \dfrac{\partial \psi}{\partial v} v^* + \dfrac{\partial \psi}{\partial w} w^*,
\end{cases}
\tag{30}
$$

or

$$
\begin{cases}
\sigma v^* = (\dfrac{\partial \varphi}{\partial v} - \alpha^2 D_1) v^* + \dfrac{\partial \varphi}{\partial w} w^*, \\[2mm]
\sigma w^* = \dfrac{\partial \psi}{\partial v} v^* + (\dfrac{\partial \psi}{\partial w} - \alpha^2 D_2) w^*,
\end{cases}
\tag{31}
$$

which can be written as a linear system as follows:

$$
AX = \sigma X,
\tag{32}
$$

$$A = \begin{bmatrix} \dfrac{\partial \varphi}{\partial v} - \alpha^2 D_1 & \dfrac{\partial \varphi}{\partial w} \\[2ex] \dfrac{\partial \psi}{\partial v} & \dfrac{\partial \psi}{\partial w} - \alpha^2 D_2 \end{bmatrix}, \quad X = \begin{bmatrix} v^* \\ w^* \end{bmatrix}. \tag{33}$$

Hence, the characteristic equation $|A - \sigma I| = 0$, can be represented by

$$\sigma^2 - \left((\frac{\partial \varphi}{\partial v} - \alpha^2 D_1) + (\frac{\partial \psi}{\partial w} - \alpha^2 D_2) \right) \sigma + \left(\frac{\partial \varphi}{\partial v} - \alpha^2 D_1 \right) \left(\frac{\partial \psi}{\partial w} - \alpha^2 D_2 \right) - \frac{\partial \varphi}{\partial w} \frac{\partial \psi}{\partial v} = 0. \tag{34}$$

As a result, the asymptotic stability according to Routh–Hurwitz criterion [34, 35] is verified if

$$\left((\frac{\partial \varphi}{\partial v} - \alpha^2 D_1) + (\frac{\partial \psi}{\partial w} - \alpha^2 D_2) \right) < 0, \quad (\frac{\partial \varphi}{\partial v} - \alpha^2 D_1)(\frac{\partial \psi}{\partial w} - \alpha^2 D_2) - \frac{\partial \varphi}{\partial w} \frac{\partial \psi}{\partial v} > 0. \tag{35}$$

As we discussed above we have four equilibrium points, then there are four cases:

Case 1: The equilibrium point $(v^1, w^1) = (0, 0)$ is asymptotically stable if

$$\begin{cases} (\dfrac{\partial \varphi}{\partial v} - \alpha^2 D_1) + (\dfrac{\partial \psi}{\partial w} - \alpha^2 D_2) = A_1 + A_2 - \alpha^2 (D_1 + D_2) < 0, \\[2ex] (\dfrac{\partial \varphi}{\partial v} - \alpha^2 D_1)(\dfrac{\partial \psi}{\partial w} - \alpha^2 D_2) - \dfrac{\partial \varphi}{\partial w} \dfrac{\partial \psi}{\partial v} = (A_1 - \alpha^2 D_1)(A_2 - \alpha^2 D_2) > 0. \end{cases} \tag{36}$$

Case 2: The equilibrium point $(v^2, w^2) = (0, \frac{A_2}{B_2})$ is asymptotically stable if

$$\begin{cases} (\dfrac{\partial \varphi}{\partial v} - \alpha^2 D_1) + (\dfrac{\partial \psi}{\partial w} - \alpha^2 D_2) = A_1 - A_2 - C_1 \dfrac{A_2}{B_2} - \alpha^2 (D_1 + D_2) < 0, \\[2ex] (\dfrac{\partial \varphi}{\partial v} - \alpha^2 D_1)(\dfrac{\partial \psi}{\partial w} - \alpha^2 D_2) - \dfrac{\partial \varphi}{\partial w} \dfrac{\partial \psi}{\partial v} = (A_1 - C_1 \dfrac{A_2}{B_2} - \alpha^2 D_1)(-A_2 - \alpha^2 D_2) > 0. \end{cases} \tag{37}$$

Case 3: The equilibrium point $(v^3, w^3) = (\frac{A_1}{B_1}, 0)$ is asymptotically stable if

$$\begin{cases} (\dfrac{\partial \varphi}{\partial v} - \alpha^2 D_1) + (\dfrac{\partial \psi}{\partial w} - \alpha^2 D_2) = -A_1 + A_2 - C_2 \dfrac{A_1}{B_1} - \alpha^2 (D_1 + D_2) < 0, \\[2ex] (\dfrac{\partial \varphi}{\partial v} - \alpha^2 D_1)(\dfrac{\partial \psi}{\partial w} - \alpha^2 D_2) - \dfrac{\partial \varphi}{\partial w} \dfrac{\partial \psi}{\partial v} = (-A_1 - \alpha^2 D_1)(A_2 - C_2 \dfrac{A_1}{B_1} - \alpha^2 D_2) > 0. \end{cases} \tag{38}$$

Case 4: The equilibrium point $(v^4, w^4) = (\frac{A_1 B_2 - A_2 C_1}{B_1 B_2 - C_1 C_2}, \frac{A_2 B_1 - A_1 C_2}{B_1 B_2 - C_1 C_2})$ is asymptotically stable if

$$\begin{cases} \left(\dfrac{\partial \varphi}{\partial v} - \alpha^2 D_1 \right) + \left(\dfrac{\partial \psi}{\partial w} - \alpha^2 D_2 \right) < 0, \\[2ex] \left(\dfrac{\partial \varphi}{\partial v} - \alpha^2 D_1 \right) \left(\dfrac{\partial \psi}{\partial w} - \alpha^2 D_2 \right) - \dfrac{\partial \varphi}{\partial w} \dfrac{\partial \psi}{\partial v} > 0, \end{cases} \tag{39}$$

where

$$
\begin{cases}
\dfrac{\partial \varphi}{\partial v} = A_1 - 2B_1 \left(\dfrac{A_1 B_2 - A_2 C_1}{B_1 B_2 - C_1 C_2} \right) - C_1 \left(\dfrac{A_2 B_1 - A_1 C_2}{B_1 B_2 - C_1 C_2} \right), \\[2ex]
\dfrac{\partial \varphi}{\partial w} = -C_1 \left(\dfrac{A_1 B_2 - A_2 C_1}{B_1 B_2 - C_1 C_2} \right), \\[2ex]
\dfrac{\partial \psi}{\partial v} = -C_2 \left(\dfrac{A_1 B_2 - A_2 C_1}{B_1 B_2 - C_1 C_2} \right), \\[2ex]
\dfrac{\partial \psi}{\partial w} = A_2 - 2B_2 \left(\dfrac{A_2 B_1 - A_1 C_2}{B_1 B_2 - C_1 C_2} \right) - C_2 \left(\dfrac{A_1 B_2 - A_2 C_1}{B_1 B_2 - C_1 C_2} \right).
\end{cases}
\tag{40}
$$

4 A review of Touchard polynomials: a convergence analysis

The goal is here to first review the main aspects of the Touchrad polynomials (TPs). Also, we mention some main properties of this set of functions. Next, the convergence analysis of TPs is studied.

An overview of Touchard polynomials

Jacques Touchard was the first who study the Touchard polynomials (TPs) associated with various enumeration problems in number theory related to the permutations [36]. These polynomials are also known as the generalization of Bell polynomials or exponential polynomilas [37]. For more applications and detailed descriptions, we refer to [31, 38, 39].

The TPs are defined through the following Rodriguez-like formula:

$$
\mathcal{T}_q(x) = \exp(-x) \left(x \frac{d}{dx} \right)^q \{ \exp(x) \}, \quad q \in \mathbb{N}.
$$

We next denote the Stirling number (of the second type) by $S_2(q, i)$. It is defined as [40, Chap. 5]

$$
S_2(q, i) := \frac{1}{i!} \sum_{j=1}^{i} (-1)^{i-j} \binom{i}{j} j^q, \quad 1 \leq i \leq q,
$$

and if $1 \leq q < i$ we have $S_2(q, i) = 0$. We also set $S_2(0, 0) = 1$ and $S_2(0, i) = 0$ for $i \geq 1$. In fact, the Stirling number indicates the number of partitions of a set of size q into i disjoint nonempty subsets. From these numbers, we have the next definition of TPs:

Definition 1 *The Touchard polynomials on $[0, 1]$ are given by*

$$
\mathcal{T}_q(x) := \sum_{i=0}^{q} S_2(q, i) \, x^i, \quad q \in \mathbb{N},
\tag{41}
$$

and $\mathcal{T}_0(x) := 1$.

It is not difficult to obtain the list of $\mathcal{T}_1(x), \ldots, \mathcal{T}_q(x)$ for $q = 5$ given as follow

$$
\begin{aligned}
\mathcal{T}_1(x) &= x, \\
\mathcal{T}_2(x) &= x^2 + x, \\
\mathcal{T}_3(x) &= x^3 + 3x^2 + x, \\
\mathcal{T}_4(x) &= x^4 + 6x^3 + 7x^2 + x, \\
\mathcal{T}_5(x) &= x^5 + 10x^4 + 25x^3 + 15x^2 + x.
\end{aligned}
$$

One can evidently see that $\mathcal{T}_q(0) = 0$ for all $q \in \mathbb{N}$. We also have $\mathcal{T}_q(1) = B_q$, where B_q represents the Bell numbers for $q \in \mathbb{N}_0 := \mathbb{N} \cup \{0\}$. By using $B_0 = B_1 = 1$, the values of the first Bell numbers are given as $1, 1, 2, 5, 15, 52, 203, 877$, and 4140.

The next result is about the zeros of TPs. These roots with some modifications can be used as the set of collocation nodes in our proposed spectral collocation algorithm, below. A proof of which was proved in [41]:

Theorem 1 *The zeros of $\mathcal{T}_q(x)$ are real, distinct, and non-positive for all $q \in \mathbb{N}$.*

The following results are useful in the subsequent error analysis of TPs. Let $Q \in \mathbb{N}$ be given. To continue, let us denote the vector of $(Q + 1)$ TPs by

$$
\boldsymbol{T}_Q(x) := \begin{bmatrix} \mathcal{T}_0(x) & \mathcal{T}_1(x) & \ldots & \mathcal{T}_Q(x) \end{bmatrix}. \tag{42}
$$

From this representation, we have:

Lemma 1 *The following representation for $\boldsymbol{T}_Q(x)$ holds*

$$
\boldsymbol{T}_Q(x) = \boldsymbol{\Sigma}_Q(x)\,\boldsymbol{P}_Q, \tag{43}
$$

where the structured upper-triangular matrix $\boldsymbol{P}_Q$ is constant. It is of size $(Q + 1) \times (Q + 1)$ and defined as

$$
\boldsymbol{P}_Q = \begin{bmatrix}
1 & S_2(1,0) & S_2(2,0) & \ldots & S_2(Q-1,0) & S_2(Q,0) \\
0 & 1 & S_2(2,1) & \ldots & S_2(Q-1,1) & S_2(Q,1) \\
0 & 0 & 1 & \ldots & S_2(Q-1,2) & S_2(Q,2) \\
\vdots & \vdots & \ddots & \ddots & \ddots & \vdots \\
0 & 0 & 0 & \ldots & 1 & S_2(Q,Q-1) \\
0 & 0 & 0 & \ldots & 0 & 1
\end{bmatrix},
$$

and the vector $\boldsymbol{\Sigma}_Q(x)$ is

$$
\boldsymbol{\Sigma}_Q(x) = \begin{bmatrix} 1 & x & x^2 & \ldots & x^Q \end{bmatrix}.
$$

Proof By considering (6) and by induction on $Q \in \mathbb{N}$ we can easily deduce the proof.

The non-singularity of the matrix $\boldsymbol{P}_Q$ is obvious as one can see that $\det(\boldsymbol{P}_Q) = 1$.

Error analysis and convergence result of TPs

The goal is to consider the sequence of TPs on $[0, 1]$. We will investigate a convergence result associated with the TPs in a detailed manner. In this respect, one is required to consider a suitable space related to $[0, 1]$. We set the weight function as $w(x) := 1$ and define

$$L_w^2[0, 1] := \{p : [0, 1] \to \mathbb{R} \ : \ p \text{ is measurable and } \|p\|_w < \infty\},$$

with the associated norm as $\|p\|_w := \sqrt{\int_0^1 |p(x)|^2 w(x) dx}$.

Let's assume that a function $p(x) \in L_w^2[0, 1]$ is given. By writing the function $p(x)$ in a series form in terms of TPs we have

$$p(x) = \sum_{q=0}^{\infty} \phi_q \, \mathcal{T}_q(x), \quad x \in [0, 1]. \tag{44}$$

The final aim would be to find the coefficients ϕ_q, $q \geq 0$ as unknowns. The next finite-dimensional subspace $\mathcal{Z}_Q \subseteq L_w^2[0, 1]$ will be considered in practical computing as

$$\mathcal{Z}_Q := \text{Span}\langle \mathcal{T}_0(x), \mathcal{T}_1(x), \ldots, \mathcal{T}_Q(x) \rangle.$$

It is evident that $\mathcal{Z}_Q$ is a closed and finite-dimensional (of dimension $Q + 1$) and therefore a complete subspace of $L_w^2[0, 1]$. This implies that one finds the finest (best) approximation element $p_\star(x) \in \mathcal{Z}_Q$ such that

$$\|p(x) - p_\star(x)\|_w \leq \|p(x) - r(x)\|_w, \quad \forall r \in \mathcal{Z}_Q.$$

As previously mentioned, we use only the first $(Q + 1)$ TPs to approximate $p(x)$. It follows that

$$p(x) \approx p_Q(x) := \sum_{q=0}^{Q} \phi_q \, \mathcal{T}_q(x), \quad x \in [0, 1]. \tag{45}$$

The approximate solution $p_Q(x)$ can be stated concisely as follows

$$p_Q(x) = \boldsymbol{T}_Q(x) \, \boldsymbol{\Phi}_Q, \tag{46}$$

where $\boldsymbol{T}_Q(x)$ is defined in (7) and the unknowns ϕ_q for $q = 0, 1, \ldots, Q$ will be put in a vector form as

$$\boldsymbol{\Phi}_Q := \begin{bmatrix} \phi_0 & \phi_1 & \cdots & \phi_Q \end{bmatrix}^t.$$

To establish our main result related to the convergence of TPs, we state the following Corollary, which is taken from [42] (without proof):

Corollary 1 *Assume that $p(x)$ has a continuous second derivative on $[-1, 1]$. Let $P_N(x)$ denote the*

interpolation polynomials (of degree at most N), based on the $N + 1$ points $x_i = \cos\left(\frac{2i+1}{N+1}\frac{\pi}{2}\right)$, $i = 0, 1, \ldots, N$. Then $P_N(x)$ converges to $p(x)$ on $[-1, 1]$ as $N \to \infty$. Indeed, we have

$$|p(x) - P_N(x)| = \mathcal{O}(\frac{1}{\sqrt{N}}). \tag{47}$$

Note that we can extend the above result on a general arbitrary domain $[a, b]$ by using the change of variable $2\bar{x} = a + b + (b - a)x$. This transformation also converts the the Chebyshev nodes x_i on $[-1, 1]$ into the associated points $\bar{x}_i$ on $[a, b]$. Here, we have $a = 0$ and $b = 1$. However, the given upper bound in (47) still is valid.

By increasing the number of bases Q, we will show in the next result that the difference between $p(x)$ and the series form $p_Q(x)$ (45) approaching zero. To do so, let us define the error $E_Q(x) := p(x) - p_Q(x)$.

Theorem 2 *Suppose that $p_Q(x) = \mathbf{T}_Q(x)\mathbf{\Phi}_Q$ indicated the best (closest) approximation to $p(x)$ out of space $\mathcal{Z}_Q$ and let $p(x) \in L^2_w[0, 1] \cap C^2[0, 1]$. Then, $E_Q(x)$ converges to zero as $Q \to \infty$. Indeed, we have*

$$\|E_Q(x)\|_2 = \mathcal{O}(Q^{-\frac{1}{2}}). \tag{48}$$

Proof We first utilize the fact that $p_Q(x)$ shows the finest approximation to $p(x)$ out of $\mathcal{Z}_Q$. Based on the above discussion, one finds that

$$\|p(x) - p_Q(x)\|_w \le \|p(x) - r(x)\|_w, \quad \forall r \in \mathcal{Z}_Q. \tag{49}$$

The last inequality (49) is still true for a specific selection for $r(x)$ to be $P_Q(x)$ as in Corollary 1 with $N = Q$. Therefore, we conclude

$$\|p(x) - p_Q(x)\|^2_w \le \|p(x) - P_Q(x)\|^2_w = \int_0^1 |p(x) - P_Q(x)|^2 \, w(x)dx.$$

Now, by virtue of (47) there is a constant C such that

$$\|p(x) - p_Q(x)\|^2_w \le \left[\frac{C}{\sqrt{Q}}\right]^2 \int_0^1 w(x)dx.$$

We then evaluate the definite integral, which is equal to one. Taking the square root yields the desired conclusion.

Remark 1 *We remark that we can use the larger interval $[0, L]$, $(L > 1)$ instead of unit interval $[0, 1]$. This can be done just by changing of variable $x \to x/L$. In other words, the above results can be easily extended to $[0, L]$. In the computational experiments, we may use a larger interval $[0, L]$ rather than $[0, 1]$.*

5 The hybrid Taylor-Touchard algorithm

The solution of the Lotka-Volterra competition system (2) can now be obtained through solving the family of discretized equations (9) together with Dirichlet boundary condition (10) or Neumann boundary conditions (11). Now, suppose that we have the approximate solution of (9) at time level $k - 1$ for $k \ge 1$. Evidently, at the first time level, namely $\tau = 0$, we have $\mathbf{U}^0(x)$ at hand. We assume that at time step k, we can state the numerical solutions of the system (9) as a finite summation of

$(Q + 1)$ Touchard basis functions. It follows that

$$\begin{cases} v^k(x) \approx v_{k,Q}(x) = \sum_{q=0}^{Q} \phi_{q,1}^{(k)} \mathcal{T}_q(x), \\ w^k(x) \approx w_{k,Q}(x) = \sum_{q=0}^{Q} \phi_{q,2}^{(k)} \mathcal{T}_q(x). \end{cases} \tag{50}$$

We now seek the coefficients $\phi_{q,r}^{(k)}$ for $r = 1, 2$ and $q = 0, 1, \ldots, Q$. We may state these unknowns in vectorized forms by

$$\boldsymbol{\Phi}_{Q,r}^{(k)} := \begin{bmatrix} \phi_{0,r}^{(k)} & \phi_{1,r}^{(k)} & \cdots & \phi_{Q,r}^{(k)} \end{bmatrix}^t, \quad r = 1, 2.$$

In accordance to the definition $\boldsymbol{T}_Q(x)$ in (42), one able to represent the foregoing equations (50) as

$$\begin{cases} v_{k,Q}(x) = \boldsymbol{T}_Q(x) \boldsymbol{\Phi}_{Q,1}^{(k)}, \\ w_{k,Q}(x) = \boldsymbol{T}_Q(x) \boldsymbol{\Phi}_{Q,2}^{(k)}. \end{cases} \tag{51}$$

With the help of relation (43) in Lemma 1, we further rewrite these equations as

$$\begin{cases} v_{k,Q}(x) = \boldsymbol{\Sigma}_Q(x) \boldsymbol{P}_Q \boldsymbol{\Phi}_{Q,1}^{(k)}, \\ w_{k,Q}(x) = \boldsymbol{\Sigma}_Q(x) \boldsymbol{P}_Q \boldsymbol{\Phi}_{Q,2}^{(k)}. \end{cases} \tag{52}$$

We now put both approximate solutions into one vector. We set $\boldsymbol{U}_Q^{(k)}(x)$ as an approximation to $\boldsymbol{U}^k(x)$ yielding

$$\boldsymbol{U}^k(x) \approx \boldsymbol{U}_Q^{(k)}(x) := \begin{bmatrix} v_{k,Q}(x) \\ w_{k,Q}(x) \end{bmatrix}. \tag{53}$$

By using the foregoing relations (52), the next matrix representations for $\boldsymbol{U}_Q^{(k)}(x)$ is provided. The proof of which is an easy job.

Lemma 2 *The approximated solution* $\boldsymbol{U}_Q^{(k)}(x)$ *in* (53) *has the following matrix representation*

$$\boldsymbol{U}_Q^{(k)}(x) = \widehat{\boldsymbol{\Sigma}}_Q(x) \widehat{\boldsymbol{P}}_Q \widehat{\boldsymbol{\Phi}}_Q^{(k)}, \tag{54}$$

where

$$\widehat{\boldsymbol{\Sigma}}_Q(x) = \begin{bmatrix} \boldsymbol{\Sigma}_Q(x) & \boldsymbol{0} \\ \boldsymbol{0} & \boldsymbol{\Sigma}_Q(x) \end{bmatrix}, \quad \widehat{\boldsymbol{P}}_Q = \begin{bmatrix} \boldsymbol{P}_Q & \boldsymbol{0} \\ \boldsymbol{0} & \boldsymbol{P}_Q \end{bmatrix}, \quad \widehat{\boldsymbol{\Phi}}_Q^{(k)} = \begin{bmatrix} \boldsymbol{\Phi}_{Q,1}^{(k)} \\ \boldsymbol{\Phi}_{Q,2}^{(k)} \end{bmatrix}.$$

By looking at (51), we find that one needs to approximate $\frac{d^2}{dx^2} \boldsymbol{U}^k(x)$. Thus, we consider the vector form

$$\frac{d^2}{dx^2} \boldsymbol{U}^k(x) \approx \frac{d^2}{dx^2} \boldsymbol{U}_Q^{(k)}(x) := \begin{bmatrix} v_{k,Q}''(x) \\ w_{k,Q}''(x) \end{bmatrix}. \tag{55}$$

To calculate the second-order derivatives of $U_Q^{(k)}(x)$, we return to the relations (53). We have to compute only derivatives of the vector $\Sigma_Q(x)$. A simple calculation yields

$$
\frac{d}{dx}\Sigma_Q(x) = \Sigma_Q(x)\,E_Q, \quad E_Q = \begin{bmatrix} 0 & 1 & 0 & \cdots & 0 \\ 0 & 0 & 2 & \cdots & 0 \\ \vdots & \vdots & 0 & \vdots & \vdots \\ 0 & 0 & 0 & \ddots & Q \\ 0 & 0 & 0 & \cdots & 0 \end{bmatrix}_{(Q+1)\times(Q+1)}. \tag{56}
$$

If we repeat the differentiation, we arrive at

$$
\frac{d^2}{dx^2}\Sigma_Q(x) = \Sigma_Q(x)\,E_Q^2. \tag{57}
$$

By combining the last relations (57) and (53) we finally get

$$
\begin{cases} v_{k,Q}''(x) = \Sigma_Q(x)\,E_Q^2\,P_Q\,\Phi_{Q,1}^{(k)}, \\ w_{k,Q}''(x) = \Sigma_Q(x)\,E_Q^2\,P_Q\,\Phi_{Q,2}^{(k)}. \end{cases} \tag{58}
$$

Lemma 3 *The approximated solution $\frac{d^2}{dx^2}U_Q^{(k)}(x)$ in (55) has the following matrix representation*

$$
\frac{d^2}{dx^2}U_Q^{(k)}(x) = \widehat{\Sigma}_Q(x)\,\widehat{E}_Q\,\widehat{P}_Q\,\widehat{\Phi}_Q^{(k)}, \tag{59}
$$

where $\widehat{\Phi}_Q^{(k)}$, $\widehat{\Sigma}_Q(x)$ and $\widehat{P}_Q$ are defined in (54) and

$$
\widehat{E}_Q = \begin{bmatrix} E_Q^2 & 0 \\ 0 & E_Q^2 \end{bmatrix}.
$$

A sequence of collocation points will be used now. This set of points can be selected as the zeros of Touchard polynomials as mentioned in Section 4. However, we use the equally distributed points on $[0, L]$. Since we have to determine $Q+1$ coefficients in the series expansion forms (50), we consider $x_s = sL/Q$ for $s = 0, 1, \ldots, Q$ as the collocation points. We now collocate the matrix Eqs. (51) at the aforementioned points to reach at

$$
M_1^{k-1}(x_s)\,\frac{d^2}{dx^2}U_Q^k(x_s) + M_2^{k-1}(x_s)\,U_Q^k(x_s) = H^{k-1}(x_s), \quad s = 0, 1, \ldots, Q, \tag{60}
$$

for $k = 1, 2, \ldots, K$. We next introduce two matrices and vectors related to the coefficients of the model as

$$
N_{k-1,j} = \begin{pmatrix} M_j^{k-1}(x_0) & 0 & \cdots & 0 \\ 0 & M_j^{k-1}(x_1) & \cdots & 0 \\ \vdots & \vdots & \ddots & \vdots \\ 0 & 0 & \cdots & M_j^{k-1}(x_Q) \end{pmatrix}, \quad j = 1, 2, \quad F_{k-1} = \begin{pmatrix} H^{k-1}(x_0) \\ H^{k-1}(x_1) \\ \vdots \\ H^{k-1}(x_Q) \end{pmatrix}.
$$

The following notations will be also set

$$
\boldsymbol{V}_k := \begin{bmatrix} \boldsymbol{U}_Q^k(x_0) \\ \boldsymbol{U}_Q^k(x_1) \\ \vdots \\ \boldsymbol{U}_Q^k(x_Q) \end{bmatrix}, \quad \boldsymbol{V}_k'' := \begin{bmatrix} \frac{d^2}{dx^2}\boldsymbol{U}_Q^k(x_0) \\ \frac{d^2}{dx^2}\boldsymbol{U}_Q^k(x_1) \\ \vdots \\ \frac{d^2}{dx^2}\boldsymbol{U}_Q^k(x_Q) \end{bmatrix}.
$$

A reformulation of the set of matrix Eqs. (60) can be done by using the former matrix and vector notations. So, we have

$$
\boldsymbol{N}_{k-1,1}\,\boldsymbol{V}_k'' + \boldsymbol{N}_{k-1,2}\,\boldsymbol{V}_k = \boldsymbol{F}_{k-1}, \qquad k = 1, 2, \dots, K. \tag{61}
$$

To proceed, we collocate two relations (54) and (59) at the collocation nodes. Therefore, we get

Lemma 4 *The matrix forms of $\boldsymbol{V}_k$ and $\boldsymbol{V}_k''$ are obtained as*

$$
\boldsymbol{V}_k = \widetilde{\widehat{\boldsymbol{\Sigma}}}_Q\,\widehat{\boldsymbol{P}}_Q\,\widehat{\boldsymbol{\Phi}}_Q^{(k)}, \qquad \boldsymbol{V}_k'' = \widetilde{\widehat{\boldsymbol{\Sigma}}}_Q\,\widehat{\boldsymbol{E}}_Q\,\widehat{\boldsymbol{P}}_Q\,\widehat{\boldsymbol{\Phi}}_Q^{(k)}. \tag{62}
$$

Here, two matrices $\widehat{\boldsymbol{P}}_Q, \widehat{\boldsymbol{\Phi}}_Q^{(k)}$ are defined in (54) and the block-diagonal matrix $\widehat{\boldsymbol{E}}_Q$ is introduced in (59). Also, we have used

$$
\widetilde{\widehat{\boldsymbol{\Sigma}}}_Q = [\widehat{\boldsymbol{\Sigma}}_Q(x_0) \quad \widehat{\boldsymbol{\Sigma}}_Q(x_1) \quad \dots \quad \widehat{\boldsymbol{\Sigma}}_Q(x_Q)]^t,
$$

where the matrix $\widehat{\boldsymbol{\Sigma}}_Q$ is previously defined in (54).

By placing two relations in (62) into (61) one gets the next (linear) fundamental matrix equation (FME)

$$
\left\{ \boldsymbol{N}_{k-1,1}\widetilde{\widehat{\boldsymbol{\Sigma}}}_Q\,\widehat{\boldsymbol{E}}_Q + \boldsymbol{N}_{k-1,2}\widetilde{\widehat{\boldsymbol{\Sigma}}}_Q \right\}\,\widehat{\boldsymbol{P}}_Q\,\widehat{\boldsymbol{\Phi}}_Q^{(k)} = \boldsymbol{F}_{k-1}, \quad k = 1, 2, \dots, K.
$$

If we rephrase the last equations, we have for $k = 1, 2, \dots, K$

$$
\boldsymbol{W}_k\,\widehat{\boldsymbol{\Phi}}_Q^{(k)} = \boldsymbol{F}_{k-1}, \quad \text{or} \quad [\boldsymbol{W}_k; \boldsymbol{F}_{k-1}], \quad \boldsymbol{W}_k := \left(\boldsymbol{N}_{k-1,1}\widetilde{\widehat{\boldsymbol{\Sigma}}}_Q\,\widehat{\boldsymbol{E}}_Q + \boldsymbol{N}_{k-1,2}\widetilde{\widehat{\boldsymbol{\Sigma}}}_Q \right)\,\widehat{\boldsymbol{P}}_Q. \tag{63}
$$

Still, we are required to implement the boundary conditions (10) or (11) and incorporate them into the matrix Eq. (63). For the first Dirichlet boundary condition in (10), we consider (54) followed by approaching x to zero. Similarly, for the second one, we tend x to L. In both cases, we have

$$
\boldsymbol{W}_k^0\,\widehat{\boldsymbol{\Phi}}_Q^{(k)} = \boldsymbol{B}_0^k, \quad \boldsymbol{W}_k^0 := \widehat{\boldsymbol{\Sigma}}_Q(0)\,\widehat{\boldsymbol{P}}_Q,
$$

$$
\boldsymbol{W}_k^L\,\widehat{\boldsymbol{\Phi}}_Q^{(k)} = \boldsymbol{B}_L^k, \quad \boldsymbol{W}_k^L := \widehat{\boldsymbol{\Sigma}}_Q(L)\,\widehat{\boldsymbol{P}}_Q.
$$

If the Neumann boundary conditions (5) are given, we first combine two relations (54) and (56) to

obtain

$$
\begin{cases}
v'_{k,Q}(x) = \boldsymbol{\Sigma}_Q(x)\, \boldsymbol{E}_Q\, \boldsymbol{P}_Q\, \boldsymbol{\Phi}^{(k)}_{Q,1}, \\
w'_{k,Q}(x) = \boldsymbol{\Sigma}_Q(x)\, \boldsymbol{E}_Q\, \boldsymbol{P}_Q\, \boldsymbol{\Phi}^{(k)}_{Q,2}.
\end{cases}
$$

Now, we let x approaches to $0, L$ to reach at

$$
\boldsymbol{W}^0_k\, \widehat{\boldsymbol{\Phi}}^{(k)}_Q = \boldsymbol{B}^k_0, \quad \boldsymbol{W}^0_k := \widehat{\boldsymbol{\Sigma}}_Q(0)\, \boldsymbol{E}_Q\, \widehat{\boldsymbol{P}}_Q,
$$
$$
\boldsymbol{W}^L_k\, \widehat{\boldsymbol{\Phi}}^{(k)}_Q = \boldsymbol{B}^k_L, \quad \boldsymbol{W}^L_k := \widehat{\boldsymbol{\Sigma}}_Q(L)\, \boldsymbol{E}_Q\, \widehat{\boldsymbol{P}}_Q.
$$

In either case of boundary conditions, we use $[\boldsymbol{W}^0_k, \boldsymbol{B}^k_0]$ or $[\boldsymbol{W}^L_k, \boldsymbol{B}^k_L]$ to substitute the first four rows of the FME $[\boldsymbol{W}_k; \boldsymbol{F}_{k-1}]$. We denote the resultant modified system given by

$$
[\widetilde{\boldsymbol{W}}_k; \widetilde{\boldsymbol{F}}_{k-1}], \quad k = 1, 2, \ldots, K. \tag{64}
$$

Once we solve (64), the unknown Touchard coefficients $\phi^{(k)}_{q,r}$ for $q = 0, 1, \ldots, Q$ and $r = 1, 2$ are obtained at each time level k for $k = 1, 2, \ldots, K$.

The strategy of the residual error function (REF) will now be utilized to measure the accuracy of the presented Taylor-Touchard collocation procedure. Toward this end, we insert the acquired approximate solutions into (2). Thus, the REFs are defined by the following relations

$$
\begin{bmatrix}
\mathrm{Res}^{(k)}_{v,Q}(x) \\
\mathrm{Res}^{(k)}_{w,Q}(x)
\end{bmatrix}
= \left| \boldsymbol{M}^{k-1}_1(x)\, \frac{d^2}{dx^2} \boldsymbol{U}^k_Q(x) + \boldsymbol{M}^{k-1}_2(x)\, \boldsymbol{U}^k_Q(x) - \boldsymbol{H}^{k-1}(x) \right| \cong 0, \tag{65}
$$

for $k = 1, 2, \ldots, K$. We note that the foregoing REF formula is useful especially when the exact solutions of system (2) are out of reach for various values of model parameters.

6 Graphical and numerical results

In this part, diverse simulation experiments are conducted to illustrate the utility of the Taylor-Touchard matrix collocation strategy once applied to the Lotka-Volterra competition model (2). Two test case studies with diverse model parameters are solved numerically to testify to the accuracy and performance of the combined approximation technique. All simulation results are performed by utilizing Matlab version R2021a on a digital computer.

Example 1 *We consider the Lotka-Volterra competition system (2) with the next initial conditions [17]*

$$
f(x) = g(x) = 0.1 \exp(-8x^2).
$$

The Dirichlet boundary conditions are taken as

$$
v_0(\tau) = w_0(\tau) = f(0), \quad v_L(\tau) = w_L(\tau) = f(L).
$$

In the following diverse coefficient parameters $A_i, B_i, C_i,$ and D_i, for $i = 1, 2$ will be considered.

We first set $Q = 5$. We also use $L, T = 1$ and $\Delta\tau = 0.01$. All parameters are set as unity except that $D_1 = 0.5$. The approximate solutions using the presented Taylor-Touchard method at the first

time level $\tau = \Delta\tau$ are given by

$$v_{1,5}(x) = 0.45827\,x^5 - 1.64989\,x^4 + 2.10134\,x^3 - 0.991429\,x^2 - 0.0182481\,x + 0.1,$$
$$w_{1,5}(x) = 0.377296\,x^5 - 1.39838\,x^4 + 1.83421\,x^3 - 0.889391\,x^2 - 0.0237062\,x + 0.1.$$

The obtained approximations at the last time level $\tau = T$ are as follows

$$v_{100,5}(x) = 0.00744598\,x^5 - 0.012201\,x^4 + 0.0307353\,x^3 - 0.0894343\,x^2 - 0.0365125\,x + 0.1,$$
$$w_{100,5}(x) = 0.00808672\,x^5 - 0.0193222\,x^4 + 0.0294968\,x^3 - 0.049399\,x^2 - 0.0688288\,x + 0.1.$$

Figure 1 shows the whole approximate solutions using the above-mentioned parameters on space-time domain $[0,1] \times [0,1]$. While the left picture presents the population density v, the right plot graphically shows the population density w. The snapshots of the associated REFs defined via (65) are also depicted in Figure 2 at different time levels $\tau = \tau_k$ for $k = 1, 2, \ldots, 100$. It is seen that the same results for both approximate solutions v, w are obtained on the unit square $[0,1] \times [0,1]$. To see the discrepancy, we need to go beyond this domain.

Figure 1. Visualization of approximate solutions $v(x,\tau)$ (left) and $w(x,\tau)$ (right) via Taylor-Touchard matrix algorithm in Example 1 with $Q = 5$, $A_1, A_2 = 1, B_1, B_2 = 1, C_1, C_2 = 1, D_1 = 0.5, D_2 = 1, \Delta\tau = 0.01$, for $(x,\tau) \in [0,1] \times [0,1]$.

Let us consider $L = 10$ and $T = 100$ in the computations. In Figure 3, we show the approximate solutions for the population densities v and w using the same parameters as above except that we take a relatively large time step $\Delta\tau = 1$. In fact, the obtained solutions at $\tau = 50$ are given as

$$v_{50,5}(x) = 0.000472878\,x^5 - 0.0149354\,x^4 + 0.168979\,x^3 - 0.836871\,x^2 + 1.66751\,x + 0.1,$$
$$w_{50,5}(x) = 0.0000459759\,x^5 - 0.00140024\,x^4 + 0.0151665\,x^3 - 0.0746089\,x^2 + 0.159923\,x + 0.1.$$

The profile of population densities at $x = 5$ is visualized in Figure 4. One can easily see from Figure 3 and Figure 4 that the population density $v(x,\tau)$ will ultimately survive with low diffusion rates $D_1 = 0.5$ while the second one, $w(x,\tau)$, with higher diffusion value $D_2 = 1$ will die out on $\tau \in [0,100]$.
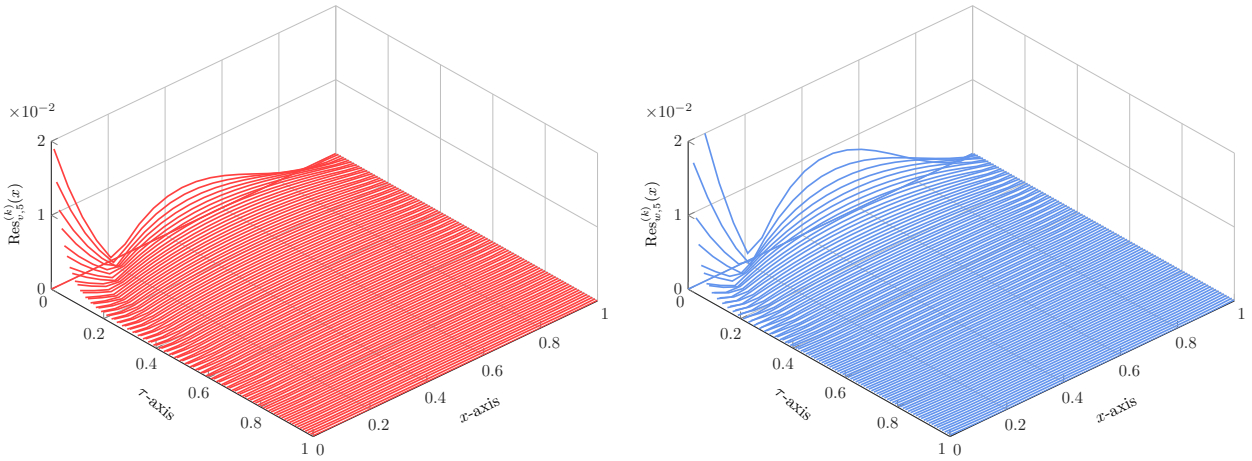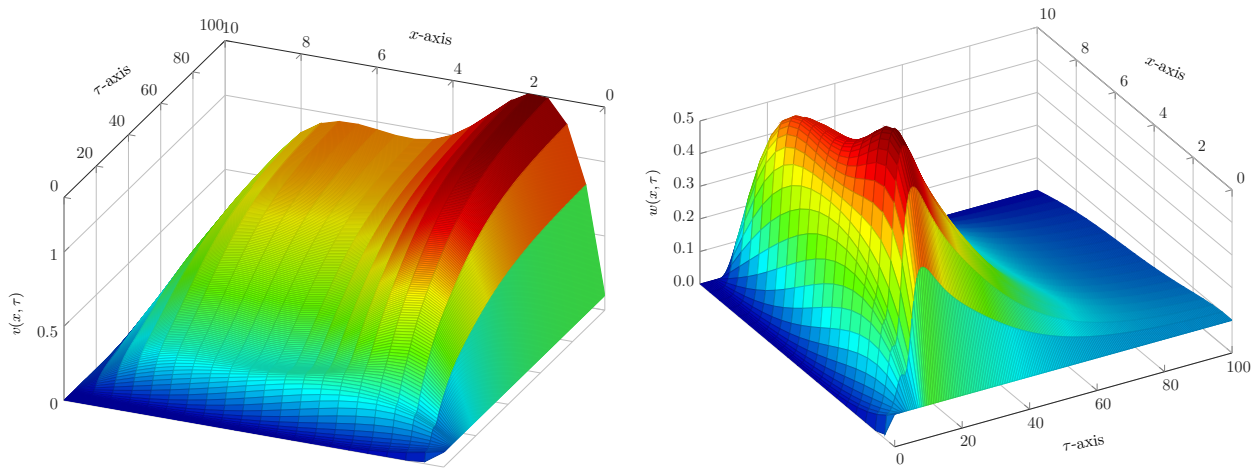
Figure 2. Visualization of REfs $\mathrm{Res}_{v,5}^{(k)}(x)$ (left) and $\mathrm{Res}_{w,5}^{(k)}(x)$ (right) via Taylor-Touchard matrix algorithm in Example 1 with $Q = 5, A_1, A_2 = 1, B_1, B_2 = 1, C_1, C_2 = 1, D_1 = 0.5, D_2 = 1, \Delta\tau = 0.01$, for $(x, \tau) \in [0,1] \times [0,1]$.

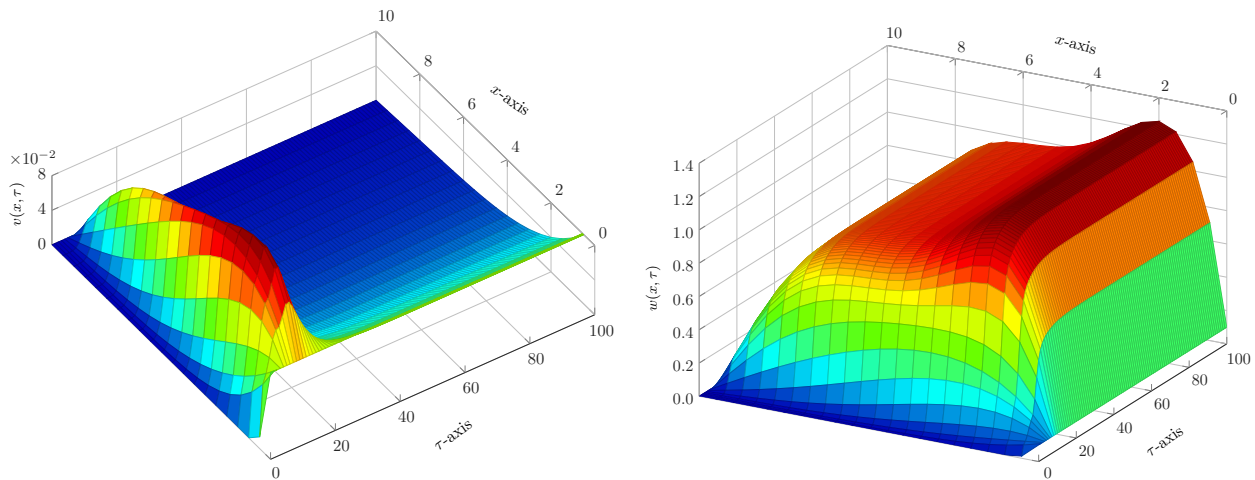**Figure 3.** Visualization of approximate solutions $v(x, \tau)$ (left) and $w(x, \tau)$ (right) via Taylor-Touchard matrix algorithm in Example 1 with $Q = 5, A_1, A_2 = 1, B_1, B_2 = 1, C_1, C_2 = 1, D_1 = 0.5, D_2 = 1, \Delta\tau = 1$, for $(x, \tau) \in [0,10] \times [0,100]$.

We next examine the impact of utilizing the growth factors A_1 and A_2 on the interaction between two species. In this respect, we set [17]

$$A_1 = 0.8, \quad A_2 = 1, \quad B_1, B_2 = 1, \quad C_1, C_2 = 1, \quad D_1, D_2 = 1.$$

From these parameters, the following approximations for the competition system are obtained. The two first ones are related to $\tau = \Delta\tau$ as follows

$$v_{1,5}(x) = -2.9310 - 6\,x^5 + 0.000120498\,x^4 - 0.00195727\,x^3 + 0.0157298\,x^2 - 0.0627584\,x + 0.1,$$
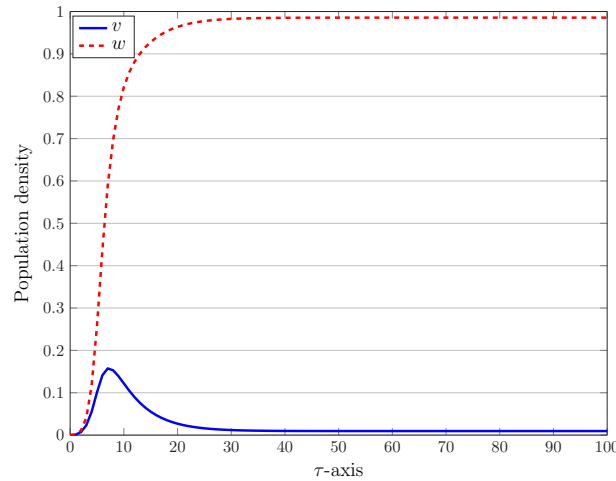$$w_{1,5}(x) = -2.7123 - 6\,x^5 + 0.000112368\,x^4 - 0.00184439\,x^3 + 0.0150341\,x^2 - 0.0611469\,x + 0.1.$$

Figure 4. Graphing of population densities via Taylor-Touchard matrix algorithm in Example 1 with $Q = 5$, $A_1, A_2 = 1, B_1, B_2 = 1, C_1, C_2 = 1, D_1 = 0.5, D_2 = 1, \Delta\tau = 1$, at $x = 5$.

The obtained approximations at the final time $\tau = T$ are given by

$$v_{100,5}(x) = -3.31577 - 7\,x^5 + 0.0000265815\,x^4 - 0.000681488\,x^3 + 0.00781148\,x^2$$
$$- 0.0432318\,x + 0.1,$$
$$w_{100,5}(x) = 0.000392573\,x^5 - 0.0123676\,x^4 + 0.140267\,x^3 - 0.713172\,x^2 + 1.5369\,x + 0.1.$$

The graphical representations of two population species are visualized on Figure 5 on the whole domain $(x, \tau) \in [0, 10] \times [0, 100]$. The profile of population densities at $x = 5$ and for $\tau \in [0, 100]$ are depicted on Figure 6.

Figure 5. Graphing of approximate solutions $v(x, \tau)$ (left) and $w(x, \tau)$ (right) via Taylor-Touchard matrix algorithm in Example 1 with $Q = 5$, $A_1 = 0.8, A_2 = 1, B_1, B_2 = 1, C_1, C_2 = 1, D_1, D_2 = 1, \Delta\tau = 1$, for $(x, \tau) \in [0, 10] \times [0, 100]$.

By looking at the plotted Figure 5 and Figure 6 we infer that under the assumption on the growth rates $A_1 < A_2$ the population $v(x, \tau)$ will wipe out at the end. However, the population $w(x, t)$ will remain alive for a long time life. The conclusion is that if the invasive population is weak, then the population will become extinct finally.

Figure 6. Graphing of population densities via Taylor-Touchard matrix algorithm in Example 1 with $Q = 5$, $A_1 = 0.8, A_2 = 1, B_1, B_2 = 1, C_1, C_2 = 1, D_1, D_2 = 1, \Delta\tau = 1$, at $x = 5$.

In the last experimental simulations for Example 1, let us investigate the competitive coexistence of two population species in the system. For this purpose, we set [17]

$$A_1 = 0.9, \quad A_2 = 1, \quad B_1, B_2 = 1, \quad C_1 = 0.8, C_2 = 1, \quad D_1 = 0.3, D_2 = 1.$$

We run our Taylor-Touchard collocation matrix algorithm with a time step $\Delta\tau = 1$ as before. Using $Q = 5$ we get the next approximations evaluated at time $\tau = \Delta\tau$ as

$$v_{1,5}(x) = -3.9490{-}6\,x^5 + 0.000157353\,x^4 - 0.00245291\,x^3 + 0.0186658\,x^2 - 0.0692296\,x + 0.1,$$
$$w_{1,5}(x) = -2.7123{-}6\,x^5 + 0.000112368\,x^4 - 0.00184439\,x^3 + 0.0150341\,x^2 - 0.0611469\,x + 0.1.$$

The obtained approximations at the given final time $\tau = T$ are given by

$$v_{100,5}(x) = 0.000499975\,x^5 - 0.0157776\,x^4 + 0.177961\,x^3 - 0.872004\,x^2 + 1.69182\,x + 0.1,$$
$$w_{100,5}(x) = 0.0000344845\,x^5 - 0.00103192\,x^4 + 0.0109967\,x^3 - 0.0555938\,x^2 + 0.133343\,x + 0.1.$$

Besides the preceding polynomial solutions, we visualize the approximate solutions $v_{k,5}(x, \tau)$ and $w_{k,5}(x, \tau)$ for all $k = 1, 2, \ldots, 100$ in Figure 7 on the whole space-time domain $(x, \tau) \in [0, 10] \times [0, 100]$. The competition results of two populations for $(x, \tau) \in \{5\} \times [0, 100]$ are shown in Figure 8.

From graphics presented in the former Figure 7 and Figure 8 one observes that both populations arrived at a coexistence state. In other words, the two competing species are equal in status, with neither complete victory nor loss in competition.

Example 2 *The second test example related to the Lotka-Volterra competition system (2) is devoted to the Neumann boundary conditions. That is, we take the following initial conditions*

$$f(x) = g(x) = 0.1 \sin^2(2.4\,\pi\,x) + 0.28 \sin^2(-0.05\,\pi\,x),$$

which is borrowed from [18]. The Neumann boundary conditions are set as follows:

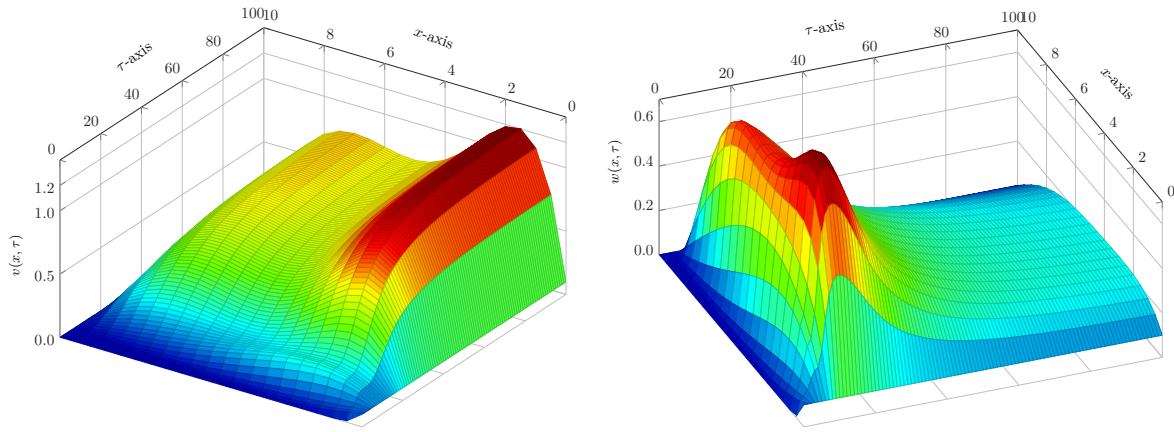$$v_0(\tau) = w_0(\tau) = f'(0), \quad v_L(\tau) = w_L(\tau) = f'(L).$$

Figure 7. Visualization of approximate solutions $v(x, \tau)$ (left) and $w(x, \tau)$ (right) via Taylor-Touchard matrix algorithm in Example 1 with $Q = 5$, $A_1 = 0.9, A_2 = 1, B_1, B_2 = 1, C_1 = 0.8, C_2 = 1, D_1 = 0.3, D_2 = 1, \Delta \tau = 1$, for $(x, \tau) \in [0, 10] \times [0, 100]$
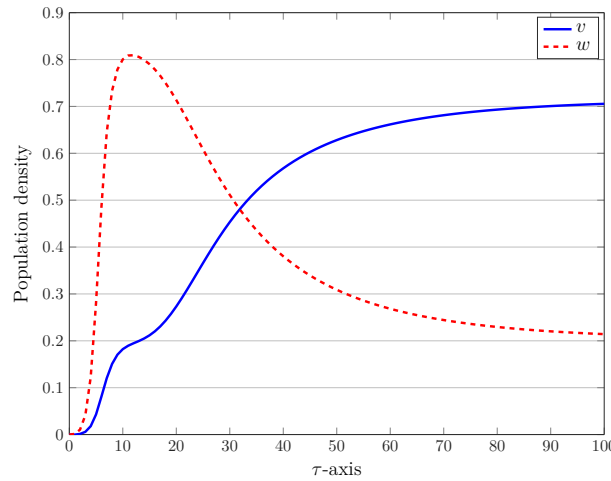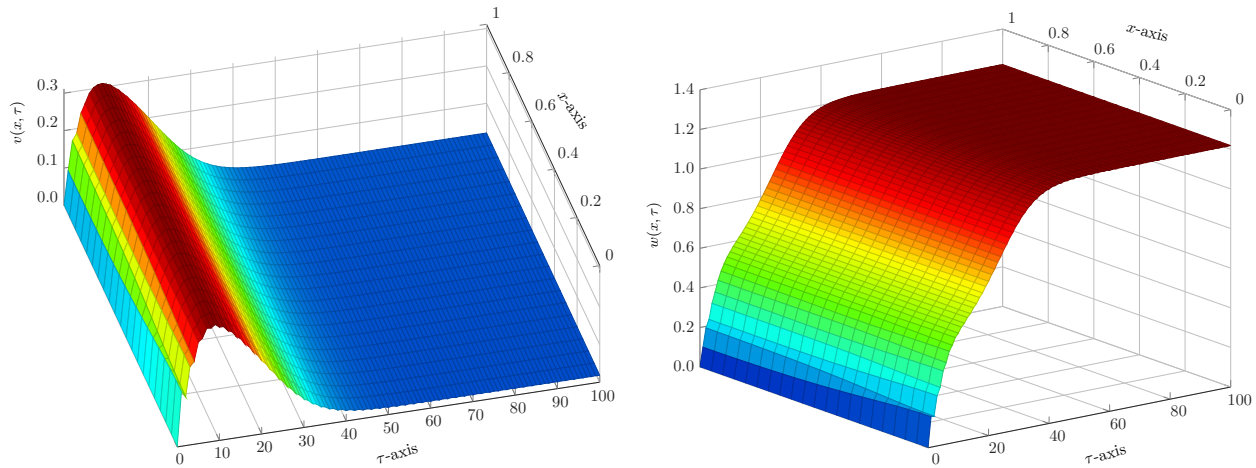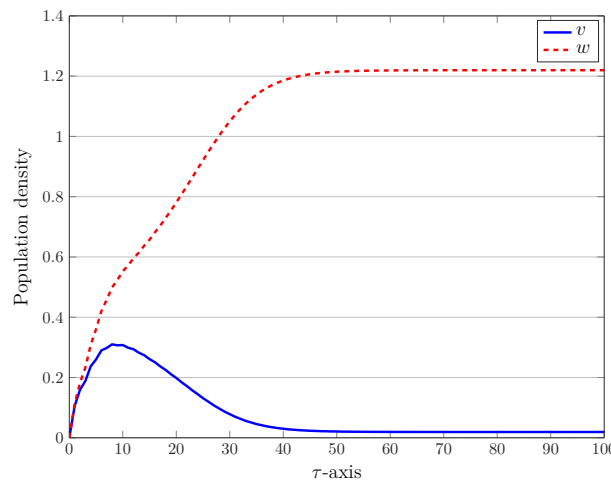

Figure 8. Visualization of population densities via Taylor-Touchard matrix algorithm in Example 1 with $Q = 5$, $A_1 = 0.9, A_2 = 1, B_1, B_2 = 1, C_1 = 0.8, C_2 = 1, D_1 = 0.3, D_2 = 1, \Delta \tau = 1$, at $x = 5$

Below, we only use the coefficient parameters A_i, B_i, C_i, and D_i, for $i = 1, 2$ in the form

$$A_1 = 0.4, A_2 = 0.5, \quad D_1 = D_2 = 0.001, \quad B_1 = 0.4, B_2 = 0.5, \quad C_1 = 0.5, C_2 = 0.8.$$

Using the aforementioned parameters and by running the Taylor-Touchard algorithm with $Q = 5$ and $\Delta \tau = 1$, we get the next approximate solutions computed at $\tau = \Delta \tau$ and for $0 \le x \le 1$ as

$$v_{1,5}(x) = 0.232195 \, x^5 - 0.774398 \, x^4 + 0.966988 \, x^3 - 0.48004 \, x^2 - 3.4{-}107 \, x + 0.145598,$$
$$w_{1,5}(x) = 0.232362 \, x^5 - 0.775521 \, x^4 + 0.96977 \, x^3 - 0.482383 \, x^2 - 6.1{-}107 \, x + 0.153403.$$

Similarly, at time level $\tau = T = 100$, we get

$$v_{100,5}(x) = -0.0137547 \, x^5 + 0.0372937 \, x^4 - 0.0340702 \, x^3 + 0.0130377 \, x^2$$
$$- 1.7{-}108 \, x + 0.0183703,$$
$$w_{100,5}(x) = -0.0139798 \, x^5 + 0.0381177 \, x^4 - 0.0346481 \, x^3 + 0.0128192 \, x^2 + 1.21895.$$

In Figure 9, we present the above approximate solutions for $k = 1, 100$ together with other values $2 \leq k \leq 99$. While the left picture shows the population density v, the right plot depicts the approximate solution w on the whole domain $(x, \tau) \in [0,1] \times [0,100]$. At $x = 0.5$, we further plot the snapshots of approximation $v(x, \tau), w(x, \tau)$ over the long time domain $\tau \in [0, 100]$ as shown in Figure 10. If we look at Figure 9 and Figure 10, we can observe that the population v will eventually disappear and the population w will survive.

Figure 9. Visualization of approximate solutions $v(x, \tau)$ (left) and $w(x, \tau)$ (right) via Taylor-Touchard matrix algorithm in Example 2 with $Q = 5$, $A_1 = 0.4$, $A_2 = 0.5$, $B_1 = 0.5$, $B_2 = 0.4$, $C_1 = 0.5$, $C_2 = 0.8$, $D_1 = D_2 = 0.001$, $\Delta \tau = 1$, for $(x, \tau) \in [0,1] \times [0,100]$.

Figure 10. Graphing of population densities via Taylor-Touchard matrix algorithm in Example 2 with $Q = 5$, $A_1 = 0.4$, $A_2 = 0.5$, $B_1 = 0.5$, $B_2 = 0.4$, $C_1 = 0.5$, $C_2 = 0.8$, $D_1 = D_2 = 0.001$, $\Delta \tau = 1$, at $x = 5$.

In terms of achieved REFs, we fix $\Delta \tau = 0.01$ and consider two different values of $Q = 4, 8$ in the computations. The other parameters are given as above for the second test example. These REFs associated with the approximate solutions $v(x, \tau)$ and $w(x, \tau)$ are displayed in Figure 11. The time domain is $[0,1]$ and the results are plotted at $x = 5$. The magnitude of REFs is decreased if one increases the number of basis functions Q.
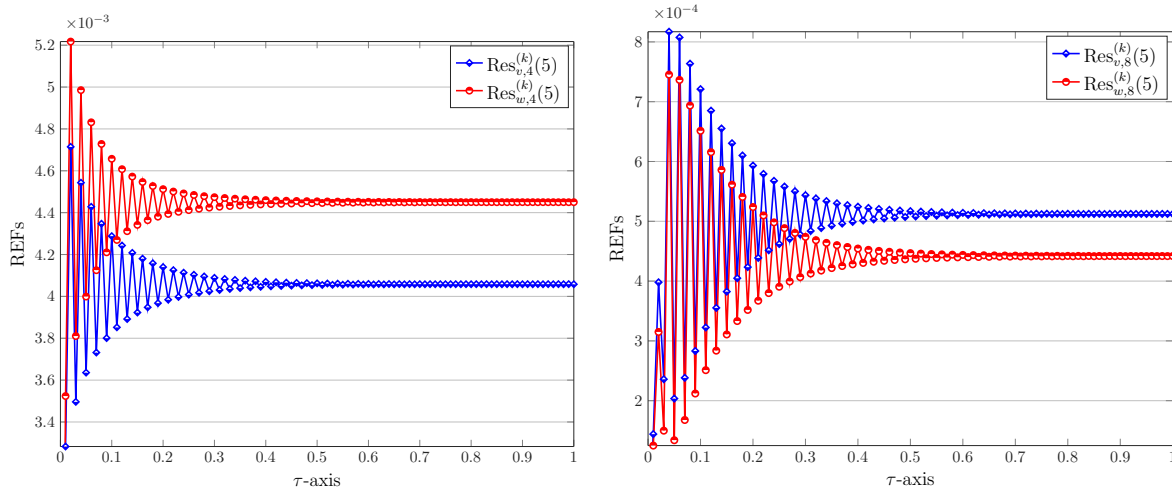
Figure 11. Visualization of REFs with $Q = 4$ (left) and $Q = 8$ (right) via Taylor-Touchard matrix algorithm in Example 2 with $A_1 = 0.4, A_2 = 0.5, B_1 = 0.5, B_2 = 0.4, C_1 = 0.5, C_2 = 0.8, D_1 = D_2 = 0.001, \Delta\tau = 0.01$, at $x = 5$

7 Conclusion

This study introduces a novel combined semi-discretized spectral matrix collocation algorithm for solving the Lotka-Volterra competition system with diffusion. The proposed algorithm utilizes the well-known Taylor series formula for the time-marching procedure and the Touchard family of polynomials for solving the resulting linear systems of ODEs using spectral matrix collocation. The convergence and error analysis of the proposed algorithm are discussed in detail. Additionally, a comprehensive qualitative analysis of the system is provided through stability analysis. Based on the performed stability analysis, equilibrium points for the system are obtained along with the conditions for a stable solution. Numerical simulations with diverse model parameters and boundary conditions are conducted to illustrate the applicability and effectiveness of the developed algorithm. The presented outcomes demonstrate that the proposed algorithm is accurate, efficient, and capable of providing stable solutions for the Lotka-Volterra competition system with diffusion. The residual error function technique is employed to further validate the accuracy and advantages of the proposed algorithm. Through the complete analysis, the accuracy of the proposed method increases with the number of used basis functions, validating the applicability of the method for solving similar complex problems.

This study makes significant contributions to the field of simulations of nonlinear PDEs and underscores the potential of the combined semi-discretized spectral matrix collocation algorithm for solving similar problems in diverse fields of science and engineering. The proposed algorithm serves as a powerful tool for modeling and simulating complex systems in areas such as ecology, biology, economics, and physics. Future research endeavors could extend the proposed algorithm to take into account other factors such as the extension of the current model to three or more species or incorporating the climate effect and investigate the effects of various parameters on the method's performance.

Declarations

Use of AI tools

The authors declare that they have not used Artificial Intelligence (AI) tools in the creation of this article.

Data availability statement

Ethical approval

Consent for publication

Conflicts of interest

Funding

Author's contributions

Acknowledgements

References

[1] Kumar, S., Kumar, A. and Odibat, Z.M. A nonlinear fractional model to describe the population dynamics of two interacting species. *Mathematical Methods in the Applied Sciences*, 40(11), 4134–4148, (2017). [CrossRef]

[2] Lotka, A.J. Contribution to the theory of periodic reactions. *The Journal of Physical Chemistry*, 14(3), 271-274, (2022). [CrossRef]

[3] Owolabi, K.M. Computational dynamics of predator-prey model with the power-law kernel. *Results in Physics*, 21, 103810, (2021). [CrossRef]

[4] Owolabi, K.M., Pindza, E. and Atangana, A. Analysis and pattern formation scenarios in the superdiffusive system of predation described with Caputo operator. *Chaos, Solitons & Fractals*, 152, 111468, (2021). [CrossRef]

[5] Pan, M.X., Wang, S.Y., Wu, X.L., Zhang, M.W. and Schiavo, A.L. Study on the growth driving model of the enterprise innovation community based on the Lotka–Volterra model: a case study of the Chinese Automobile Manufacturing Enterprise Community. *Mathematical Problems in Engineering*, 2022, 8743167, (2023). [CrossRef]

[6] Han, J. The Impact of epidemic infectious diseases on the ecological environment of three

species based on the Lotka–Volterra model. *World Scientific Research Journal*, 7(1), 340-345, (2021). [CrossRef]

[7] Ni, W., Shi, J. and Wang, M. Global stability and pattern formation in a nonlocal diffusive Lotka–Volterra competition model. *Journal of Differential Equations*, 264(11), 6891-6932, (2018). [CrossRef]

[8] Lin, G. and Ruan, S. Traveling wave solutions for delayed reaction–diffusion systems and applications to diffusive Lotka–Volterra competition models with distributed delays. *Journal of Dynamics and Differential Equations*, 26, 583-605, (2014). [CrossRef]

[9] Wijeratne, A.W., Yi, F. and Wei, J. Bifurcation analysis in the diffusive Lotka–Volterra system: an application to market economy. *Chaos, Solitons & Fractals*, 40(2), 902-911, (2009). [CrossRef]

[10] Cherniha, R. Construction and application of exact solutions of the diffusive Lotka–Volterra system: a review and new results. *Communications in Nonlinear Science and Numerical Simulation*, 113, 106579, (2022). [CrossRef]

[11] Zhang, S., Zhu, X. and Liu, X. A diffusive Lotka–Volterra model with Robin boundary condition and sign-changing growth rates in time-periodic environment. *Nonlinear Analysis: Real World Applications*, 72, 103856, (2023). [CrossRef]

[12] Ma, L., Gao, J., Li, D. and Lian, W. Dynamics of a delayed Lotka–Volterra competition model with directed dispersal. *Nonlinear Analysis: Real World Applications*, 71, 103830, (2023). [CrossRef]

[13] Barker, W. Existence of traveling waves of Lotka Volterra type models with delayed diffusion term and partial quasimonotonicity. *ArXiv Preprint, ArXiv:2303.11145*, (2023). [CrossRef]

[14] Guo, S. Global dynamics of a Lotka-Volterra competition-diffusion system with nonlinear boundary conditions. *Journal of Differential Equations*, 352, 308-353, (2023). [CrossRef]

[15] Kudryashov, N.A. and Zakharchenko, A.S. Analytical properties and exact solutions of the Lotka–Volterra competition system. *Applied Mathematics and Computation*, 254, 219-228, (2015). [CrossRef]

[16] Islam, M., Islam, B. and Islam, N. Exact solution of the prey-predator model with diffusion using an expansion method. *Applied Sciences*, 15, 85-93, (2013).

[17] Wang, J., Liu, Q. and Luo, Y. The numerical analysis of the long time asymptotic behavior for Lotka-Volterra competition model with diffusion. *Numerical Functional Analysis and Optimization*, 40(6), 685-705, (2019). [CrossRef]

[18] Sabawi, Y.A., Pirdawood, M.A. and Sadeeq, M.I. A compact fourth-order implicit-explicit Runge-Kutta type method for solving diffusive Lotka–Volterra system. In Proceedings, *Journal of Physics: Conference Series* (Vol. 1999, No. 1, p. 012103). *IOP Publishing*, (2021, April). [CrossRef]

[19] Izadi, M. Numerical approximation of Hunter-Saxton equation by an efficient accurate approach on long time domains. *UPB Scientific Bulletin Series A Applied Mathematics and Physics*, 83(1), 291-300, (2021).

[20] Izadi, M. and Yuzbasi, S. A hybrid approximation scheme for 1-D singularly perturbed parabolic convection-diffusion problems. *Mathematical Communications*, 27(1), 47-62, (2022).

[21] Izadi, M. and Roul, P. Spectral semi-discretization algorithm for a class of nonlinear parabolic PDEs with applications. *Applied Mathematics and Computation*, 429, 127226, (2022). [CrossRef]

[22] Izadi, M. and Zeidan, D. A convergent hybrid numerical scheme for a class of nonlinear

diffusion equations. *Computational and Applied Mathematics*, 41, 318, (2022). [CrossRef]

[23] Günerhan, H., Dutta, H., Dokuyucu, M.A. and Adel, W. Analysis of a fractional HIV model with Caputo and constant proportional Caputo operators. *Chaos, Solitons & Fractals*, 139, 110053, (2020). [CrossRef]

[24] El-Sayed, A.A., Baleanu, D. and Agarwal, P. A novel Jacobi operational matrix for numerical solution of multi-term variable-order fractional differential equations. *Journal of Taibah University for Science*, 14(1), 963-974, (2020). [CrossRef]

[25] Srivastava, H.M. and Izadi, M. Generalized shifted airfoil polynomials of the second kind to solve a class of singular electrohydrodynamic fluid model of fractional order. *Fractal and Fractional*, 7(1), 94, (2023). [CrossRef]

[26] Sabermahani, S., Ordokhani, Y. and Hassani, H. General Lagrange scaling functions: application in general model of variable order fractional partial differential equations. *Computational and Applied Mathematics*, 40, 269, (2021). [CrossRef]

[27] Abbasi, Z., Izadi, M. and Hosseini, M.M. A highly accurate matrix method for solving a class of strongly nonlinear BVP arising in modeling of human shape corneal. *Mathematical Methods in the Applied Sciences*, 46(2), 1511-1527, (2023). [CrossRef]

[28] Razavi, M., Hosseini, M.M. and Salemi, A. Error analysis and Kronecker implementation of Chebyshev spectral collocation method for solving linear PDEs. *Computational Methods for Differential Equations*, 10(4), 914–927, (2022). [CrossRef]

[29] Srivastava, H.M., Adel, W., Izadi, M. and El-Sayed, A.A. Solving some physics problems involving fractional-order differential equations with the Morgan-Voyce polynomials. *Fractal and Fractional*, 7(4), 301, (2023). [CrossRef]

[30] Izadi, M., Yüzbası, S. and Adel, W. Accurate and efficient matrix techniques for solving the fractional Lotka–Volterra population model. *Physica A: Statistical Mechanics and its Applications*, 600, 127558, (2022). [CrossRef]

[31] Mihoubi, M. and Maamra, M.S. Touchard polynomials, partial Bell polynomials and polynomials of binomial type. *Journal of Integer Sequences*, 14(3), (2011).

[32] Boyadzhiev, K.N. Exponential polynomials, Stirling numbers, and evaluation of some gamma integrals. *Abstract and Applied Analysis*, 2009, 168672, (2009). [CrossRef]

[33] Sabermahani, S. and Ordokhani, Y. A computational method to solve fractional-order Fokker-Planck equations based on Touchard polynomials. *Computational Mathematics and Computer Modeling with Applications (CMCMA)*, 1(2), 65-73, (2022). [CrossRef]

[34] Aldurayhim, A., Elsonbaty, A. and Elsadany, A.A. Dynamics of diffusive modified Previte-Hoffman food web model. *Mathematical Biosciences and Engineering*, 17(4), 4225-4256, (2020). [CrossRef]

[35] Ahmed, N., Elsonbaty, A., Raza, A., Rafiq, M. and Adel, W. Numerical simulation and stability analysis of a novel reaction–diffusion COVID-19 model. *Nonlinear Dynamics*, 106, 1293-1310, (2021). [CrossRef]

[36] Touchard, J. Sur les cycles des substitutions. *Acta Mathematica*, 70, 243-297, (1939). [CrossRef]

[37] Bell, E.T. Exponential polynomials. *Annals of Mathematics*, 35(2), 258-277, (1934). [CrossRef]

[38] Mansour, T. and Schork, M. The generalized Touchard polynomials revisited. *Applied Mathematics and Computation*, 219(19), 9978-9991, (2013). [CrossRef]

[39] Kim, T., Herscovici, O., Mansour, T. and Rim, S.H. Differential equations for p, q-Touchard

polynomials. *Open Mathematics*, 14(1), 908-912, (2016). [CrossRef]

[40] Comtet, L. The art of finite and infinite expansions. In Advanced Combinatorics (pp. xi-343). D. Reidel Publishing Co. Dordrecht, (1974).

[41] Harper, L.H. Stirling behavior is asymptotically normal. *The Annals of Mathematical Statistics*, 38(2), 410-414, (1967). [CrossRef]

[42] Isaacson, E. and Keller, H.B. *Analysis of Numerical Methods*. Courier Corporation: North Chelmsford, United States, (1994).

Mathematical Modelling and Numerical Simulation with Applications (MMNSA)
(https://dergipark.org.tr/en/pub/mmnsa)

RESEARCH PAPER

A fractional mathematical model approach on glioblastoma growth: tumor visibility timing and patient survival

Nurdan Kar [ID] [1,*,‡] and **Nuri Özalp** [ID] [1,‡]

[1]Department of Mathematics, Ankara University, 06100 Ankara, Türkiye
*Corresponding Author
‡ kar@ankara.edu.tr (Nurdan Kar); nozalp@science.ankara.edu.tr (Nuri Özalp)

Abstract

In this paper, we introduce a mathematical model given by

$$^{c}\mathfrak{D}_t^{\alpha} u = \nabla \cdot \mathrm{D} \nabla u + \rho f(u) \quad \text{in } \Omega, \tag{1}$$

where $f(u) = \frac{1}{1-u/\mathrm{K}}$, $u/\mathrm{K} \neq 1$, $\mathrm{K} > 0$, to enhance established mathematical methodologies for better understanding glioblastoma dynamics at the macroscopic scale. The tumor growth model exhibits an innovative structure even within the conventional framework, including a proliferation term, $f(u)$, presented in a different form compared to existing macroscopic glioblastoma models. Moreover, it represents a further refined model by incorporating a calibration criterion based on the integration of a fractional derivative, α, which differs from the existing models for glioblastoma. Throughout this study, we initially discuss the modeling dynamics of the tumor growth model. Given the frequent recurrence observed in glioblastoma cases, we then track tumor mass formation and provide predictions for tumor visibility timing on medical imaging to elucidate the recurrence periods. Furthermore, we investigate the correlation between tumor growth speed and survival duration to uncover the relationship between these two variables through an experimental approach. To conduct these patient-specific analyses, we employ glioblastoma patient data and present the results via numerical simulations. In conclusion, the findings on tumor visibility timing align with empirical observations, and the investigations into patient survival further corroborate the well-established inter-patient variability for glioblastoma cases.

Keywords: Glioblastoma; tumor visibility; recurrence; survival; fractional mathematical model
AMS 2020 Classification: 35K57; 35K67; 65M06; 92B05; 92C37

1 Introduction

Glioblastoma, an aggressive brain tumor known for its high lethality, exhibits an elusive structure owing to its intricate cellular nature. Due to this challenging cellular architecture and histological

diversity, glioblastomas have long been recognized as exemplars of tumor heterogeneity, earning the appellation "multiforme" [1]. In accordance with the 2021 classification of Central Nervous System (CNS) tumors by the World Health Organization (WHO), glioblastomas are officially categorized as *Isocitrate dehydrogenase* (IDH) wild type, signifying the most aggressive variant among diffuse gliomas [2].

The current therapeutic approaches for glioblastoma include a multimodal strategy involving surgical intervention, radiation therapy, and chemotherapy [3]. The standard treatment protocols for newly diagnosed glioblastoma patients typically begin with a maximally safe resection, followed by a combined treatment phase comprising both radiotherapy and chemotherapy. In the aftermath, a monotherapy phase comprising adjuvant chemotherapy ensues. Unfortunately, despite this intensive treatment schedule and advancements in medical imaging for early glioblastoma detection, instances of recurrence near the resection margin persist [4–6]. Even though chemotherapy appears to be the most efficient way to reach all tumor cells, leading to apparent regression on magnetic resonance imaging (MRI), the extent of tumor spread is almost unaffected due to the continued motility of tumor cells [7]. As a result, extensively invaded tumor cells remain below the detection capabilities of MRI, and recurrences manifest upon treatment cessation. Considering this reality, we delve into an exploration of recurrence periods in a cohort of ten patients as part of this study. By doing this, we aim to predict the timing of tumor visibility on MRI. We consider that there are at least three benefits to this analysis: 1) There may be an opportunity for early detection of tumor recurrence; 2) Understanding recurrence trends may contribute to a more personalized approach to patient care; 3) The focus on predicting tumor visibility on MRI scans may help optimize imaging resources. In conducting this analysis, we take into account the dynamics of the angiogenesis process. Angiogenesis involves the formation of new capillary blood vessels from existing microvessels as well as the differential recruitment of relevant supporting cells to different parts of the vascular system [8]. New blood vessels formed through angiogenesis provide the means for further cell proliferation by ensuring a constant supply of nutrients and oxygen. On the other hand, one of the pathological features that distinguish glioblastoma from low-grade glial tumors is microvascular proliferation [9]. However, T1-weighted MRI with gadolinium contrast (T1Gd) images the abnormally leaky vasculature within the tumor and outlines the bulk of the lesion [10]. Taking into account all these factors and acknowledging a direct correlation between the count of proliferating tumor cells and blood vessels, we produce results regarding the visibility of the tumor by taking the count of glioblastoma cells into consideration. Therefore, we assign all parameter values for the model while considering T1Gd.

The objectives behind mathematically modeling brain tumor growth are multifaceted. These encompass mechanisms for deciphering the regulation of disease progression, adapting models to individual patients, and correlating them with clinically relevant data to gauge tumor occurrences such as recurrence trends, aggressiveness, and treatment response. Unlike microscopic models, which are not suitable for medical images, macroscopic models prove more efficient in capturing the average behavior of tumor cells and modeling the evolution of local tumor cell densities than individual cells [11]. In mathematical models at the macroscopic scale, tumors undergo classification based on their motility, denoting invasiveness, and the rate of cellular division, denoting proliferation, and are typically elucidated through the lens of reaction-diffusion formalism [7, 11–24]. However, it is noteworthy that existing models utilize classical reaction-diffusion approaches, particularly in the context of glioblastoma growth. To the best of our knowledge, fractional reaction-diffusion modeling for glioblastoma growth has not been reported in the literature, despite the increasing prevalence of fractional models for disease modeling [25–29]. In this work, we propose a fractional tumor growth model at a macroscopic scale, rooted in a mathematical problem known as the quenching problem [30], which incorporates a type of

reaction-diffusion equation. In the context of the quenching problem, studies have delved into the global existence of its solutions, and analyses pertaining to quenching and non-quenching scenarios [31–35]. The relationship between quenching and blow-up problems has been another focal point to investigate [36, 37]. This investigation has been extended to parabolic systems, with a specific focus on quenching behavior in the presence of singular multi-nonlinearities [38–42]. More recently, attention has turned towards fractional versions of the problem [43, 44]. This shift is driven by the burgeoning interest in fractional calculus that has evolved over the last few decades. In addition, fractional differential equations have gained significant attention due to their potential applications across diverse areas in science and engineering along with their notable theoretical importance [9, 45–49]. Various definitions of fractional derivatives have been proposed in the literature. Among these, one of the most widely recognized is the Caputo fractional derivative [45, 47, 50, 51], notable for its memory effect. Additionally, it is known that the Caputo fractional derivative becomes equivalent to the conventional derivative as the fractional derivative order approaches a conventional derivative order. Considering all of these, we employ the Caputo derivative within the glioblastoma growth model to discern the memory effect and observe its differences from the classical derivative. We consider that such a selection serves as an appropriate operator for conducting analyses in this work that incorporate temporal assessments. Therefore, we anticipate that a more effective fitting of the growth model to patient data can be achieved by employing the Caputo derivative as a calibration criterion. To build up the growth model, we enhance the conventional framework of the quenching problem to more effectively capture glioblastoma dynamics through tailored modifications. Since temporal considerations are in question here, we first introduce the Caputo fractional derivative to the time-dependent term in the mathematical equation. As a second modification, we incorporate a term that represents the maximum cell carrying capacity of the tissue, K, into the proliferation term, $f(u)$. We consider that this approach offers a more efficient modeling framework, facilitating an investigation into the potential trajectory of tumor cell density over a meaningful time frame.

The subsequent sections of this paper are organized as follows: Section 2 provides a brief exploration of the theoretical groundwork for the tumor growth model, including properties of the Caputo fractional derivative. Section 3 presents the tumor growth model, its initialization and implementation along with the numerical scheme. Section 4 presents key findings, encompassing an exploration of the fundamental dynamics and operational principles of the model, investigations into the timing of tumor visibility in a patient cohort, and an analysis of the relationship between tumor growth speeds and patient survival.

2 Theoretical background

In this section, we provide an overview of the growth model's background and highlight some properties related to the Caputo fractional derivative.

In 1975, Kawarada proposed a one-dimensional initial-boundary-value problem, which is known as the quenching problem, denoted as

$$\begin{cases} u_t(x,t) = u_{xx}(x,t) + \dfrac{1}{1-u} & \text{in } (0,L) \times (0,T), \\ u(0,t) = u(L,t) = 0 & \text{in } (0,T), \\ u(x,0) = 0 & \text{on } [0,L], \end{cases} \tag{2}$$

where L is a positive real number indicating the length of spatial domain [30]. Mathematically, a

solution of problem (2) is said to quench if there exists a finite time T such that

$$\lim_{t \to T^-} \sup \{| u_t(x,t) |: x \in [0,L]\} \to \infty. \tag{3}$$

The value of T represents the quenching time. A necessary condition for appearance of quenching is

$$\lim_{t \to T^-} \max\{| u(x,t) |: x \in [0,L]\} \to 1^-. \tag{4}$$

One of the important results for problem (2) is provided by the following lemma.

Lemma 1 *[32] If $T < +\infty$, then there exists $x^* \in [0,L]$ such that*

$$\lim_{(x,t) \to (x^*,T)} u(x,t) = 1. \tag{5}$$

We now provide the relevant definitions for the Caputo fractional derivative. Let $\Gamma(\cdot)$ be Euler's gamma function.

Definition 1 *[45, page 92] Let $0 < \alpha < 1$ and $u(x) \in AC[a,b]$. Then the left-sided and right-sided Caputo fractional derivatives of u exist almost everywhere and are respectively defined as*

$$\left({}_a^c\mathfrak{D}_x^\alpha \right) (u(x)) = \left({}_aI_x^{1-\alpha} \right) \frac{du(x)}{dx}, \quad x > a,$$

$$\left({}_x^c\mathfrak{D}_b^\alpha \right) (u(x)) = -\left({}_xI_b^{1-\alpha} \right) \frac{du(x)}{dx}, \quad x < b.$$

The set $AC[a,b]$ denotes the collection of all functions that are absolutely continuous in domain $[a,b]$.

In a similar manner, one can articulate a partial fractional derivative for a function with multiple variables as follows.

Definition 2 *[45, page 358] The Caputo fractional derivative of a function $u(x,t)$, with $0 < \alpha < 1$ denoting the order of the derivative, is defined as*

$$\left({}^c\mathfrak{D}_t^\alpha \right) (u(x,t)) = \frac{1}{\Gamma(1-\alpha)} \int_0^t (t-s)^{-\alpha} \frac{\partial u(x,s)}{\partial s} ds,$$

where $0 < x < L$ and $t > 0$.

Remark 1 *[47, page 79] If $u(x,t)$ is continuously differentiable on t, then $\left({}^c\mathfrak{D}_t^\alpha \right) (u(x,t)) \to \frac{\partial u(x,t)}{\partial t}$ as $\alpha \to 1$.*

3   Method

In the subsequent part of this section, we present our tumor growth model, its initialization and implementation along with the specified numerical scheme.

Tumor growth model

In this work, we model the spatio-temporal evolution of glioblastoma growth using a time-fractional partial differential equation with $\Omega = (0, L) \times (0, T)$ given by

$$\underbrace{^c\mathfrak{D}^\alpha_t u}_{\substack{\text{the distribution} \\ \text{of glioblastoma cell density}}} = \underbrace{\nabla \cdot D\nabla u}_{\substack{\text{net invasion} \\ \text{of glioblastoma cells}}} + \underbrace{\rho f(u)}_{\substack{\text{net proliferation} \\ \text{of glioblastoma cells}}} \quad \text{in} \underbrace{\Omega}_{\substack{\text{brain} \\ \text{anatomy}}}, \tag{6}$$

where α, $0 < \alpha \leq 1$, is the Caputo fractional derivative order, $u = u(t, x, y)$ ($cells/mm^3$) is the glioblastoma cell density, D ($mm^2/year$) is the net invasion rate, ρ ($1/year$) is the net proliferation rate, and the proliferation term satisfy

$$f(u) = \frac{1}{1 - u/K}, \quad u/K \neq 1, \quad K > 0, \tag{7}$$

where K ($cells/mm^3$) is the maximum cell carrying capacity of tissue for tumor cells. The equation (6) can be solved under various dimensional assumptions. Here, we employ a two-dimensional spatial derivative in the equation.

Hypothesis

To provide a theoretical foundation for our findings, we propose the following hypothesis, considering statements (3)-(4) and Lemma 1 given in Section 2.

Hypothesis. If the glioblastoma cell density, u, approaches the maximum cell carrying capacity of the tissue, K

$$u \to K, \quad K < +\infty, \quad t \to T, \tag{8}$$

then the distribution of glioblastoma cell density, $^c\mathfrak{D}^\alpha_t u$, increases

$$^c\mathfrak{D}^\alpha_t u \to \infty, \quad t \to T. \tag{9}$$

Then, there exist a critical point (T, x^*, y^*), such that the glioblastoma cell density, u, reaches the maximum cell carrying capacity of tissue, K

$$\lim_{(t,x,y) \to (T,x^*,y^*)} u = K, \quad T < +\infty. \tag{10}$$

This allows the model to approximate the critical point at which the glioblastoma cell density reaches the maximum cell carrying capacity of the tissue, K, allowing the examination of the time interval leading to this important event. At this juncture, we make two assumptions: *i*) When the glioblastoma cell density reaches the maximum cell carrying capacity of tissue, K, a critical and lethal cell population becomes detectable on MRI; *ii*) When the glioblastoma cell density reaches the maximum cell carrying capacity of tissue, K, it results in necrosis, detectable through MRI. In both cases, the glioblastoma cell density should become visible at a certain time $t \in (0, T)$ before reaching the maximum cell carrying capacity of the tissue, K. Hence, this implies that equation (6) can serve as a prognostic tool for predicting the timing of tumor visibility.

Note that, given that the model is defined in a closed domain, the statement (9) refers to a growth in the distribution of glioblastoma cell density, $^c\mathfrak{D}^\alpha_t u$, rather than a true approximation to infinity.

Once the glioblastoma cell density, u, reaches the maximum cell carrying capacity of the tissue, K, in a finite time period $T < +\infty$, the distribution of glioblastoma cell density, $^c\mathfrak{D}_t^\alpha u$, proceeds over the same time period.

Model initialization and implementation

The complete specification of equation (6) necessitates the inclusion of both initial and boundary conditions. The tumor theoretically begins with a single cancerous cell, but the timing and specifics of its initial growth and spread are unknown. We assume that at the time of diagnosis, any previous, presumably uniform distribution of cells has already been disrupted. Thus, in order to characterize the current behavior of tumor cells, we employ the Gaussian distribution as given by

$$u(0, x, y) = u_0 \exp\left(-\frac{|x - x_0|^2 + |y - y_0|^2}{2\sigma^2}\right) > 0, \tag{11}$$

where u_0 is the initial cell density, σ is the standard deviation, and x_0, y_0 is the peak of the Gaussian distribution. Utilizing such an initial condition, we anticipate that tumor cells exhibit denser clustering around the center of the tumor, gradually decreasing in density as one moves away from the center. We impose a no-flux boundary condition

$$\nabla u \cdot \vec{n} = 0, \quad \text{in } \partial\Omega, \tag{12}$$

where $\vec{n}$ is the outward unit normal to $\partial\Omega$. The skull and ventricles are not invaded by the tumor cells and serve as domain boundaries as indicated by equation (12).

We implement a finite difference scheme to solve the time-fractional equation (6), along with the initial condition (11) and the boundary condition (12), by following [43]. In particular, we employ a numerical scheme that incorporates the Caputo fractional derivative for the time-dependent term along with the two-dimensional space-dependent derivative, as given by

$$
\begin{aligned}
\frac{1}{\Gamma(1-\alpha)} &\sum_{m=0}^{k-1} \frac{u(t_{m+1}, x_i, y_j) - u(t_m, x_i, y_j)}{\tau} \int_{t_m}^{t_{m+1}} (t_k - s)^{-\alpha}\, ds \\
&= D\left\{\frac{u(t_{k-1}, x_{i-1}, y_j) - 2u(t_{k-1}, x_i, y_j) + u(t_{k-1}, x_{i+1}, y_j)}{\Delta x^2}\right\} \\
&+ D\left\{\frac{u(t_{k-1}, x_i, y_{j-1}) - 2u(t_{k-1}, x_i, y_j) + u(t_{k-1}, x_i, y_{j+1})}{\Delta y^2}\right\} + \rho f(u(t_{k-1}, x_i, y_j)),
\end{aligned}
\tag{13}
$$

where the time step size is τ. Accordingly, the temporal nodes are given by $t_k = k\tau, k = 0, 1, \ldots, Nt$. Similarly, the spatial nodes are defined as $x_i = i\Delta x, i = 0, 1, \ldots, Nx$ with $\Delta x = Lx/Nx$ and $y_j = j\Delta y, j = 0, 1, \ldots, Ny$ with $\Delta y = Ly/Ny$, representing the spatial step sizes.

Note that the Caputo fractional derivative, which is given in Definition 2, is applicable only within the order interval of $0 < \alpha < 1$. Thus, incorporating the fractional derivative order of 1 directly into the numerical scheme (13) is not feasible. However, Remark 1 indicates that the Caputo fractional derivative converges toward the classical derivative as the values of α approach 1. This implies that the fractional numerical scheme (13) turns into a classical scheme. Hence, we additionally implement and execute the well-known classical finite difference scheme to conduct comparative assessments in the subsequent parts. We explore the distinctions between

the fractional and classical derivatives by utilizing α values that are smaller and closer to 1.

4 Results

In this section, we first discuss the dynamics of the growth model under different fractional derivative orders of α. We observe that the growth model is characterized by predominant proliferation behavior. Recognizing the potential utility of this outcome as a tool for monitoring tumor mass formation, we proceed to estimate the timing of tumor visibility on MRI for a specified patient cohort. Finally, we analyze the correlation between variations in tumor growth speed and patient survival through an experimental study. For all computational approaches and simulations here, we use Python programming language.
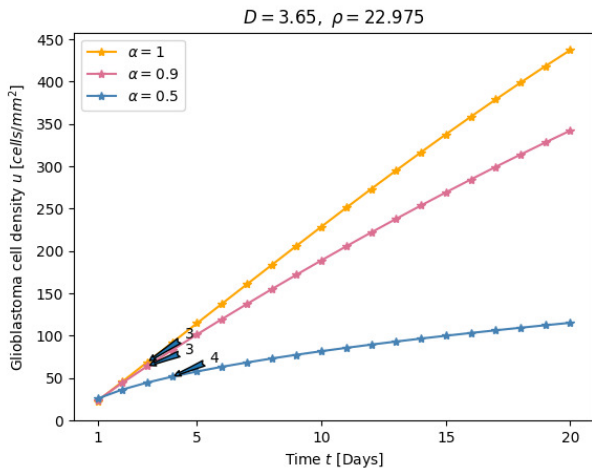
Dominance assessment of proliferation rate

Throughout our investigations, we integrate the parameter values from the existing studies considering T1Gd MRI into our growth model. In this section, we explain the dynamics modeled by equation (6), along with the initial condition (11) and the boundary condition (12), before discussing results on tumor visibility timing. To conduct these analyses, we leverage the numerical data pertaining to invasion, D, and proliferation, ρ, rates for a cohort of glioblastoma patients provided in [52]. These values, estimated from lesion volumes obtained from MRI scans, including post-contrast T1Gd [7, 20, 52], are derived from a single MRI time point before treatment. In this work, we set a range for the data presented in [52] and perform investigations on this specific patient cohort. We confine our investigation to a numerical interval for invasion rates, ranging from 1.1542 to 7.2827, as specified in Table 1.

Table 1. D: net rate of invasion; ρ: net rate of proliferation; Surv. Days: Overall survival days; Censorship (1=censored): The term 'censored' signifies incomplete information, as the event (e.g., death or failure) did not occur within the study period or the patient was lost to follow-up.; The units are D $\sim mm^2/year$; $\rho \sim 1/year$

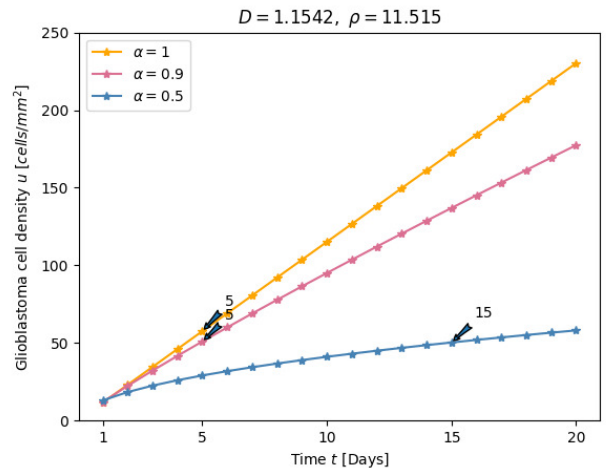| Patient	Gender	D	ρ	Surv. Days	Censorship
1	F	3.65	22.975	1292	0
2	F	1.1542	11.515	375	0
3	F	4.5951	22.975	65	0
4	F	7.2827	18.25	124	0
5	F	5.7849	14.496	115	0
6	M	2.303	36.414	126	0
7	M	4.5951	11.515	2139	1
8	M	7.2827	29.924	224	0
9	M	3.65	14.496	260	0
10	M	5.7849	9.1467	1143	0
Mean	-	4.60826	19.17067	586.3	-

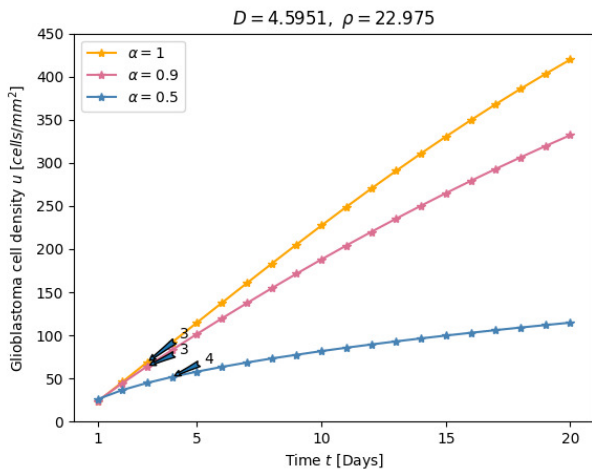The data presented in this table is sourced from Reference [52]

Considering the Caputo fractional derivative definition given by Definition 2, it is clear that directly assigning the derivative order of 1 to the model is not applicable. Taking into account Remark 1, it is seen that in the scenario where $\alpha = 1$, the numerical scheme (13) transitions into the classical numerical scheme. Therefore, we set one of the α values to 0.9 to facilitate observation of the approximation to the classical numerical scheme characterized by $\alpha = 1$. Accordingly, we execute the model individually for each patient, utilizing fractional derivative orders of $\alpha = 0.5$, $\alpha = 0.9$, and $\alpha = 1$ for the analyses. We place the peak of the Gaussian distribution given by (11) at the center of the domain.
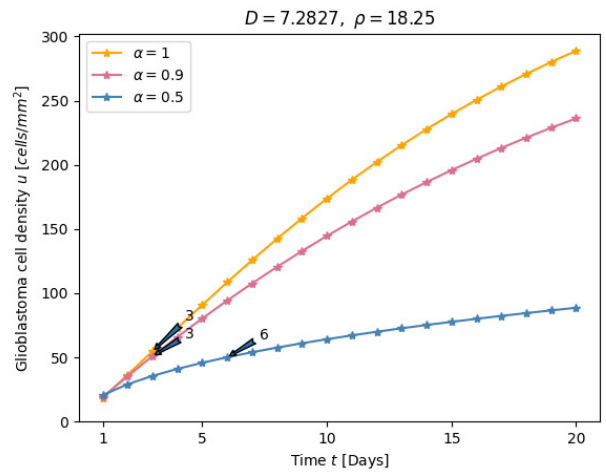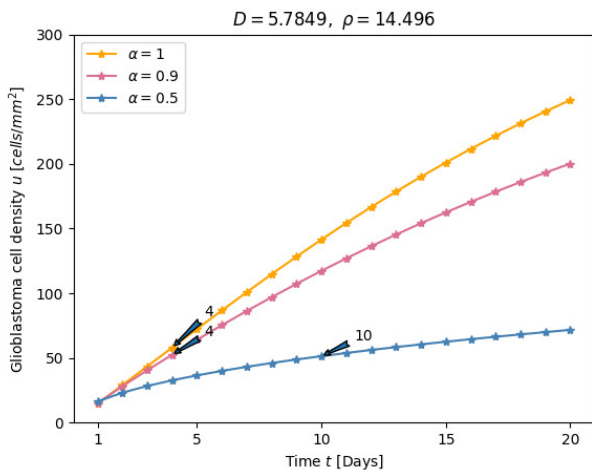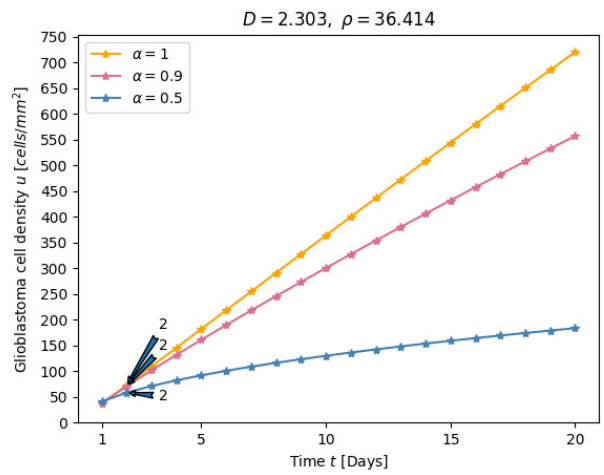
(a) Patient 1

(b) Patient 2

(c) Patient 3

(d) Patient 4

(e) Patient 5

(f) Patient 6

(g) Patient 7

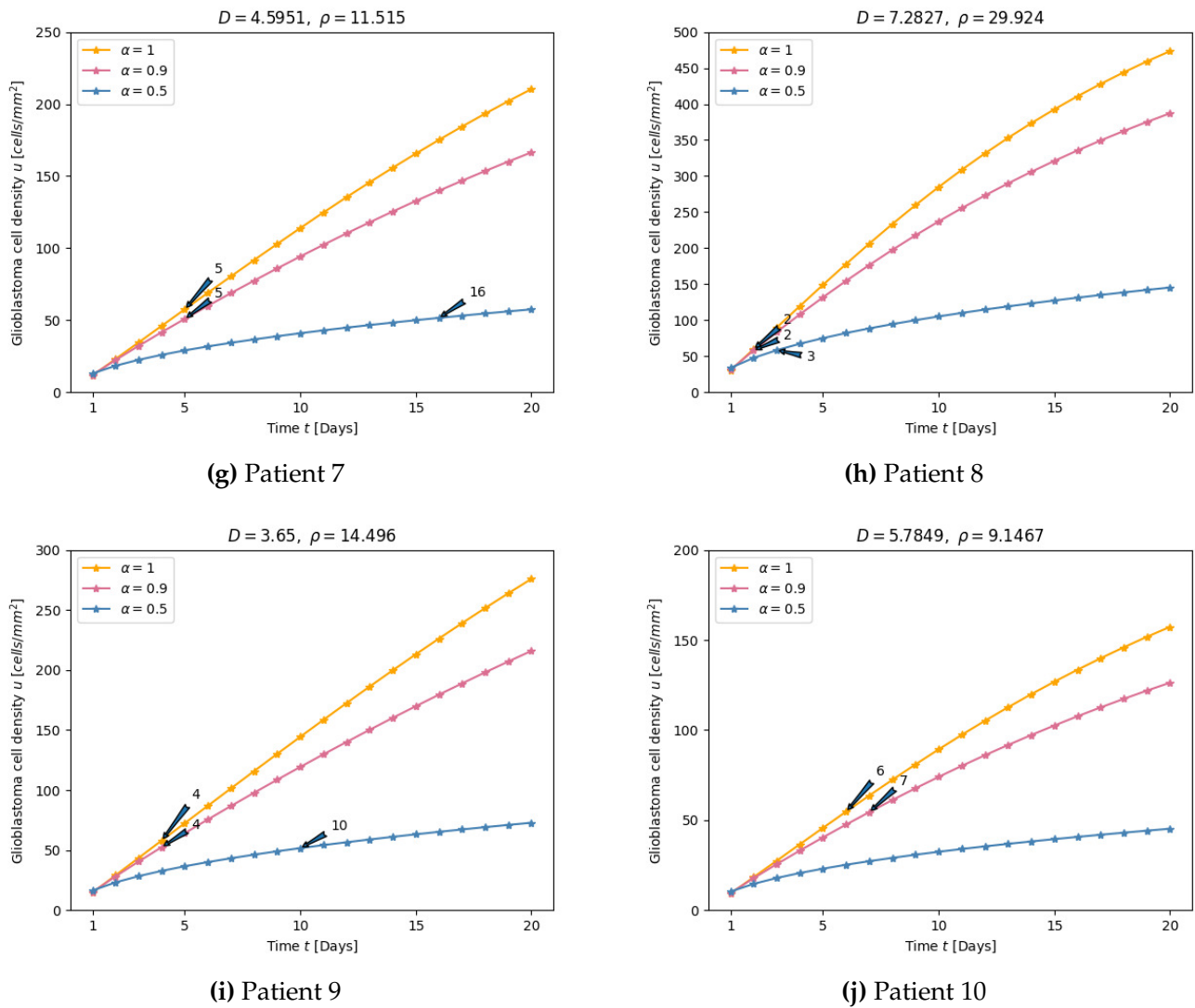**(h)** Patient 8

(i) Patient 9

(j) Patient 10

Figure 1. The maximum glioblastoma cell density observed each day over a twenty-day period under the three different derivative orders for each patient listed in Table 1 and the corresponding tumor visibility timing. Each small data point on the curves, depicted as asterisks, corresponds to consecutive days. Arrow symbols, along with corresponding numerical annotations, signify the days on which the tumor cell count achieved the threshold of $50 \, cells/mm^2$ within the respective day. The term α represents the Caputo fractional derivative order

We keep both the initial cell density, $u_0 = 0.0147$, and the standard deviation, $\sigma = 2.86 \, mm$, in the Gaussian distribution constant, in accordance with [13, 14, 18, 19]. We hold the maximum cell carrying capacity of the tissue constant at $K = 10^8 \, cells/mm^3$ for all simulations, consistent with [20]. We consider invasion and proliferation coefficients, denoted as D and ρ, respectively, as patient-specific values, as in Table 1. To execute the model, we employ the numerical scheme with a time step of $\tau = 0.01$, and a spatial discretization involving a domain length of $50 \, mm$ with 25 grid points. With the adjustments above, we generate daily glioblastoma cell densities for each patient over a twenty-day period, as demonstrated in Figure 1.

As a result, in Figure 1, the consideration of both proliferation rates and glioblastoma cell density values on the *y*-axes revealed a conspicuous trend, showcasing the dominance of proliferation rates in the model across all examined cases. Stated differently, the model notably initiated the generation of glioblastoma cell densities, with a specific focus on proliferation rates. This indicates that the tumor growth model may be an effective tool for tracking the temporal evolution of tumor

mass formation. Upon comparison of data from cases where each pair has the same proliferation rates, such as in the cases of Patients 1 and 3, Patients 2 and 7, or Patients 5 and 9, it was observed that a higher value of the invasion parameter slowed down the effect of the proliferation parameter. Accordingly, a slowdown in the growth rate of glioblastoma cell density was observed.

On the other hand, the numerical range identified in Table 1 for invasion parameter values, which comes from the data source, resulted in consistently smaller invasion rates than their proliferation counterparts in each case. Therefore, we now conduct an additional analysis to assess the dominance of the proliferation rate in the reverse case. To do this, we select arbitrary invasion and proliferation rates, namely, $D = 7.01$ and $\rho = 4.99$, while maintaining consistency with all other parameters and methodologies employed in the preceding analyses. Accordingly, we present a magnified visualization illustrating the early stages of glioblastoma cell density for the three distinct derivative orders of α, as shown in Figure 2.
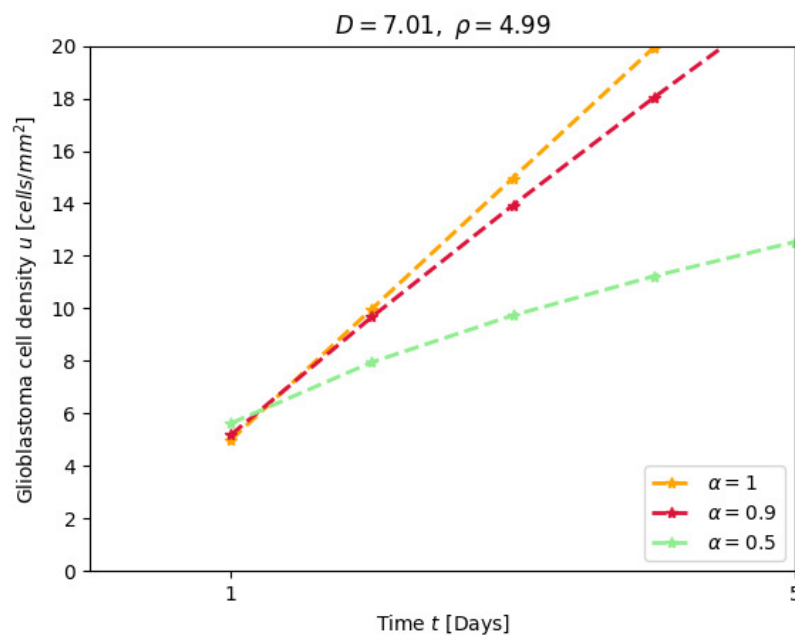

Figure 2. Magnified view of the initiation of glioblastoma cell density under the three different derivative orders of α with the arbitrary parameter values of D and ρ

For the arbitrary parameter values, it was clearly observed that glioblastoma initiation commences with a numerical value closely aligned with the proliferation rate, $\rho = 4.99$, for all three derivative orders of α, as shown in Figure 2. In conclusion, the proliferation rate being smaller than the invasion rate does not constitute a transformative factor influencing the dominance of the proliferative behavior in the model. Therefore, this analysis further underscores the tumor growth model's efficacy in capturing the process of glioblastoma mass formation.

Investigation of tumor visibility timing

The complexity of glioblastoma and its propensity for recurrence underscore the need for a nuanced understanding of its recurrence patterns for improved patient-specific management. In this section, we address this void and perform a patient-specific short-term follow-up to investigate the timing of glioblastoma cell visibility on MRI for the recurrence period. The analyses conducted in the preceding section emphasize the efficacy of the tumor growth model in

tracking the glioblastoma formation process, thereby affirming its ability to predict tumor visibility timing. In light of this finding, we proceed with our further discussions over the patient cohort presented in Table 1, which comprises ten patients newly diagnosed with glioblastoma.

Due to the invasive nature of glioblastoma, only a portion of the tumor can be detected with available medical imaging techniques. Examinations of computed tomography (CT) images and microscopic studies on postmortem brain slices indicate a detection threshold of $40,000\ cells/cm^2$ for advanced CT scans [23]. This threshold corresponds to approximately $400\ cells$ in the approximately $1\ mm^2$ area covered by a 10x objective, or approximately $25\ cells$ in the same area covered by a 40x objective for a histopathologist [21]. In this study, we adopt a threshold value of $50\ cells/mm^2$ as a threshold. For a histopathologist, this threshold may correspond to approximately $5\ cells$ in an area covered by a $10\times$ objective, following [21]. Here, we conduct examinations assuming that all patients receive standard treatment. With the same numerical scheme adjustments as in the previous section, we consider a twenty-day recurrence period following standard treatment. As mentioned in Subsection 4 and illustrated in Figure 1, under the three specified α values, the maximum glioblastoma densities were generated, which were attained daily throughout the considered recurrence time frame. Then, we determine the days on which the $50\ cells/mm^2$ threshold was reached for each patient under the three derivative orders of α.
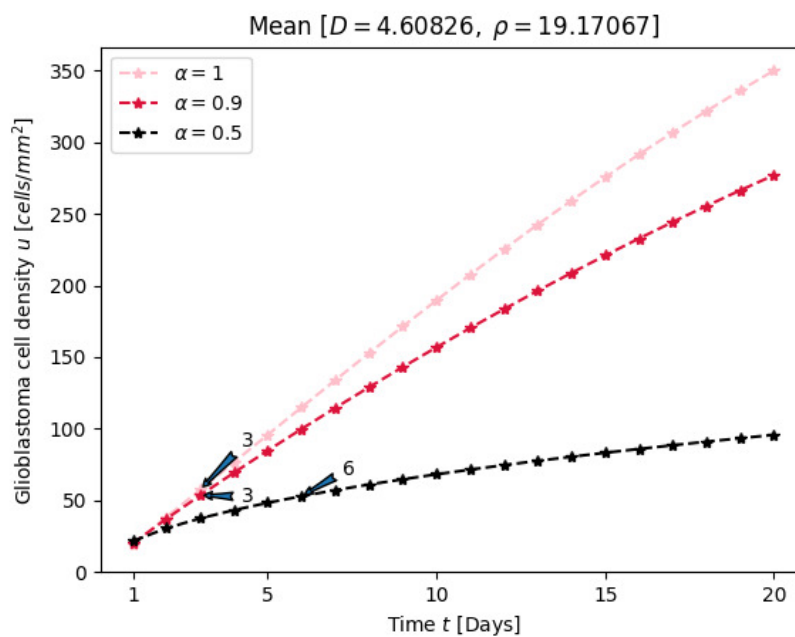

Figure 3. The maximum glioblastoma cell density observed each day over a twenty-day period under the three different derivative orders of α for the mean value and the corresponding tumor visibility timing

In conclusion, the classical derivative, defined by the order of $\alpha = 1$, depicted a growth pattern that rapidly reached the tumor visibility threshold of $50\ cells/mm^2$ in the initial time steps, exhibiting a rapid departure from this threshold. A similar trend was observed when choosing $\alpha = 0.9$ as a value close to the classical order. In contrast, when the fractional derivative order was set to $\alpha = 0.5$, the model showed a higher sensitivity to the tumor visibility threshold. That is, significant variations in the time for the tumor to reach the visibility threshold were observed for $\alpha = 0.5$ across the examined time span. Moreover, upon comparing Patient 2 and Patient 7, both exhibiting identical proliferation rates, it became evident that a higher invasion rate led to a delay in tumor visibility timing for $\alpha = 0.5$, unlike other derivative orders. In contrast to the remaining cases,

Patient 10, characterized by a comparatively lower proliferation rate and a higher invasion rate, it was observed that the tumor visibility threshold for $\alpha = 0.5$ was not reached in the relevant time period. However, given its proximity to the tumor visibility threshold on the twentieth day, it can be anticipated that the visibility threshold will likely be reached in the ensuing days. Consequently, analyses revealed that fractional derivatives model a more controlled growth behavior in contrast to the classical derivative.

It is notable that the tumor typically reached the $50\,cells/mm^2$ threshold within the same day for the derivative orders of $\alpha = 0.9$ and $\alpha = 1$, except for Patient 10. It is essential to elucidate that this does not necessarily denote the same cell count. Rather, this means that the glioblastoma densities exceeded the threshold on the specified day and manifested varied values beyond this threshold for both derivative orders.

As a final step, we investigate the timing of tumor visibility for the mean value of both invasion and proliferation rates presented in Table 1. As observed in Figure 3, the glioblastoma cell density surpassed the tumor visibility threshold within six days for the mean under all three distinct derivative orders of α. Given that the empirical evidence indicates the presence of glioma cells throughout the CNS within seven days following the implantation of tumors into a rat brain [21], our findings appear to be coherent with this observed phenomenon.

Investigation of tumor growth speed and survival correlation

As an additional experimental study, we examine the connection between patient survival and tumor growth speed for patients with glioblastoma in this part. To accomplish this, we employ a metric that considers the successive interday tumor growth speed. Here we consider a period from the initial diagnosis of glioblastoma to the day of death for the simulations. We use the numerical data extracted from [52], and presented in Table 2. To execute the model, we adopt identical parameter values as detailed in Subsection 4, with the exception of the time step, which is set to $\tau = 0.1$ with a fractional order of $\alpha = 0.5$.

Table 2. D : net rate of invasion; ρ: net rate of proliferation; Surv. Days: Overall survival days (from diagnosis to death); The units are $D \sim mm^2/year$; $\rho \sim 1/year$

Patient	Gender	D	ρ	Surv. Days
1	F	1.1542	11.515	375
2	F	1.8293	289.24	446
3	M	2.303	36.414	126
4	M	0.91684	5.7712	862

The data presented in this table is sourced from Reference [52]

We first explore the temporal trends of glioblastoma densities considering the survival duration of patients, as illustrated in Figure 4. When glioblastoma cell densities were examined, tumor growth trends within this group revealed the predominance of the proliferation term, as in the patient group discussed in Subsection 4. To further analyze the current growth trend for each patient, we apply a metric given by

$$\Delta\text{GCV}_k = u_{max}^{k+1} - u_{max}^k, \tag{14}$$

where $k \in [1, S-1]$. Here, S is the total number of survival days in the period after diagnosis, expressed as survival days in Table 2, u_{max} is the maximum cell density, and k is the time index. To reveal potential patterns among the patients, we apply metric (14) to the daily maximum glioblastoma cell densities obtained above, as visualized in Figure 5. In conclusion, the glioblas-
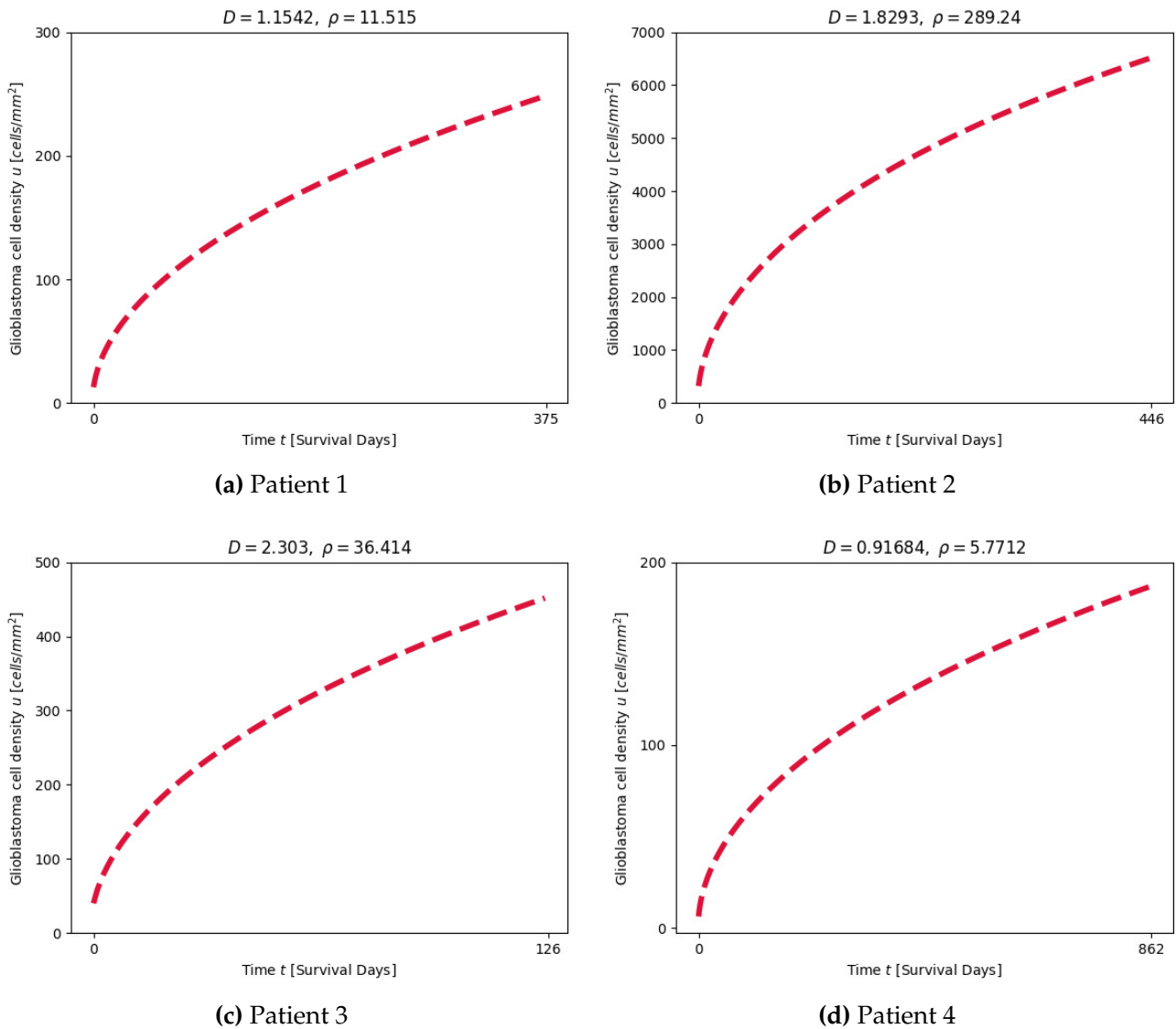
(a) Patient 1

(b) Patient 2

(c) Patient 3

(d) Patient 4

Figure 4. The maximum glioblastoma cell densities over the survival duration of patients listed in Table 2

toma cell densities exhibited a deceleration in growth speed when compared to the preceding days, as a specific pattern across four patients. This deceleration may be attributed to necrosis formation, indicating cell death within the tumor tissue, particularly given the dominance of the proliferation phenomenon in the model. To perform a patient-specific analysis of this change, we impose two arbitrary thresholds indexed to each patient's own tumor cell densities. These express two criteria of the form $T1 = 0.20\max(\Delta\mathrm{GCV}_k)$ and $T2 = 0.06\max(\Delta\mathrm{GCV}_k)$. We then determine the first days when the glioblastoma cell variation, $\Delta\mathrm{GCV}_k$, fell below these thresholds for each patient. When reviewing the outcomes, it was observed that in the case of Patient 1, death ensued relatively quickly after the $\Delta\mathrm{GCV}_k$ value fell below the second threshold, $T2$, while in the cases of Patients 2 and 4, death occurred much later. In contrast, in the instance of Patient 3, death was noted after the $\Delta\mathrm{GCV}_k$ value fell below the first threshold, $T1$, before attaining the second threshold, $T2$. Consequently, no remarkable patterns were observed linking the thresholds to the glioblastoma cell variation during the survival days. We also examine the final delta values of the patients, as shown in Figure 6. The values displayed on the y-axis in Figure 6 correspond to the final delta values for the two days preceding the occurrence of death. In conclusion, the examined patient cohort did not exhibit any significant patterns in this temporal window. How-

ever, these conclusions further corroborated the long-recognized yet unexplained heterogeneity in inter-patient variability among glioblastoma cases, as mentioned in [53, 54].
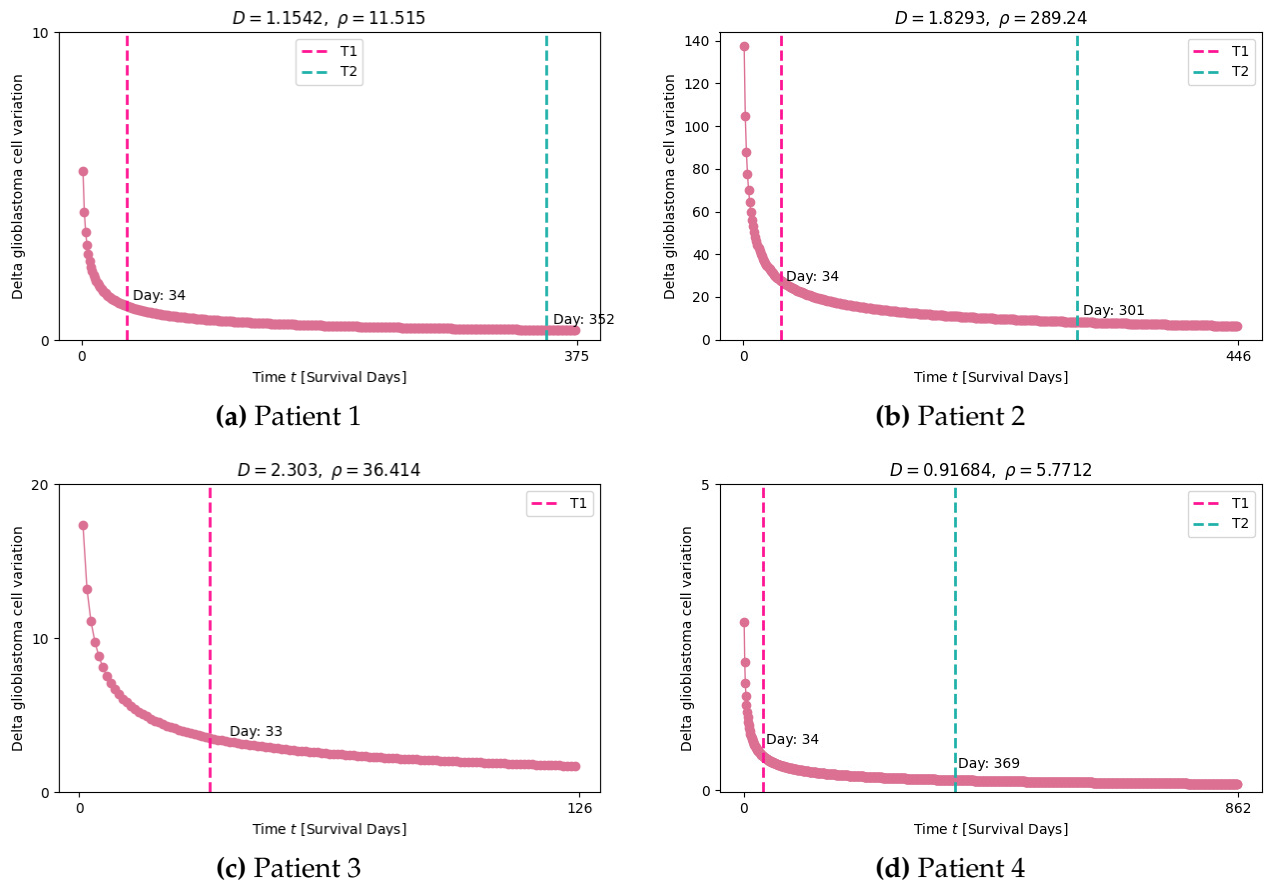

Figure 5. Correlation of glioblastoma cell variation with patient survival under the fractional order of $\alpha = 0.5$. Each pink marker on the curves signifies the values commencing from the initial delta, ΔGCV_1, which corresponds to the first two days after diagnosis, extending to the final delta value, ΔGCV_{S-1}, representing the consecutive two days before mortality. The pink dotted line denotes the first threshold, $T1$, representing the point at which the ΔGCV_k value reaches %20 of the maximum value of ΔGCV_k. Similarly, the sea green dotted line delineates the second threshold, $T2$, symbolizing the point at which the ΔGCV_k value reaches %6 of the maximum value of ΔGCV_k. The days marked in black adjacent to the dotted lines signify the initiation of these events

5 Discussion

In this work, we use an explicit fractional finite difference scheme for the simulations. In addition to the established stability issues associated with explicit schemes, it is noteworthy that the inclusion of fractional derivatives in the employed numerical scheme introduced an additional layer of complexity to this challenging scenario. In cases not included in this study but defined with relatively larger invasion rates, difficulties were encountered in managing these high values. The applied fractional numerical scheme faced challenges in handling a wider range of invasion parameter values, particularly for values below the fractional order $\alpha = 0.5$, which serves as the lower limit in the investigative scope of this study. To address these challenges, a finer-scale temporal discretization strategy was employed. However, this adjustment resulted in a significant escalation of computational time with simulations extending up to thirty-six hours. These findings recommended the adoption of implicit methods in future studies as a prudent and feasible strategy
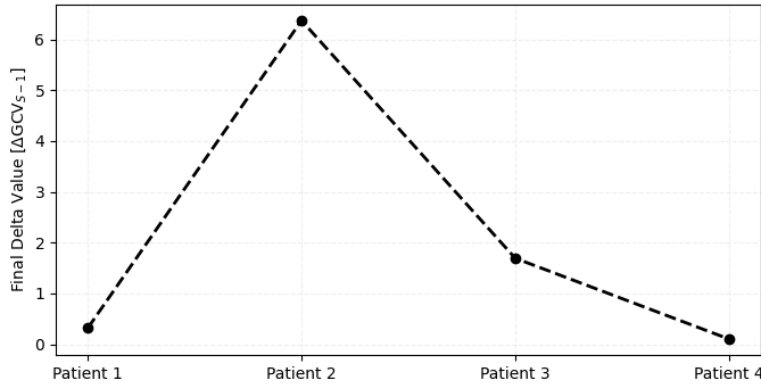
Figure 6. The values of the final delta, ΔGCV_{S-1}, for the patients listed in Table 2

to mitigate computational time and efficiently handle extensive numerical data. By this means, it appears possible to leverage the subtle effects of smaller fractional orders across a broad range of parameter values.

Upon theoretical evaluation of the decrease in the speed of increase in maximum cell densities for each day over the survival period discussed in Subsection 4, it can be inferred that the observed deceleration reflects convergence behavior to a singular point in the proliferation term, $f(u)$. However, this deceleration may be attributed to necrosis formation, which signifies cell death in the tumor tissue, particularly when considering the dominance of the proliferation phenomenon in the model. Examining the growth model's ability to effectively capture necrosis occurrences would have been facilitated with more detailed information about the studied patient cohort. Regrettably, this study was unable to access such detailed data. Future research endeavors are anticipated to provide opportunities for more comprehensive analysis in this regard. In the context of the final experiments, the ΔGCV_k value for all four patients fell below the initial threshold, $T1$, on nearly the same days, as illustrated in Figure 5. This is attributable to the proximate invasion rates observed across the cases. Working with patient data characterized by higher invasion rates may lead to variability in this regard.

Overall, the findings presented in this study should be contextualized within the scope of experimental investigations conducted through a mathematical equation. To transparently evaluate the advantages of the proposed growth model, conducting rigorous assessments involving clinical validations, such as *in vivo* or *in vitro*, would be highly enlightening. To the best of our knowledge, our growth model, even in its classical form has not been explored in the context of cancer research. This suggests the model's potential as a focal point for future cancer investigations within the realm of mathematical modeling.

6 Conclusion

In this work, we introduced a mathematical model to investigate glioblastoma growth at a macroscopic scale, presenting a structure that incorporates a calibration criterion based on fractional derivatives. The findings highlighted the importance of incorporating fractional derivatives in refining mathematical models to better capture real-life observations. The analyses strongly revealed the dominance of the proliferation phenomenon in the proposed growth model, suggesting its robustness as a tool for tracking glioblastoma mass formation and predicting the timing of tumor visibility on MRI during recurrence follow-up. Estimates of tumor visibility timing, conducted with consideration for three distinct derivative orders, pointed towards a more controlled approach with small fractional derivative orders. The obtained findings regarding tumor visibility

timing exhibited consonance with the empirical observations, reinforcing the validity of our methodology. The analyses of the relationship between patient survival and tumor growth speed, utilizing the growth model developed in this research, further substantiated the well-established, yet inexplicable, variations in inter-patient variability for glioblastoma cases.

Declarations

Use of AI tools

The authors declare that they have not used Artificial Intelligence (AI) tools in the creation of this article.

Data availability statement

All data generated or analyzed during this study are included in this article.

Ethical approval

Not applicable

Consent for publication

Not applicable

Conflicts of interest

The authors declare that they have no conflict of interest.

Funding

Not applicable

Author's contributions

N.K.: Conceptualization, Methodology, Investigation, Visualization, Writing-Original draft preparation, Software, Validation, Writing-Reviewing and Editing. N.Ö.: Supervision. All authors have read and agreed to the submitted version of the manuscript.

Acknowledgements

References

[1] Yabo, Y.A., Niclou, S.P. and Golebiewska, A. Cancer cell heterogeneity and plasticity: a paradigm shift in glioblastoma. *Neuro-Oncology*, 24(5), 669-682, (2022). [CrossRef]

[2] Louis, D.N., Perry, A., Wesseling, P., Brat, D.J., Cree, I.A., Figarella-Branger, D. et al. The 2021 WHO classification of tumors of the central nervous system: a summary. *Neuro-Oncology*, 23(8), 1231-1251, (2021). [CrossRef]

[3] Carlsson, S.K., Brothers, S.P. and Wahlestedt, C. Emerging treatment strategies for glioblastoma multiforme. *EMBO Molecular Medicine*, 6(11), 1359-1370, (2014). [CrossRef]

[4] Kelley, P.J. and Hunt, C. The limited value of cytoreductive surgery in elderly patients with malignant gliomas. *Neurosurgery*, 34(1), 62-67, (1994).

[5] Piroth, M.D., Pinkawa, M., Holy, R., Klotz, J., Schaar, S., Stoffels, G. et al. Integrated boost IMRT with FET-PET-adapted local dose escalation in glioblastomas. *Strahlentherapie und Onkologie*, 188(4), 334-339, (2012). [CrossRef]

[6] Silbergeld, D.L. and Chicoine, M.R. Isolation and characterization of human malignant glioma cells from histologically normal brain. *Journal of Neurosurgery*, 86(3), 525-531, (1997). [CrossRef]

[7] Harpold, H.L.P., Alvord Jr, E.C. and Swanson, K.R. The evolution of mathematical modeling of glioma proliferation and invasion. *Journal of Neuropathology & Experimental Neurology*, 66(1), 1-9, (2007). [CrossRef]

[8] Pandya, N.M., Dhalla, N.S. and Santani, D.D. Angiogenesis-a new target for future therapy. *Vascular Pharmacology*, 44(5), 265-274, (2006). [CrossRef]

[9] Das, S. *Functional Fractional Calculus for System Identification and Controls*. Springer: New York, (2008). [CrossRef]

[10] Curtin, L., Whitmire, P., White, H., Bond, K.M., Mrugala, M.M., Hu, L.S. et al. Shape matters: morphological metrics of glioblastoma imaging abnormalities as biomarkers of prognosis. *Scientific Reports*, 11(1), 23202, (2021). [CrossRef]

[11] Konukoglu, E., Clatz, O., Bondiau, P.Y., Delingette, H. and Ayache, N. Extrapolating glioma invasion margin in brain magnetic resonance images: suggesting new irradiation margins. *Medical Image Analysis*, 14(2), 111-125, (2010). [CrossRef]

[12] Burgess, P.K., Kulesa, P.M., Murray, J.D. and Alvord Jr., E.C. The interaction of growth rates and diffusion coefficients in a three-dimensional mathematical model of gliomas. *Journal of Neuropathology & Experimental Neurology*, 56(6), 704-713, (1997). [CrossRef]

[13] Jacobs, J., Rockne, R.C., Hawkins-Daarud, A.J., Jackson, P.R., Johnston, S.K., Kinahan, P. et al. Improved model prediction of glioma growth utilizing tissue-specific boundary effects. *Mathematical Biosciences*, 312, 59-66, (2019). [CrossRef]

[14] Jbabdi, S., Mandonnet, E., Duffau, H., Capelle, L., Swanson, K.R., Pelegrini-Issac, M. et al. Simulation of anisotropic growth of low-grade gliomas using diffusion tensor imaging. *Magnetic Resonance in Medicine*, 54(3), 616-624, (2005). [CrossRef]

[15] Konukoglu, E., Clatz, O., Menze, B.H., Stieltjes, B., Weber, M.A., Mandonnet, E. et al. Image guided personalization of reaction-diffusion type tumor growth models using modified anisotropic eikonal equations. *IEEE Transactions on Medical Imaging*, 29(1), 77-95, (2010). [CrossRef]

[16] Le, M., Delingette, H., Kalpathy-Cramer, J., Gerstner, E.R., Batchelor, T., Unkelbach, J. et al. MRI based Bayesian personalization of a tumor growth model. *IEEE Transactions on Medical Imaging*, 35(10), 2329-2339, (2016). [CrossRef]

[17] Lipkova, J., Angelikopoulos, P., Wu, S., Alberts, E., Wiestler, B., Diehl, C. et al. Personalized radiotherapy design for glioblastoma: integrating mathematical tumor models, multimodal scans, and Bayesian inference. *IEEE Transactions on Medical Imaging*, 38(8), 1875-1884, (2019). [CrossRef]

[18] Rockne, R., Alvord Jr, E.C., Reed, P.J. and Swanson, K.R. Modeling the growth and invasion of gliomas, from simple to complex: the goldie locks paradigm. *Biophysical Reviews and Letters*, 03(01n02), 111-123, (2008). [CrossRef]

[19] Rockne, R., Alvord Jr, E.C., Rockhill, J.K. and Swanson, K.R. A mathematical model for brain tumor response to radiation therapy. *Journal of Mathematical Biology*, 58, 561-578, (2009).

[CrossRef]

[20] Rockne, R., Rockhill, J.K., Mrugala, M., Spence, A.M., Kalet, I., Hendrickson, K. et al. Predicting the efficacy of radiotherapy in individual glioblastoma patients in vivo: a mathematical modeling approach. *Physics in Medicine and Biology*, 55(12), 3271-3285, (2010). [CrossRef]

[21] Swanson, K.R, Alvord Jr, E.C. and Murray, J.D. A quantitative model for differential motility of gliomas in grey and white matter. *Cell Proliferation*, 33(5), 317-329, (2000). [CrossRef]

[22] Swanson, K.R., Bridge, C., Murray, J.D. and Alvord Jr, E.C. Virtual and real brain tumors: using mathematical modeling to quantify glioma growth and invasion. *Journal of the Neurological Sciences*, 216(1), 1-10, (2003). [CrossRef]

[23] Tracqui, P., Cruywagen, G.C., Woodward, D.E., Bartoo, G.T., Murray, J.D. and Alvord Jr, E.C. A mathematical model of glioma growth: the effect of chemotherapy on spatio-temporal growth. *Cell Proliferation*, 28(1), 17-31, (1995). [CrossRef]

[24] Woodward, D.E., Cook, J., Tracqui, P., Cruywagen, G.C., Murray, J.D. and Alvord Jr, E.C. A mathematical model of glioma growth: the effect of extent of surgical resection. *Cell Proliferation*, 29(6), 269-288, (1996). [CrossRef]

[25] Ucar, E., Ozdemir, N. and Altun, E. Fractional order model of immune cells influenced by cancer cells. *Mathematical Modelling of Natural Phenomena*, 14(3), 308, (2019). [CrossRef]

[26] Ozdemir, N., Ucar, S. and Eroglu, B.B.I. Dynamical analysis of fractional order model for computer virus propagation with kill signals. *International Journal of Nonlinear Sciences and Numerical Simulation*, 21(3-4), 239-247, (2020). [CrossRef]

[27] Ozkose, F., Yilmaz, S., Yavuz, M., Ozturk, I., Senel, M.T., Bagci, B.S. et al. A fractional modeling of tumor–immune system interaction related to Lung cancer with real data. *The European Physical Journal Plus*, 137, 1-28, (2022). [CrossRef]

[28] Rahman, M., Arfan, M. and Baleanu, D. Piecewise fractional analysis of the migration effect in plant-pathogen-herbivore interactions. *Bulletin of Biomathematics*, 1(1), 1-23, (2023). [CrossRef]

[29] Mustapha, U.T., Ado, A., Yusuf, A., Qureshi, S. and Musa, S.S. Mathematical dynamics for HIV infections with public awareness and viral load detectability. *Mathematical Modelling and Numerical Simulation with Applications*, 3(3), 256-280, (2023). [CrossRef]

[30] Kawarada, H. On solutions of Initial-Boundary Problem for $u_t = u_{xx} + 1/(1-u)$. *Publications of the Research Institute for Mathematical Sciences*, 10(3), 729-736, (1975). [CrossRef]

[31] Acker, A. and Walter, W. On the global existence of solutions of parabolic differential equations with a singular nonlinear term. *Nonlinear Analysis, Theory, Methods and Applications*, 2(4), 499-504, (1978). [CrossRef]

[32] Ke, L. and Ning, S. Quenching for degenerate parabolic equations. *Nonlinear Analysis*, 34, 1123-1135, (1998).

[33] Levine, H.A. and Montgomery, J.T. The quenching of solutions of some nonlinear parabolic equations. *SIAM Journal on Mathematical Analysis*, 11(5), 842-847, (1980). [CrossRef]

[34] Levine, H.A. Levine, The phenomenon of quenching: a survey Trends in the theory and practice of nonlinear analysis. In Proceedings, *Sixth International Conference on Document Analysis and Recognition* (Vol. 110) pp. 275-286, North-Holland, Amsterdam, (1985).

[35] Levine, H.A. Quenching, nonquenching, and beyond quenching for solution of some parabolic equations. *Annali di Matematica Pura ed Applicata*, 155, 243–260, (1989). [CrossRef]

[36] Deng, K. and Levine, H.A. On the blow up of u_t at quenching. In Proceedings *American*

Mathematical Society, pp. 1049-1056, 106(4), (1989, August).

[37] Guo, J.S. On the quenching behavior of the solution of a semilinear parabolic equation. *Journal of Mathematical Analysis and Applications*, 151, 58-79, (1990).

[38] de Pablo, A., Quiros, F. and Rossi, J.D. Nonsimultaneous quenching. *Applied Mathematics Letters*, 15(3), 265-269, (2002). [CrossRef]

[39] Ji, R., Zhou, S. and Zheng, S. Quenching behavior of solutions in coupled heat equations with singular multi-nonlinearities. *Applied Mathematics and Computation*, 223, 401-410, (2013). [CrossRef]

[40] Jia, Z., Yang, Z. and Wang, C. Non-simultaneous quenching in a semilinear parabolic system with multi-singular reaction terms. *Electronic Journal of Differential Equations*, 2019(100), 1-13, (2019).

[41] Mu, C., Zhou, S. and Liu, D. Quenching for a reaction-diffusion system with logarithmic singularity. *Nonlinear Analysis: Theory, Methods & Applications*, 71(11), 5599-5605, (2009). [CrossRef]

[42] Zheng, S. and Wang, W. Non-simultaneous versus simultaneous quenching in a coupled nonlinear parabolic system. *Nonlinear Analysis: Theory, Methods & Applications*, 69(7), 2274-2285, (2008). [CrossRef]

[43] Xu, Y. and Zheng, Z. Quenching phenomenon of a time-fractional diffusion equation with singular source term. *Mathematical Methods in the Applied Sciences*, 40(16), 5750-5759, (2017). [CrossRef]

[44] Xu, Y. and Wang, Z. Quenching phenomenon of a time-fractional Kawarada equation. *Journal of Computational and Nonlinear Dynamics*, 13(10), 101010, (2018). [CrossRef]

[45] Kilbas, A.A., Srivastava, H.M. and Trujillo, J.J. *Theory and Applications of Fractional Differential Equations* (Vol. 204). Elsevier: Amsterdam, (2006).

[46] Oldham, K.B. and Spariier, J. *The Fractional Calculus*. Academic Press, New York-London, (1974).

[47] Podlubny, I. *Fractional Differential Equations*. Academic Press: San Diego, (1999).

[48] Samko, S.G., Kilbas, A.A. and Marichev, O.I. *Fractional Integrals and Derivatives: Theory and Applications*. Gordon and Breach Science Publishers, Switzerland, (1993).

[49] Du, M., Wang, Z. and Hu, H. Measuring memory with the order of fractional derivative. *Scientific Reports*, 3, 3431, (2013). [CrossRef]

[50] Caputo, M. *Elasticità e Dissipazione*. Bologna: Zanichelli, (1969).

[51] Caputo, M. and Mainardi, F. A new dissipation model based on memory mechanism. *Pure and Applied Geophysics*, 91, 134-147, (1971).

[52] Yang, W., Warrington, N.M., Taylor, S.J., Whitmire, P., Carrasco, E., Singleton, K.W. et al. Sex differences in GBM revealed by analysis of patient imaging, transcriptome, and survival data. *Science Translational Medicine*, 11(473), eaao5253, (2019). [CrossRef]

[53] Bi, J., Khan, A., Tang, J., Armando, A.M., Wu, S., Zhang, W. et al. Targeting glioblastoma signaling and metabolism with a re-purposed brain-penetrant drug. *Cell Report*, 37, 109957, (2021). [CrossRef]

[54] Skaga, E., Kulesskiy, E., Fayzullin, A., Sandberg, C.J., Potdar, S., Kyttälä, A. et al. Intertumoral heterogeneity in patient-specific drug sensitivities in treatment-naïve glioblastoma. *BMC Cancer*, 19, 628, (2019). [CrossRef]

Mathematical Modelling and Numerical Simulation with Applications (MMNSA)
(https://dergipark.org.tr/en/pub/mmnsa)

RESEARCH PAPER

Free convection at different locations of adiabatic elliptic blockage in a square enclosure

Sayeda Sadia Billah [1,‡], **Muhammad Sajjad Hossain** [1,*,‡], **Md. Fayz-Al-Asad** [2,3,‡], **Muhammad Saiful Islam Mallik** [1,‡], **Sreebash Chandra Paul** [1,‡], **Md. Jahirul Haque Munshi** [4,‡] **and Md. Manirul Alam Sarker** [3,‡]

[1]Department of Arts and Sciences, Ahsanullah University of Science and Technology (AUST), Dhaka-1208, Bangladesh, [2]Department of Mathematics, American International University – Bangladesh, Kuratoli, Khilkhet, Dhaka-1229, Bangladesh, [3]Department of Mathematics, Bangladesh University of Engineering and Technology, Dhaka-1000, Bangladesh, [4]Department of Mathematics, Hamdard University Bangladesh (HUB), Hamdard Nagar, Gazaria, Munshigonj-1510, Bangladesh

*Corresponding Author
‡ sayedasadiabillahs@gmail.com (S.S. Billah); msh80edu@gmail.com (M.S. Hossain); fayzmath.buet@gmail.com (M.F.A. Asad); saiful_math.as@aust.edu (M.S.I. Mallik); sreebash.as@aust.edu (S.C. Paul); jahir.buet.bd@gmail.com (M.J.H. Munshi); masarker45@gmail.com (M.M.A. Sarker)

Abstract

The numerical simulation of free convection flow within a square-shaped enclosure for various orientations of elliptic blockage (EB) is performed in the present study. The bottom wall of the cavity remains uniformly heated, where the left and right (side) walls as well as the boundary wall of the elliptic blockage are insulated and the top wall remains at a cool temperature. As Pr remains constant, the effects of different values of Ra have a great influence on overall fluid flow and temperature gradient for three different locations: bottom elliptic blockage (BEB), center elliptic blockage (CEB) and top elliptic blockage (TEB), as a mass flow circulation has been identified, and a state of equilibrium has been established within the fluid flow simulations along with the isotherm contours. The outcomes of the numerical analysis are presented with the streamlines, isotherms, and variations of the average Nusselt number.

Keywords: Free convection; square cavity; elliptic blockage; streamlines; isotherms; heat transfer rates
AMS 2020 Classification: 76A05; 76D05; 76D07; 76N10

1 Introduction

Over the last decade, free convection in a square cavity has grown in popularity as a research topic. The widespread use of such flows in industrial and natural contexts contributes to their popularity.

The cavity flow with a block inside is considered a benchmark problem in computational fluid dynamics (CFD) and experimental fluid dynamics research. It helps in understanding complex flow behaviors, such as vortex shedding, recirculation zones, and boundary layer development. Also, it helps us understand the flow patterns around obstacles in aerodynamic flow. Aerodynamic performance can be improved and design optimization can be aided by understanding the flow behavior around buildings, aircraft wings, and other structures through the cavity flow with a block inside.

Studies on heat transport can also benefit from this issue. By analyzing the flow and temperature fields within the cavity, researchers can understand heat transfer mechanisms, which are useful in the design of cooling systems, electronic devices, and thermal management solutions. Cavity flows with barriers are useful for research in industries involving fluid mixing, such as chemical engineering and pharmaceuticals. Product quality is enhanced and mixing procedures are optimized by having a better understanding of how fluids interact and mix inside the cavity. Additionally, it can shed light on these kinds of limited flow phenomena. Cavity flow with an internal block is a useful instrument for studying fluid dynamics that may be applied in many different industrial and engineering fields. When designing chemical reactors, food processing machinery, and filtration systems, among other industrial processes, cavity flows with blocks inside can be analyzed to help maximize efficiency. The study of cavity flow may also be beneficial for cardiovascular disorders and the improvement of medical devices such as stents and prosthetic heart valves. It is used in the environmental field to estimate erosion patterns and sediment transformation, among other things. That´s why, recent attention has been drawn to the phenomenon of natural convection in fluid flow within a square cavity containing elliptical blockages oriented in various ways. This intriguing phenomenon has also emerged as a pivotal subject in diverse thermal engineering applications, such as reactor insulation, fire prevention, safeguarding electronic equipment, controlling the dispersion of chemical pollutants in water-saturated oil, and optimizing the solidification process in casting. In industrial practice, square cavities, along with other geometric shapes like triangles and cylinders, are commonly employed.

Saury et al. [1] studied free convection in the cavity, where the suppositions allow for the calculation of Rayleigh number values leading to 1.2×10^{11} at $(T = 20^0C)$. Sajjadi et al. [2] examined turbulent flow in a square cavity, where the streamlines, the isotherm counters, and the local and the average Nusselt number all show the impact of an increase in the Rayleigh number. Shati et al. [3] studied radiation and turbulent fluid flow in square & rectangular cavity, which provides an equation for the mean Nusselt number with no radiation as a function of Prandtl Grashof and numbers. Estebe et al.[4] provided the validation of turbulent fluid flow in a square cavity and a 3D simulation's findings were presented together with an estimation of the cooling system's performance. Choi et al. [5] performed the simulation of turbulent free convection in rectangular cavities and the relative effectiveness of turbulence models is investigated, and both their advantages and disadvantages are discussed. Jani et al. [6] analyzed the impact of MHD in a square cavity and found that the strength of the magnetic field and the Rayleigh number play a great role in the overall simulation. The natural convection of differentially heated enclosures was studied by Butler et al. [7]. The contact between the cylinder and cavity results in an increase in cylinder heat transfer. Xin et al. [8] studied turbulent natural convection in partially heated cavities and showed that the thin stratification is caused by surface radiation. Carvalho et al. [9] studied turbulent free convection in a porous square cavity and discovered that the Nusselt number decreases when the material porosity is raised. Kefayati et al. [10] performed Lattice Boltzmann's exploration of free convection, where the findings showed that at large Rayleigh

numbers, the magnetic field enhances the action of nanoparticles.

Bahoosh et al. [11] numerically examined the fluid flow in a square cavity, where the rotational direction was either inside or outside, and the tilting angles were either 3 or 5 degrees. Jani et al. [12] surveyed free convection in the square cavity and demonstrated that for large Rayleigh numbers, positioning a hot fin in the center of the lower wall has a more notable impact on the flow region and heat transfer within the cavity. Asad et al. [13] examined the effects of twice stratification and various fluid characteristics on the chemically acting upper-convected Maxwell fluid. Islam et al. [14] studied the influence of MHD on the unsteady flow for $Fe_3O_4 - H_2O$ and $TiO_2 - H_2O$ based nanofluids within a square cavity. After comparing, they found a notable difference between their heat transport rates. Asad et al. [15] numerically examined the effect of magneto-combined convection heat transmission of fin length in the lid-driven curvy enclosure. Sajjadi et al. [16] performed a simulation of turbulent free convection utilizing the Lattice Boltzmann method, where heat transfer decreased as the Rayleigh number changed. Miroshnichenko et al. [17] looked into a comparative study of standard $\kappa - \epsilon$ and $\kappa - \omega$ turbulence models and found that the usual model performed better. Tabet et al. [18] investigated convection in a partially heated square cavity, where the outlines of temperature and the evolution of the Nusselt number were provided for several Rayleigh numbers. Zhao et al. [19] scrutinized the field flow of convection and the findings demonstrated the ability of the current method to exactly model the convection difficulties associated with unstable natural processes and are all in strong agreement with individuals found in the literature. Aithal et al. [20] examined turbulent flow in a square cavity and achieved that the Rayleigh number increased and the average and peak Nusselt numbers almost doubled. Massinissa et al. [21] studied the characteristics of different Prandtl numbers, where the increase of Prandtl and Rayleigh numbers had turned the flow field slightly more prominent.

Benchabi et al. [22] analyzed 2D simulation of natural convection in a square cavity and obtained the influence of Rayleigh number caused by a change in size or a difference in temperature on the thermal and dynamic behavior as well as the intensity of the flow caused by the buoyant force. Solomon et al. [23] studied the effect of the aspect ratio of a square cavity on fluid flow and discovered that the Nusselt number and heat transfer coefficient were notably impacted by the enclosure's AR. Yang et al. [24] provided Rans modelling for temperature modification in couple heat transfer and showed that it can accurately predict the distribution of temperature change within the fluid and solid regions. Razera et al. [25] examined the conserving of semi-elliptical blocks constructed into a rectangular enclosure. The results revealed considerable improvements in the heat transmission and fluid flow performances of roughly 76% and 125%, respectively. Selimefendigil et al. [26] investigated heat transmission and fluid flow in the presence of an elliptically-shaped porous item and found that the mean heat transport rate declines with the optimal value of Nu. Khatamifar et al. [27] studied momentary couple free convection heat transport. They found the thermal conductivity ratio effect around the range of $0.1 - 10$, but as the partition changes, the effect turns out to be insignificant as the thermal conductivity ratio is very significant. Devi et al. [28] examined the effects of exterior MHD on non-Newtonian fluid in a square cavity. Results exposed that the buoyant force rises as the temperature gradient increases. Wen et al. [29] investigated to better understand how major temperature fluctuations affect the unstable fluid flow and found that the hot wall region exhibits a boundary layer instability with high-frequency undulations in addition to the top corner impact instability. Goswami et al. [30] calculated free convection in a square cavity and found that the mean Nusselt number grows at $Ra = 10^4$. Hattab et al. [31] studied turbulent natural convection in a square cavity and found that the heat transport was increased with the increase of the volume percentage. Turkyilmazoglu

[32] studied nonuniform heating in free convection and found the best heat deletion rate close to the top wall of a cavity. Bilal et al [33] studied the power law fluid in a square cavity and found that heat conduction rises as the Rayleigh number increases, driven by the generation of temperature variations within the fluid domain. Sondur et al. [34] performed a benchmark simulation on fluid flow inside a square cavity and they showed that the most accurate results were found for the steady flow solver *Open FOAM* which took a comparatively short time. Asad et al. [35, 36] explored the natural convection and heat transmit performance on a curvy enclosure. They detected that the mean Nusselt number expands with expanding undulations number. The study conducted by Hossain et al. [37] examined the impact of a cylinder arranged the phenomenon of free convection contained by a square enclosure. The rectangular bar source of heat in a blocked area for free convection flow over a triangular enclosure was examined by Asad et al. [38]. Furthermore, more information is provided in [39–42] on free convection, the finite element (FE) method, and the properties of heat transport with different geometries.

As per the extensive research works conducted by various scientists, it seems that there is a notable absence of exploration regarding the analysis of free convection flow within a square enclosure concerning the various orientations of elliptic blockage. The lack of research in this area concerns important data related to the characteristics of heat transport, which is crucial for understanding its significance in various industries. The flow patterns within the field have been illuminated by the streamlines, while the thermal distribution has been outlined by the isotherms and the average Nusselt number. For the numerical study, the fluid flow within the cavity is characterized by the Prandtl number, $Pr = 0.71$, and Rayleigh number, $Ra = 10^3 - 10^7$.

2 Problem specification

The physical model under consideration along with important geometrical details is displayed in Figure 1. The bottom part of the system is subjected to the uniformly heated temperature (T_h), the left and the right walls are thermally insulated (T_i) and the top wall remains at cold temperature (T_c). An elliptic blockage (EB) is placed in different orientations of that cavity whose bottom wall is kept as thermally insulated (T_i). The fluid's Prandtl number $(Pr = 0.7)$, Newtonian properties and laminar fluid movement were all thought to be present. It has been assumed that the fluid's properties are constant.
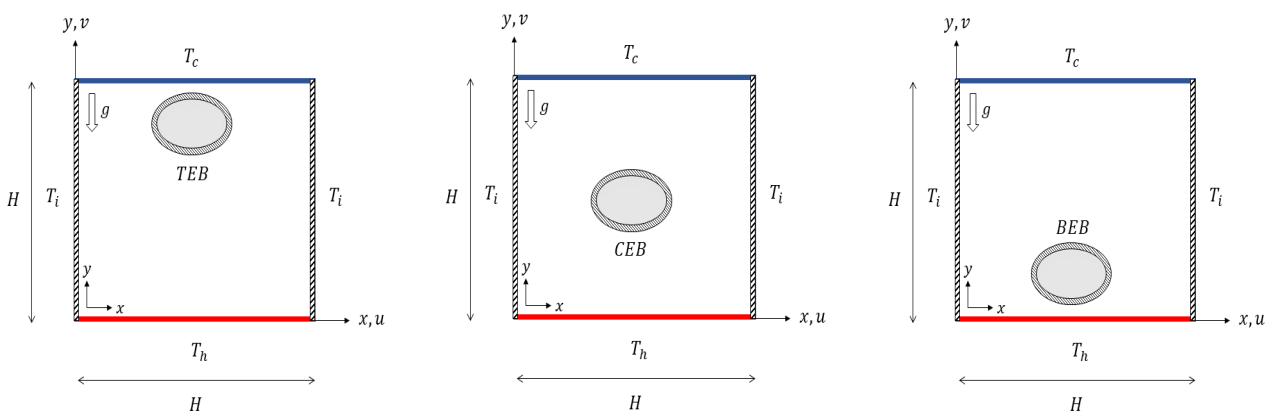

Figure 1. Schematic diagram of physical system

3 Governing equations

The governing equations for the two-dimensional steady flow following the invocation of the equations that govern the steady two-dimensional flow, considering the Boussinesq approximation and neglecting radiation and viscous dissipation, can be formulated in the following manner [6, 33, 39–42]:

Continuity equation:

$$\frac{\partial u}{\partial x} + \frac{\partial v}{\partial y} = 0. \tag{1}$$

Momentum equations:

$$u\frac{\partial u}{\partial x} + v\frac{\partial u}{\partial y} = -\frac{1}{\rho}\frac{\partial p}{\partial x} + \nu\left(\frac{\partial^2 u}{\partial x^2} + \frac{\partial^2 u}{\partial y^2}\right), \tag{2}$$

$$u\frac{\partial v}{\partial x} + v\frac{\partial v}{\partial y} = -\frac{1}{\rho}\frac{\partial p}{\partial y} + \nu\left(\frac{\partial^2 v}{\partial x^2} + \frac{\partial^2 v}{\partial y^2}\right) + \rho g\beta(T - T_c). \tag{3}$$

Energy equation:

$$u\frac{\partial T}{\partial x} + v\frac{\partial T}{\partial y} = \frac{k}{\rho c_p}\left(\frac{\partial^2 T}{\partial x^2} + \frac{\partial^2 T}{\partial y^2}\right). \tag{4}$$

Boundary conditions for governing equations

The followings are the boundary conditions for the current problem:

At the left and right vertical wall:

$$u(0,y) = 0, \ v(0,y) = 0, \ \frac{\partial T}{\partial n} = 0.$$

At the bottom wall:

$$u(x,0) = 0, \ v(x,0) = 0, \ T = T_h.$$

At the top wall:

$$u(x,y) = 0, \ v(x,y) = 0, \ T = T_c.$$

At the insider elliptic blockage:

$$u(x,y) = 0, \ v(x,y) = 0, \ \frac{\partial T}{\partial n} = 0.$$

Non-dimensional variables

Non-dimensional variables (5) are used for making the governing Eqs. (1)-(4) into dimensionless form are stated as follows:

$$X = \frac{x}{H}, \ Y = \frac{y}{H}, \ U = \frac{uH}{\alpha}, \ P = \frac{pH^2}{\rho\alpha^2}, \ \theta = \frac{T - T_c}{T_h - T_c}, \ Pr = \frac{\nu}{\alpha}, \ Ra = \frac{g\beta(T_h - T_c)H^3}{\alpha\nu}. \quad (5)$$

Non-dimensional governing equations

By using the aforementioned variables, the dimensionless form of the Eqs. (1)-(4) are as follows:
Continuity equation:

$$\frac{\partial U}{\partial X} + \frac{\partial V}{\partial Y} = 0. \quad (6)$$

Momentum equations:

$$U\frac{\partial U}{\partial X} + V\frac{\partial U}{\partial Y} = -\frac{\partial P}{\partial X} + Pr\left(\frac{\partial^2 U}{\partial X^2} + \frac{\partial^2 U}{\partial Y^2}\right), \quad (7)$$

$$U\frac{\partial V}{\partial X} + V\frac{\partial V}{\partial Y} = -\frac{\partial P}{\partial Y} + Pr\left(\frac{\partial^2 V}{\partial X^2} + \frac{\partial^2 V}{\partial Y^2}\right) + RaPr\theta. \quad (8)$$

Energy equation:

$$U\frac{\partial \theta}{\partial X} + V\frac{\partial \theta}{\partial Y} = \left(\frac{\partial^2 \theta}{\partial X^2} + \frac{\partial^2 \theta}{\partial Y^2}\right). \quad (9)$$

The heat transfer coefficient which is the local Nusselt number and mean Nusselt number is defined by

$$Nu_{local} = -\frac{\partial \theta}{\partial n} \text{ and } Nu_{av} = \int_0^1 Nu_{local}dx, \quad (10)$$

respectively, where the normal orientation of a plane is indicated by n.

Boundary conditions for non-dimensional governing equations

The dimensionless boundary conditions which are considered can be expressed as:
At the left and right vertical wall:

$$U = 0, \ V = 0, \ \frac{\partial \theta}{\partial n} = 0.$$

At the bottom wall:

$$U = 0, \ V = 0, \ \theta = 1 \text{ (Uniformly heated)}.$$

At the top wall:

$$U = 0, \ V = 0, \ \theta = 0.$$

At the insider elliptic blockage:

$$U = 0, \quad V = 0, \quad \frac{\partial \theta}{\partial n} = 0.$$

4 Method of solution

For solving governing Eqs. (7)-(9), the Galerkin finite element method [43, 44] has been utilized. Eq. (6) is employed as a constraint owing to the conservation of mass. This constraint may be utilized to earn pressure distribution [43, 44]. Regarding the resolution of Eqs. (7)-(9), Eq. (6) is being influenced by the introduction of a penalty parameter, denoted as γ, while the pressure P is being replaced with the subsequent expression [43], which is as follows:

$$P = -\gamma \left(\frac{\partial U}{\partial X} + \frac{\partial V}{\partial Y} \right). \tag{11}$$

Value of $\gamma = 10^7$ perfectly fulfills Eq. (7). Eq. (11) is employed to simplify the expressions in Eqs. (8)-(9), as follows:

$$U\frac{\partial U}{\partial X} + V\frac{\partial U}{\partial Y} = \gamma\frac{\partial}{\partial X}\left(\frac{\partial U}{\partial X} + \frac{\partial V}{\partial Y}\right) + Pr\left(\frac{\partial^2 U}{\partial X^2} + \frac{\partial^2 U}{\partial Y^2}\right), \tag{12}$$

$$U\frac{\partial V}{\partial X} + V\frac{\partial V}{\partial Y} = \gamma\frac{\partial}{\partial Y}\left(\frac{\partial U}{\partial X} + \frac{\partial V}{\partial Y}\right) + Pr\left(\frac{\partial^2 V}{\partial X^2} + \frac{\partial^2 V}{\partial Y^2}\right) + RaPr\theta. \tag{13}$$

Value of U, V and θ are expanded as:

$$U \approx \sum_{k=1}^{N} U_k \Phi_k(X, Y), V \approx \sum_{k=1}^{N} V_k \Phi_k(X, Y), \theta \approx \sum_{k=1}^{N} \theta_k \Phi_k(X, Y). \tag{14}$$

By using the fact that $X \geq 0$ and $Y \leq 0$, the following equations are formed in the domain Ω,

$$\begin{aligned}
R_1^{(1)} = \ & \sum_{k=1}^{N} U_k \int_\Omega \left[\left(\sum_{k=1}^{N} U_k \Phi_k \right) \frac{\partial \Phi_k}{\partial X} + \left(\sum_{k=1}^{N} U_k \Phi_k \right) \frac{\partial \Phi_k}{\partial Y} \right] \Phi_i dXdY \\
& + \gamma \left[\sum_{k=1}^{N} U_k \int_\Omega \frac{\partial \Phi_i}{\partial X} \frac{\partial \Phi_k}{\partial X} dXdY + \sum_{k=1}^{N} V_k \int_\Omega \frac{\partial \Phi_i}{\partial X} \frac{\partial \Phi_k}{\partial X} dXdY \right] \\
& + Pr \sum_{k=1}^{N} U_k \int_\Omega \left[\frac{\partial \Phi_i}{\partial X} \frac{\partial \Phi_k}{\partial X} + \frac{\partial \Phi_i}{\partial Y} \frac{\partial \Phi_k}{\partial Y} \right] dXdY,
\end{aligned} \tag{15}$$

$$R_1^{(2)} = \sum_{k=1}^{N} V_k \int_{\Omega} \left[\left(\sum_{k=1}^{N} U_k \Phi_k \right) \frac{\partial \Phi_k}{\partial X} + \left(\sum_{k=1}^{N} V_k \Phi_k \right) \frac{\partial \Phi_k}{\partial Y} \right] \Phi_i dXdY$$
$$+ \gamma \left[\sum_{k=1}^{N} U_k \int_{\Omega} \frac{\partial \Phi_i}{\partial X} \frac{\partial \Phi_k}{\partial X} dXdY + \sum_{k=1}^{N} V_k \int_{\Omega} \frac{\partial \Phi_i}{\partial X} \frac{\partial \Phi_k}{\partial X} dXdY \right]$$
$$+ Pr \sum_{k=1}^{N} V_k \int_{\Omega} \left[\frac{\partial \Phi_i}{\partial X} \frac{\partial \Phi_k}{\partial X} + \frac{\partial \Phi_i}{\partial Y} \frac{\partial \Phi_k}{\partial Y} \right] dXdY$$
$$+ RaPr \int_{\omega} \left(\sum_{k=1}^{N} \theta_k \Phi_k \right) \Phi_i dXdY, \tag{16}$$

and

$$R_1^{(3)} = \sum_{k=1}^{N} U_k \int_{\Omega} \left[\left(\sum_{k=1}^{N} U_k \Phi_k \right) \frac{\partial \Phi_k}{\partial X} + \left(\sum_{k=1}^{N} V_k \Phi_k \right) \frac{\partial \Phi_k}{\partial Y} \right] \Phi_i dXdY$$
$$+ \sum_{k=1}^{N} \theta_k \int_{\Omega} \left[\frac{\partial \Phi_i}{\partial X} \frac{\partial \Phi_k}{\partial X} + \frac{\partial \Phi_i}{\partial Y} \frac{\partial \Phi_k}{\partial Y} \right] dXdY. \tag{17}$$

The expressions given by Eqs. (15)-(17) can be depicted using matrix notation as follows:

$$(K_1 + \gamma K_2)a = F, \tag{18}$$

where K_1, K_2 matrices are derived from the Jacobian of the residuals, $'a'$ signifies the unidentified vector, as $\gamma \sim 10^7$, Eq. (6) is better content, which tends to the following:

$$K_1 a = \frac{F}{\gamma}. \tag{19}$$

The Newton-Raphson method has been employed to address the non-linear Eqs. (15)-(17), yielding the subsequent linear system as follows:

$$J(a^n)[a^n - a^{n+1}] = R(a^n). \tag{20}$$

At the end of the iterative process, $\left[\sum \left(R_i^j \right)^2 \right]^{0.5} \leq 10^{-6}$ is utilized. Each of the nine-node bi-quadratic elements that we applied is approximated from $(X - Y) \to (\zeta - \eta)$, which are:

$$X = \sum_{i=1}^{9} X_i \Phi_i(\zeta - \eta) \text{ and } Y = \sum_{i=1}^{9} Y_i \Phi_i(\zeta - \eta), \tag{21}$$

on the $(\zeta - \eta)$ domain, where $\Phi_i(\zeta, \eta)$ are the local bi-quadratic basis functions. The following

assumptions can be used to analyze the domain of the integrals in Eqs. (15)-(17):

$$\begin{bmatrix} \frac{\partial \Phi_i}{\partial X} \\ \frac{\partial \Phi_i}{\partial Y} \end{bmatrix} = \frac{1}{|J|} \begin{bmatrix} \frac{\partial Y}{\partial \eta} & -\frac{\partial Y}{\partial \zeta} \\ -\frac{\partial X}{\partial \eta} & \frac{\partial X}{\partial \zeta} \end{bmatrix} \begin{bmatrix} \frac{\partial \Phi_i}{\partial \zeta} \\ \frac{\partial \Phi_i}{\partial \eta} \end{bmatrix} \text{ and } dXdY = |J|d\zeta d\eta, \tag{22}$$

where $J = \left| \frac{\partial(X,Y)}{\partial(\zeta,\eta)} \right|$. According to Eq. (10), the local Nusselt number takes a normal derivative that can be found over a bi-quadratic basis set in the $(\zeta - \eta)$ domain by using Eqs. (21) and (22).

Evaluation of stream function

The 2D stream function is formed from the velocity elements U and V, as follows:

$$U = \frac{\partial \psi}{\partial Y}, V = -\frac{\partial \psi}{\partial X}, \tag{23}$$

which can be utilized in the single equation as,

$$\frac{\partial^2 \psi}{\partial X^2} + \frac{\partial^2 \psi}{\partial Y^2} = \frac{\partial U}{\partial Y} - \frac{\partial V}{\partial X}. \tag{24}$$

The Galerkin finite element method is utilized to derive the subsequent linear resultant equations for Eq. (14). This is achieved by replacing the stream function with $\{\Phi_k\}_{k=1}^N$ as $\psi = \sum_{k=1}^N \psi_k \Phi_k(X,Y)$ from Eq. (24):

$$\begin{aligned} R_i^{(s)} &= \sum_{k=1}^N \psi_k \int_\Omega \left[\frac{\partial \Phi_i}{\partial X} \frac{\partial \Phi_k}{\partial X} + \frac{\partial \Phi_i}{\partial Y} \frac{\partial \Phi_k}{\partial Y} \right] dXdY \\ &+ \sum_{k=1}^N U_k \int_\Omega \Phi_i \frac{\partial \Phi_k}{\partial Y} dXdY - \sum_1^N V_k \int_\Omega \Phi_i \frac{\partial \Phi_k}{\partial X} dXdY. \end{aligned} \tag{25}$$

Through the utilization of $\psi = 0$, the no-slip boundary condition is imposed due to the absence of cantankerous flows.

5 Model algorithm

The initial goal of the iterative Newton-Raphson algorithm is to analyze the discrete dimensions of continuity, momentum, and energy equations in order to assess the significance of speed and temperature. It is necessary to take into account the initial values of the variables. After that matrix factorization was found clearly discussed by Rahman et al. [45] before convergence criteria. When the convergence criteria are satisfied, the numerical solutions for the variables are then obtained. A straightforward algorithm is depicted in the flow chart (see Figure 2) below.
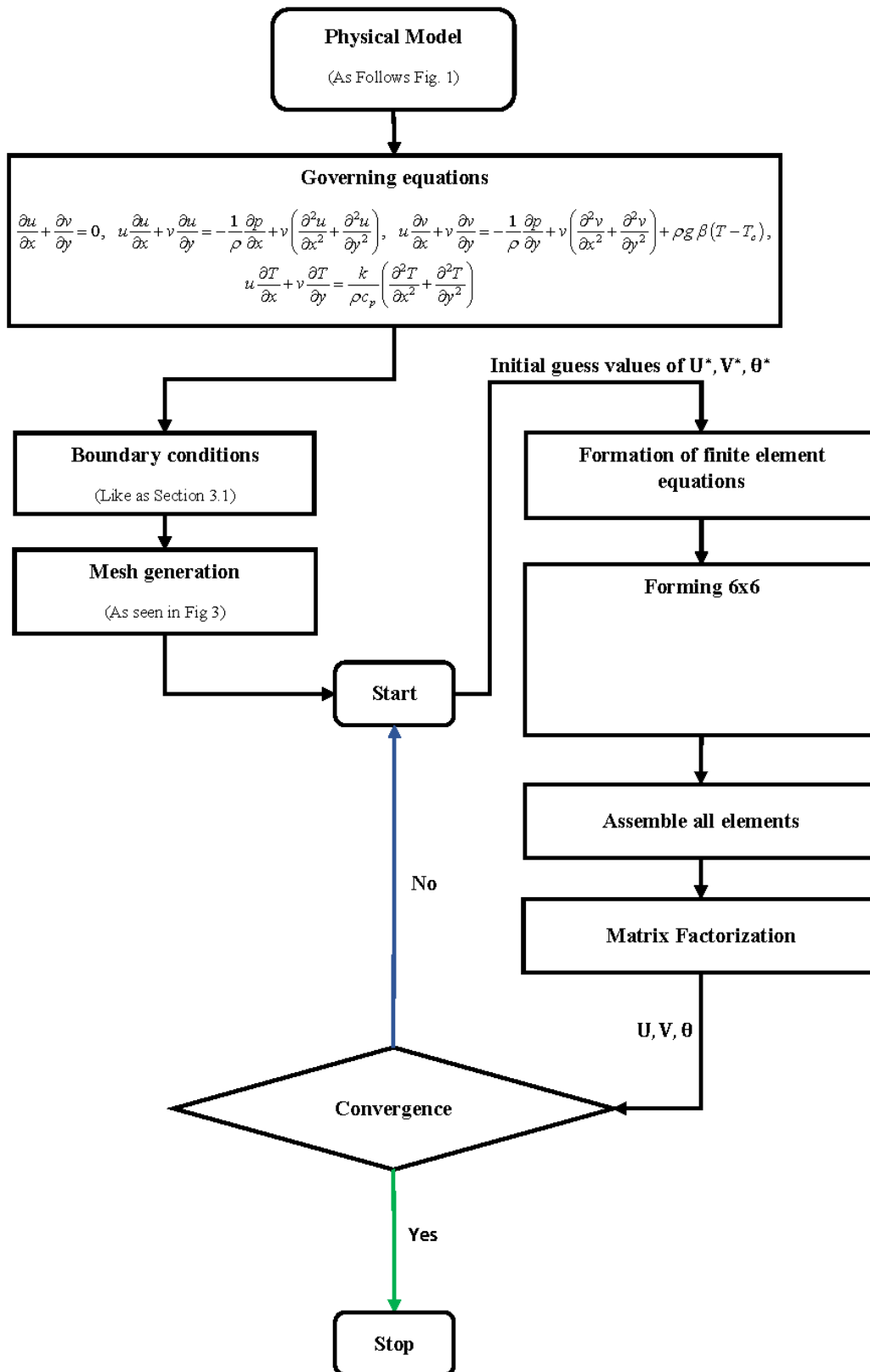
Figure 2. Flow algorithm diagram of the computational process

6 Test for grid sensitivity

Significant progress has been made in the exploration of grid-independent solutions for the field variables, yielding promising initial outcomes. A comprehensive analysis has been carried out to assess the precision of grid performance and ascertain the most suitable grid quantity. To attain grid-independent results for a square cavity with EB, a thorough investigation involving grid refinement was conducted for $Pr = 0.71$ and $Ra = 10^5$. In Figure 3, the convergence of the Nusselt number (Nu) at the heated surface is depicted as grid refinement is implemented. Grid independence has been achieved with the utilization of 31256 nodes. However, as the number of mesh elements increases beyond this point, the impact on Nu becomes negligible, rendering the changes insignificant. Therefore, any insignificance observed prior to the 31256 nodes should not be regarded as an indication of grid independence. For the grid independence tests, six distinct non-uniform grids were employed, each of them characterized by varying numbers of nodes and elements. The configurations used are as follows: 16012 nodes, 3698 elements; 18564 nodes, 3785 elements; 21343 nodes, 4134 elements; 23412 nodes, 4421 elements; 31256 nodes, 5893 elements; and 37895 nodes, 6598 elements. These details are presented in Table 1.

Table 1. Grid independence test at $Pr = 0.71$ and $Ra = 10^5$

Nodes	16012	18564	21343	23412	31256	37895
Elements	3698	3785	4134	4421	5893	6598
Nu_{av}	0.140123	0.140933	0.141894	0.144403	0.145403	0.145403
Time(s)	15.321	19.204	22.532	26.577	36.625	38.442

Based on the provided values, it is recommended to consistently utilize 31256 nodes and 5893 elements throughout the simulation to effectively locate the required accuracy and computing time. Figure 4-Figure 5 display the mesh design and finite element discretization of a domain respectively for this research work.
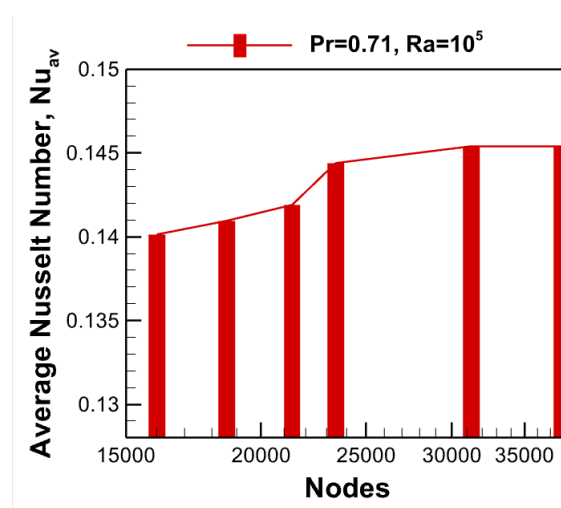

Figure 3. Convergence of Nusselt number with grid refinement for $Pr = 0.71$, and $Ra = 10^5$

7 Numerical validation

For the validation of the accuracy of the numerical technique, the problem that is considered for the present work was solved with $Pr = 0.71$, $Ha = 50$ and $Ra = 10^4$ for stream function
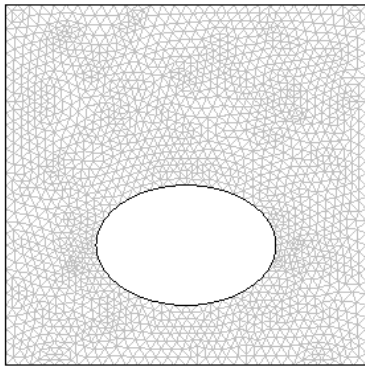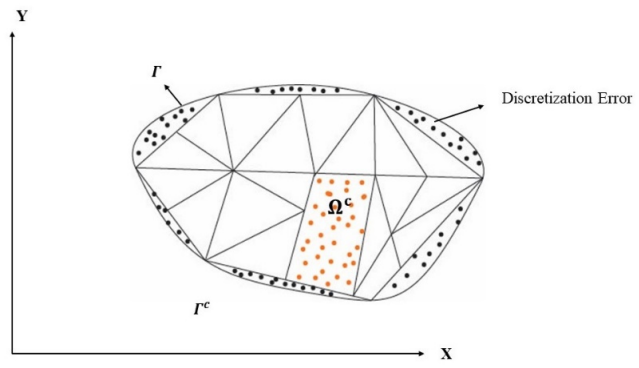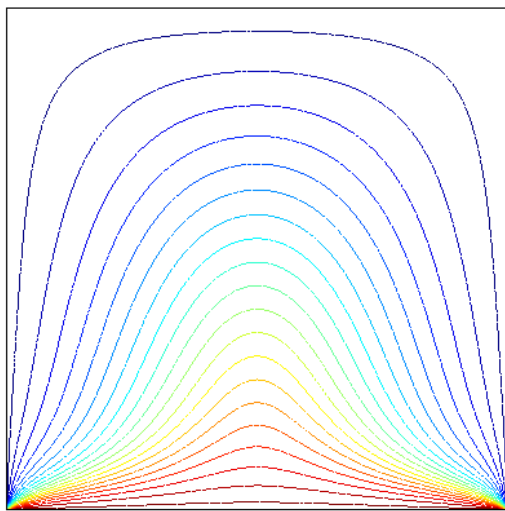
Figure 4. The mesh design

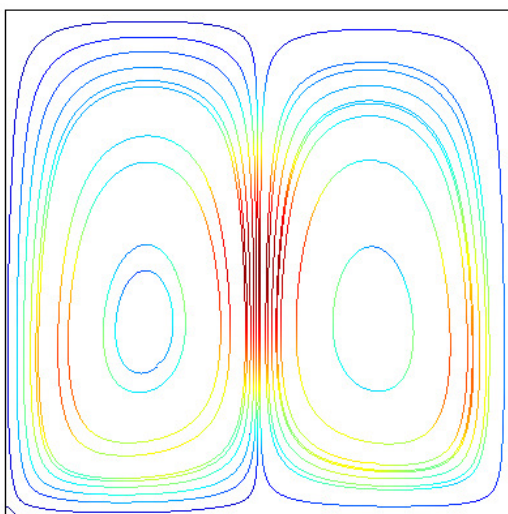**Figure 5.** Finite elements discretization of a domain

(streamlines) and isotherms within a square cavity. The result was checked by comparing it with the paper of Jani et al. [6], and found a good agreement which is shown in Figure 6.
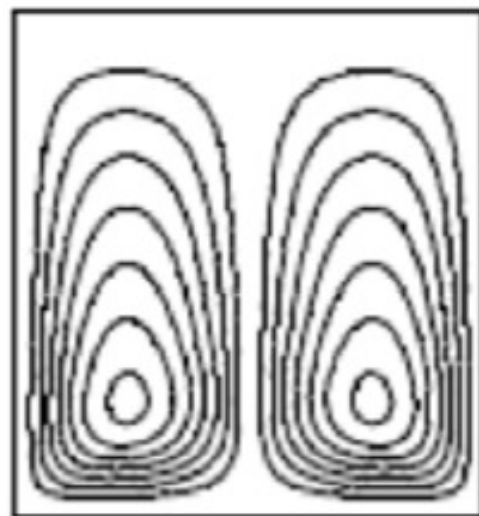

(a) Isotherms for present research work

(b) Isotherms for Jani et al. [6]

(c) Streamlines for present research work

(d) Streamlines for Jani et al. [6]

Figure 6. Stream function and isotherms of present work compared with Jani et al. [6] for $Pr = 0.71$, $Ha = 50$ and $Ra = 10^4$

8   Results and discussion

A numerical study on free convection flow within a square enclosure for various orientations of elliptic blockage (EB) has been carried out. The electrically conductive fluid with $Pr = .71$ is being examined within a square cavity in the presence of EB, where other parameters are taken as $Ra = 10^3 - 10^7$. The numerical outcomes have been depicted through visual representations of streamlines and isotherms within the square cavity along with EB, as well as through data on heat transfer rates via average Nusselt numbers.

Streamlines and isotherms: effect of Ra for different locations of EB

Streamlines and isotherms for governing parameters Pr and Ra, along with EB have been shown in Figure 7-Figure 9. The bottom wall of the cavity was uniformly heated and the bottom wall of the EB was thermally insulated. Several eddy circulation cells were circulated from the heating bottom wall due to the heated fluid flow, spinning along the insulated side walls for all governing parameters Pr and Ra. In order to discover the changes in streamlines and isotherms, a numerical simulation was completed at the bottom wall of the cavity with the elliptic blockage (BEB), at the center of the cavity with the elliptic blockage (CEB), and at the top wall of the cavity with the elliptic blockage (TEB) with $Pr = 0.71$ and $Ra = 10^3 - 10^7$. At the BEB phase, the EB is placed near the bottom wall of the cavity for $Ra = 10^3 - 10^7$ (see Figure 7a). It is seen from the streamlines that two large eddy circulation cells have been formed at the top of the EB and two vortices have been found at the bottom wall where the left one is significantly smaller than the right one and the right one has a few small vortices inside it. As Ra is considered $Ra = 10^4$, any notable changes have not been found in the streamlines (see Figure 7b). But when $Ra = 10^5$ is applied, the top two cells become much dense than before and the right bottom big vortex decreases in size as well as the number of embedded vortices decreases to one same vortex (see Figure 7c). At $Ra = 10^6$, in Figure 7d, the top two cells become much thicker than before where the left cell becomes dense than the right one and also the bottom two vortices are now almost in the same shape and several small vortices have been formed inside them but the right vortex seems thicker than the left one. At 10^7 (Figure 7e), the top two rotating cells seem to decreasing in thickness and the left bottom vortex is now in small size without any embedded vortices and the right bottom vortex also decreases in thickness with one small vortex embedded inside it.

From the isotherms, for $Ra = 10^3$ (Figure 7a), linear lines are found at the top cold wall which begins to turn into non-linear lines near the EB. Dense temperature lines are found at the left and right walls near the EB. The lowest temperature of the cavity $\theta = 0.03$ has been found at the top cold wall and the highest temperature of the cavity $\theta = 0.98$ has been found at the bottom heated wall. The lowest temperature on EB $\theta = 0.28$ has been found at the top cold wall and the highest temperature on EB $\theta = 0.93$ has been found at the bottom heated wall. No significant changes are found for $Ra = 10^4$ (Figure 7b) in the isotherms. But at $Ra = 10^5$ (Figure 7c), the shape of the isotherms is notably changed where non-linear lines at the top cold wall grow in numbers and the curved lines at the insulated sidewalls are seen to be changed than before where the temperature lines are becoming dense at the sidewalls. The only changes in temperature are seen for the lowest temperature at the top wall of EB at $\theta = 0.23$. At $Ra = 10^6$ (Figure 7d), the isotherms are turned to a chaotic shape, where many non-linear lines are formed around the EB. The highest and the lowest temperatures are found to remain unchanged but the lowest temperature at EB changes to $\theta = 0.13$. When $Ra = 10^7$ (Figure 7e), the highest chaotic stage of the isotherms is discovered where many non-linear curved lines are forming around the EB and the lowest temperature at the EB changes to $\theta = 0.18$. The temperature lines are at the highest dense position at the

insulated side walls. The EB is placed at the center of the cavity, at the CEB phase, for $Pr = 0.71$ and $Ra = 10^3 - 10^7$ (see Figure 8a). It is viewed that four symmetric eddy circulation cells are formed around the EB in the streamlines, where the top two cells are much more dense than the bottom two cells. As Ra changes to $Ra = 10^4 - 10^5$ (Figure 8b – Figure 8c), no significant changes have been found in the fluid flow. Slight changes are found when $Ra = 10^6$ (see Figure 8d) is applied. The top two cells become much more packed than before, where the right cell is thicker than the left one. At $Ra = 10^7$, the highest thickness of the eddy circulation cells has been seen in the fluid flow, where the top left cell is the thickest of all. Also, the space between the top cells and the bottom cells grew larger than in the previous simulations. As for the isotherms, at $Ra = 10^3$ (Figure 8a), linear smooth curves are only seen at the top and the bottom wall and the rest are non-linear lines where most of them are generated from the surface of the EB. The temperature curves are thickest at the insulted left and right side walls. The lowest temperature of the cavity is $\theta = 0.03$ and the highest temperature of the cavity is $\theta = 0.98$ which has been found for convectional fluid flow. In Figure 8b, the lowest temperature of the surface of EB is $\theta = 0.23$ and the highest temperature of the surface of EB is $\theta = 0.78$. At $Ra = 10^4$ (Figure 8b), no notable changes are found at the temperature curve. But at $Ra = 10^5$ (Figure 8c), curves are taking chaotic forms, which seem to be drawing to the surface of EB. The changes in temperature are seen only on the surface of the EB, the lowest temperature $\theta = 0.13$ and the highest temperature $\theta = 0.83$. When $Ra = 10^6$ (Figure 8d), it is now in a complete chaotic form, where the highest dense curves are seen at the two side walls, the curves at the top and the bottom wall are also found in dense position. At the surface of EB, the lowest and the highest temperature are respectively $\theta = 0.18$ and $\theta = 0.88$. At $Ra = 10^7$ (Figure 8e), isotherms are taking a complete new shape, where the curves at the two side walls along with the top and bottom walls are at the peak of density. The only change is found at the lowest temperature of the surface of the EB, $\theta = 0.13$. At the TEB phase, where the EB is placed at the top of the cavity, for $Pr = 0.71$ and $Ra = 10^3$ (Figure 9a), two large rotating eddies are found at the bottom of the EB in the streamlines, where the right one is much thicker than the left one. Two distinct vortices have also been formed at the EB while the right one is much bigger than the left one. When Ra increases to $Ra = 10^4$ (Figure 9b), the density of the two large eddies is increased than before and it is continually increasing at $Ra = 10^5 - 10^6$ (Figure 9c – Figure 9d). A thick borderline has formed around the two vortices at the top wall, the right vortex is now smaller than the left one. At $Ra = 10^7$ (Figure 9e), the density of the left eddy circulation cell is decreased than the left one, and the shape of the two vortices at the top wall is slightly changed. In the case of the isotherms study, at $Ra = 10^3$ (Figure 9a), only a linear temperature curve is seen at the bottom wall and the rest of them are non-linear curves, attracting to the surface of the EB. The density of the temperature curves is the highest at the insulated left and right sidewalls. The lowest temperature of the cavity is found at $\theta = 0.03$ and the highest temperature of the cavity is found at $\theta = 0.98$. Also, the lowest temperature of the surface of the EB is recorded at $\theta = 0.08$ and the highest temperature of the surface of the EB is recorded at 0.68. No significant changes are found in the isotherms for $Ra = 10^4$ (Figure 9b). But at $Ra = 10^5$ (Figure 9c), the temperature curves turn to chaotic shapes, and the highest curvature is found at the bottom of the EB. Only changes in the temperature value are found on the surface of the EB where the temperature is highest at $\theta = 0.78$. At $Ra = 10^6$ (see Figure 9d), isotherms are changed completely and the density of the curves at the sidewalls is increased a lot. As before, only changes of temperature value are found for the surface of the EB, lowest at $\theta = 0.03$ and highest at $\theta = 0.88$. And when Ra increases to $Ra = 10^7$ (Figure 9e), temperature curves are at the peak of the chaotic stage, where the density of curves at the side walls is higher than before. Similarly, only changes are found for the surface of the EB for the lowest temperature at $\theta = 0.08$ and the highest temperature at $\theta = 0.83$ due to the effect of convection fluid flow.
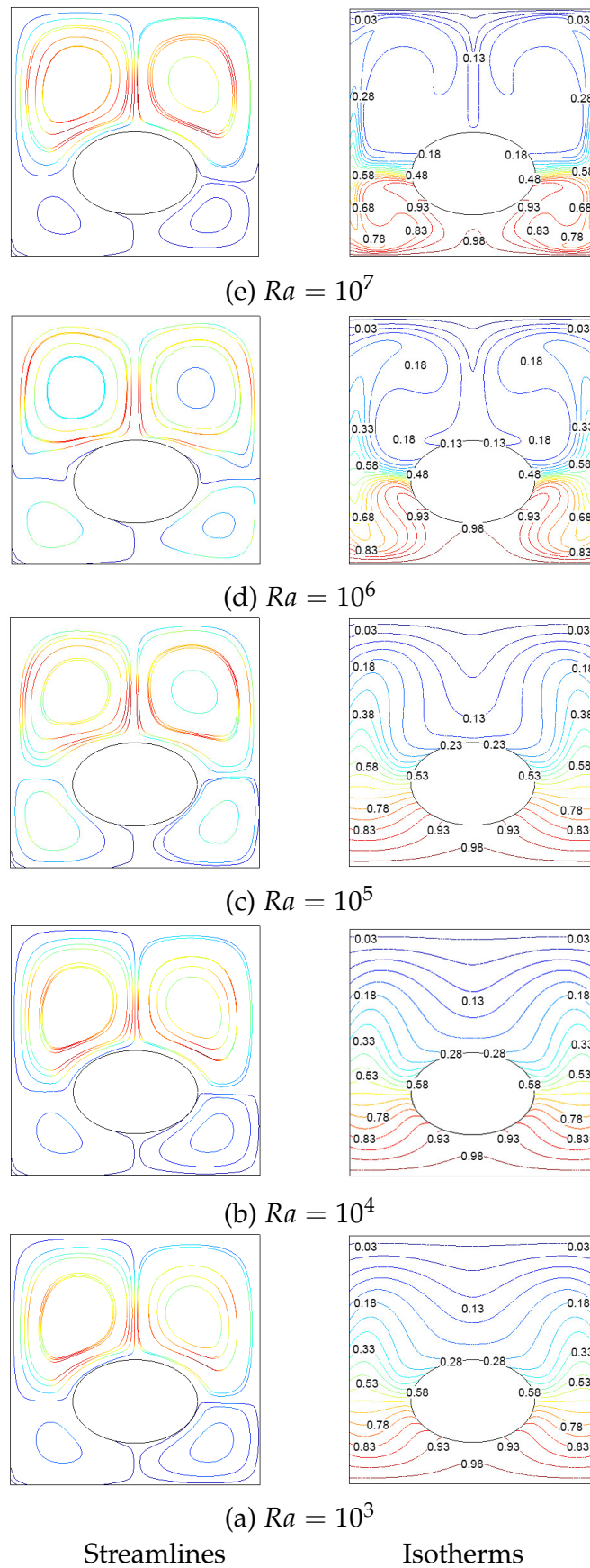
(e) $Ra = 10^7$

(d) $Ra = 10^6$

(c) $Ra = 10^5$

(b) $Ra = 10^4$

(a) $Ra = 10^3$

Streamlines   Isotherms

Figure 7. Streamlines and Isotherms for $Pr = 0.71$ and $Ra = 10^3 - 10^7$ for BEB

(e) $Ra = 10^7$

(d) $Ra = 10^6$

(c) $Ra = 10^5$

(b) $Ra = 10^4$

(a) $Ra = 10^3$

Streamlines   Isotherms

Figure 8. Streamlines and Isotherms for $Pr = 0.71$ and $Ra = 10^3 - 10^7$ for CEB

(e) $Ra = 10^7$

(d) $Ra = 10^6$

(c) $Ra = 10^5$

(b) $Ra = 10^4$

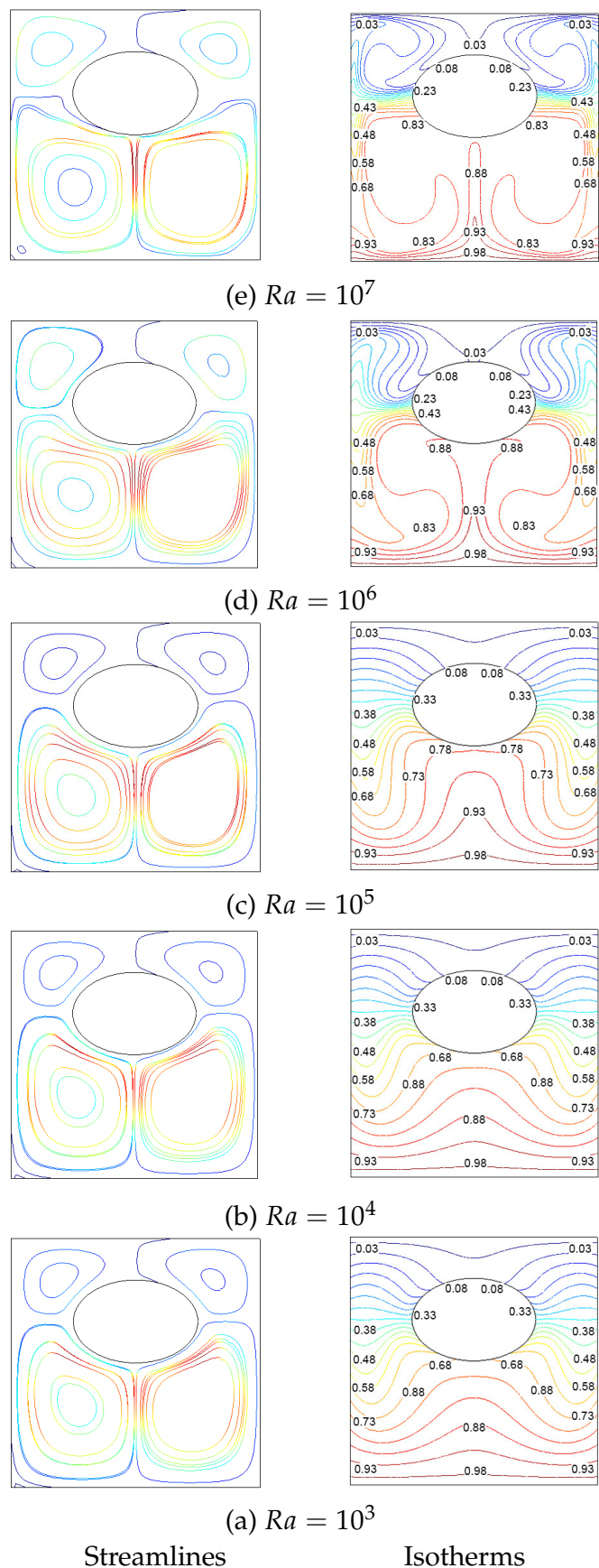

(a) $Ra = 10^3$

Streamlines   Isotherms

Figure 9. Streamlines and Isotherms for $Pr = 0.71$ and $Ra = 10^3 - 10^7$ for TEB

Heat transfer rates: Nu_{av} vs Ra for bottom wall of the cavity and insulated EB

The overall changes of average Nusselt number with increasing Rayleigh number for $Pr = 0.71$ and $Ra = 10^3 - 10^7$, are displayed in Figure 10-Figure 11 for the heated bottom wall of the cavity and bottom wall of insulated EB for different orientation BEB, CEB, and TEB.
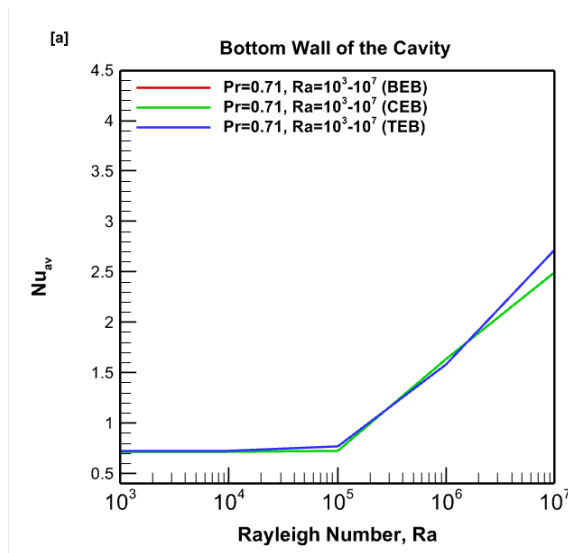

Figure 10. Average Nusselt number for (a) bottom wall of the cavity

From Figure 10, for (a), the heated bottom of the cavity, there is a logarithmic relationship being seen between Nu_{av} and Ra. A slow increase of Nu_{av} is found up to $Ra = 10^5$ for all three different orientations and when $Ra \geq 10^6$, the graph begins to rise for BEB, CEB, and TEB. This happens due to the transition from the conduction phase to the convection phase. The lowest value of Nu_{av} is recorded for $Ra = 10^3$ at CEB and the highest value of Nu_{av} is recorded for $Ra = 10^7$ at TEB. As for (b), the bottom wall of insulated EB, from Figure 11, the gradual increase of Nu_{av} occurs as Ra increases.
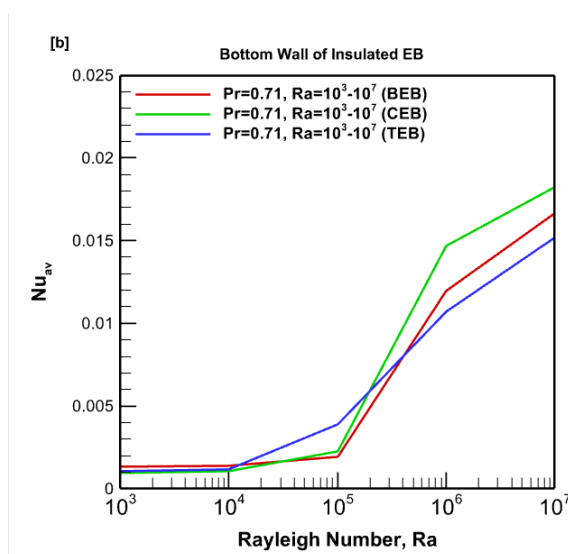

Figure 11. Average Nusselt number for (b) bottom wall of EB

For BEB and CEB orientations, the drastic change in the graph is started from $Ra \geq 10^5$ due to

convectional flow, whereas for TEB orientation, it is at $Ra \geq 10^4$. After reaching $Ra = 10^6$, the graph turns to a constant curve up to $Ra \geq 10^7$ for all three locations. The lowest heat transfer rate is found at $Ra = 10^3$ for CEB and the highest value at $Ra = 10^7$ for CEB.

9 Conclusion

An inclusive research work of free convection flow within a square enclosure for various locations of elliptic blockage for $Pr = 0.71$ and $Ra = 10^3 - 10^7$ has been analyzed numerically in the present study. The Galerkin weighted residual technique has been utilized to address the governing parameters Pr and Ra within finite element formulations aimed at solving the governing equations. The results are shown using stream functions, isotherms, heat transfer rates, and average Nusselt numbers, both for the bottom wall of the cavity and the bottom wall of the insulated EB. The key assumptions are concisely outlined as follows:

- Heat transfer mechanisms, flow characteristics, and the distribution of isotherms within the cavity depend exclusively on four key factors: EB, the temperature of the heated bottom wall, and two dimensionless numbers – the Prandtl number (Pr) and the Rayleigh number (Ra).
- The streamlines show that the area around the EB contains multiple vortex cells and swirling eddy currents for all three different orientations.
- At the heated bottom wall of the cavity, Nu_{av} is seen to have a logarithmic relation with Ra at $Pr = 0.71$ and $Ra = 10^3 - 10^7$, due to the transition from the conduction stage to the convection stage. The lowest value of Nu_{av} is recorded for $Ra = 10^3$ at CEB and the highest value of Nu_{av} is recorded for $Ra = 10^7$ at TEB.
- At the bottom wall of insulated EB, Nu_{av} is seen to be increasing with the value of Ra, and a quick change of the graph is found for the flow of strong convection at $Ra = 10^5$ for BEB and CEB and at $Ra = 10^4$ for TEB. At $Ra = 10^6$, a constant increasing graph is found for all three locations which implies invariant heat transfer. The lowest heat transfer rate is found at $Ra = 10^3$ for CEB and the highest value at $Ra = 10^7$ for CEB.

Declarations

List of symbols

C_p	Specific heat at constant pressure (J/kg K)
g	Gravitational acceleration (m/s^2)
h	Convective heat transfer coefficient (W/m^2 K)
k	Thermal conductivity of fluid (W/m K)
K	Thermal conductivity ratio fluid
N	Non-dimensional distance
Nu_{av}	Average Nusselt number
P	Non-dimensional pressure
p	Pressure
Pr	Prandtl number
Ra	Rayleigh number
T	Non-dimensional temperature
T_c	Cold temperature
T_h	Hot temperature
T_i	Thermal insulated Temperature
U	Dimensionless horizontal velocity
u	Velocity in x-direction (m/s)
V	Dimensionless vertical velocity
v	Velocity in y-direction (m/s)
x, y	Cartesiancoordinates
X, Y	Dimensionless cartesian coordinates

Greek symbols

β Coefficient of thermal expansion (1/K)
ρ Density of the fluid (kg/m^3)
α Thermal diffusivity (m^2/s)
$\Delta\theta$ Temperature difference
θ Fluid temperature
μ Dynamic viscosity of the fluid (Pa s)
ν Kinematic viscosity of the fluid (m^2/s)
σ Fluid electrical conductivity(Ω-1 m-1)

List of abbreviations

BEB   Bottom elliptic blockage
CEB   Center elliptic blockage
EB   Elliptic blockage
TEB   Top elliptic blockage

Use of AI tools

The authors declare that they have not used Artificial Intelligence (AI) tools in the creation of this article.

Data availability statement

All authors declare that data availability is not applicable to this article.

Ethical approval

Not applicable

Consent for publication

Not applicable

Conflicts of interest

The authors declare that they have no known competing financial interests or personal relationships that could have appeared to influence the work reported in this paper.

Funding

Not applicable

Author's contributions

S.S.B.: Writing - first draft, Methodology, Software, Investigation. M.S.H.: Conceptualization, Validation, Methodology, Software, Investigation, Writing - Original Draft, Writing - Review & Editing, Administration, Supervision. M.F.A.A.: Visualization, Validation, Methodology, Data Curation, Investigation, Writing – Review & Editing. M.S.I.M.: Methodology, Visualization, Investigation, Writing - Review & Editing. S.C.P.: Formal analysis, Visualization, Suggestion, Writing – Review & Editing: M.J.H.M.: Formal analysis, Visualization, Data Curation, Investigation. M.M.A.S.: Review, Suggestion, Administration and Supervision. All authors have read and agreed to the published version of the manuscript.

References

[1] Saury, D., Rouger, N., Djanna, F. and Penot, F. Natural convection in an air-filled cavity: experimental results at large Rayleigh numbers. *International Communications in Heat and Mass Transfer*, 38(6), 679-687, (2011). [CrossRef]

[2] Sajjadi, H., Gorji, M., Kefayati, G.H.R., Ganji, D.D. and Shayan Nia, M. Numerical analysis of turbulent natural convection in a square cavity using Large-Eddy simulation in lattice Boltzmann method. *Iranian Journal of Science & Technology Transactions of Mechanical Engineering*, 35(M2), 33-143, (2011). [CrossRef]

[3] Shati, A.K.A., Blakey, S.G. and Beck, S.B.M. A dimensionless solution to radiation and turbulent natural convection in square and rectangular enclosures. *Journal of Engineering Science and Technology*, 7(2), 257-279, (2012).

[4] Durand-Estebe, B., Lebot, C., Arquis, E. and Mancos, J. Validation of turbulent natural convection in a square cavity for application of CFD modeling to heat transfer and fluid flow in a data center. In Proceedings, *Biennial Conference on Engineering Systems Design and Analysis (ESDA)*, pp. 111-127, Nantes, France, (2012, July).

[5] Choi, S.K. and Kim, S.O. Turbulence modeling of natural convection in enclosures: a review. *Journal of Mechanical Science and Technology*, 26, 283-297, (2012). [CrossRef]

[6] Jani, S., Mahmoodi, M. and Amini, M. Magnetohydrodynamic free convection in a square cavity heated from below and cooled from other walls. *International Journal of Mechanical, Industrial Science and Engineering*, 7(4), 750-755, (2013).

[7] Butler, C., Newport, D. and Geron, M. Natural convection experiments on a heated horizontal cylinder in a differentially heated square cavity. *Experimental Thermal and Fluid Science*, 44, 199-208, (2013). [CrossRef]

[8] Xin, S., Salat, J., Joubert, P., Sergent, A., Penot, F. and Le Quéré, P. Resolving the stratification discrepancy of turbulent natural convection in differentially heated air-filled cavities. Part III: A full convection–conduction–surface radiation coupling. *International Journal of Heat and Fluid Flow*, 42, 33-48, (2013). [CrossRef]

[9] Carvalho, P.H.S. and De Lemos, M.J.S. Turbulent free convection in a porous square cavity using the thermal equilibirum model. *International Communications in Heat and Mass Transfer*, 49, 10-16, (2013). [CrossRef]

[10] Kefayati, G.H. Lattice Boltzmann simulation of natural convection in a nanofluid-filled inclined square cavity at presence of magnetic field. *Scientia Iranica*, 20(5), 1517-1527, (2013). [CrossRef]

[11] Bahoosh, R., Mohamadi, F. and Karimi, M. Numerical investigation of natural convection in a square cavity with tilting walls. *Journal of Thermophysics and Heat Transfer*, 29(4), 725-731, (2014). [CrossRef]

[12] Jani, S., Mahmoodi, M., Amini, M. and Jam, J.E. Numerical investigation of natural convection heat transfer in a symmetrically cooled square cavity with a thin fin on its bottom wall. *Thermal Science*, 18(4), 1119-1132, (2014). [CrossRef]

[13] Asad, M.F.A., M., Oreyeni, T., Yavuz, M. and Olanrewaju, P.O. Analytic simulation of MHD boundary layer flow of a chemically reacting upper-convected Maxwell fluid past a vertical

surface subjected to double stratifications with variable properties. *The European Physical Journal Plus,* 137, 813, (2022). [CrossRef]

[14] Islam, T., Yavuz, M., Parveen, N. and Asad, M.F.A. Impact of non-uniform periodic magnetic field on unsteady natural convection flow of nanofluids in square enclosure. *Fractal and Fractional,* 6(2), 101, (2022). [CrossRef]

[15] Asad, M.F.A., Yavuz, M., Alam, M.N., Sarker, M.M.A. and Bazighifan, O. Influence of fin length on magneto-combined convection heat transfer performance in a lid-driven wavy cavity. *Fractal and Fractional,* 5(3), 107, (2021). [CrossRef]

[16] Sajjadi, H. and Kefayati, R. Lattice Boltzmann simulation of turbulent natural convection in tall enclosures. *Thermal Science,* 19(1), 155-166, (2015). [CrossRef]

[17] Miroshnichenko, I. and Sheremet, M. Comparative study of standard $k - \epsilon$ and $k - \epsilon$ turbulence models by giving an analysis of turbulent natural convection in an enclosure. In *EPJ Web of Conferences,* 82, 1-4, (2015). [CrossRef]

[18] Zineddine, D.A., Tabet, S. and Azzi, A. Natural convection in partially heated square cavity. *Mechanics,* 22(2), 119-124, (2016). [CrossRef]

[19] Zhao, B. and Tian, Z. High-resolution high-order upwind compact scheme-based numerical computation of natural convection flows in a square cavity. *International Journal of Heat and Mass Transfer,* 98, 313-328, (2016). [CrossRef]

[20] Aithal, S.M. Turbulent natural convection in a square cavity with a circular cylinder. *Journal of Thermo physics and Heat Transfer,* 30(4), 843-853, (2016). [CrossRef]

[21] Adnani, M., Meziani, B., Ourrad, O. and Zitoune, M. Natural convection in a square cavity: numerical study for different values of prandtl number. *Fluid Dynamics and Material Processing,* 12(1), 1-14, (2016).

[22] Benchabi, R. and Lanani, A. Two-Dimensional numerical simulation of natural convection in a square cavity. *Mechanics,* 23(4), 545-551, (2017). [CrossRef]

[23] Solomon, A.B., van Rooyen, J., Rencken, M., Sharifpur, M. and Meyer, J.P. Experimental study on the influence of the aspect ratio of square cavity on natural convection heat transfer with Al2O3/Water nanofluids. *International Communications in Heat and Mass Transfer,* 88, 254-261, (2017). [CrossRef]

[24] Yang, G., Iacovides, H., Craft, T. and Apsley, D. RANS modelling for temperature variance in conjugate heat transfer. In Proceedings *5th World Congress on Mechanical, Chemical, and Material Engineering,* pp. 15-17, Lisbon, Portugal, (2019, August). [CrossRef]

[25] Razera, A.L., da Fonseca, R.J.C., Isoldi, L.A., Dos Santos, E.D., Rocha, L.A.O. and Biserni, C. A constructal approach applied to the cooling of semi-elliptical blocks assembled into a rectangular channel under forced convection. *International Journal of Heat and Mass Transfer,* 184, 122293, (2022). [CrossRef]

[26] Selimefendigil, F. and Öztop, H.F. Optimization of convective heat transfer performance for fluid flow over a facing step by using an elliptic porous object. *Case Studies in Thermal Engineering,* 27, 101233, (2021). [CrossRef]

[27] Khatamifar, M., Lin, W. and Dong, L. Transient conjugate natural convection heat transfer in a differentially-heated square cavity with a partition of finite thickness and thermal conductivity. *Case Studies in Thermal Engineering,* 25, 100952, (2021). [CrossRef]

[28] Devi, T.S., Lakshmi, C.V., Venkatadri, K. and Reddy, M.S. Influence of external magnetic wire on natural convection of non-Newtonian fluid in a square cavity. *Partial Differential Equations*

in Applied Mathematics, 4, 100041, (2021). [CrossRef]

[29] Wen, X., Wang, L.P. and Guo, Z. Development of unsteady natural convection in a square cavity under large temperature difference. *Physics of Fluids,* 33, 084108, (2021). [CrossRef]

[30] Goswami, N., Randive, P.R. and Pati, S. Natural convection from a pair of heated cylinders in a square cavity with non-uniform temperature on the side walls. *Journal of The Institution of Engineers (India): Series C,* 102, 389-396, (2021). [CrossRef]

[31] El, H.M. and Lafdaili, Z. Turbulent natural-convection heat transfer in a square cavity with nanofluids in presence of inclined magnetic field. *Thermal Science,* 26(4), 3201-3213, (2022).

[32] Turkyilmazoglu, M. Exponential nonuniform wall heating of a square cavity and natural convection. *Chinese Journal of Physics,* 77, 2122-2135, (2022). [CrossRef]

[33] Bilal, S., Khan, N.Z., Shah, I.A., Awrejcewicz, J., Akgül, A. and Riaz, M.B. Numerical study of natural convection of power law fluid in a square cavity fitted with a uniformly heated T-fin. *Mathematics,* 10(3), 342, (2022). [CrossRef]

[34] Sondur, S.R., Meuris, B. and Mescher, A.M. Benchmarked simulations of natural convection airflow in a square cavity. *Numerical Heat Transfer, Part A: Applications,* 84(4), 297-314, (2023). [CrossRef]

[35] Asad, M.F.A., Alam, M.N., Tunç, C. and Sarker, M.M.A. Heat transport exploration of free convection flow inside enclosure having vertical wavy walls. *Journal of Applied and Computational Mechanics,* 7(2), 520-527, (2021). [CrossRef]

[36] Asad, M.F.A., Alam, M.N., Rashad, A.M. and Sarker, M.M.A. Impact of undulation on magneto-free convective heat transport in an enclosure having vertical wavy sides. *International Communications in Heat and Mass Transfer,* 127, 105579, (2021). [CrossRef]

[37] Hossain, M.S., Asad, M.F.A., Mallik, M.S.I., Yavuz, M., Alim, M.A. and Khairul Basher, K.M. Numerical study of the effect of a heated cylinder on natural convection in a square cavity in the presence of a magnetic field. *Mathematical and Computational Applications,* 27(4), 58, 1-17, (2022). [CrossRef]

[38] Asad, M.F.A., Alam, M.N., Ahmad, H., Sarker, M.M.A., Alsulami, M.D. and Gepreel, K.A. Impact of a closed space rectangular heat source on natural convective flow through triangular cavity. *Results in Physics,* 23, 104011, (2021). [CrossRef]

[39] Hossain, M.S., Sarder, C.K., Hoque, K.E., Bangalee, M.Z.I., Billah, M.M. and Uddin, M.A. Finite element simulation on MHD free convection in a square enclosure with elliptical shaped obstacle. *Ganit: Journal of Bangladesh Mathematical Society,* 43(1), 63-75, (2023).

[40] Hossain, M.S., Alim, M.A. and Andallah, L.S. Numerical simulation of MHD natural convection flow within porous trapezoidal cavity with heated triangular obstacle. *International Journal of Applied and Computational Mathematics,* 6, 166, (2020). [CrossRef]

[41] Hossain, M.S. and Alim, M.A. MHD free convection within trapezoidal cavity with non-uniformly heated bottom wall. *International Journal of Heat and Mass Transfer,* 69, 327–336, (2014). [CrossRef]

[42] Hossain, M.S., Alim, M.A. and Andallah, L.S. Numerical investigation of natural convection flow in a trapezoidal cavity with non-uniformly heated triangular block embedded inside. *Journal of Advances in Mathematics and Computer Science,* 28(5), 1-30, (2018). [CrossRef]

[43] Taylor, C. and Hood, P. A numerical solution of the Navier-Stokes equations using the finite element technique. *Computers & Fluids,* 1(1), 73-100, (1973). [CrossRef]

[44] Reddy J.N. An introduction to the finite element method. In *Dynamics of Earth's Fluid System* (pp.). McGraw-Hill, New York, 1985.

[45] Rahman, M.M., Alim, M.A. and Mamun, M.A.H. Finite element analysis of mixed convection in a rectangular cavity with a heat-conducting horizontal circular cylinder. *Nonlinear Analysis: Modelling and Control*, 14(2), 217-247, (2009).

Mathematical Modelling and Numerical Simulation with Applications (MMNSA)
(https://dergipark.org.tr/en/pub/mmnsa)

How to cite this article: Billah, S.S., Hossain, M.S., Asad, M.F.A., Mallik, M.S.I., Paul, S.C., Munshi, M.J.H. & Sarker, M.M.A. (2024). Free convection at different locations of adiabatic elliptic blockage in a square enclosure. *Mathematical Modelling and Numerical Simulation with Applications*, 4(1), 86-109. https://doi.org/10.53391/mmnsa.1382516

RESEARCH PAPER

Spectral collocation with generalized Laguerre operational matrix for numerical solutions of fractional electrical circuit models

İbrahim Avcı [ID] [1],*,‡

[1]Department of Computer Engineering, Faculty of Engineering, Final International University, Kyrenia, Northern Cyprus, via Mersin 10, Türkiye

*Corresponding Author
‡ ibrahim.avci@final.edu.tr (İbrahim Avcı)

Abstract

In this paper, we introduce a pioneering numerical technique that combines generalized Laguerre polynomials with an operational matrix of fractional integration to address fractional models in electrical circuits. Specifically focusing on Resistor–Inductor (RL), Resistor–Capacitor (RC), Resonant (Inductor–Capacitor) (LC), and Resistor–Inductor–Capacitor (RLC) circuits within the framework of the Caputo derivative, our approach aims to enhance the accuracy of numerical solutions. We meticulously construct an operational matrix of fractional integration tailored to the generalized Laguerre basis vector, facilitating a transformation of the original fractional differential equations into a system of linear algebraic equations. By solving this system, we obtain a highly accurate approximate solution for the electrical circuit model under consideration. To validate the precision of our proposed method, we conduct a thorough comparative analysis, benchmarking our results against alternative numerical techniques reported in the literature and exact solutions where available. The numerical examples presented in our study substantiate the superior accuracy and reliability of our generalized Laguerre-enhanced operational matrix collocation method in effectively solving fractional electrical circuit models.

Keywords: Numerical analysis; electrical circuits; generalized Laguerre polynomials; fractional integrals; fractional derivatives

AMS 2020 Classification: 41A58; 26A33; 34A08

1 Introduction

In recent years, an escalating interest has emerged among researchers in harnessing the power of fractional calculus and Fractional Differential Equations (FDEs). Fractional calculus, a field rooted in the generalization of integration and differentiation to arbitrary orders, finds its origins in the

musings of G.W. Leibniz (1695) and L. Euler (1730). Despite its longstanding history, fractional calculus and the corresponding FDEs have only recently surged in attention and popularity, driven by their unparalleled ability to model complex phenomena. Various definitions of fractional derivatives, including Riemann–Liouville, Caputo, Grünwald–Letnikov, Weyl, Marchaud, Prabhakar, and others, populate the literature, underscoring the versatility of this mathematical tool. The Riemann-Liouville definition is among the earliest formulations in the field of fractional calculus. It emerged as a significant contribution to the theory's development, offering foundational insights into fractional derivatives and integrals. Caputo's definition, introduced later, has become widely used in engineering applications. Its effectiveness lies in its ability to accurately model systems commonly encountered in engineering problems. Particularly in scenarios where boundary conditions predominantly involve integer-order derivatives, Caputo's operator excels in providing precise representations of physical systems, especially those exhibiting intricate behaviors, thereby contributing to its popularity. Grünwald–Letnikov, Weyl, Marchaud, and Prabhakar provide alternative approaches, each tailored to specific analytical or computational demands. The flexibility offered by these definitions allows researchers to tailor their approach to the particular characteristics of the problem at hand, making fractional calculus a powerful tool in mathematical modeling. The history of this topic can be found in [1–5].

The interdisciplinary applications of fractional calculus span an impressive array of fields, expanding beyond bioengineering, biology, chaotic systems, control theory, economics, electrochemistry, finance, quantum mechanics, optics, oncology, physics, rheology, social sciences, viscoelasticity, and so on [6–16]. This expansive scope underscores the versatility and profound impact of fractional calculus in addressing intricate challenges across diverse scientific and engineering domains. As we delve into this multifaceted landscape, it becomes evident that the marriage of mathematical rigor with innovative numerical techniques is paving the way for groundbreaking advancements and novel solutions in scientific inquiry.

Fractional calculus emerges as a superior modeling framework, often outperforming traditional calculus, particularly in capturing memory effects crucial for describing long-term interactions [17, 18]. This distinctive feature enhances the accuracy of representing diverse dynamical and engineering models, becoming indispensable in scientific investigations. Confronted with the inherent difficulty of obtaining exact analytic solutions for nonlinear FDEs, researchers have developed an arsenal of numerical and approximate methods. In addition to spectral collocation [19], variational iteration [20], differential quadrature [21], adomian decomposition [22], fractional reduced differential transform [23], and wavelet methods [24–26], innovative techniques such as finite element method [27], and radial basis function methods [28] have been meticulously crafted to surmount these challenges. On the other hand, many numerical techniques for solving fractional models face limitations, including accuracy issues with complex dynamics and non-standard boundaries, computational inefficiency for large-scale simulations, and restricted applicability to specific equations or systems. Moreover, the lack of a clear geometric interpretation in fractional calculus complicates algorithm development, hindering intuitive understanding and implementation. Additionally, convergence and stability challenges arise, particularly with nonlinear or stiff equations. Addressing these limitations requires the development of novel techniques to improve accuracy, efficiency, and applicability across a wide range of fractional systems and boundary conditions. Electrical circuit models serve as fundamental tools in understanding and analyzing the behavior of electrical systems [29]. Among the widely studied circuit configurations are the RC (resistor-capacitor), RL (resistor-inductor), LC (inductor-capacitor), and RLC (resistor-inductor-capacitor) circuits. In the RC circuit, the combination of a resistor and a capacitor introduces time-dependent characteristics, influencing the circuit's response to input signals. The RL circuit, incorporating a resistor and an inductor, exhibits distinctive behaviors

due to the inductor's role in storing energy. LC circuits, consisting of an inductor and a capacitor, demonstrate oscillatory behavior and resonance. RLC circuits, combining all three elements, showcase a rich spectrum of responses, including damped and undamped oscillations, resonance, and transient behaviors. Understanding the dynamics of these circuit models is crucial for various applications in electronics, communication systems, and signal processing, making them focal points in both theoretical analysis and practical design considerations. In recent years, there has been a growing interest in extending the analysis of electrical circuit models to the realm of fractional derivatives. This approach introduces a new dimension to the understanding of RC, RL, LC, and RLC circuit dynamics, incorporating fractional calculus principles. By considering fractional derivatives, which generalize conventional derivatives to arbitrary orders, researchers aim to capture more accurately the intricate behavior and memory effects exhibited by electrical circuits [30, 31]. In this study, we employ a sophisticated numerical approach that combines the strengths of both operational matrix and collocation methods for solving fractional-order electrical circuit models, including RL, RC, LC, and RLC configurations. Specifically, we leverage the operational matrix of fractional integration, which streamlines the complex calculations associated with fractional derivatives. This operational matrix is strategically applied to the generalized Laguerre basis vector, forming the backbone of our methodology. Subsequently, we introduce collocation by judiciously selecting equally spaced nodes, effectively transforming the fractional differential equations into a well-structured system of linear equations. This dual methodology harnesses the computational efficiency of operational matrices while benefiting from the simplicity and accuracy conferred by collocation techniques. The resulting system of linear equations is then systematically solved, providing a precise numerical solution to the intricate dynamics inherent in these electrical circuit models. This innovative combination of operational matrix and collocation methods demonstrates a powerful and versatile approach to addressing fractional order systems, showcasing its efficacy in obtaining accurate numerical solutions for a broad spectrum of electrical circuit configurations.

This paper is structured as follows: In Section 2, we lay the foundation with a discussion on fractional calculus, introducing the definitions of generalized Laguerre polynomials and their application in function approximation. Section 3 is dedicated to the construction of the generalized Laguerre operational matrix of fractional integration. Moving on to Section 4, we delve into the specific problem statements addressed in this paper and elaborate on the methodology employed, focusing on the Generalized Laguerre Operational Matrix Method (GLOMM). Section 5 is dedicated to Error Estimation based on Residual Analysis, providing a comprehensive investigation into the accuracy and reliability of our proposed approach. Section 6 presents four illustrative examples, showcasing the applicability, accuracy, and performance of our proposed technique. The paper concludes in Section 7 with a summary of findings and directions for future research.

2 Preliminaries

Definition 1 *[3] The definition of the Riemann-Liouville fractional integral of order μ for $\text{Re}(\mu) > 0$ is as follows:*

$$ {}^{RL}_a I^\mu_x f(x) = \frac{1}{\Gamma(\mu)} \int_a^x (x-t)^{\mu-1} f(t) dt. \tag{1} $$

From the above definition, it is clear that,

$$ {}^{RL}_0 I^\mu_x (x^p) = \frac{\Gamma(1+p)}{\Gamma(1+p+\mu)} x^{p+m}. $$

Definition 2 *[4] The definition of the Caputo fractional derivative for* $\operatorname{Re}(\mu) \geq 0$ *is as follows:*

$$_a^C D_x^\mu f(x) = \frac{d^n}{dx^n} \, _a^{RL} I_x^{n-\mu} f(x), \qquad n := \lfloor \operatorname{Re}(\mu) \rfloor + 1.$$

The Newton–Leibniz identity establishes a fundamental relationship between the Riemann–Liouville fractional integral and the Caputo fractional derivative, expressed as follows:

$$_0^{RL} I_x^\mu (_0^C D_x^\mu f(x)) = f(x) - \sum_{k=0}^{\lceil \mu \rceil - 1} f^{(k)}(0) \frac{x^k}{k!}.$$

Definition 3 *Consider the interval* $\Lambda = (0, \infty)$, *and let* $\omega^{(\alpha)}(x) = x^\alpha e^{-x}$ *represent a weight function in* Λ *in the conventional sense. Define*

$$L^2_{\omega^{(\alpha)}} = \{v | v \text{ is measurable on } \Lambda \text{ and } \|v\|_{\omega^{(\alpha)}} < \infty\},$$

with the inner product and norm

$$(u, v)_{\omega^{(\alpha)}} = \int_\Lambda u(x) v(x) \omega^{(\alpha)}(x) dx,$$

$$\|v\|_{\omega^{(\alpha)}} = (v, v)^{\frac{1}{2}}_{\omega^{(\alpha)}}.$$

Definition 4 *(Generalized Laguerre Polynomial) [32] Let* $L_{n,\alpha}(x)$ *be the generalized Laguerre polynomials to degree n. According to [33], for* $\alpha > -1$, *we have*

$$L_{n+1,\alpha}(x) = \frac{1}{n+1} [(2n + \alpha - 1 - x) L_{n,\alpha}(x) - (n+\alpha) L_{n-1,\alpha}(x)], \, n = 1, 2, ...,$$

where the first few terms of the generalized Laguerre polynomials are given by

$$L_{0,\alpha}(x) = 1,$$
$$L_{1,\alpha}(x) = 1 + \alpha - x,$$
$$L_{2,\alpha}(x) = \frac{1}{2!} [2 + 3\alpha + \alpha^2 - 2\alpha x - 4x + x^2],$$
$$L_{3,\alpha}(x) = \frac{1}{3!} [6 + 11\alpha + 6\alpha^2 + \alpha^3 - 13\alpha x + 3\alpha x^2 - 3\alpha^2 x - 18x + 9x^2 - x^3].$$

The analytical expression for generalized Laguerre polynomials over the interval $\Lambda = (0, \infty)$ *is given by:*

$$L_{n,\alpha}(x) = \sum_{k=0}^n (-1)^k \frac{\Gamma(n+\alpha+1)}{\Gamma(k+\alpha+1)(n-k)!k!} x^k, \, n = 0, 1, ... \tag{2}$$

Note that, setting $\alpha = 0$ *in Eq. (2), we arrive to the classical Laguerre Polynomials* $L_n(x)$.

Approximation of function

A function $f(x) \in L^2_{\omega^{(\alpha)}}(\Lambda)$ can be represented using generalized Laguerre polynomials as:

$$
\begin{aligned}
f(x) &= \sum_{j=0}^{\infty} \psi_j L_{j,\alpha}(x), \\
\psi_j &= \frac{1}{h_r} \int_0^{\infty} f(x) L_{j,\alpha} w^{\alpha} dx, \quad j = 0, 1, 2, ...
\end{aligned}
\tag{3}
$$

Considering the first $(N+1)$ terms of generalized Laguerre polynomials, we get

$$
f \simeq f_n = \sum_{j=0}^{m} \psi_j L_{j,\alpha}(x) = \Psi^T \mathbf{L}_{m,\alpha}(x),
\tag{4}
$$

where the unknown coefficient vector Ψ^T and the generalized Laguerre polynomial vector $\mathbf{L}_{m,\alpha}(x)$ are defined as

$$
\Psi^T = \left[\psi_0, \psi_1, \ldots, \psi_N\right]^T \text{ for } N \in \mathbb{N},
\tag{5}
$$

and

$$
\mathbf{L}_{m,\alpha}(x) = \left[L_{0,\alpha}(x), L_{1,\alpha}(x), \ldots, L_{m,\alpha}(x)\right]^T \text{ for } m \in \mathbb{N}.
\tag{6}
$$

3 Formulation of the generalized Laguerre operational matrix for fractional integration

In this section, we construct the operational matrix of fractional integration for the generalized Laguerre polynomials. Employing the Riemann-Liouville fractional integration (1) to the order μ on the analytical representation of generalized Laguerre polynomials $L_{i,\alpha}(x)$ provided in (2), yields:

$$
\begin{aligned}
I^{\mu} L_{i,\alpha}(x) &= \sum_{k=0}^{i} (-1)^k \frac{\Gamma(i+\alpha+1)}{(i-k)! k! \Gamma(k+\alpha+1)} I^{\mu} x^k \\
&= \sum_{k=0}^{i} (-1)^k \frac{\Gamma(i+\alpha+1)}{(i-k)! \Gamma(k+\alpha+1) \Gamma(k+\mu+1)} x^{k+\mu}.
\end{aligned}
\tag{7}
$$

By approximating $x^{k+\mu}$ using $N+1$ terms of the generalized Laguerre series, we obtain:

$$
x^{k+\mu} = \sum_{j=0}^{N} \psi_j L_{j,\alpha},
\tag{8}
$$

where ψ_j is defined in Eq. (3) with $f(x) = x^{k+\mu}$, that is,

$$
\psi_j = \sum_{r=0}^{j} (-1)^r \frac{j! \Gamma(k+\mu+\alpha+r+1)}{(j-r)! r! \Gamma(r+\alpha+1)}, \quad j = 1, 2, ..., N.
\tag{9}
$$

Utilizing Eqs. (7) and (8), we obtain:

$$I^\mu L_{i,\alpha}(x) = \sum_{j=0}^{N} D_\mu(i,j) L_{j,\alpha}(x), \quad i = 0, 1, ..., N, \tag{10}$$

where

$$D_\mu(i,j) := \sum_{k=0}^{i} \sum_{r=0}^{j} \frac{(-1)^{k+r} j! \Gamma(i+\alpha+1) \Gamma(k+\mu+\alpha+r+1)}{(i-k)!(j-r)!r! \Gamma(k+\mu+1) \Gamma(k+\alpha+1) \Gamma(\alpha+r+1)}. \tag{11}$$

Accordingly, Eq. (10) can be written in a vector form as follows:

$$I^\mu L_{i,\alpha}(x) = [D_\mu(i,0), D_\mu(i,1), ..., D_\mu(i,N)] \mathbf{L}_{N,\alpha}, \quad i = 0, 1, ..., N, \tag{12}$$

where $\mathbf{L}_{N,\alpha}$ is the generalized Laguerre vector defined in Eq. (2).
Consider $\mathbf{G}^{(\mu)}$, an operational matrix of fractional integration of order μ, with dimensions $(N+1) \times (N+1)$, defined as:

$$\mathbf{G}^{(\mu)} = \begin{pmatrix} D_\mu(0,0) & D_\mu(0,1) & D_\mu(0,2) & \cdots & D_\mu(0,N) \\ D_\mu(1,0) & D_\mu(1,1) & D_\mu(1,2) & \cdots & D_\mu(1,N) \\ \vdots & \vdots & \ddots & \vdots \\ D_\mu(N,0) & D_\mu(N,1) & D_\mu(N,2) & \cdots & D_\mu(N,N) \end{pmatrix}.$$

Then, we can rewrite system (12) as

$$I^\mu \mathbf{L}_{N,\alpha}(x) = \mathbf{G}^{(\mu)} \mathbf{L}_{N,\alpha}(x). \tag{13}$$

4   Problem statement and method of solution

In this section, we delineate the specific problems at the core of our investigation and introduce the Generalized Laguerre Operational Matrix Method (GLOMM) as the key solution approach. Our focus lies on deriving numerical solutions for fractional-order electrical circuit models encompassing $RL, RC, LC,$ and RLC configurations. By applying the GLOMM to these circuit models, we aim to provide a comprehensive and efficient numerical methodology for analyzing their fractional dynamics, contributing to the advancement of computational techniques in the field of electrical circuit modeling.

RL circuit

In this section, we focus on the numerical solutions of fractional order RL circuit. An RL circuit is an electrical circuit that consists of a resistor (R) and an inductor (L). The resistor represents the element that resists the flow of electrical current, generating heat in the process, while the inductor is a coil of wire that stores energy in its magnetic field when current flows through it. The fractional-order generalized RL circuit is given as

$$D^\mu u(x) + \frac{R}{L} u(x) = E(x), \quad x \in [0,1], \quad 0 < \mu \le 1, \quad u(0) = u_0. \tag{14}$$

When $\mu = 1$, the fractional-order RL circuit equation (14) reduces to the classical case. Applying the Riemann-Liouville fractional integral of order μ to both sides of Eq. (14), we obtain:

$$u(x) - \sum_{k=0}^{\lceil \mu \rceil - 1} u^{(k)}(0) \frac{x^k}{k!} + \frac{R}{L} I^\mu u(x) = I^\mu(E(x)). \tag{15}$$

Substituting initial condition into Eq. (15) and approximating the function $u(x)$ by the generalized Laguerre polynomials (4), we get

$$\Psi^T \mathbf{L}_{m,\alpha}(x) - u_0 + \frac{R}{L} \Psi^T (I^\mu \mathbf{L}_{m,\alpha}(x)) = I^\mu(E(x)).$$

Further, using the operational matrix of fractional integration defined in Eq. (13), we obtain

$$\Psi^T \mathbf{L}_{m,\alpha}(x) + \frac{R}{L} \Psi^T (\mathbf{G}^{(\mu)} \mathbf{L}_{m,\alpha}(x)) = F(x), \tag{16}$$

where $F(x) = I^\mu(E(x)) + u_0$.

RC **circuit**

In this section, our attention shifts to the numerical analysis of the fractional order RC circuit. A RC circuit is an electrical circuit configuration comprising a resistor (R) and a capacitor (C). The resistor impedes the flow of electrical current, generating heat in the process, while the capacitor stores electrical energy in its electric field when voltage is applied across it. The fractional-order generalized RC circuit is defined as

$$D^\mu v(x) + \frac{1}{RC} v(x) = E(x), \quad x \in [0,1], \quad 0 < \mu \leq 1, \quad v(0) = v_0. \tag{17}$$

When $\mu = 1$, the fractional-order RC circuit equation (17) reduces to the classical case. By applying the same procedure proposed in Subsection 4 on Eq. (17), we get,

$$\Psi^T \mathbf{L}_{m,\alpha}(x) + \frac{1}{RC} \Psi^T (\mathbf{G}^{(\mu)} \mathbf{L}_{m,\alpha}(x)) = F(x), \tag{18}$$

where $F(x) = I^\mu(E(x)) + v_0$.

LC **circuit**

In this section, our focus turns to the numerical exploration of the fractional order LC circuit. The LC circuit is an electrical circuit composition consisting of an inductor (L) and a capacitor (C). The inductor stores energy in its magnetic field as current flows through it, while the capacitor stores electrical energy in its electric field when voltage is applied. The fractional-order generalized LC circuit is described as

$$L D^\mu q(x) + \frac{1}{C} q(x) = E(x), \quad 1 < \mu \leq 2, \quad q(0) = q_0, \quad q'(0) = q_1. \tag{19}$$

This fractional-order LC circuit equation (19) reduces to the classical one when $\mu = 2$. Applying the Riemann-Liouville fractional integral of order μ to both sides of Eq. (19) and dividing by L, we

get

$$q(x) - \sum_{k=0}^{\lceil \mu \rceil - 1} q^{(k)}(0) \frac{x^k}{k!} + \frac{1}{LC} I^\mu q(x) = \frac{1}{L} I^\mu (E(x)). \tag{20}$$

Substituting initial condition into Eq. (20) and approximating the function $q(x)$ by the generalized Laguerre polynomials (4), we get

$$\Psi^T \mathbf{L}_{m,\alpha}(x) - q_0 - x q_1 + \frac{1}{LC} \Psi^T I^\mu \mathbf{L}_{m,\alpha}(x) = \frac{1}{L} I^\mu (E(x)). \tag{21}$$

Next, using the operational matrix of fractional integration defined in Eq. (13), we obtain

$$\Psi^T \mathbf{L}_{m,\alpha}(x) + \frac{1}{LC} \Psi^T (\mathbf{G}^{(\mu)} \mathbf{L}_{m,\alpha}(x)) = F(x), \tag{22}$$

where $F(x) = \frac{1}{L} I^\mu (E(x)) + q_0 + x q_1$.

RLC circuit

In this section, our focus transitions to the numerical analysis of the fractional order *RLC* circuit. The *RLC* circuit is a complex electrical configuration integrating a resistor (R), an inductor (L), and a capacitor (C). The resistor hinders the flow of electrical current, the inductor stores energy in its magnetic field, and the capacitor stores electrical energy in its electric field when voltage is applied. The fractional-order generalized *RLC* circuit is characterized by

$$D^\beta w(x) + \frac{R}{L} D^\mu w(x) + \frac{1}{LC} w(x) = E(x), \ x \in [0,1], \quad 0 < \mu \le 1, 1 < \beta \le 2, \tag{23}$$

with

$$w^{(i)}(0) = w_i, \ i = 0, 1, ..., \lceil \beta \rceil - 1.$$

This fractional-order *RLC* circuit equation (23) reduces to the classical one when $\beta = 2$ and $\mu = 1$. Applying the R–L fractional integration to the order β on both sides of Eq. (23), we get

$$w(x) - \sum_{k=0}^{\lceil \beta \rceil - 1} w^{(k)}(0) \frac{x^k}{k!} + \frac{R}{L} I^{\beta - \mu} \left(w(x) - \sum_{k=0}^{r} w^{(k)}(0) \frac{x^k}{k!} \right) + \frac{1}{LC} I^\beta w(x) = I^\beta (E(x)), \tag{24}$$

where $r - 1 < \mu < r$.

Substituting initial condition into Eq. (24) and approximating the function $w(x)$ by the generalized Laguerre polynomials (4), we get

$$w(x) - w_0 - x w_1 + \frac{R}{L} \Psi^T I^{\beta - \mu} \mathbf{L}_{m,\alpha}(x) - \frac{R}{L} I^{\beta - \mu} \left(\sum_{k=0}^{r} w^{(k)}(0) \frac{x^k}{k!} \right) + \frac{1}{LC} \Psi^T I^\beta \mathbf{L}_{m,\alpha}(x) = I^\beta (E(x)). \tag{25}$$

Next, using the operational matrix of fractional integration defined in Eq. (13), we obtain

$$w(x) + \frac{R}{L}\Psi^T(\mathbf{G}^{(\beta-\mu)}\mathbf{L}_{m,\alpha}(x)) + \frac{1}{LC}\Psi^T(\mathbf{G}^{(\beta)}\mathbf{L}_{m,\alpha}(x)) = F(x), \tag{26}$$

where $F(x) = I^\beta(E(x)) + w_0 + xw_1 + \frac{R}{L}I^{\beta-\mu}\left(\sum_{k=0}^r w^{(k)}(0)\frac{x^k}{k!}\right)$.

Finally, by using the collacation points $x_i = \frac{i}{N}$ where $i = 0, 1, \cdots, N$ in Eqs. (16), (18), (22) and (26), we get a system of $N+1$ algebraic equations for each circuit model [34]. Solving these systems of algebraic equations for the unknown vector Ψ^T and using Eq. (4), we get an accurate approximation solution to the given models.

5 Error analysis

In this section, we introduce an error estimation method based on the residual error function for our proposed GLOMM. The residual error, a quantification of the difference between computed and true solutions in numerical methods, serves as a pivotal tool in assessing accuracy and convergence. By monitoring the residual during the solution process, it offers insights into method convergence, facilitates error control, and aids in adaptive strategies.

Consider the general fractional-order electrical circuit equation:

$$D^\beta y(x) + AD^\mu y(x) + By(x) = E(x), \; x \in [0,1], \quad 0 < \mu \le 1, \quad 1 < \beta \le 2, \tag{27}$$

with

$$y^{(i)}(0) = y_i, \; i = 0, 1, ..., \lceil \beta \rceil - 1,$$

where D^β and D^μ represent the fractional derivative of order β and μ, respectively. A and B are coefficients related to the circuit components (e.g. resistance, inductance, capacitance). Let $y_N(x)$ be the numerical solution of given initial value problem (27). Substituting $y_N(x)$ into Eq. (27), we get

$$D^\beta y_N(x) + AD^\mu y_N(x) + By_N(x) - E(x) = R_N(x), \tag{28}$$

where $R_N(x)$ is the residual function. By using Eqs. (27) and (28), we get

$$D^\beta(y(x) - y_N(x)) + AD^\mu(y(x) - y_N(x)) + B(y(x) - y_N(x)) = R_N(x). \tag{29}$$

Now, let us define the error function as $\epsilon_N(x) = (y(x) - y_N(x))$. Subsequently, employing this error function in Eq. (29), we derive

$$D^\beta \epsilon_N(x) + AD^\mu \epsilon_N(x) + B\epsilon_N(x) = R_N(x), \tag{30}$$

with initial conditions $\epsilon_N(0) = 0$ and $\epsilon'_N(0) = 0$. Solving Eq. (30) using the approach outlined in Section 4 yields the approximate error estimation $\epsilon_N(x)$ for the proposed method. Consequently, the approximation of maximum absolute error can be estimated by

$$E_N = \max|\epsilon_N|, \quad 0 \le x \le T.$$

6 Numerical simulations and comparative discussions

In this section, we illustrate the dynamics of fractional electrical circuit models, specifically RL, RC, LC, and RLC, through four distinct examples. These demonstrations showcase the efficacy of the Generalized Laguerre Operational Matrix Method (GLOMM) under various fractional derivative orders. To validate the accuracy and versatility of our proposed method, we conduct comprehensive comparisons with existing techniques reported in the literature. This comparative analysis serves as a robust means of affirming the reliability and applicability of the GLOMM in accurately capturing the behavior of fractional electrical circuit models across different fractional derivative orders. All computations are performed using Matlab R2021a.

Example 1 *(RL Circuit) In this illustrative instance, we contemplate the fractional-order RL circuit model defined by Eq. (14) in the presence of a constant voltage source, where $E(x) = 0$. Specifically, when considering $\mu = 1$, the precise solution to Eq. (14) can be expressed as*

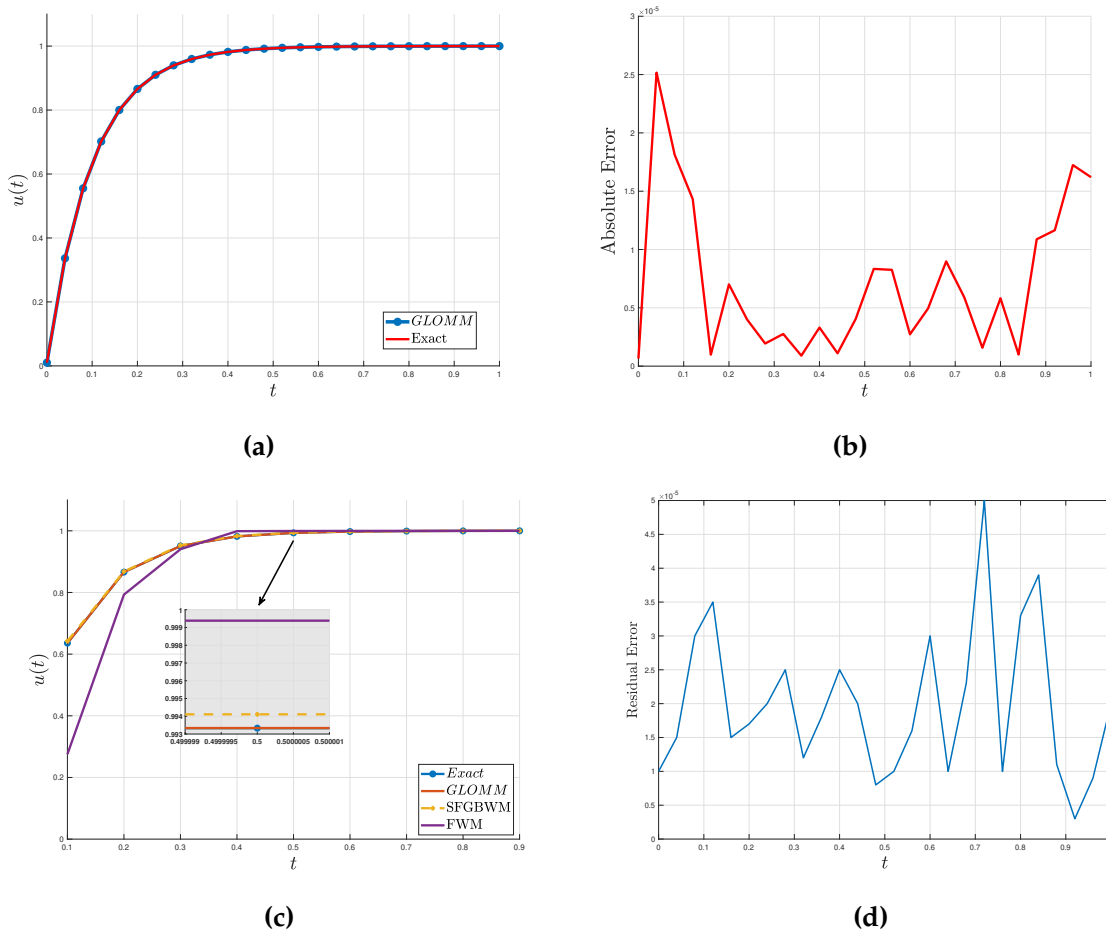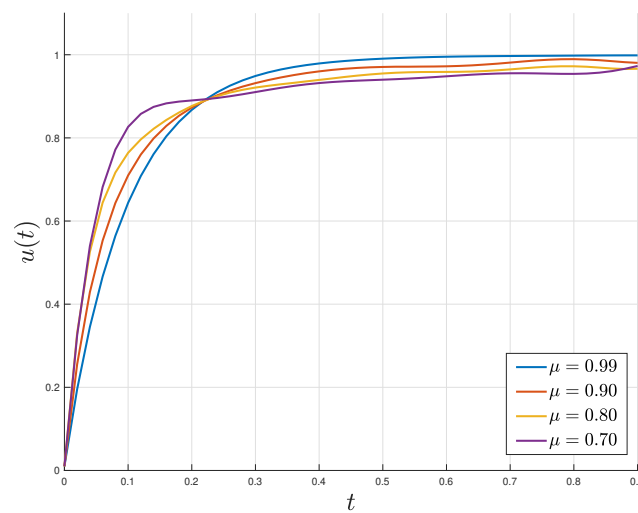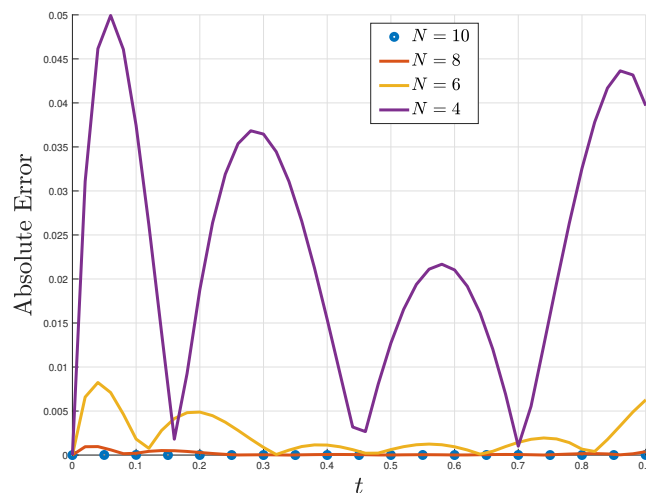$$u(x) = \left[u_0 - \frac{E(x)L}{R} \right] e^{\frac{-R}{L}x} + \frac{E(x)L}{R}.$$

Figure 1. (a) Comparative illustration of approximate solutions for the fractional-order RL circuit in contrast to the exact solution. (b) Absolute error obtained from GLOMM. (c) Comparative illustration of exact, GLOMM, SFGBWM, and FWM solutions for the RL circuit model at $\mu = 1.00$. (d) Residual error estimation for RL circuit model

In Figure 1a, we present a visual comparison between the exact solution and the approximation obtained through the Generalized Laguerre Operational Matrix Method (GLOMM), as introduced in Subsection 4, for the fractional-order RL circuit. The analysis involves specific parameter values $R = 10$, $L = 1$, an initial condition of $u_0 = 10$, and a derivative order of $\mu = 1$. Additionally, Figure 1b illustrates the associated absolute error resulting from the application of GLOMM to the RL circuit under the same settings. In Figure 1c, a graphical comparison unfolds between the exact solution, our proposed method, and established methods from the literature, namely Shifted fractional order Gegenbauer wavelets method (SFGBWM) [25] and Fibonacci wavelet (FWM) [26]. The visual representation distinctly highlights the remarkable alignment between our method and the exact solution, showcasing its superior performance compared to existing approaches. Figure 1d illustrates the estimation results of the residual error function for the RL circuit model. These estimation results demonstrate a concordance between the absolute error and the estimated error, both of which are around 10^{-5}, showcasing the accuracy of the proposed method.

(a)

(b)

Figure 2. (a) Dynamic response of GLOMM solution for the *RL* circuit at varying values of the fractional parameter μ. (b) Absolute errors for the *RL* circuit at different N values

In Figure 2a, we depict the graphical behavior of the *RL* circuit across various fractional derivative orders, specifically for $\mu = 0.99, 0.90, 0.80, 0.70$. This illustration unveils the dynamic response of the RL circuit model to alterations in fractional derivative orders. Notably, as the fractional derivative order diminishes, the function reaches its maximum value at an earlier stage. This trend indicates that a lower fractional derivative order induces an expedited response in the RL circuit, leading to a more rapid attainment of its peak value. In Figure 2b, we showcase the absolute errors derived from the application of GLOMM with varying numbers of basis vectors for generalized Laguerre polynomials, specifically for $N = 4, 6, 8, 10$. This graphical representation highlights an improved performance of GLOMM with increasing values of N, indicating enhanced accuracy and convergence as the number of basis vectors for Laguerre polynomials expands.

Example 2 *(RC Circuit) In this illustration, we examine the fractional-order RC circuit model as defined by Eq. (17), assuming a constant voltage source with $E(x) = 0$. When $\mu = 1$, the precise solution to Eq. (17) is obtained as*
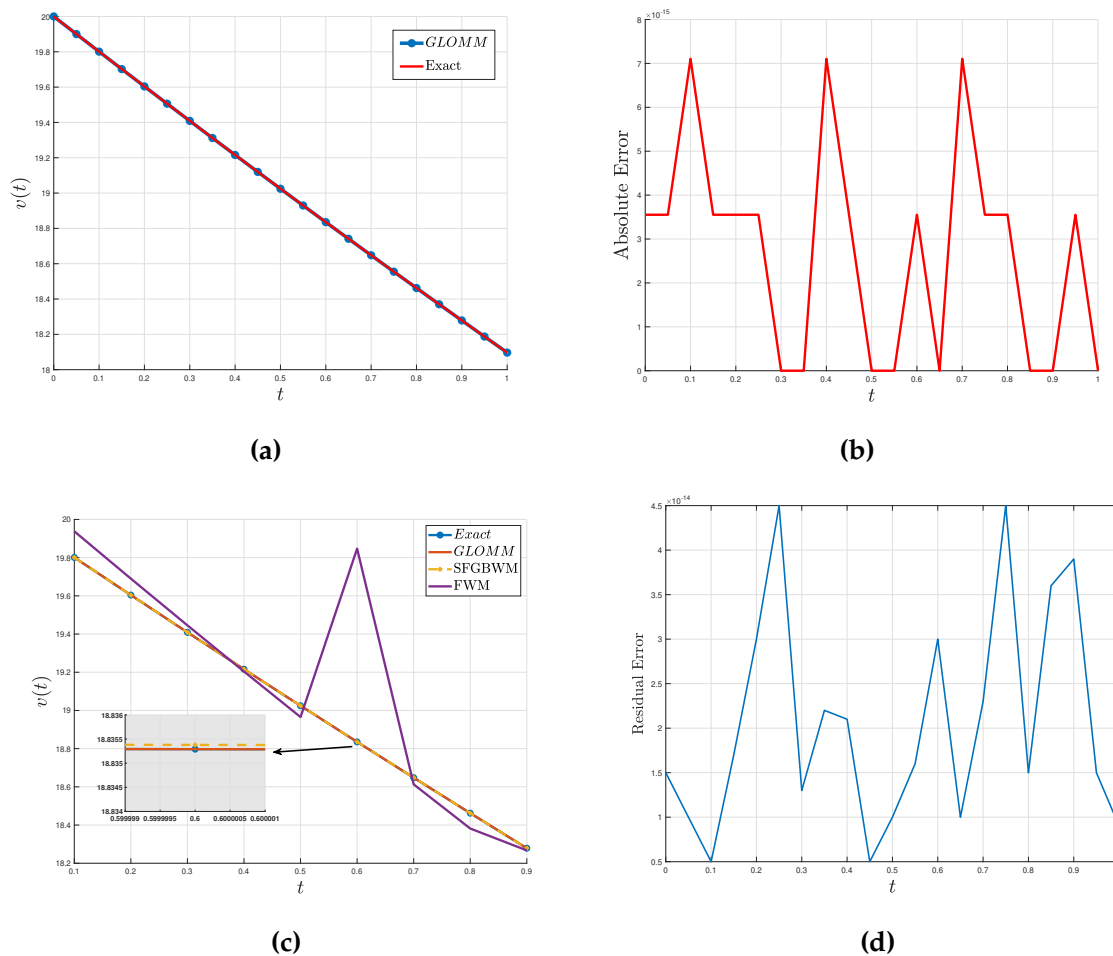
$$v(x) = v_0 e^{\frac{-x}{RC}}.$$

(a)

(b)

(c)

(d)

Figure 3. (a) Comparative illustration of approximate solutions for the fractional-order *RC* circuit in contrast to the exact solution. (b) Absolute error obtained from GLOMM. (c) Comparative illustration of exact, GLOMM, SFGBWM, and FWM solutions for the *RC* circuit model at $\mu = 1.00$. (d) Residual error estimation for *RC* circuit model

In Figure 3a, we present a visual juxtaposition of the exact solution and the approximation achieved through the GLOMM, as introduced in Subsection 4, for the fractional-order RC circuit. The analysis encompasses specific parameter values $R = 10$, $C = 1$, an initial condition of $v_0 = 20$, and a derivative order of $\mu = 1$. Furthermore, Figure 3b illustrates the corresponding absolute error resulting from the application of GLOMM to the RC circuit under the same settings. In Figure 3c, a graphical comparison unfolds between the exact solution, our proposed method, and established methods from the literature, namely the SFGBWM [25] and FWM [26]. The visual representation distinctly highlights the notable alignment between our method and the exact solution, underscoring its superior performance relative to existing approaches. Figure 3d illustrates the estimation results of the residual error function for the RC circuit model. These estimation results demonstrate an agreement between the absolute error and the estimated error.
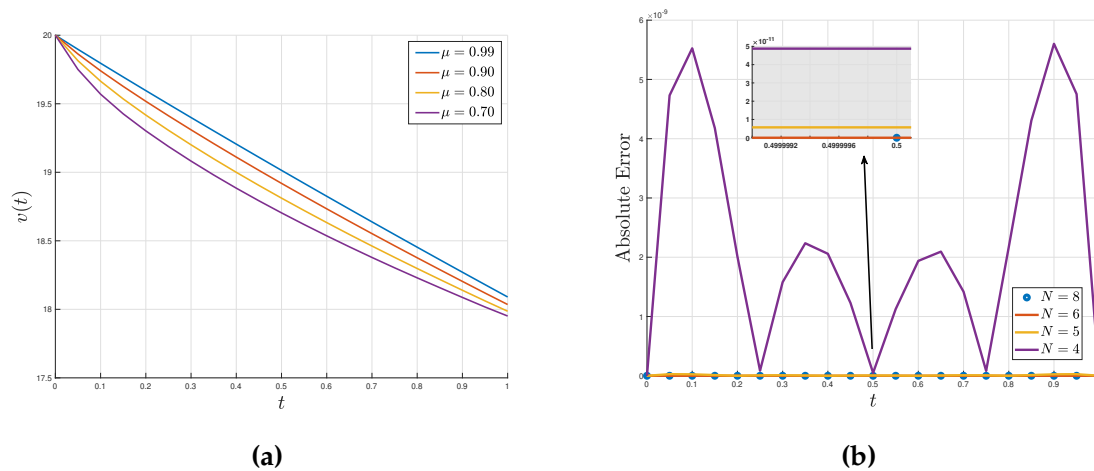

Figure 4. (a) Dynamic response of GLOMM solution for the *RC* circuit at varying values of the fractional parameter μ. (b) Absolute errors for the *RC* circuit at different N values

In Figure 4a, we depict the graphical behavior of the fractional-order RC circuit across various fractional derivative orders, specifically for $\mu = 0.99, 0.90, 0.80, 0.70$. In Figure 4b, we present the absolute errors resulting from the application of GLOMM with different numbers of basis vectors for generalized Laguerre polynomials, specifically considering $N = 4, 5, 6, 8$. This graphical representation underscores the improved performance of GLOMM as the value of m increases, suggesting enhanced accuracy and convergence with the expansion of the number of basis vectors for generalized Laguerre polynomials. In the subsequent analysis, we alter the configuration for the fractional-order RC circuit by setting $R = 1$ and applying GLOMM under a fractional order of $\mu = 0.5$.

Table 1 provides a comparative analysis of solutions obtained using the GLOMM, ABM, and Ch3WM for the fractional-order RC circuit model. The analysis is conducted under a fractional derivative order of $\mu = 0.5$. The resulting outcomes are visually compared with established techniques, such as the Chebyshev Wavelets of the third kind Method (Ch3WM) [24], in Figure 5. Given that the exact solution of the RC circuit is defined for integer derivative orders, rendering it unsuitable as a reference under fractional order $\mu = 0.5$, we employ the Adams-Bashforth method (ABM) [35] as a reference technique. The comparison between our method, Ch3WM, and ABM reveals a notable alignment. The obtained results strongly indicate that GLOMM exhibits superior agreement compared to other techniques.

Table 1. Comparison of GLOMM, Ch3WM, and ABM solutions for fractional order *RC* circuit model with $\mu = 0.5$

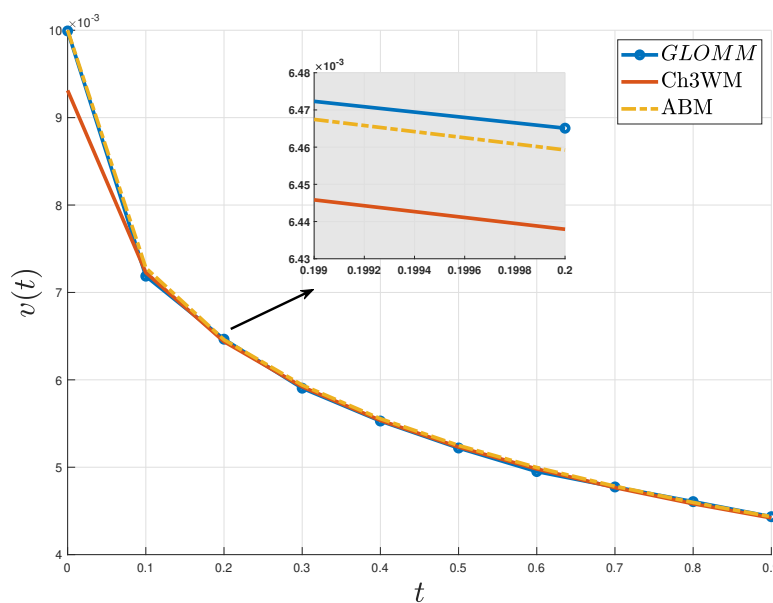|	ABM	GLOMM	Ch3WM
0	0.01	0.010006099	0.009311492
0.1	0.007280578	0.007195621	0.007227947
0.2	0.006459239	0.006429888	0.006437929
0.3	0.005940309	0.005921566	0.005920666
0.4	0.005555113	0.005525782	0.005536186
0.5	0.005249442	0.005209207	0.005231222
0.6	0.004996976	0.004985988	0.004980178
0.7	0.004782689	0.004785824	0.004766949
0.8	0.004597144	0.004561122	0.00458242
0.9	0.004434009	0.004411648	0.004420164

Figure 5. Comparative illustration of GLOMM, Ch3WM, and ABM solutions for the *RC* circuit model at $\mu = 0.5$

Example 3 *(LC Circuit) In this instance, we examine the fractional-order LC circuit model described by Eq.* (19). *Assuming a constant voltage source with $E(x) = 0$, the precise solution to Eq.* (19) *is derived for $\mu = 2$ as follows:*

$$q(x) = q_0 cos\left(\sqrt{\frac{1}{LC}}x\right) + CE(x) - CE(x)cos\left(\sqrt{\frac{1}{LC}}x\right).$$

In Figure 6a, we showcase a visual comparison between the exact solution and the approximation obtained through GLOMM, as introduced in Subsection 4, for the fractional-order LC circuit. The analysis considers specific parameter values $L = 10$, $C = 1$, an initial condition of $q_0 = 0.01$, and a derivative order of $\mu = 2$. Additionally, Figure 6b illustrates the corresponding absolute error resulting from the application of GLOMM to the LC circuit under the same settings. In Figure 6c, a graphical comparison unfolds between the exact solution, our proposed method, and established methods from the literature, namely SFGBWM [25] and FWM [26]. The visual representation distinctly highlights the remarkable alignment between our method and the exact solution, emphasizing its superior performance compared to existing

approaches. Moreover, in Figure 6d, we depict the comparison between GLOMM and the exact solution of the fractional-order LC circuit model over an extended time interval, $t \in [0, 10]$. This illustration underscores the high accuracy demonstrated by GLOMM, particularly for longer time intervals. Figure 6e illustrates the estimation results of the residual error function for the LC circuit model. These estimation results demonstrate an agreement between the absolute error and the estimated error, both of which are around 10^{-15}.
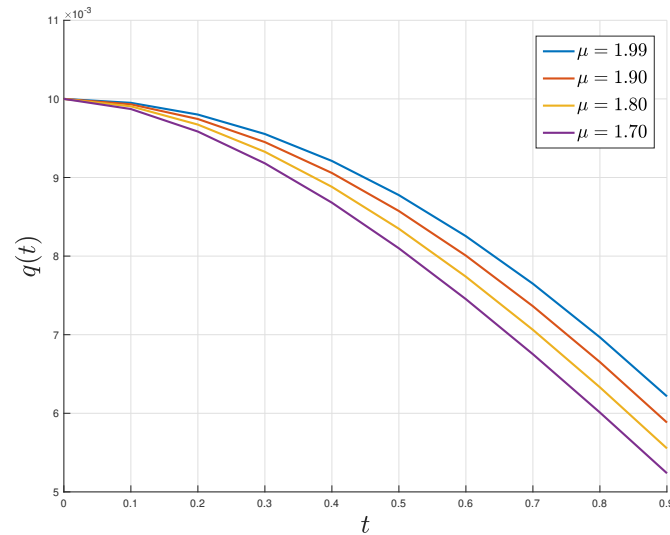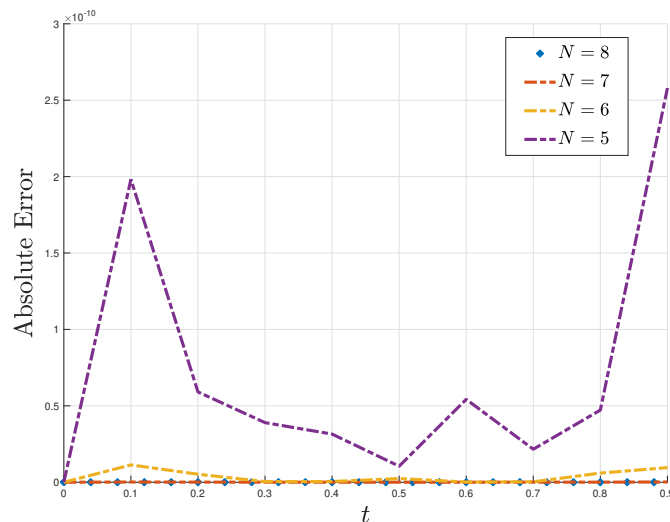

(a)

(b)

(c)

(d)

(e)

Figure 6. (a) Comparative illustration of approximate solutions for the fractional-order *LC* circuit in contrast to the exact solution. (b) Absolute error obtained from GLOMM. (c) Comparative illustration of exact, GLOMM, SFGBWM, and FWM solutions for the *LC* circuit model at $\mu = 2.00$. (d) Comparison of fractional-order *LC* circuit solutions with the exact solution for $t \in [0, 10]$. (e) Residual error estimation for *LC* circuit model

In Figure 7a, we illustrate the graphical behavior of the fractional-order LC circuit across varying fractional derivative orders, specifically for $\mu = 1.99, 1.90, 1.80, 1.70$. Concurrently, in Figure 7b, we present the absolute errors resulting from the application of GLOMM with varying numbers of basis vectors for generalized Laguerre polynomials, specifically considering $N = 5, 6, 7, 8$. This graphical representation underscores the improved performance of GLOMM as the value of m increases, indicating enhanced accuracy and convergence with the expansion of the number of basis vectors for Laguerre polynomials.

(a)

(b)

Figure 7. (a) Dynamic response of GLOMM solution for the *LC* circuit at varying values of the fractional parameter μ. (b) Absolute errors for the *LC* circuit at different N values

In Figure 8, we modify the configuration for the fractional-order LC circuit by setting $\mu = 1.5$ and applying GLOMM. The resulting outcomes are visually contrasted with well-established techniques, such as the Bernoulli Wavelet Method (BWM) [24]. Considering that the exact solution of the LC circuit is defined for integer derivative orders, making it unsuitable as a reference under fractional order $\mu = 1.5$, we again resort to the ABM [35] as a reference technique. The comparison involving our method, BWM, and ABM

reveals a noteworthy alignment. The obtained results strongly indicate that GLOMM exhibits superior agreement compared to other techniques.
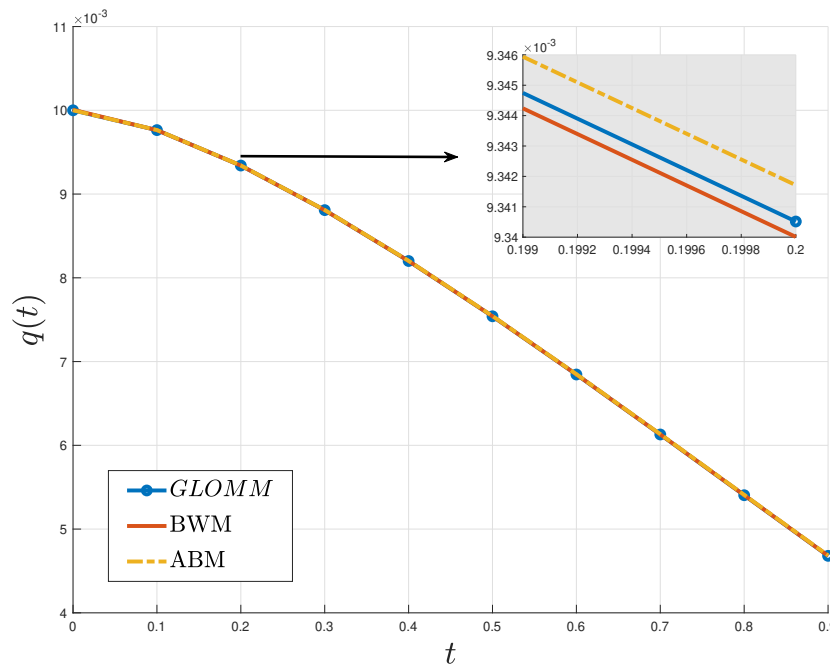

Figure 8. Comparative illustration of GLOMM, BWM, and ABM solutions for the *LC* circuit model at $\mu = 1.5$

Table 2 provides a comparative analysis of solutions obtained using the GLOMM, ABM, and BWM for the fractional-order LC circuit model. The analysis is conducted under a fractional derivative order of $\mu = 1.7$.
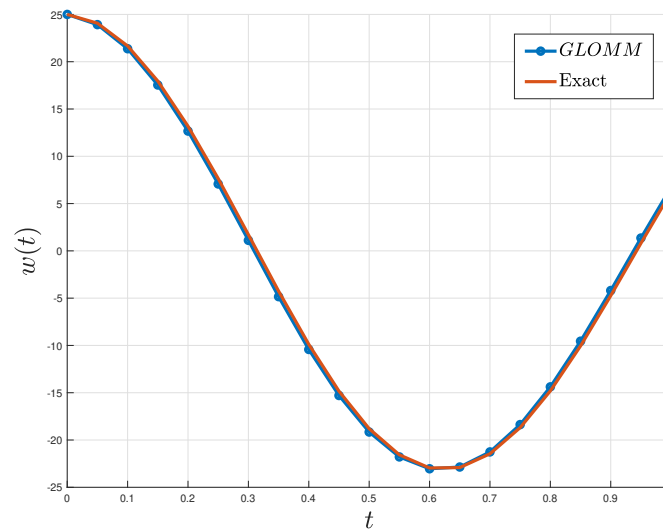
Table 2. Comparison of GLOMM, BWM, and ABM solutions for fractional order *LC* circuit model with $\mu = 1.7$

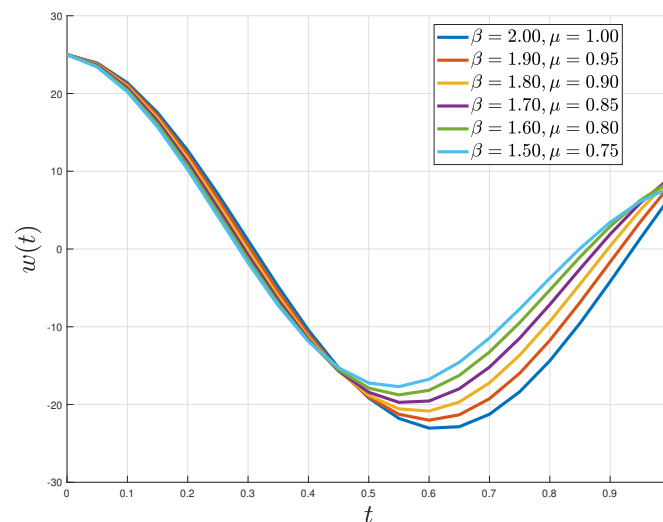|	ABM	GLOMM	BWM
0	0.01	0.01	0.010001716
0.1	0.009871448	0.009871159	0.009870358
0.2	0.009585093	0.009584501	0.009583816
0.3	0.009181335	0.009180212	0.009179646
0.4	0.008681298	0.008679638	0.008679286
0.5	0.008101184	0.008098930	0.008099095
0.6	0.007454966	0.007452128	0.007452203
0.7	0.006755332	0.006751900	0.006752166
0.8	0.006014079	0.006010103	0.006010442
0.9	0.005242306	0.005237790	0.00523831

Example 4 *(RLC Circuit) In this instance, we delve into the RLC circuit model described by Eq. (23). Assuming a constant voltage source with $E(x) = 0$, the exact solution to Eq. (23) is derived for $\beta = 2$ and $\mu = 1$ as follows:*

$$w(x) = w_0 e^{\frac{-Rx}{2L}} \cos\left(\sqrt{\frac{1}{LC} - \frac{R^2}{4L^2}} x\right).$$

In *Figure 9a*, we present a visual comparison between the exact solution and the approximation obtained through GLOMM, as introduced in Subsection *4*, for the fractional-order RLC circuit. The analysis considers specific parameter values $R = 10$, $L = 10$, $C = 10$, an initial condition of $w_0 = 0.01$, and derivative orders $\beta = 2$ and $\mu = 1$. Additionally, in *Figure 9b*, we illustrate the graphical behavior of the fractional-order RLC circuit across varying fractional derivative orders, specifically for $\beta = 2.00, \mu = 1.00$, $\beta = 1.90, \mu = 0.95$, $\beta = 1.80, \mu = 0.90$, $\beta = 1.70, \mu = 0.85$, $\beta = 1.60, \mu = 0.80$, and $\beta = 1.50, \mu = 0.75$.

(a)

(b)

Figure 9. (a) Comparative illustration of approximate solutions for the fractional-order RLC circuit in contrast to the exact solution. (b) Dynamic response of GLOMM solution for the RLC circuit at varying values of the fractional parameters β and μ

Table 3 showcases the CPU time (in seconds) required for solving RC, RL, LC, and RLC circuits utilizing the Generalized Laguerre Operational Matrix Method. These results underscore the ability of GLOMM to deliver fast and efficient numerical solutions, making it a promising technique for applications that demand

both accuracy and computational speed.

Table 3. CPU time (in seconds)

	RC	RL	LC	RLC
CPU time(s)	0.3081	0.3025	0.2812	0.3438

In Table 4, we provide a comprehensive comparison of the maximum absolute errors achieved by our proposed GLOMM in contrast to FWM, SFGWM, and BWM for the RC, RL, and LC electrical circuit models. This comparison emphasizes the superior accuracy and precision of GLOMM in delivering numerical solutions for fractional-order electrical circuits.

Table 4. Comparison of Maximum Absolute Errors for RC, RL, and LC circuits

	GLOMM	FWM	SFGWM	BWM
RC	7.1054×10^{-15}	9.7149×10^{-5}	9.6041×10^{-5}	6.11×10^{-2}
RL	2.1278×10^{-5}	5.5706×10^{-4}	6.7269×10^{-3}	-
LC	3.2682×10^{-15}	1.6238×10^{-6}	2.8394×10^{-6}	1.16×10^{-5}

7 Conclusion and further research

In conclusion, this research introduces a novel and efficient numerical approach, the Generalized Laguerre Operational Matrix Method (GLOMM), for solving fractional electrical circuit models represented by RL, RC, LC, and RLC configurations within the framework of the Caputo derivative. By leveraging the distinctive properties of generalized Laguerre polynomials and developing an operational matrix of fractional integration, our method offers a powerful tool for accurately capturing the intricate dynamics of these circuits. Through a series of numerical examples conducted using Matlab R2021a, we demonstrated the robustness and versatility of our proposed approach across varying fractional derivative orders. Notably, we observed maximum absolute errors of approximately 10^{-15} for the RC circuit, 10^{-5} for the RL circuit, and 10^{-15} for the LC circuit, highlighting the superior accuracy of our method compared to existing approaches. Furthermore, the high level of agreement in the approximate solution for the RLC circuit, as evidenced in the illustrations, further validates the efficacy of our approach. Additionally, CPU time serves as a crucial metric for assessing computational efficiency, directly reflecting the computational resources required to execute our algorithm. The maximum CPU time of 0.3438 obtained using GLOMM underscores the computational efficiency of our proposed technique. The results underscore the potential of our method as a valuable tool in the analysis and design of fractional electrical circuits, showcasing its ability to provide precise solutions and enhance our understanding of the underlying dynamic behaviors.

Future research directions stemming from this study could explore the extension of the GLOMM to address nonlinear fractional electrical circuit models, assessing its performance under varying degrees of nonlinearity. Additionally, incorporating alternative orthogonal basis functions or operational matrices alongside generalized Laguerre polynomials may be investigated to enhance the method's versatility. Parametric studies and sensitivity analyses can be conducted to evaluate the robustness of the GLOMM in response to variations in circuit parameters and fractional orders. In addition, integration with machine learning techniques could be explored to optimize the selection of collocation nodes and further refine the approximation process, ultimately improving the accuracy and efficiency of the GLOMM.

Declarations

Use of AI tools

The author declares that he has not used Artificial Intelligence (AI) tools in the creation of this article.

Data availability statement

All data generated or analyzed during this study are included in this article.

Ethical approval

The author states that this research complies with ethical standards. This research does not involve either human participants or animals.

Consent for publication

Not applicable

Conflicts of interest

The author declares that he has no conflict of interest.

Funding

Not applicable

Author's contributions

The author has read and agreed to the published version of the manuscript.

Acknowledgements

Not applicable

References

[1] Machado, J.T., Kiryakova, V. and Mainardi, F. Recent history of fractional calculus. *Communications in Nonlinear Science and Numerical Simulation*, 16(3), 1140-1153, (2011). [CrossRef]

[2] Miller, K.S. and Rosso, B. *An Introduction to the Fractional Calculus and Fractional Differential Equations*. Wiley: New York, (1993).

[3] Oldhalm, K.B. and Spainer, J. *The Fractional Calculus*. Academic Press: New York, USA, (1974).

[4] Caputo, M. Linear models of dissipation whose Q is almost frequency independent—II. *Geophysical Journal International*, 13(5), 529-539, (1967). [CrossRef]

[5] Debnath, L. Recent applications of fractional calculus to science and engineering. *International Journal of Mathematics and Mathematical Sciences*, 2003, 3413-3442, (2003). [CrossRef]

[6] Tarasov, V.E. Mathematical economics: application of fractional calculus. *Mathematics*, 8(5), 660, (2020). [CrossRef]

[7] Alinei-Poiana, T., Dulf, E.H. and Kovacs, L. Fractional calculus in mathematical oncology. *Scientific Reports*, 13, 10083, (2023). [CrossRef]

[8] Mainardi, F. *Fractional Calculus and Waves in Linear Viscoelasticity: An Introduction to Mathematical Models*. World Scientific: Singapore, (2022). [CrossRef]

[9] Avcı, İ., Lort, H. and Tatlıcıoğlu, B.E. Numerical investigation and deep learning approach for fractal–fractional order dynamics of Hopfield neural network model. *Chaos, Solitons & Fractals*, 177, 114302, (2023). [CrossRef]

[10] Chen, S.B., Soradi-Zeid, S., Jahanshahi, H., Alcaraz, R., Gómez-Aguilar, J.F., Bekiros, S. et al. Optimal control of time-delay fractional equations via a joint application of radial basis functions and collocation method. *Entropy*, 22(11), 1213, (2020). [CrossRef]

[11] Joshi, H. and Yavuz, M. Transition dynamics between a novel coinfection model of fractional-order for COVID-19 and tuberculosis via a treatment mechanism. *The European Physical Journal Plus*, 138, 468, (2023). [CrossRef]

[12] Soradi-Zeid, S., Jahanshahi, H., Yousefpour, A. and Bekiros, S. King algorithm: a novel optimization approach based on variable-order fractional calculus with application in chaotic financial systems. *Chaos, Solitons & Fractals*, 132, 109569, (2020). [CrossRef]

[13] Rezapour, S., Asamoah, J.K.K., Etemad, S., Akgül, A., Avcı, İ. and El Din, S.M. On the fractal-fractional Mittag-Leffler model of a COVID-19 and Zika Co-infection. *Results in Physics*, 55, 107118, (2023). [CrossRef]

[14] Zhao, W., Leng, K., Chen, J., Jiao, Y. and Zhao, Q. Research on statistical algorithm optimization of fractional differential equations of quantum mechanics in ecological compensation. *The European Physical Journal Plus*, 134, 316, (2019). [CrossRef]

[15] Duran, S., Durur, H., Yavuz, M. and Yokus, A. Discussion of numerical and analytical techniques for the emerging fractional order murnaghan model in materials science. *Optical and Quantum Electronics*, 55, 571, (2023). [CrossRef]

[16] Yilmaz, B. A new type electromagnetic curves in optical fiber and rotation of the polarization plane using fractional calculus. *Optik*, 247, 168026, (2021). [CrossRef]

[17] Barros, L.C.D., Lopes, M.M., Pedro, F.S., Esmi, E., Santos, J.P.C.D. Sánchez, D.E. et al. The memory effect on fractional calculus: an application in the spread of COVID-19. *Computational and Applied Mathematics*, 40, 72, (2021). [CrossRef]

[18] Tarasov, V.E. On history of mathematical economics: application of fractional calculus. *Mathematics*, 7(6), 509, (2019). [CrossRef]

[19] El-Gamel, M., Mohamed, N. and Waleed, A. Genocchi collocation method for accurate solution of nonlinear fractional differential equations with error analysis. *Mathematical Modelling and Numerical Simulation with Applications*, 3(4), 351-375, (2023). [CrossRef]

[20] Wu, G.C. A fractional variational iteration method for solving fractional nonlinear differential equations. *Computers & Mathematics with Applications*, 61(8), 2186-2190, (2011). [CrossRef]

[21] Mohamed, S.A. A fractional differential quadrature method for fractional differential equations and fractional eigenvalue problems. *Mathematical Methods in the Applied Sciences*, (2020). [CrossRef]

[22] Albogami, D., Maturi, D. and Alshehri, H. Adomian decomposition method for solving fractional Time-Klein-Gordon equations using Maple. *Applied Mathematics*, 14(6), 411-418, (2023). [CrossRef]

[23] Abuasad, S., Hashim, I. and Abdul Karim, S.A. Modified fractional reduced differential transform method for the solution of multiterm time-fractional diffusion equations. *Advances in Mathematical Physics*, 2019, 5703916, (2019). [CrossRef]

[24] Tural-Polat, S.N. and Dincel, A.T. Wavelet methods for fractional electrical circuit equations.

Physica Scripta, 98(11), 115203, (2023). [CrossRef]

[25] Yadav, P., Jahan, S. and Nisar, K.S. Shifted fractional order Gegenbauer wavelets method for solving electrical circuits model of fractional order. *Ain Shams Engineering Journal*, 14(11), 102544, (2023). [CrossRef]

[26] Ahmed, S., Shah, K., Jahan, S. and Abdeljawad, T. An efficient method for the fractional electric circuits based on Fibonacci wavelet. *Results in Physics*, 52, 106753, (2023). [CrossRef]

[27] Li, M., Huang, C. and Wang, P. Galerkin finite element method for nonlinear fractional Schrödinger equations. *Numerical Algorithms*, 74, 499-525, (2017). [CrossRef]

[28] Zafarghandi, F.S., Mohammadi, M., Babolian, E. and Javadi, S. Radial basis functions method for solving the fractional diffusion equations. *Applied Mathematics and Computation*, 342, 224-246, (2019). [CrossRef]

[29] Alexander, C.K. *Fundamentals of Electric Circuits*. McGraw-Hill, (2013).

[30] Kaczorek, T. and Rogowski, K. Positive fractional electrical circuits. In *Fractional Linear Systems and Electrical Circuits* (Vol. 13) (pp. 49-80). Switzerland: Springer Cham, (2015). [CrossRef]

[31] Ibrahim Nuruddeen, R., Gómez-Aguilar, J.F., Garba Ahmad, A. and Ali, K.K. Investigating the dynamics of Hilfer fractional operator associated with certain electric circuit models. *International Journal of Circuit Theory and Applications*, 50(7), 2320-2341, (2022). [CrossRef]

[32] Bhrawy, A.H., Baleanu, D., Assas, L.M. and Tenreiro Machado, J.A. On a generalized Laguerre operational matrix of fractional integration. *Mathematical Problems in Engineering*, 2013, 569286, (2013). [CrossRef]

[33] Dimitrov, D.K., Marcellán, F. and Rafaeli, F.R. Monotonicity of zeros of Laguerre–Sobolev-type orthogonal polynomials. *Journal of Mathematical Analysis and Applications*, 368(1), 80-89, (2010). [CrossRef]

[34] Avcı, İ. Numerical simulation of fractional delay differential equations using the operational matrix of fractional integration for fractional-order Taylor basis. *Fractal and Fractional*, 6(1), 10, (2021). [CrossRef]

[35] Diethelm, K., Ford, N.J. and Freed, A.D. Detailed error analysis for a fractional Adams method. *Numerical Algorithms*, 36, 31-52, (2004). [CrossRef]

Mathematical Modelling and Numerical Simulation with Applications (MMNSA)
(https://dergipark.org.tr/en/pub/mmnsa)